10/10-31-94 OSTI

SANDIA REPORT

SAND94—2572 • UC—706
Unlimited Release
Printed September 1994

High Frequency Current Sensors Using the Faraday Effect in Optical Fibers

R. W. Cernosek

Prepared by
Sandia National Laboratories
Albuquerque, New Mexico 87185 and Livermore, California 94550
for the United States Department of Energy
under Contract DE-AC04-94AL85000

Approved for public release; distribution is unlimited.

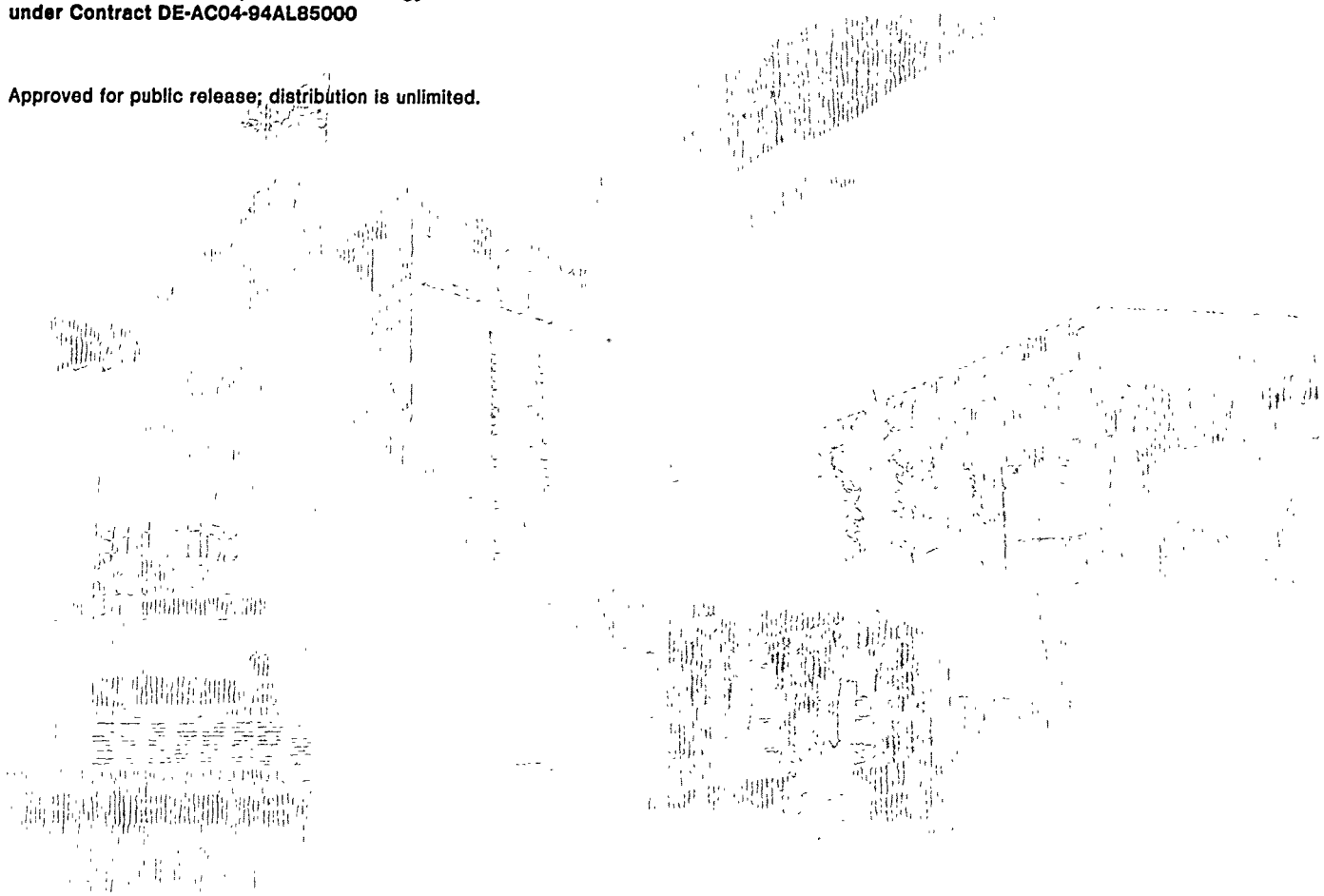

DISTRIBUTION OF THIS DOCUMENT IS UNLIMITED

Issued by Sandia National Laboratories, operated for the United States Department of Energy by Sandia Corporation.

NOTICE: This report was prepared as an account of work sponsored by an agency of the United States Government. Neither the United States Government nor any agency thereof, nor any of their employees, nor any of their contractors, subcontractors, or their employees, makes any warranty, express or implied, or assumes any legal liability or responsibility for the accuracy, completeness, or usefulness of any information, apparatus, product, or process disclosed, or represents that its use would not infringe privately owned rights. Reference herein to any specific commercial product, process, or service by trade name, trademark, manufacturer, or otherwise, does not necessarily constitute or imply its endorsement, recommendation, or favoring by the United States Government, any agency thereof or any of their contractors or subcontractors. The views and opinions expressed herein do not necessarily state or reflect those of the United States Government, any agency thereof or any of their contractors.

Printed in the United States of America. This report has been reproduced directly from the best available copy.

Available to DOE and DOE contractors from
Office of Scientific and Technical Information
PO Box 62
Oak Ridge, TN 37831

Prices available from (615) 576-8401, FTS 626-8401

Available to the public from
National Technical Information Service
US Department of Commerce
5285 Port Royal Rd
Springfield, VA 22161

NTIS price codes
Printed copy: A11
Microfiche copy: A01

DISCLAIMER

Portions of this document may be illegible in electronic image products. Images are produced from the best available original document.

SAND94-2572
Unlimited Release
Printed September 1994

Distribution
Category UC-706

HIGH FREQUENCY CURRENT SENSORS USING THE FARADAY EFFECT IN OPTICAL FIBERS

R. W. Cernosek
Microsensor Research and Development Department
Sandia National Laboratories
Albuquerque, NM 87185

ABSTRACT

This study investigates the high frequency response of Faraday effect optical fiber current sensors that are bandwidth-limited by the transit time of the light in the fiber. Mathematical models were developed for several configurations of planar (collocated turns) and travelling wave (helical turns) singlemode fiber sensor coils, and experimental measurements verified the model predictions. High frequency operation above 500 MHz, with good sensitivity, was demonstrated for several current sensors; this frequency region was not previously considered accessible by fiber devices.

Planar fiber coils in three configurations were investigated: circular cross section with the conductor centered coaxially; circular cross section with the conductor noncentered; and noncircular cross section with arbitrary location of the conductor. Centered, circular coil sensors have a frequency response easily characterized by light transit time. In this category, a 20-turn, 6.4mm diameter annealed fiber sensor was tested up to 1 GHz. It has a 3dB bandwidth of approximately 230 MHz and a sensitivity-bandwidth product of approximately 0.8 MHz-°/A. Both noncentered coils and noncircular coils exhibit a resonant response at the higher frequencies that mimics the response of tapped, recirculating fiber delay lines. Coils with large eccentricity in the cross section feature the same sensitivity in the resonance bands as they do at low frequencies. This frequency response was successfully modeled using a point interaction between the magnetic field and the light in the fiber.

The helical travelling wave fiber coils were immersed in the dielectric of a coaxial transmission line to improve velocity phase matching between the field and light. Three liquids (propanol, methanol, and water) and air were used as transmission line dielectrics. Complete models, which must account for liquid dispersion and waveguide dispersion from the multilayer dielectric in the transmission line, were developed to describe the Faraday response of the travelling wave sensors. Large enhancements in current sensor bandwidth are possible without a loss in system sensitivity. A maximum bandwidth of approximately 300 MHz was achieved in a water-dielectric sensor cell containing a 14-turn coil with a 3 cm diameter and a 3 cm helical pitch. This sensor has a sensitivity-bandwidth product of approximately 1.08 MHz-°/A.

Other travelling wave current sensors with potentially greater Faraday sensitivity, wider bandwidth and smaller size are investigated using the theoretical models developed for the singlemode fiber coils.

MASTER

DISTRIBUTION OF THIS DOCUMENT IS UNLIMITED

ACKNOWLEDGEMENTS

The author gratefully acknowledges the support and assistance of the following people and organizations:

Dr. Michael A. Butler for his technical support on many theoretical and experimental problems;

Kent B. Pfeifer for his technical assistance and laboratory support;

The Project Machining and Ceramic Processing Organizations for their fabrication of devices and fixtures;

The Electromagnetic Test and Analysis Organization for their assistance in device design and characterization;

Dr. Kenneth C. Jungling of the University of New Mexico for his technical direction; and.

Drs. Gordon W. Day and Allen J. Rose of the National Institute of Standards and Technology in Boulder, Colorado for their technical advice on optical fiber current sensors and their support in the fabrication and testing of the annealed fiber sensor

TABLE OF CONTENTS

LIST OF FIGURES

LIST OF TABLES

CHAPTER 1

INTRODUCTION

The use of optical methods to measure environmental parameters and physical quantities is becoming highly commonplace in today's technology. Optical sensors, or more commonly photonic or fiber optic sensors, can perform very sensitive measurements often with the inherent speed afforded by the optical processes and with the added advantage of making remote and nonperturbing interrogations. In recent years, photonic sensing has found use in applications for characterizing electromagnetic (EM) quantities [1-3]. Here, the reduced interference of the optical or dielectric media serves a dual purpose: the presence of the instrumentation, or sensor, does not perturb the environment being measured like conductive materials often can; and the measurement itself is EMI (electromagnetic interference) -proofed, the environment does not perturb the measurement. This property has been the main reason that optical technology is being developed for detection of EM parameters, since in general, photonic sensors have yet to attain the high frequency sensitivities or the sensitivity-bandwidth products achieved by the conventional techniques. This is particularly true for electrical current sensors. Wideband operation that extends well into the microwave region (beyond 500 MHz) is desired while maintaining reasonable current detection sensitivity.

Conventional wideband electrical probes use an inductive loop or inductive transformer to sense current. These devices are quite sensitive, capable of measuring less than 1 mA near their upper frequency limit of ~ 1 GHz [4]. However, extending probe frequency response much beyond 1 GHz is unlikely due to the inductance associated with the transduction technique. Other conventional methods exist that measure steady state currents at RF and microwave frequencies (tens of GHz); most have applications for determining weapon component susceptibility and ordnance safety. These probes sense the thermal rise produced by Joule heating when current passes through a resistance point

in the conduction path. Most common are electrical thin film thermocouples and thermistors used to measure currents in electroexplosive devices (EEDs) [5]. Fiber optic thermometric techniques have been developed that replace the thermocouple/thermistor to determine currents and powers in EEDs or substitute resistors [6]. These hybrid optical-electrical sensors still incur some signal perturbations, and since they record only the magnitude of the RF currents they are incapable of measuring transients faster than the thermal response time.

Two competing optical techniques can be used to measure magnetic field or current waveforms: magnetostriction and Faraday rotation. Each has its advantages [3], and both have been adapted to optical fiber current sensing. In magnetostrictive sensors [7] an external magnetic field produces a deformation or strain in a magnetostrictive material that is in intimate contact with a singlemode fiber. The strain is transferred to the fiber creating perturbations in geometry and refractive index. Deviations in the optical path length are sensed interferometrically. This technique is quite sensitive; magnetic fields as small as 0.07 $pT/\sqrt{Hz}$ have been detected [8]. However, bandwidths are generally limited to a few tens of kilohertz because of the mechanical movement required in the magnetostrictive material. Sensors with frequency response beyond 1 MHz have been constructed by mixing the signal with a field from an RF oscillator [9]; the detection band is shifted to a higher center frequency but the detection bandwidth remains unchanged.

The Faraday effect, on the other hand, is an inherently fast optical process in most materials. In the sensing medium, the magnetic field produces a rotation in the plane of polarization of the propagating light. Field and current sensors which exploit this fast process have been reported [10-14]. Measurement at frequencies above 1 MHz are easily accomplished, although response sensitivities do not approach those of the magnetostrictive sensors. The strength of the Faraday interaction is relatively weak in most materials. Common silica optical fibers exhibit particularly small rotations per unit

length. As a result, fiber sensors have mainly been used to measure kiloampere or megampere currents [15] most notably produced in the power generation [16-17] and fusion research [11,18-20] industries. (In these applications high electrical isolation is definitely a benefit.)

Much effort in recent years has concentrated on improving the sensitivity of Faraday effect fiber current sensors. Sensitivity is improved by increasing the interaction length between the field and the light or by using materials that produce a larger Faraday rotation per unit length (possess a larger Verdet constant). Longer fiber lengths, however, often lead to large, bulky sensors while limiting bandwidth due to light transit time. Recent investigations into fiber annealing [21,22], circularly-birefringent [23] and elliptically-birefringent [24] singlemode fibers, higher Verdet constant fibers [25-27], and other special fiber processes [28,29] have allowed for the fabrication of small, sensitive multiturn coils and provided the direction needed to achieve subampere current detection using optical fiber systems.

Other material studies have identified the ferromagnetic (or ferrimagnetic) crystals such as the iron garnets [12,13,30,31] and paramagnetic crystals such as CdMnTe [10,32] as possessing excellent Faraday sensitivity for field sensing applications. Rotation sensitivity in these crystals exceed that in silica by more than three orders of magnitude. Also, one current sensor configuration has recently been developed using the ferromagnetics [30]. The huge increase in detection sensitivity, however, often means that frequency response is reduced due to the required reorientation times of the magnetic ions or domains in the optical material.

The tradeoff between sensitivity and bandwidth is apparent in all classes of magneto-optic materials and processes and, subsequently, in any field or current sensor that utilizes them. Diamagnetic glasses and crystals (silica fibers belong to this group) have small Faraday sensitivities but possess extremely wide material bandwidths. For this reason, optical fiber current sensors are always limited in high frequency response by

the transit time of the light through the fiber. Thus, tradeoffs between sensitivity and bandwidth require compromising on fiber length. For most applications the required current detection sensitivity determines the fiber and coil parameters and response bandwidth is estimated from the fiber length. This practice is widely accepted, and little attention is given to bandwidth considerations during sensor design unless large currents are being detected. However, many current monitoring applications require wideband detection of milliampere-level signals. Faraday effect sensors, and particularly optical fiber sensors, have the potential to fill these needs should their high frequency response be better understood.

A formal characterization of the frequency response of fiber current sensors, including expressions for 3 dB bandwidth and the sensitivity-bandwidth relationship, has recently been presented [33]. The theoretical discussions in Ref. 33 are mostly limited to the simplest of fiber sensor coils, those that are circular and concentric with the current conductor. In addition, experimental measurements are performed on a single coil at frequencies up to 5 MHz, which is limited to just above the sensor 3 dB bandwidth.

In this study a complete picture is given for the high frequency response of Faraday effect fiber current sensors. Theoretical models are generated and response functions are measured for many different fiber coil configurations. These include sensors with planar, circular coils centered on the axis of the current conductor; circular sensing coils with the axes displaced from that of the conductor; noncircular or elongated fiber coils with concentric and displaced axes; and helical coils aligned coaxially with the conductor. Varying coil diameters and the number of coil turns further extends each category. Many other configurations (some of them non-physical) are explored theoretically to provide further insight into current sensor models. Measurements are made for frequencies between 1 MHz and 1 GHz. For many sensor coils this represents frequencies well above the 3 dB bandwidth and the response function cutoff frequency. Fiber current sensing in this frequency range has not been demonstrated or reported

previously.

Planar fiber coil sensors — those with collocated or closely assembled turns — have well-defined bandwidths as determined primarily by light transit time. Manipulations of the coil cross section or off-center placement of the conductor axis within the coil introduces response resonances at higher frequencies. These can be exploited for narrowband current sensing; demonstration of the technique is performed at frequencies above 500 MHz. Within the high frequency bands, relative increases in detection sensitivity occur, while the bandwidth remains as described by the lower frequency response.

The fundamental bandwidth limitation dictated by the light transit time in the fiber current sensor can be overcome by using travelling wave techniques. Improved phase matching between the propagating magnetic field and the light in the fiber is accomplished by spreading the coil turns in a helix then immersing the coil in the dielectric of a coaxial transmission line. This can be accomplished without a loss in measurement sensitivity, thereby increasing the sensitivity-bandwidth product of the Faraday effect current sensor. Demonstrations of the technique use liquids as the dielectric medium in the slow-wave transmission line structure. Measured bandwidths of 300 MHz with bandwidth enhancements of greater than four (compared to planar coils) are reported. Because of the orientation of the magnetic field relative to the light in the fiber, phase matching in a Faraday effect travelling wave current sensor is much more difficult to achieve than in electro-optic travelling wave field sensors. Perfect phase matching is virtually impossible to attain, although an optimum set of sensor travelling wave parameters exists such that large bandwidth enhancements are achievable.

Following this introduction, Chapter 2 gives an overview of the Faraday effect in bulk optics and optical fibers with specific applications to current sensing. Limitations on measurement sensitivity and bandwidth are discussed in relation to material properties, fiber birefringences, and common system noise sources. Chapter 3 presents

the general theoretical description of the frequency dependence of the Faraday rotation in fiber current sensors when light transit time through the fiber is the constraining factor. These mathematical developments are then continued in the later chapters as specific model responses are generated for particular fiber sensor coil configurations. After Chapter 3, this document branches in two fundamental directions. Chapters 4 through 7 cover fiber current sensors that utilize planar coils, while Chapters 8 through 12 discuss travelling wave fiber sensors with helically shaped coils.

The details of experimental hardware and procedures are presented in Chapter 4. Included among the hardware is the expanded coaxial transmission cells that contain the fiber coils and produce the magnetic fields [34]. Additional discussion about these cells is given in Appendix A. Many of the apparatus and procedural details related in Chapter 4 and Appendix A also apply to the travelling wave sensors. Starting with Chapter 5, mathematical models and experimental measurements of the frequency dependent Faraday response are presented for specific categories of fiber coil configurations. Chapter 5 covers circular coil sensors with the current conductor centered in the coil cross section. Several coils with varying geometry are characterized, highlighted by testing of a small diameter (6.4 mm) annealed coil sensor. Noncentered, circular coil sensors are discussed in Chapter 6. This discussion includes theoretical response predictions for a sensor system with the conductor totally outside the coil cross section. Chapter 7 presents fiber coils with noncircular cross sections. "Delta function" or point interaction models are developed from a highly eccentric coil geometry. Rectangular coils are used to describe the Faraday response in generic noncircular fiber sensors. Important in the accurate determination of current sensor frequency response is the inclusion of effects due to the fiber coil leads. Appendix B gives an exact mathematical treatment of these lead effects for a planar coil geometry.

Chapter 8 begins the study of the travelling wave fiber current sensors with a discussion of the basic sensing concepts. Bandwidth enhancement is a key element in the

use of the travelling wave configurations and performance criteria are established in this chapter. The experimental travelling wave transmission cells are presented in Chapter 9. Cells contain either air as a dielectric or one of three liquid dielectrics: 1-propanol, methanol, or water. The peculiarities associated with precise sensor response modeling for the liquid travelling wave structures are detailed in Chapter 10. Complete models are developed and include effects created by liquid dispersion, waveguide dispersion and multimoding in the coaxial transmission cells, and relative permittivity perturbations due to fiber coil supports. Mathematical supplements to the models are provided by Appendices C and D which derive the effective relative permittivity in the coaxial lines and the waveguide modes in a multilayer dielectric coaxial line with complex relative permittivity. Chapter 11 presents the experimental measurements using the fiber travelling wave sensors and compares the Faraday response data to model predictions.

Further enhancements to the bandwidth and high frequency response of Faraday effect current sensors are discussed in Chapter 12 for several other travelling wave configurations. These include solid dielectric coaxial transmission line structures, combination travelling wave/noncentered (or noncircular) fiber coil sensors, helical waveguide sensors using higher sensitivity materials, bulk-optic helical-conductor travelling wave sensors, and a serpentine, planar waveguide in an RF stripline. Finally, Chapter 13 summarizes the high frequency response model predictions and experimental measurements for all planar and travelling wave fiber current sensors.

CHAPTER 2

FARADAY EFFECT CURRENT SENSORS

The Faraday effect is an induced circular birefringence created by a magnetic field interacting with an optical medium [35]. The resulting rotation of the plane of polarization, Θ, of light propagating in a medium of length L is described (in MKS units) by

$$\Theta = V \int_0^L \mathbf{B} \cdot d\mathbf{l} \ . \tag{2-1}$$

Only that component of the magnetic flux density, **B**, which lies in the direction of the incremental length, dl, of the light propagation contributes to the effect. The proportionality factor, V, is the Verdet constant and determines the strength of the interaction created by the field. The Verdet constant is a material parameter that is also dependent upon the temperature [36], the wavelength of the propagating light and the modulation frequency of the magnetic field [37,38]. Verdet constants for some common materials used in sensors are given in Table 2-1 [39,40].

Current sensors using the Faraday effect can be quite simple. Ampere's law states that for a static magnetic field **H**, the current, i, is given by

$$i = \oint \mathbf{H} \cdot d\mathbf{l} \ . \tag{2-2}$$

Thus, allowing the interrogating light beam to propagate in a loop around the current conductor produces a rotation that is independent of the beam path. Optical fibers wound in a coil represent an ideal method for directing light around a current carrier. Multiple

Table 2-1.

Verdet Constants for Several Materials Used in Faraday Effect Sensors. Parameters were measured at a wavelength of 633 nm and at 25 °C. (Refs. 39,40).

Material	Type	V (rad/T/m)
$Cd_{1-x}Mn_xTe$	Paramagnetic Crystal	~2000
ZnSe	Diamagnetic Crystal	118
$Bi_4Ge_3O_{12}$	Diamagnetic Crystal	28.8
FR-5	Paramagnetic Glass	-71
FR-4	Paramagnetic Glass	-30.5
SiO_2	Diamagnetic Glass	3.6
SF-57	Diamagnetic Glass	20

turns of the fiber have the effect of amplifying the resulting Faraday rotation. Such a sensor has a rotation described simply by

$$\Theta_0 = \mu_f V N i \ , \tag{2-3}$$

where μ_f is the permeability of the interaction medium, usually taken to be that of free space since materials are typically nonmagnetic dielectrics, and N is the number of loops of optical fiber. Sensitivity to currents can be enhanced even further by using several turns of the conductor through the optical fiber coil to increase the magnetic field. The zero subscript used in Eq. (2-3) denotes the dc or low frequency rotation produced by a static or slowly-varying magnetic field. If the amplitude of the field changes

significantly in the time it takes the light to traverse the closed path, then Ampere's law, Eq. (2-2), is no longer valid.

A typical current sensing system using an optical fiber [41] is shown in Fig. 2-1. The light output from a laser source is passed through a polarizer injecting linearly polarized light into the fiber. Light exiting the fiber is analyzed with a second polarizer converting induced rotations to transmitted intensity changes that can be detected by the photodiode receiver. The sensing fiber must be singlemode in order to preserve the instantaneous polarization state of the light. The measured light intensity, I, for the system in Fig. 2-1 when the polarizers are aligned is given by

$$I = I_0 \cos^2 \Theta_0 \ , \tag{2-4}$$

where I_0 is the maximum transmitted light intensity and Θ_0 is taken from Eq. (2-3). For a system using crossed polarizers, the transmitted intensity is

$$I = I_0 \sin^2 \Theta_0 \ . \tag{2-5}$$

For this case, the relative intensity is zero with no current. The intensity reaches a

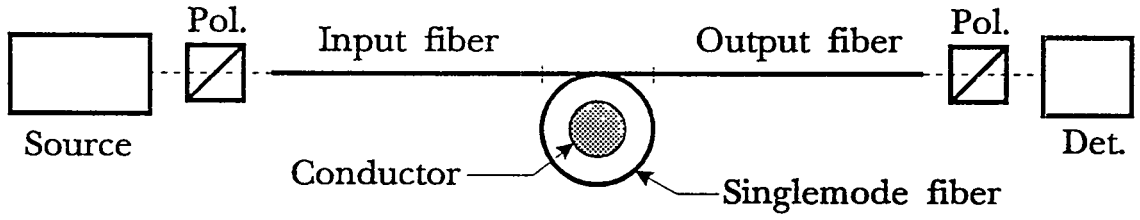

Fig. 2-1. A simple optical fiber system for Faraday effect current sensing. This polarimetric configuration uses singlemode fiber between input and output polarizers.

maximum when a current is present that produces a rotation of $\Theta_0 = \pi/2$, or odd multiples of $\pi/2$. It is obvious from Eqs. (2-4) and (2-5) that a measured intensity could represent any number of currents. This has an advantage in current sensing since saturation cannot occur as in magnetic core current probes. However, difficulties can be encountered when determining large currents where several of these intensity "fringes" are observed. Usually in this case, two polarization states 45° apart are monitored simultaneously at the fiber output [42]. A ratio of the two detected signals gives an unambiguous determination of the current. The relative intensity response of the fiber sensor in Fig. 2-1 is plotted in Fig. 2-2 as a function of measured current. The effect of several polarizer configurations are shown.

Small currents are measured with the greatest sensitivity in a system using input and output polarizers oriented at $\pi/4$ (45°) with respect to one another. The transmitted relative intensity at zero current (see Fig. 2-2) is biased to ½, and bipolar current signals produce an increase or decrease in intensity about this point. More importantly, the intensity slope, dI/di, is maximum. If the currents are small enough so that rotations are much less than $\pi/4$, then measured changes in intensities are linear with changes in current. From Fig. 2-2, polarizers aligned at +45° and -45° produce equivalent intensity changes but with different signs. Sensing both of these polarization states simultaneously and then taking the difference in intensities produces a measurement with twice the sensitivity. A system incorporating this scheme is identical to that in Fig. 2-1, except the output polarizers and detectors are arranged as in Fig. 2-3. The polarizing beam splitter selects the orthogonal polarization components, one for each photodiode receiver. This system has a response with rotation, or current, of

$$I = I_0 \sin(2\Theta_0) \ . \qquad (2\text{-}6)$$

Using this differential detection scheme also reduces system common mode relative

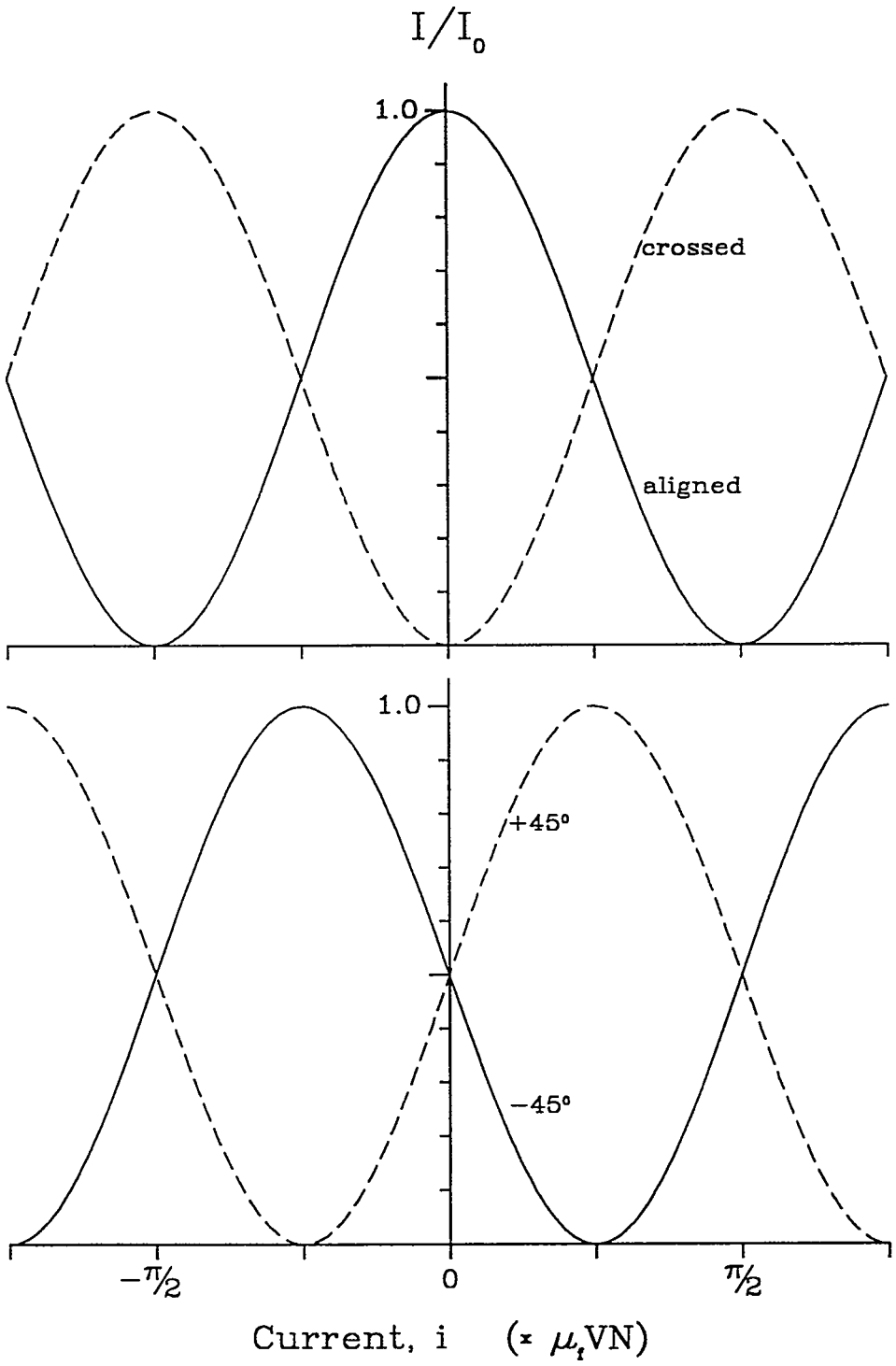

Fig. 2-2. The relative intensity response versus current for a polarimetric fiber current sensor. (Top) With polarizers aligned and crossed. (Bottom) With polarizers oriented at ± 45° to one another.

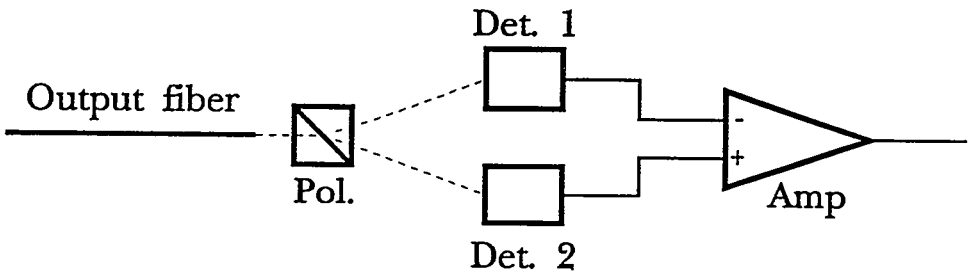

Fig. 2-3. The optical output in Fig. 2-1 is split using a beam-splitting polarizer or a Wollaston prism for dual polarization detection.

intensity noise such as carrier fluctuations in semiconductor diode lasers.

In addition to the polarimetric sensing schemes illustrated in Figs. 2-1 and 2-3, optical fiber Faraday effect current sensors can also be constructed using interferometers. In particular, the Sagnac interferometer [43], shown in Fig. 2-4, provides a very simple method for sensing currents. The counter-propagating beams in the fiber are rotated nonreciprocally by the magnetic field resulting in a doubling of the detected response compared to the polarimetric sensor. Reciprocal effects produced by some noise sources (e.g., laser phase noise and stress-induced polarization changes from temperature drift), however, are inherently compensated for when the two signals are combined at the fiber coupler. The Sagnac interferometric sensor also has the advantage of not requiring external polarizers. Its greatest drawback is that the response is likened to that of crossed polarizers in the polarimetric current sensor. The detected intensity is zero with zero slope, as shown in Fig. 2-2, when no current is present. Recently, current sensors that use the fiber Sagnac interferometer with a 3 x 3 fiber coupler have been studied [44]. With this system, it is possible to bias the zero current response to a relative intensity of 1/3, with a nonzero response slope. This fiber current sensor has many advantages for detection of small currents.

Faraday effect current sensors are not limited to optical fibers, although working

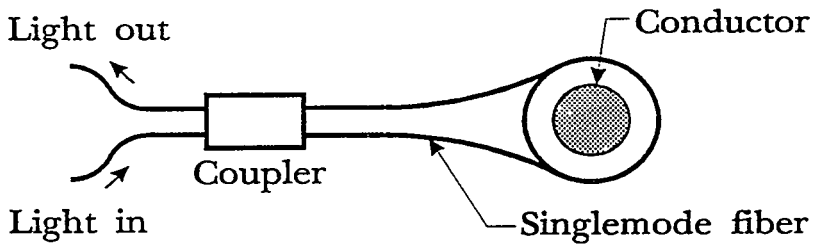

Fig. 2-4. A fiber Sagnac interferometer configured as a Faraday effect current sensor. The fiber coupler launches two counter-propagating beams of light that are recombined at the coupler output for optical detection.

with fibers is usually much easier. Several glasses have been used to construct sensors that either slip around a current conductor or have the conductor pass through a hole in them [45,46]. Also, a Ga:YIG (ferromagnetic crystal) sensor, consisting of four separate rods that form a path around the conductor, has been developed [30]. For these bulk optic sensors, materials are selected that have much higher Verdet constants or much larger rotations per unit field than a silica fiber. This leads to a more sensitive current detection system. Fibers are still necessary to transport light to and from the basic sensor, and lenses and other optical elements are required to collimate and direct the light through the bulk glass.

Sensor Sensitivity

Faraday effect optical fiber current sensors do not always have an ideal response that is only dependent on the optical rotation. Singlemode fibers are a birefringent medium and controlling the exact state of polarization of the propagating light is difficult [47,48]. Stress introduced in the fiber during manufacturing or simply by winding it into a coil creates a linear birefringence, or retardance, that is coupled to the circular birefringence produced by the Faraday rotation. This effect can mask the rotation, resulting in loss of sensor sensitivity. Inherent stresses due to manufacturing can be

reduced significantly through careful processing [49]; however, bending stresses cannot be reduced quite so easily. Fortunately, the linear birefringence induced by bending is controllable and well defined [50]. For a fiber under zero tension, the bend-induced birefringence per unit length is given as

$$\Delta\beta = K_\lambda \frac{r_f^2}{R^2} \quad , \tag{2-7}$$

where r_f is the fiber radius, R is the bend or coil radius and K_λ is a parameter related to the stress-optic coefficient and dependent upon the fiber material and the wavelength of light. For a silica fiber with $\lambda = 633$ nm (HeNe laser light), $K_\lambda = 7.7 \times 10^7$ deg/m.

In a linearly birefringent medium, the effects of Faraday rotation are best expressed as an operation on the complex field amplitudes, E_x and E_y. Using the Jones Calculus, these amplitudes are described by [51]

$$\begin{vmatrix} E_x(z) \\ E_y(z) \end{vmatrix} = \begin{vmatrix} A & -B \\ B & A^* \end{vmatrix} \begin{vmatrix} E_x(0) \\ E_y(0) \end{vmatrix} \quad , \tag{2-8a}$$

$$A = \cos\left(\frac{\phi'}{2}z\right) - j\frac{\Delta\beta}{\phi'}\sin\left(\frac{\phi'}{2}z\right) \quad , \tag{2-8b}$$

$$B = \frac{2F}{\phi'}\sin\left(\frac{\phi'}{2}z\right) \quad , \tag{2-8c}$$

and

$$\left(\frac{\phi'}{2}\right)^2 = \left(\frac{\Delta\beta}{2}\right)^2 + F^2 \quad . \tag{2-8d}$$

Here, $\Delta\beta$ is the total retardance per unit length and F is the total Faraday rotation per unit length. The field amplitudes are assumed to have a known state at $z = 0$, the entrance to

the fiber coil. The axes for linear birefringence are also assumed to remain constant throughout the fiber coil, with the fast axis in the plane of the fiber bend. From Eqs. (2-8), it is seen that if $F >> \Delta\beta$, the operation on the field amplitudes is a pure rotation. Conversely, if $\Delta\beta >> F$, $B \rightarrow 0$ and a pure retardance results. Under the latter condition, the sensing of Faraday rotation can be quenched.

The effects of linear birefringence in the fiber sensor coil can be reduced in several ways. Twisting of the optical fiber along its axis introduces a circular birefringence that acts to bias the sensor response to Faraday rotation [47,52]. The twisting rotation per unit length, Ω', is given by

$$\Omega' = g' \xi_f \quad , \tag{2-9}$$

where ξ_f is the number of twists per unit length and g' is a material dependent parameter. At λ = 633 nm, $g' \approx 0.08$. The rotation induced by twisting adds algebraically to the field-induced Faraday rotation to produce the quantity, F, required for Eqs. (2-8). Since twisting has a nonsymmetric effect on bipolar signals, it is important that care be taken in sensor coil design.

In general, most commercially available optical fibers can withstand a twist rate of 50 turns per meter [15]. This is more than adequate to offset the effects of linear birefringence in large diameter coils, but in fiber coils produced of many small turns, it is not sufficient. More rotation can be achieved through the use of circularly and elliptically birefringent optical fibers. A circularly birefringent fiber is manufactured with a helical core [23]; elliptically birefringent fibers are produced from high linearly birefringent fiber by spinning the preform during the fiber pulling process [24,53]. Current sensors constructed from these fibers have led to relatively high sensitivity measurements.

The linear birefringence in small multiturn fiber coils can essentially be

eliminated through annealing [21, 22, 54]. The fiber is wound in the desired geometry, heated to near the glass softening point and then returned slowly to room temperature. The annealed coil retains its predetermined configuration but has orders of magnitude less linear birefringence with only a slight increase in attenuation. Fiber sensors produced using this technique have resulted in the highest sensitivity measurements to date, noise equivalent currents of ~100 $\mu A/\sqrt{Hz}$ for 188 turns of silica fiber in a coil 1 cm in diameter [54].

Improved sensitivity is also possible through the use of higher Verdet constant optical materials. Many materials are available that have a much greater current measurement potential than do silica fibers (see Table 2-1). Attempts have been made to produce optical fibers from special glasses [25], such as FR-5, and from silica with high concentrations of rare earth dopants [26,27]. In general, the resulting fibers have contributed little to sensor applications because of large increases in fiber attenuation, increased linear birefringence resulting from the manufacturing process or only minor improvements in Verdet constant for dopants in a stable glass matrix. Should production of quality higher Verdet constant fibers become prossible, one material in particular is of interest: SF-57 glass [45], with a Verdet constant 5.5 times that of silica and with a stress-optic coefficient (for reduced bend birefringence) about 100 times less.

Bulk optic sensors have been fabricated from the diamagnetic materials SF-57 glass and polycrystalline ZnSe [46]. These devices show increases in Faraday rotation that reflect their larger Verdet constants. Most bulk materials have been used for magnetic field sensors, but configurations for current sensors have been developed [45,46]. Temperature dependence of the Verdet constant and thermal expansion of the optical material set a limit on the measurement precision of the Faraday rotation. Diamagnetic materials are typically less temperature dependent than paramagnetic or ferromagnetic materials [35] which often makes them more desirable for sensor applications. A compensation mechanism for reducing the temperature dependence in

diamagnetic materials through use of input polarization control has also been developed [55].

For greater Faraday sensitivity, the paramagnetic materials with even larger Verdet constants can be used. One in particular is the dilute magnetic semiconductor, $Cd_{1-x}Mn_xTe$, which offers sensitivities as great as three orders of magnitude above that of silica [10,39,56]. Additionally, a wavelength of operation can be selected for a given Manganese concentration that results in temperature independent Faraday rotation [57]. Because of its crystalline structure, however, this material has yet to be adapted to current sensor applications. Devices have primarily been confined to small volume magnetic field sensors [10].

The largest Faraday rotations are produced in ferromagnetic (or ferrimagnetic) crystals [2,13,39]. The most notable ferromagnetics are the iron garnets (e.g., YIG. yttrium iron garnet). In these materials, an applied magnetic field aligns the magnetic dipoles of the individual domains. The specific rotation per unit applied field (equivalent to the Verdet constant in diamagnetic or paramagnetic materials) is the ratio of the saturation rotation, Θ_F^{sat}, to the saturation magnetic field, H_{sat}. This parameter is comparatively quite large, especially in the substituted iron garnets [12,58]. In 20% gallium substituted YIG (for the iron), Faraday sensitivity is reported to be 2.5×10^4 larger than in silica, which is approximately 20 times greater than in $Cd_{1-x}Mn_xTe$ [12]. High sensitivity magnetic field sensors have been constructed using YIG [13] and Ga:YIG [12], and small rods of Ga:YIG have been arranged around a conductor in a current sensor configuration [30]. By the nature of the ferromagnetic material, saturation magnetization can be a limiting factor [58]. However, for the measurement of small fields or currents, for which these materials would be targeted, this saturation limit should not interfere.

Ultimately, the sensitivity limit for a Faraday effect current sensing system will be established by noise levels. Sources of noise are fluctuations in optical power

throughout the system and shot and thermal noise in the optical receiver. Laser noise sources and polarization variations due to temperature or stress vibrations can be large, but through careful component selection and system design, these fluctuations can be reduced significantly. The minimum measurable currents will then depend upon the receiver characteristics, in particular, the average optical detector output current, i_{det}, and the amplifier feedback resistance, R_f. An expression for the noise equivalent current, NEI, given per unit root bandwidth [59], is

$$NEI = \frac{\sqrt{\frac{2k_B T}{R_f} + e\, i_{det}}}{2\mu_f V N\, i_{det}} , \qquad (2\text{-}10)$$

where k_B is Boltzmann's constant, T is the absolute temperature, e is the magnitude of the electron charge, and N is the number of turns in the fiber sensor coil. A plot of Eq. (2-10) for a single turn sensor coil with several values of the feedback resistor is shown in Fig. 2-5. For small values of the resistor, R_f, a slope of unity between NEI and the average detector current is approached, indicating dominant Johnson or thermal noise. For large resistor values, shot noise dominates and the curve approaches a constant slope of ½ for all detector currents. It is expected that average detector output currents are not likely to exceed about 1 mA, resulting in system NEIs of ~1 mA/$\sqrt{\text{Hz}}$/turn for the most sensitive fiber sensor systems [45]. Further improvements in system response can only be gained through more turns in the fiber coil or through the use of higher Verdet constant materials.

Sensor Bandwidth

The bandwidth of Faraday effect current sensors is limited by four basic factors: (1) the intrinsic response of the Faraday rotator material; (2) the response time of the

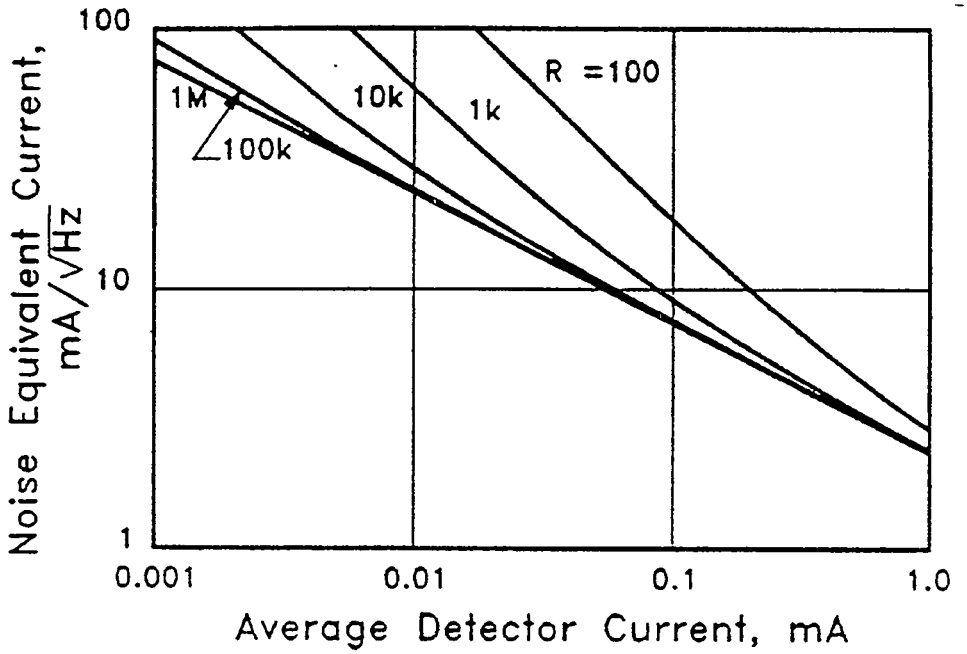

Fig. 2-5. The noise equivalent current per root unit bandwidth for a single turn fiber current sensor plotted as a function of the average detector output current. The effect of varying the feedback resistance in the transimpedance detection amplifier is shown.

photodiode and the bandwidth of the amplifier used in the receiver circuit; (3) the dispersion of the propagating light while passing through the sensing and transmitting medium; and (4) the transit time of the light propagating through the sensor material. For most sensor systems, items (2) and (3) are of little concern. Photodiodes with a few tens of picoseconds of response time are available as are amplifiers with greater than 10 GHz bandwidths. And since relatively short lengths of singlemode fibers and high quality glasses or crystals are used in sensor systems along with laser sources, dispersion effects should not begin limiting bandwidths until tens of gigahertz.

The intrinsic response in Faraday rotator materials is determined by the relaxation or spin reorientation time of the interacting magnetic ions or domains. Each class of materials — diamagnetic, paramagnetic and ferromagnetic — can have a different microscopic interaction mechanism for the Faraday effect, resulting in effective Verdet

constants that are widely distributed in frequency response. In some paramagnetic glasses and crystals the frequency dependent Faraday rotation, $\Theta_m(\omega)$, is described by a simple Debye relaxation function [37]

$$\Theta_m(\omega) = \frac{\Theta_m(0)}{\sqrt{1+\omega^2\tau_R^2}} \quad , \tag{2-11}$$

where $\Theta_m(0)$ is the zero frequency response of the material, $\omega = 2\pi f$ is the angular modulation frequency of the magnetic field, and τ_R is the material relaxation time constant. This model has been compared to measurements made on $Cd_{1-x}Mn_xTe$ sensors [38]. The frequency dependent Faraday rotation (effective Verdet constant) for the $Cd_{1-x}Mn_xTe$ system is shown in Fig. 2-6 for two different compositions. Different laser wavelengths were required for maximum Faraday response since the bandgap changes with composition. When the Manganese concentration is increased from 10% to 45%, the relaxation time decreases, resulting in nearly an order of magnitude increase in the frequency response.

In ferromagnetic materials, the frequency dependence of the Faraday effect is also highly dependent on composition [30,31]. Typically, the larger the enhancement of the localized magnetic field, the slower the movement of the domain walls. In Fig. 2-7, the frequency response is plotted for samples of pure YIG [13] and Ga:YIG [30]. The YIG sample has a -3 dB frequency of approximately 700 MHz, while the Ga:YIG sample has a bandwidth of ~ 7.5 MHz. These frequency responses scale inversely (though not linearly) with the increases in their relative Faraday sensitivities; the Ga:YIG has a significantly larger rotation per unit field.

In diamagnetic and paramagnetic glasses, the magnetic ion relaxation times are usually less than one picosecond [37]. Thus, in fiber current sensor systems where the singlemode fiber has been drawn from common glasses or glasses doped with magnetic

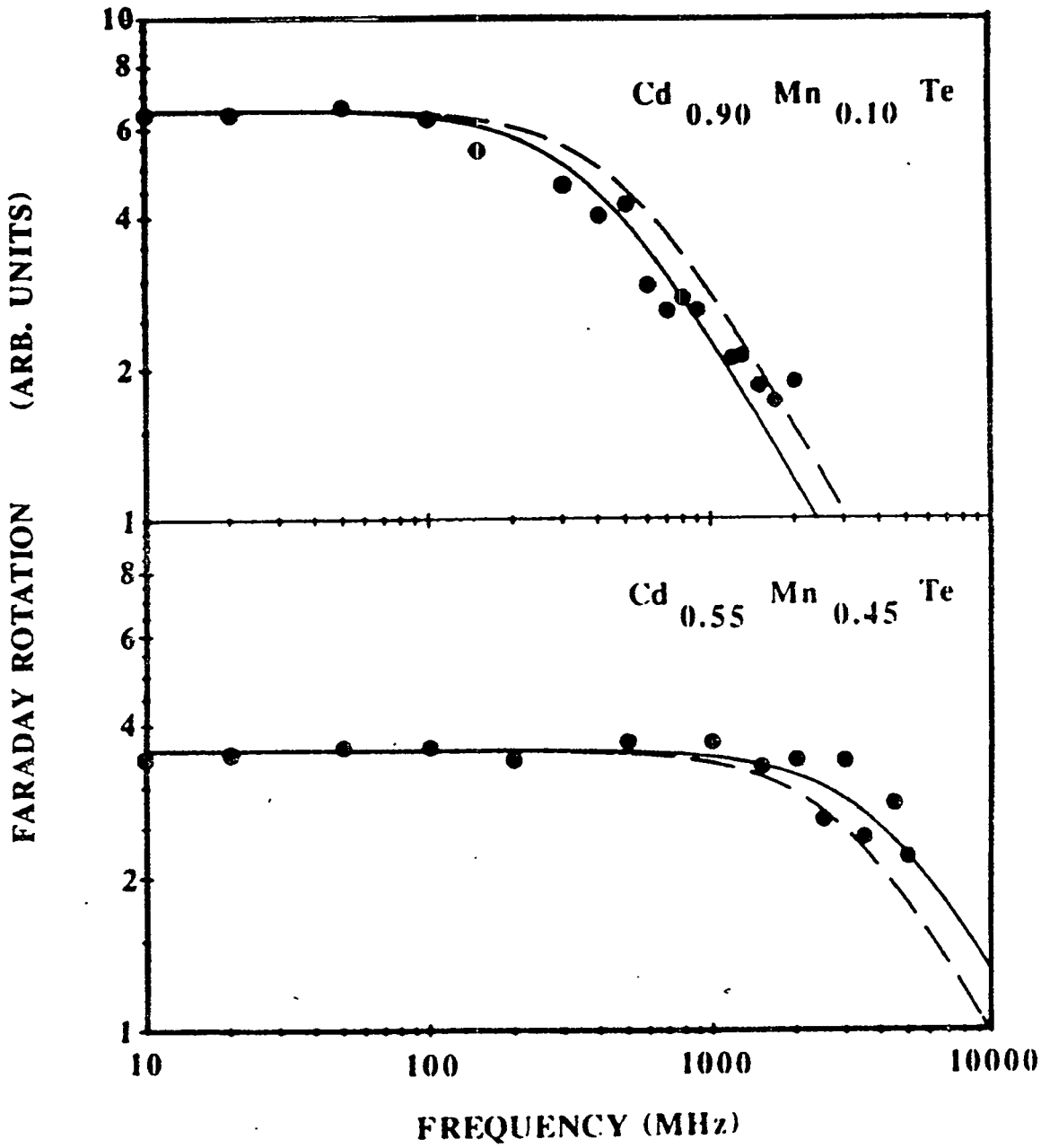

Fig. 2-6. Relative changes in the Faraday rotation versus frequency for two Manganese concentrations in $Cd_{1-x}Mn_xTe$ [38]. Each set of data was taken using a laser wavelength optimized for material response with that Mn concentration. Solid and dashed lines represent theoretical fits to the frequency dependence.

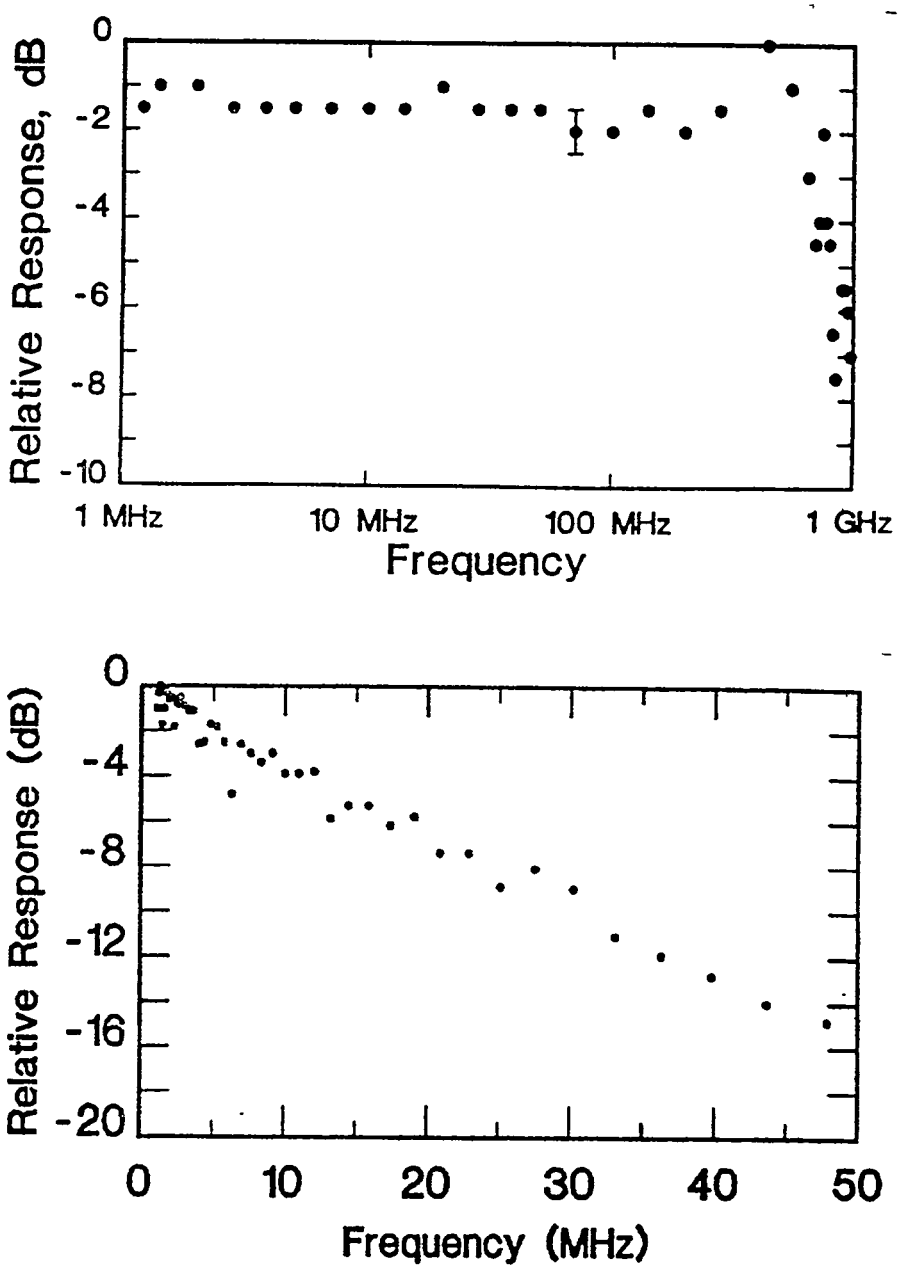

Fig. 2-7. The frequency response of the Faraday rotation for two compositions of YIG crystals. (Top) A 5 mm diameter by 3 mm long sample of pure YIG [13]. (Bottom) A 1.5 mm diameter by 5 mm long sample of Ga:YIG [30].

ions, it is safe to assume that intrinsic material frequency response will not be the limiting factor in system bandwidth. In most practical applications, the bandwidth will be constrained by the light transit time through the sensing material. This is particularly true for fiber sensors in which many turns have been used in a coil for increasing measurement sensitivity. In order for the rotation to be described by Eq. (2-3), the amplitude variations in the conducted current (or the associated magnetic field) must be small during the time it takes for the light to propagate from one end of the fiber coil to the other. Otherwise, changes in the field become convolved with the propagating light rotations. The dependence of fiber current sensor frequency response on the light transit time and the subsequent limitations on bandwidth are the subject of this study. Theoretical and experimental descriptions of the frequency dependent Faraday rotation for many current sensor configurations appear throughout the remainder of this document.

CHAPTER 3

TRANSIT TIME FREQUENCY RESPONSE THEORY

In order to derive an expression for the frequency dependent Faraday rotation, three assumptions are made about the optical fiber current measurement system: (1) the circular birefringence produced by the Faraday effect dominates the polarization state in the fiber; (2) the magnetic field propagating along with the current on the conductor is planar and azimuthally symmetric — in general, a transverse electromagnetic (TEM) wave; and (3) the current flowing along the conductor is treated as an infinitely long filament of moving charge centered at the conductor's longitudinal axis. The first assumption implies that any significant linear birefringence in the fiber has been removed through annealing or twisting so that uncharacteristic polarization shifts in the fiber are not convolved with the remaining electromagnetic interactions. And the last two assumptions assure that all points along the fiber that fall in a plane perpendicular to the conductor experience simultaneous exposure to the passing magnetic wave.

The magnetic flux density from the passing TEM wave has a spatial and temporal dependence given by

$$\mathbf{B}(r,t) = \frac{\mu_f i}{2\pi r} \, e^{-j(\omega t - \mathbf{k}\bullet\mathbf{l})} \, \hat{\phi} \quad , \tag{3-1}$$

where r is the radial distance from the conductor to the light element propagating in the fiber, $\omega = 2\pi f$ is the angular modulation frequency of the field, $\mathbf{k}$ is the propagation vector of the TEM wave pointing in a direction parallel to the conductor, $\mathbf{l}$ is the length vector for the fiber coil, and $\hat{\phi}$ is the unit vector in the azimuthal direction. In Eq. (3-1) the current, i, is taken to be static, or slowly varying with respect to ω. The fiber coil and its position relative to the conductor is allowed to be in many configurations. In general,

the coil will not have a circular cross section, the conductor will not be centered in the coil cross section, and the coil turns will not be collocated (allowed to form a helix). Thus, **B** and **dl** in Eq. (2-1) will not be codirectional as is the case for a circular coil with a centered conductor, and the vectors **k** and **l** in Eq. (3-1) will not be orthogonal as with a coil with collocated turns.

The angles formed between the field vectors and the light elements in the fiber are illustrated in Fig. 3-1. **B** and **dl** subtend an angle γ and **k** and **dl** subtend an angle ψ, so that

$$\mathbf{B} \bullet d\mathbf{l} = B \cos\gamma \sin\psi \, dl \quad , \tag{3-2}$$

and

$$\mathbf{k} \bullet \mathbf{l} = kl \cos\psi \quad . \tag{3-3}$$

Substituting the information from Eqs. (3-1) through (3-3) into Eq. (2-1) results in an expression for the frequency dependent Faraday rotation:

$$\Theta(\omega) = \frac{\mu_f V i}{2\pi} \int_0^L \frac{1}{r} \cos\gamma \sin\psi \; e^{-j(\omega t - kl\cos\psi)} \, dl \quad . \tag{3-4}$$

The wave propagation constant can be expressed as $k = \omega/v_{ph}$, where v_{ph} is the wave phase velocity (usually the speed of light in the medium surrounding the conductor). The surrounding medium totally immerses the fiber and may be a material other than air or vacuum. In general, the medium will have permittivity of ε and permeability of μ. Then the phase velocity is given by

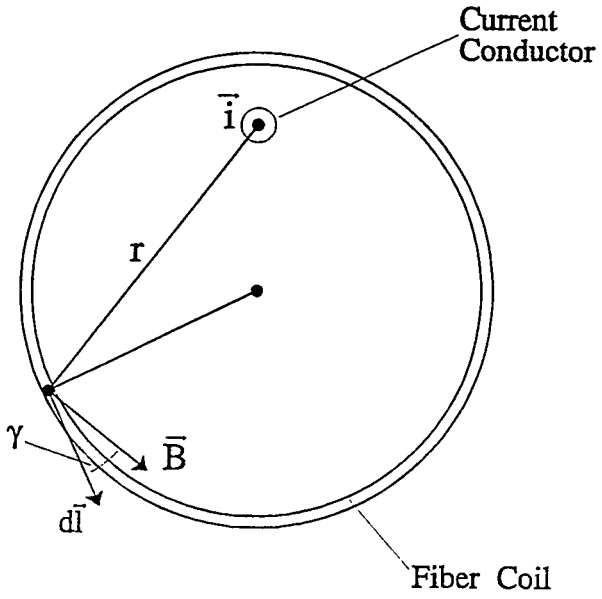

(a) Side View

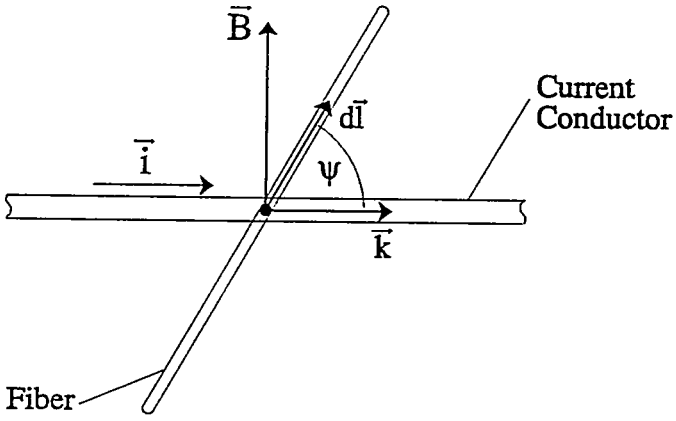

(b) Top View

Fig. 3-1. Angles formed between the light propagating in the fiber coil and the magnetic field associated with the conducted current.

$$v_{ph} = \frac{1}{\sqrt{\mu \varepsilon}} \quad . \tag{3-5}$$

Since $\varepsilon = \varepsilon_0 \varepsilon_r$ and $\mu = \mu_0 \mu_r$, where ε_0 and μ_0 are the free space permittivity and permeability, and ε_r and μ_r are the material relative permittivity and permeability, the phase velocity can be rewritten as

$$v_{ph} = \frac{1}{\sqrt{\mu_0 \varepsilon_0}} \frac{1}{\sqrt{\mu_r \varepsilon_r}} = \frac{c}{\sqrt{\mu_r \varepsilon_r}} \quad , \tag{3-6}$$

with c being the speed of light in a vacuum.

As the light in the fiber propagates through the coil, r, γ and ψ in Eq. (3-4) can vary, making them time, or position, dependent parameters. Equation (3-4) is changed from a length integral to a time integral, using the relationship $l = (c/n)t$, where n is the fiber refractive index. The expression for k, incorporating Eq. (3-6), and the time dependencies of all parameters are substituted into Eq. (3-4) to give

$$\Theta(\omega) = \Theta_0 \frac{1}{2\pi N} \left(\frac{c}{n}\right) \int_0^{\tau} \frac{\cos[\gamma(t)] \sin[\psi(t)]}{r(t)} \; e^{-j\omega t\left[1 - \frac{\sqrt{\mu_r \varepsilon_r}}{n} \cos[\psi(t)]\right]} \, dt \quad , \tag{3-7}$$

where $\tau = (n/c)L$ is the transit time of the light through the fiber. In Eq. (3-7), the low frequency Faraday rotation, Θ_0 , has been introduced through substitution of Eq. (2-3). The frequency dependent Faraday rotation as expressed by Eq. (3-7) is then a function of the position of the current-carrying conductor relative to the fiber coil, the coil shape (cross section and helical parameters), and the relative phase between the magnetic field and the light propagating in the fiber.

For a given current measurement system, Eq. (3-7) can be solved to predict the

Faraday rotation frequency response. Solutions for particular system geometries are presented in the following chapters of this document. Two simplifications of Eq. (3-7) are of greatest interest in providing the starting foundation for those developments. First is the case where the fiber coil turns are collocated and the plane of the coil is perpendicular to the conductor. In this configuration all points along the fiber coil are simultaneously exposed to the passing magnetic field. With $\psi = 90°$, the expression for the frequency dependent Faraday rotation becomes [14]

$$\Theta(\omega) = \Theta_0 \frac{1}{2\pi N} \left(\frac{c}{n}\right) \int_0^{\tau} \frac{\cos[\gamma(t)]}{r(t)} \; e^{-j\omega t} \; dt \; . \qquad (3\text{-}8)$$

Sensor coils having this planar geometry are discussed in detail in Chapters 4 through 7.

The second case fixes the conductor at the center of a circular cross section coil, but allows the coil turns to be spread apart. This configuration represents a travelling wave geometry that increases the phase matching between the propagating light in the fiber and the passing electromagnetic wave [60]. With the conductor centered, r = R (fixed radius of the circular coil), and $\gamma = 0$. Then Eq. (3-7) reduces to

$$\Theta(\omega) = \Theta_0 \frac{1}{2\pi NR} \left(\frac{c}{n}\right) \int_0^{\tau} \sin[\psi(t)] \; e^{-j\omega t\left[1-\frac{\sqrt{\mu_r \varepsilon_r}}{n}\cos[\psi(t)]\right]} \; dt \; . \qquad (3\text{-}9)$$

Travelling wave fiber current sensors are presented in Chapters 8 through 11.

Throughout this paper, particular interest is generated from the magnitude of the Faraday response relative to its low frequency value, $|\Theta(\omega)/\Theta_0|$. The frequency dependent response can be calculated using either Eq. (3-8) or Eq. (3-9), or directly from Eq. (3-7) if more complex configurations wish to be explored. At frequencies near zero

(static or d.c. conditions), the relative magnitude is always unity. At the higher frequencies, this magnitude will rolloff, but in general, it can have values anywhere between zero and one at any given frequency. A frequency, ω_u, is defined at the point where the relative magnitude is first reduced from its static value to

$$\left| \frac{\Theta(\omega_u)}{\Theta_0} \right| = \frac{1}{\sqrt{2}} \quad . \tag{3-10}$$

This frequency provides the 3 dB bandwidth, ΔB, for the current measurement system under investigation. The bandwidth is a useful parameter for comparing the response and performance of systems that use different types of optical fiber coils. In general, the bandwidths are strong functions of the transit time, τ. A second parameter of interest is the cutoff frequency, $\omega_{co} = 2\pi f_{co}$, which is defined as that frequency where the Faraday response first equals zero. Multiple nulls and high frequency lobes of the Faraday rotation response occur for many of the fiber systems studied here.

The assumption that a TEM wave surrounds the current carrier is useful in simplifying the theoretical development needed to model fiber current measurement systems and providing a framework within which an experimental verification is possible. A single wire conductor produces non-TEM fields consisting of many modes and exhibiting strong spatial distributions [61]. Wave impedances vary with frequency, and a simple relationship between currents and fields may not be possible to determine. This obviously would introduce additional complexity into the Faraday response computations of Eqs. (3-7) through (3-9). A coaxial transmission line, however, produces a magnetic flux density given by Eq. (3-1) and satisfies the TEM condition. The fiber current sensor models developed in this study do not attempt to treat the additional high frequency effects produced by the single wire conductor; that is left for future study.

CHAPTER 4

EXPERIMENTAL APPARATUS AND PROCEDURES

The instrumentation used in the high frequency measurements of fiber current sensor coils is shown in the schematic of Fig. 4-1. Linearly polarized light from a laser source passes through beam expansion optics and a half-wave retarder, then is injected into a singlemode fiber lead using a 10x microscope objective. Light in the fiber lead is

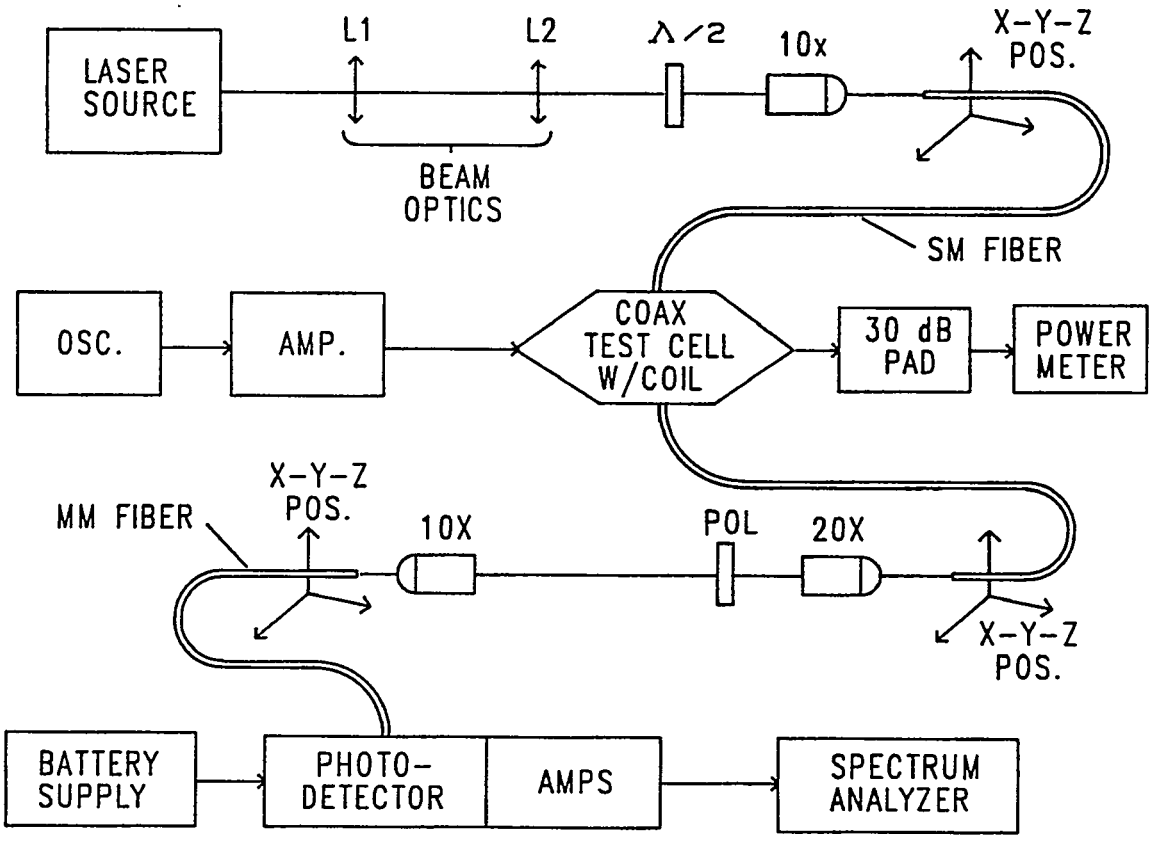

Fig. 4-1. Arrangement used for measuring the frequency response of the Faraday effect in optical fiber current sensor coils. L1 and L2 are lenses used for beam expansion and collimation, $\lambda/2$ is a double Fresnel rhomb half-wave plate, and the components marked by 10X and 20X are microscope objectives used for light injection into the optical fibers and collimation of light exiting from the fibers.

carried to the sensor coil located inside a special coaxial test cell. The light undergoes a rotation (induced by the conducted current), is transported out of the cell via the output fiber coil lead, and then exits the fiber. The polarization is analyzed, and the resultant optical signal is reinjected into a multimode fiber leading to a high speed photodiode. Signals are amplified and their magnitudes are displayed on a spectrum analyzer. Three different laser sources were used during experimentation: a He-Ne laser (633 nm, 8 mW) and two GaAlAs diode lasers (780 nm, 3 mW and 840 nm, 30 mW). Figure 4-2 is a bench-top photograph of the optical components used in the experimental arrangement.

Single frequency RF signals were generated by an oscillator or synthesized signal generator and then amplified to a maximum of 10 Watts before injection into the coaxial test cell. The power transmitted through the test cell was attenuated (usually 30 dB) and monitored by a power meter. All the RF instrumentation in the drive line operates into a 50 Ω impedance, thus producing a maximum rms test current of approximately 0.45 A.

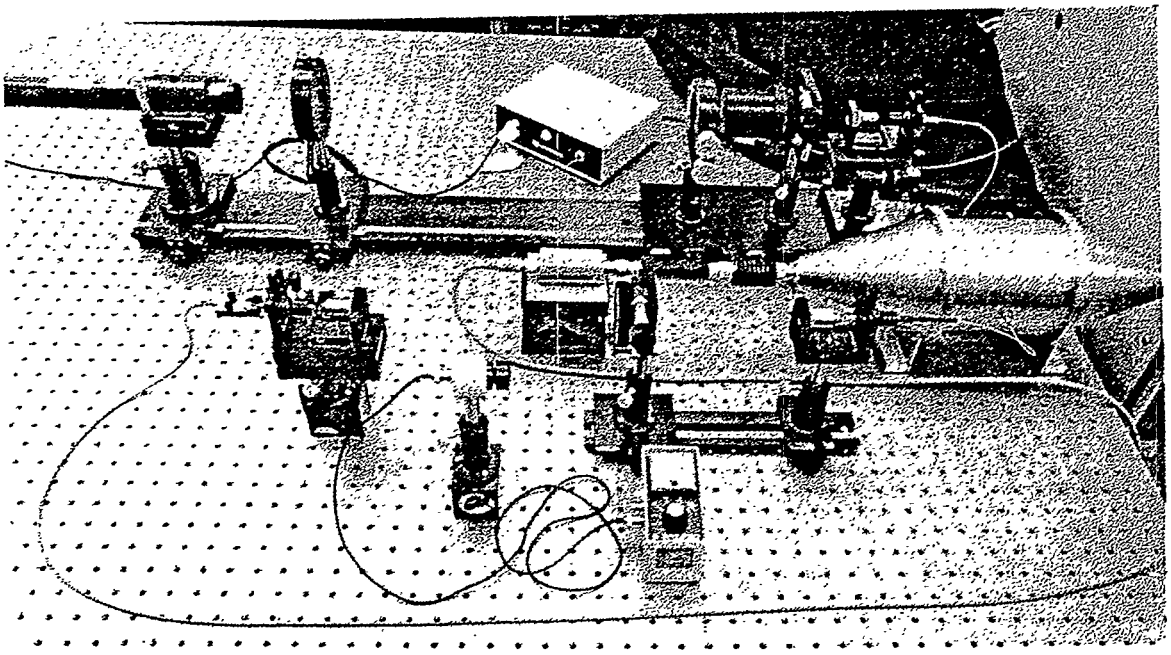

Fig. 4-2. A photograph of the optical components on the bench top used in the measurement of fiber current sensor response.

The general frequency range covered during experimentation was 500 kHz to 1 GHz. The photograph in Fig. 4-3 shows the RF instrumentation used: signal generators, high-power amplifiers, power meter, photodetectors and spectrum analyzers.

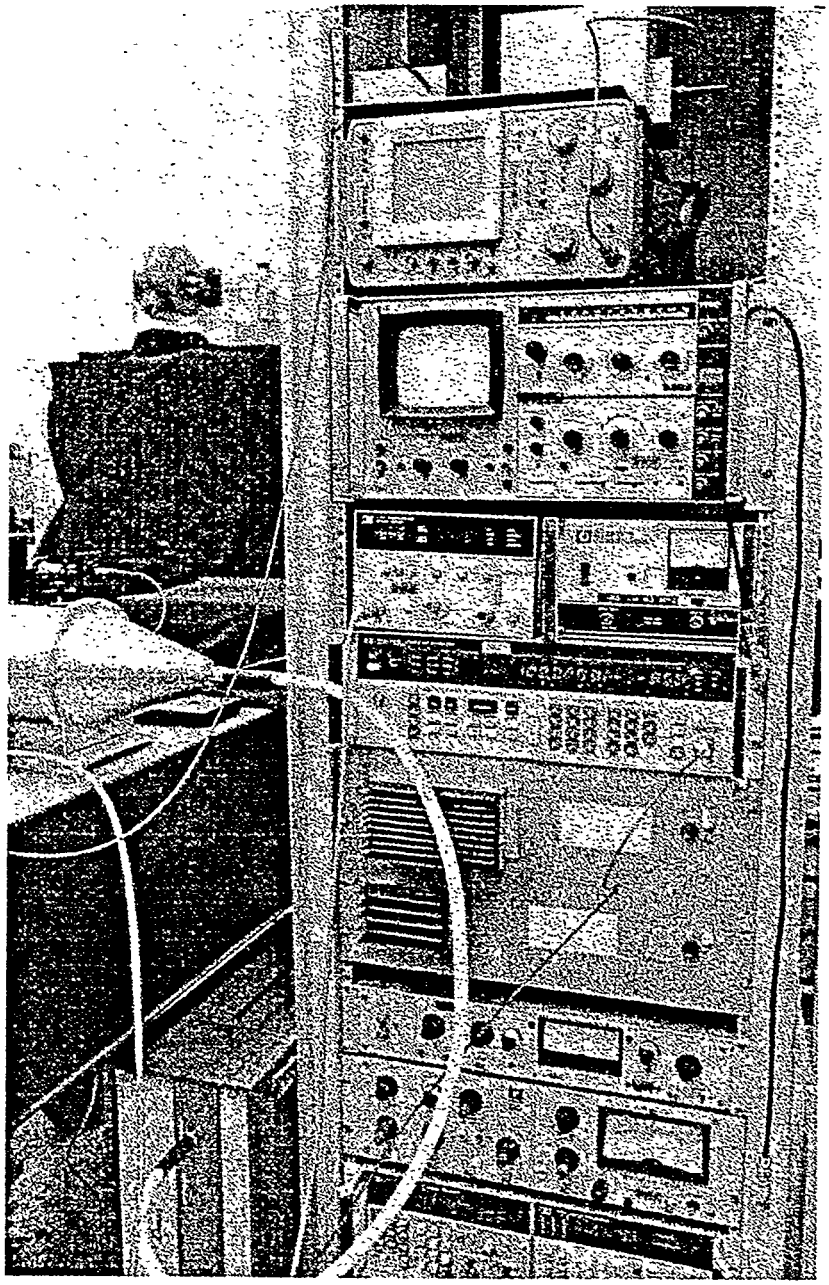

Fig. 4-3. The RF drive and measurement instrumentation used in characterizing the response of fiber current sensor coils.

One of three high speed photodiodes was used at the front end of the photodetection system. These include a silicon PIN photodiode, a silicon avalanche photodiode (APD) and a GaAlAs photodiode. Each has a response bandwidth in excess of 1 GHz. The diodes along with bias circuitry and small-signal RF amplifiers were housed in shielded enclosures to reduce interference from the high power RF drive sources.

In Fig. 4-4, the schematic of the silicon PIN photodetection system is shown. The system includes 42 dB of amplification and a dc bias port for monitoring light intensities during setup and alignment. A 1.2 AH rechargeable battery pack served as the +15 Vdc supply. The frequency response of this photodetector is plotted in Fig. 4-5. In generating this response curve, an Ortel high speed GaAlAs semiconductor laser drove the input to the silicon PIN photodiode. Detector response does not deviate greater than± 2 dB for frequencies below ~ 1.1 GHz; however, the oscillations above 500 MHz are

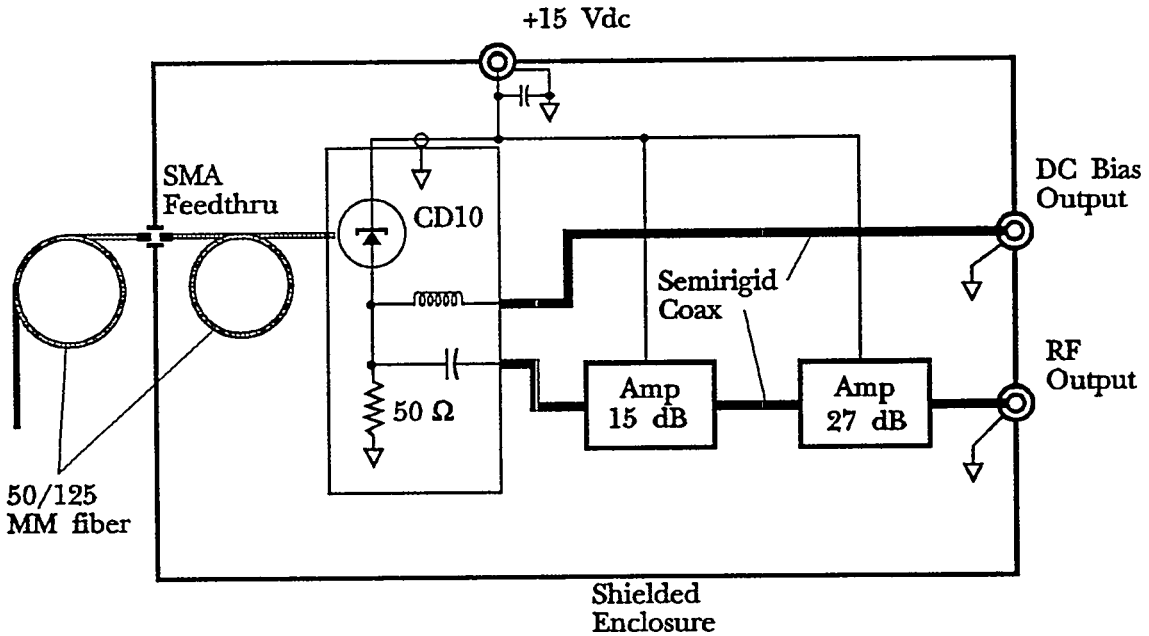

Fig. 4-4. Silicon PIN photodetection system built into a shielded enclosure.

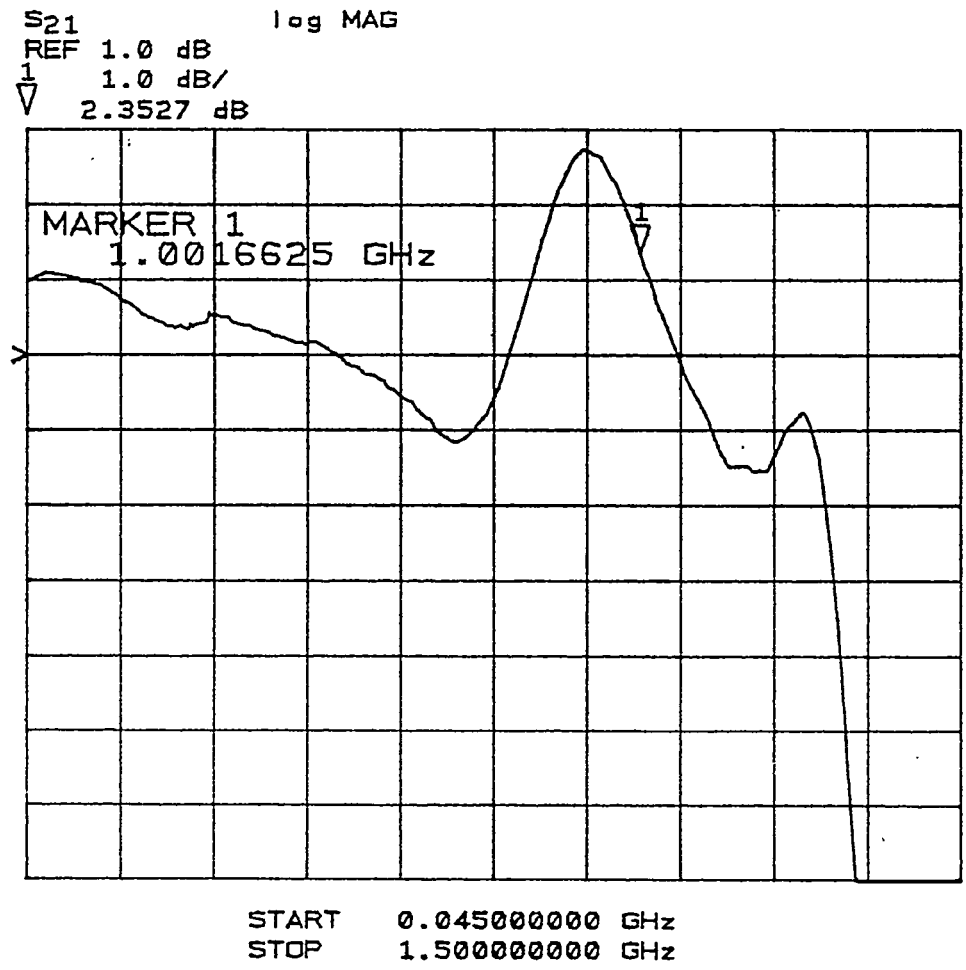

Fig. 4-5. The frequency response of the silicon PIN photodiode with 42 dB of serial, small-signal RF amplification.

large enough to warrant corrections in the measured current sensor data. The large response increase near 1 GHz is caused by resonant amplification between the photodiode circuit and the first RF amplifier. This anomaly does not occur in all the photodetector systems.

The coaxial test cells are expanded transmission line chambers that provide near ideal electromagnetic environments that impinge on the fiber coils [34]. Discussions of pertinent coaxial line properties and the characteristics of fabricated airlines are given in Appendix A. A cross sectional view of one of the test cells is presented in Fig. 4-6, and a

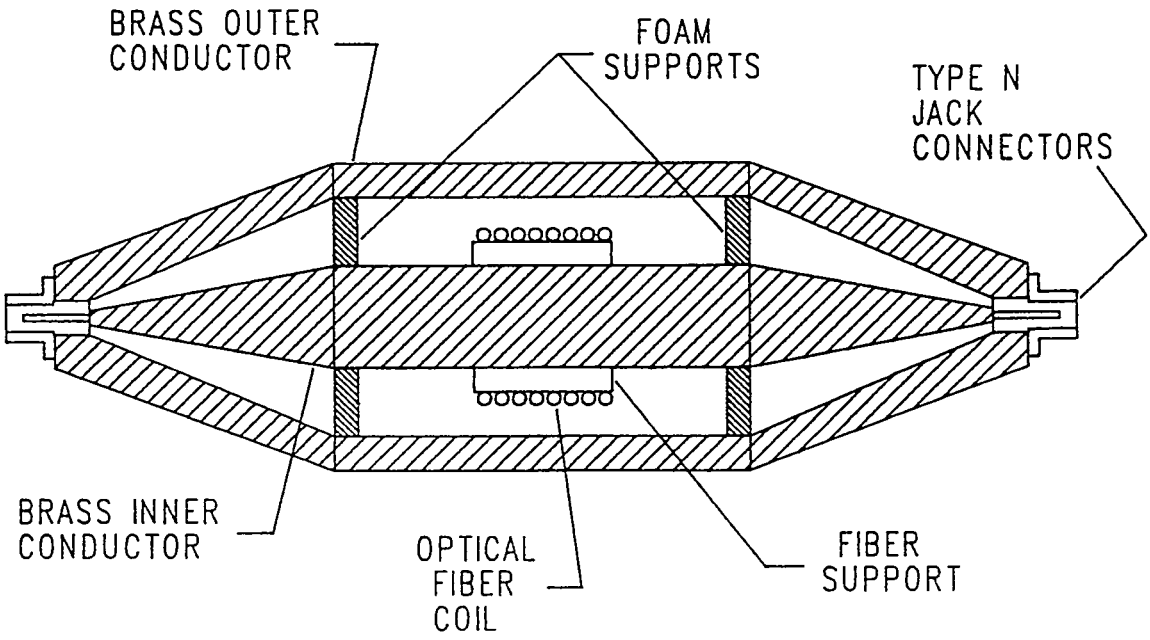

Fig. 4-6. A cross sectional view of an expanded coaxial airline test cell with an optical fiber coil mounted in the working volume.

close-up photograph of the cell is shown in Fig. 4-7a. The cells are designed to open easily for mounting of the optical fiber coils in the cell working volume. The position of the coil inside the cell is seen in Fig. 4-7b. A transverse electromagnetic (TEM) wave is launched in the air space in the cell, and travels with a phase velocity equal to the speed of light. Cell impedance is designed for 50 Ω, requiring the outer to inner conductor diameter ratio to be 2.3. The conductor diameters also dictate the highest frequency to which TEM mode operation can be sustained. Three cells with higher-order mode cutoff frequencies of 1.0, 2.3 and 13.7 GHz were used in these measurements; selection among these devices was dependent on the fiber sensor coil size.

All the cells were characterized with the fiber coils and any additional support structures mounted inside. Measurements of the standing wave ratios (SWR) and impedances of the cells indicate that electromagnetic properties varied minimally from the design. The 1-GHz airline test cell was used most frequently during experimentation;

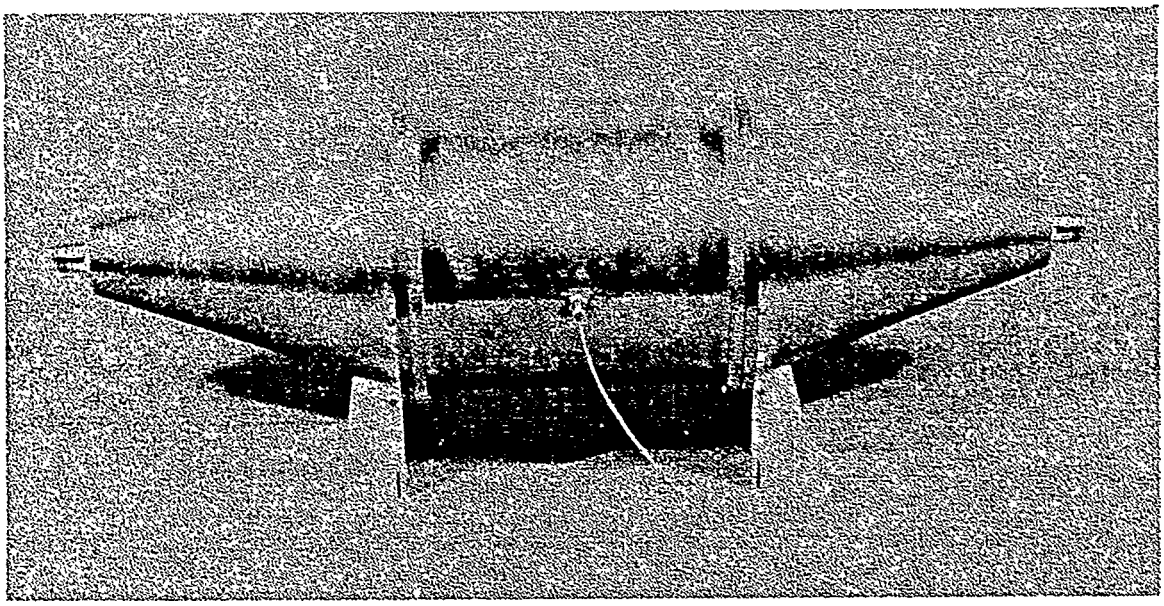

(a)

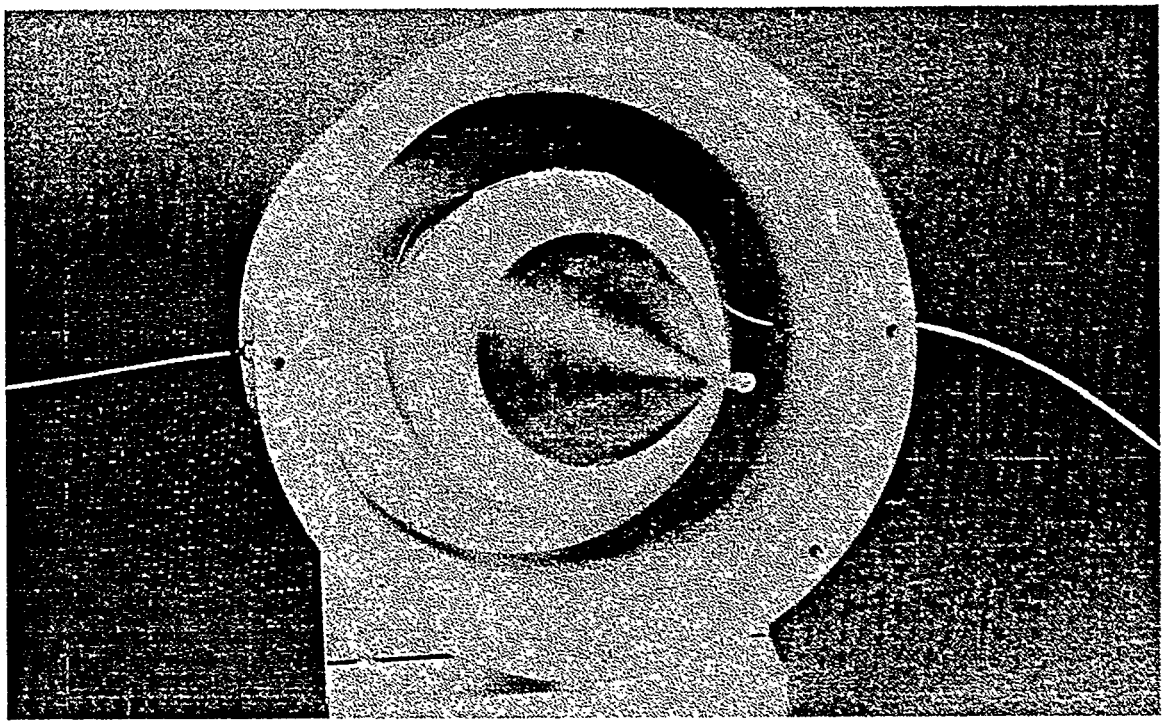

(b)

Fig. 4-7. Photographs of the 1-GHz expanded coaxial test cell. (a) The fully assembled cell, and (b) the opened cell showing a fiber coil mounted around the center conductor.

its SWR and impedance magnitude are plotted in Fig. 4-8. Below 1 GHz, the maximum cell SWR is approximately 1.21, and the impedance varies no more than 7 Ω from its 50 Ω nominal value (0.7 dB maximum deviation). These excellent cell impedances allow for the simple relationship between power and current, $P = i^2 Z$, to be utilized. Thus, only power monitoring was needed during coil testing to determine the relative magnitude of the sensed currents. The maximum error in estimating the currents was always less than 0.7 dB, and corrections for impedance deviations at individual frequencies could be applied where greater precision was required.

The coaxial transmission cells were also configured in non-airline modes with liquid dielectrics. These configurations are used in conjunction with travelling wave current sensor concepts and are discussed in detail in Chapter 9.

Optical fiber coils were constructed from low birefringence singlemode fiber with an 80 μm cladding diameter. In order to overcome the effects of bend-induced linear birefringence [50], fiber twisting [52] or fiber annealing [21] was employed during coil fabrication. For most of the sensors, a twisted and rejacketed fiber was used [29]. This fiber has an outer buffer diameter of 1 mm and can have twist rates as large as 40 turns/meter. With this fiber, coil construction is greatly simplified. Fiber coils were mounted approximately in the center of the test volume of the expanded coaxial test cells as illustrated in Figs. 4-6 and 4-7b. Some of the circular cross section coils were wound directly on the cell center conductor or were wound in a self-supporting form using the twisted and rejacketed fiber. Other circular coils were supported using machined polyurethane foam (10 lb/ft^3) or a polycarbonate. Fibers entered and exited the cell volume through the outer conductive wall (see Fig. 4-7a).

Using the half-wave retarder, the linear polarization angle of the light injected into the singlemode fiber was aligned with one of the fiber coil linear birefringence axes. Orientation of the axes (in all but the annealed fiber coils) are established by bend birefringence and twist-induced circular birefringence. The output polarizer/analyzer

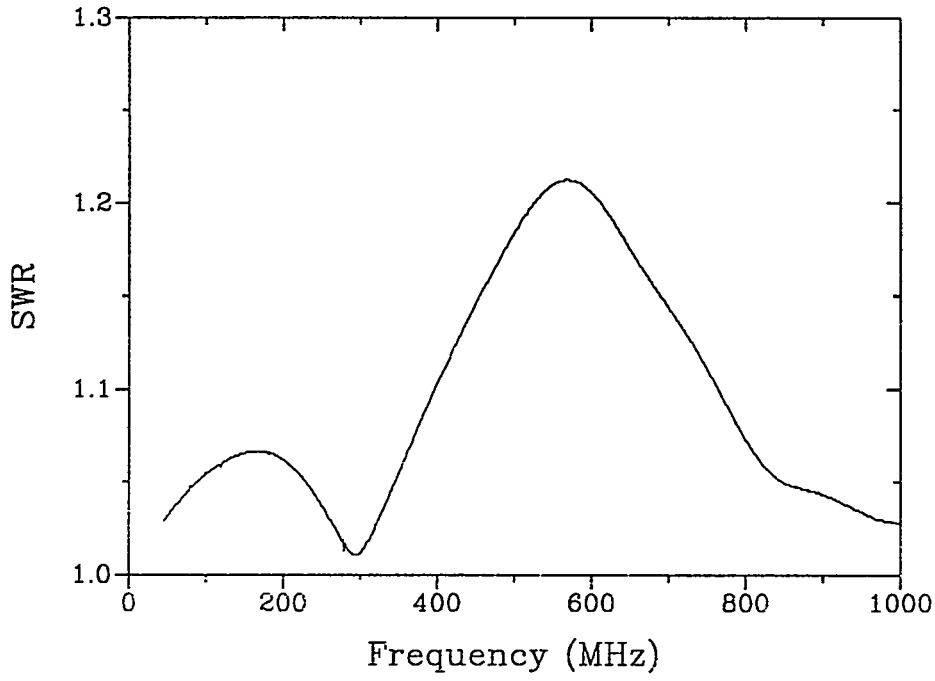

(a)

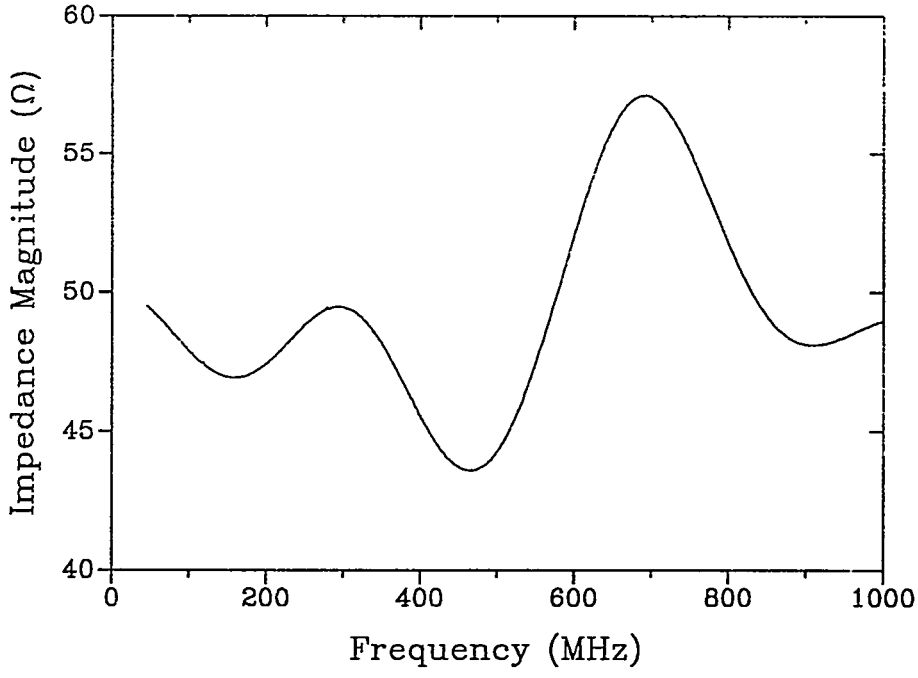

(b)

Fig. 4-8. The SWR (a) and the impedance magnitude (b) for the 1-GHz coaxial test cell with an optical fiber coil inside.

was set at 45° to the exiting linear polarization state. The detected intensity versus rotation then follows the response shown in the bottom of Fig. 2-2 and is described by

$$I(i,\omega) = \tfrac{1}{2} I_0 \left[1 \pm \sin\left[2\Theta(\omega)\right]\right] , \qquad (4\text{-}1)$$

where $\Theta(\omega)$ is the frequency dependent Faraday rotation introduced in Chapter 3. The linear dependence of $\Theta(\omega)$ on the current, i, is established by Eq. (3-4). Maximum sensitivity to the Faraday rotation is achieved since the slope of the response curve in Eq. (4-1) is largest at zero current. The choice of sign in Eq. (4-1) depends on whether a + 45° or - 45° analyzer setting is used. For the RF currents used in testing, the bipolar signals oscillate about zero and the magnitude of the ac component is all that is recorded. Then in the absence of any linear birefringence in the coil fibers, the sign of the response slope near zero in Eq. (4-1) is not important, and the system output polarizers can be set at either + 45° or - 45°. In the present measurements, maximum rotations were approximately 200 μrad (rms) making the argument of Eq. (4-1) very small. Under these conditions, the change in the measured light intensity is directly proportional to changes in the induced Faraday rotation, $\Delta I \propto \Delta\Theta$. Subsequently, the intensity variations follow the signal drive current, $\Delta I \propto \Delta i$.

Spectrum analysis was used to determine the Faraday rotation in the fiber sensor coils through frequency domain measurements of response magnitudes. No attempts were made at measuring phase shifts in the sensor systems or monitoring the time domain response. Instrument sensitivities make such measurements far more difficult than the magnitude determination. Relative response magnitudes were generated for each of the current sensor coils of interest by establishing a low frequency reference. For all of the systems studied, this reference magnitude was recorded at 1 MHz or below. At discrete higher frequencies magnitude changes were measured. A plot of the relative

frequency response was produced directly from these results. Care was taken during all measurements to keep the RF power transmitted through the cell and the dc laser light level constant. Any significant deviations in these parameters were corrected in the measured magnitudes.

The small Faraday rotation angles produced in the silica optical fibers required measuring signals with magnitudes less than -70 dBm. Photodetection was usually limited by thermal noise at a level near -120 dBm for a 10 Hz spectrum analyzer bandwidth. When using the GaAlAs semiconductor diode laser sources, carrier noise often dominated the system; levels were typically 10 to 20 dB greater than detector thermal noise. Signal-to-noise ratios (S/N) at the lowest frequencies (~ 1 MHz) were always greater than 30 dB, regardless of the source used, and occasionally exceeded 40 dB for some of the fiber sensor systems. At the higher frequencies the S/N dropped as the response diminished. Consequently, significant RF shielding was required to preserve signal integrity at these higher frequencies. Isolation between the RF drive amplifier output (up to + 40 dBm) and the spectrum analyzer input (noise levels at less than -110 dBm) needed to be greater than 150 dB up to 1 GHz. Shielding was provided at all component stages: semirigid coaxial cable for all electrical interconnects; the closed coaxial test cell; multimode fiber isolation of the detected optical intensity; complete shielded enclosures with coaxial feedthroughs for the photodetection system; and shielded, battery-operated sources for supply voltages. RF interference occasionally degraded system performance at the highest frequencies, but did not prohibit the characterization of any current sensor coil response.

CHAPTER 5

CENTERED AND CIRCULAR FIBER SENSOR COILS

The most common configuration for a Faraday effect fiber current sensor is a planar, circularly shaped coil with the current-carrying conductor centered in the coil cross section. This geometry is considered baseline for most sensor systems, and experimenters often strive to assemble fiber coils in this configuration if for no other reason than the resultant symmetry. Because of the high degree of symmetry, the mathematical developments needed to describe the high frequency response of the Faraday rotation are greatly simplified. Much of the related theory for the circular, centered coil is presented in Ref. 33; it is repeated here to provide a foundation for the circular coils and establish comparative relationships for later model developments.

Centered Coil Model

In addition to earlier assumptions given in Chapter 3, it is now assumed that all fiber turns are circular in cross section, collocated in space and concentric with the conductor axis. Then if the fields associated with the current are planar, all points on the fiber coil are simultaneously exposed to the same magnetic flux density. Variations in field modulation with time are all that create a frequency dependence in the induced Faraday rotation. In Eq. (3-8), r is a constant value R, which is the fiber coil radius, and γ is zero at all times since the magnetic field vector direction always coincides with the direction of light propagation in the fiber. Equation (3-8) then reduces to the simple form:

$$\Theta(\omega) = \Theta_0 \left(\frac{1}{\tau}\right) \int_0^{\tau} e^{-j\omega t}\, dt \quad , \tag{5-1}$$

where $\tau = (n/c)L = 2\pi RN(n/c)$. The solution to Eq. (5-1) is

$$\Theta(\omega) = \Theta_0 \left(\frac{1}{\tau}\right) \frac{1 - e^{-j\omega\tau}}{j\omega} , \tag{5-2}$$

which further simplifies to

$$\Theta(\omega) = \Theta_0 \left[\frac{\sin\left(\omega\tau/2\right)}{\left(\omega\tau/2\right)}\right] e^{-j\omega\tau/2} . \tag{5-3}$$

Equation (5-3) is a familiar relationship, describing the response of many systems involving the convolution of two propagating electromagnetic signals [62]. The magnitude of the Faraday response relative to its low frequency value is

$$\left| \frac{\Theta(\omega)}{\Theta_0} \right| = \left| \frac{\sin\left(\omega\tau/2\right)}{\left(\omega\tau/2\right)} \right| , \tag{5-4}$$

and the phase, ϕ, is given by

$$\phi = \arg[\Theta(\omega)] = -\frac{\omega\tau}{2} . \tag{5-5}$$

Plots of the magnitude and phase described by Eqs. (5-4) and (5-5) are shown in Fig. 5-1 as a function of the normalized frequency, $\omega\tau/2$. Presentation of theoretical responses versus normalized frequency removes the dependence on coil size. This practice is commonly used throughout this document.

In the most generalized case, Eq. (5-3) also includes a phase factor, $e^{-j\omega t_0}$, which accounts for an arbitrary starting point of the light in the fiber coil relative to the zero

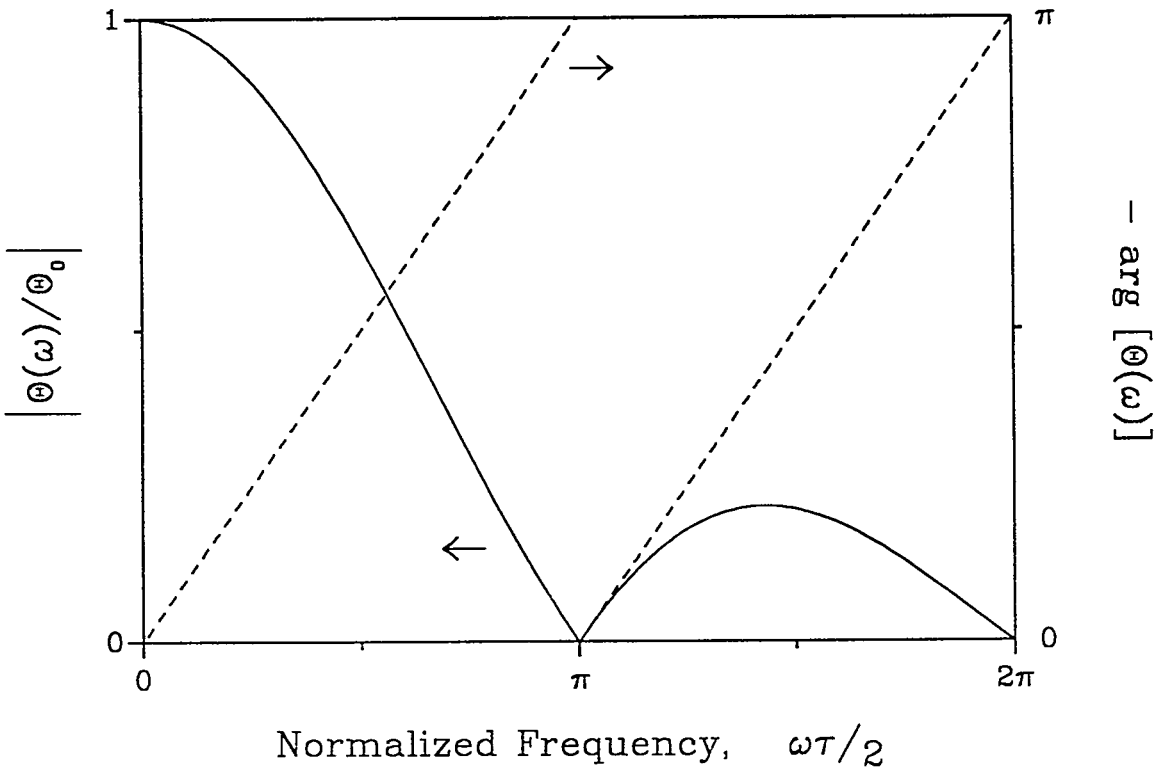

Fig. 5-1. The relative magnitude (solid curve) and phase (dashed curve) of the frequency dependent Faraday rotation for an optical fiber current sensor system with a centered, circular coil.

phase point of the oscillating magnetic field. The time delay, t_0, can be introduced into Eq. (5-1) by modifying the integration limits, t_0 to $\tau + t_0$, or by changing the integrand to $e^{-j\omega(t + t_0)}$. Using either approach, the resulting phase delay is the same and has no affect on the Faraday rotation magnitude, Eq. (5-4). The response phase becomes $\phi = -(\omega/2)(\tau + t_0)$, but its frequency dependence is not altered from that in Eq. (5-5). Consequently, the arbitrary phase delay has no significant affect on Faraday response for the centered, circular coils, and t_0 is set to zero without any loss of generality.

By combining Eqs. (3-10) and (5-4), the 3 dB bandwidth, ΔB, occurs when

$$\left| \frac{\sin\left(\omega_u \tau / 2\right)}{\left(\omega_u \tau / 2\right)} \right| = \frac{1}{\sqrt{2}} \quad , \tag{5-6}$$

from which $\omega_u \tau/2 = 1.392$ and

$$\Delta B = \frac{0.696\, c}{\pi^2 R\, n\, N} \quad . \tag{5-7}$$

An estimate of the sensor bandwidth was made in Ref. 33 by noting that $\omega_u \tau/2 \approx \sqrt{2}$ from Eq. (5-6). Thus

$$\Delta B \approx \frac{c}{\sqrt{2}\,\pi^2 R\, n\, N} \quad . \tag{5-8}$$

The difference in the bandwidths computed using Eqs. (5-7) and (5-8) is only 1.6%. The current sensor high frequency cutoff (first response null) occurs at

$$f_{co} = \frac{1}{\tau} = \frac{c}{2\pi R\, n\, N} \quad . \tag{5-9}$$

Additional response function nulls occur at integer multiples of f_{co}.

A sensitivity-bandwidth product was introduced in Ref. 33 and has been used by other researchers [30] to compare the high frequency measurement performance of current sensing systems, both optical fiber and bulk optic. The sensitivity-bandwidth product is formed by combining Eqs. (2-3) and (5-8):

$$SBP = \left[\left(\frac{\Theta_0}{i} \right) \cdot \Delta B \right] \approx \frac{\mu_f V c}{\sqrt{2}\,\pi^2 R\, n} \quad . \tag{5-10}$$

Equation (5-10) indicates that fiber current sensor bandwidth can be increased without a loss in sensitivity by reducing the coil radius. At small radii, however, the effects of bend-induced linear birefringence begin to quench the Faraday sensitivity [50]. Under such conditions, the SBP is a more complex relationship involving R. In fact, the response function for fiber coils that exhibit significant linear birefringence will contain other frequency dependent factors in addition to those described by Eq. (5-3). During experimentation with one tightly wound coil, this anomalous behavior was observed. It was quickly dismissed as being caused by linear birefringence; no mathematical description of this perturbed frequency response was attempted.

As mentioned previously, the effects of linear birefringence can be overcome in the fiber sensor by twisting the optical fiber [52] before forming it into a coil. This procedure creates a circular birefringence bias that leads to acceptable sensor response. Practical mechanical limitations on fiber twisting, however, are approximately 50 twists/m, which constrains coil radii to greater than 1.5 cm for current sensor operation in the red or near infrared portions of the spectrum. Smaller coil radii are possible by using fiber annealing to remove bend-induced birefringence and the intrinsic stresses due to manufacturing [21]. Coils of 10 to 20 turns with 2.5 mm radii [63] and 100 to 200 turns with 5 mm radii [54] have been manufactured. With fiber sensors having these small radii, significant improvements in the sensitivity-bandwidth product are possible. Thus, high frequency measurements on an annealed coil sensor are included in this study to demonstrate these improvements.

Measured Response Functions

High frequency responses were measured on several optical fiber current sensor coils to demonstrate the utility of Faraday effect sensors at extremely high frequencies and to verify the theoretical predictions. Fiber test coils were fabricated in several configurations; these are summarized in Table 5-1. Mean coil diameters ranged from

Table 5-1.

Summary of High Frequency Response Measurements on Centered, Circular Optical Fiber Current Sensor Coils.

Coil #	Mean Coil Diameter (cm)	Number of Turns	Fiber/ Coil Construction	3 dB Bandwidth, ΔB (MHz)		Cutoff Frequency, f_{co} (MHz)		Highest Measurement Frequency (MHz)
				Measured	Theory	Measured	Theory	
1	10.7	100	Twisted, 15/m Rejacketed	2.7	2.7	6.1	6.1	15
2	9.5	42	Twisted, 10/m	7.1	7.3	16.1	16.4	50
3	6.0	20	Twisted, 40/m Rejacketed	24.5	24.2	55.4	54.5	110
4	6.0	10	Twisted, 40/m Rejacketed	45.4	48.3	102.5	109.0	215
5	8.95	15	Twisted, 40/m Rejacketed	20.7	21.6	46.8	48.7	100
6	0.64	20	Annealed	229.1	226.4	517.1	511.0	1000
7	9.6	10	Twisted, 40/m Rejacketed	29.5	30.2	66.7	68.1	800
8	2.95	21	Twisted, 20/m	46.7	46.8	105.4	105.6	215

approximately 6.4 mm to 10.7 cm and the number of coil turns varied between 10 and 100. The smallest coil, #6, was annealed during fabrication while all the other coils used twisted fiber.

(The annealed coil was prepared by the Optical Electronic Metrology Group at the National Institute of Standards and Technology (NIST). NIST personnel also contributed significantly to the fabrication and characterization of the coaxial transmission cell used to hold the coil and the experimental measurement of the sensor response.)

A summary of the high frequency response parameters for each of the different sensors is also presented in Table 5-1. Both measured and theoretically predicted values are given for bandwidth and cutoff frequency. Equations (5-7) and (5-9) were used for the predictions. The 3 dB bandwidths for the coils in Table 5-1 ranged from 2.7 to 229 MHz. High frequency measurements were made on all coils to well beyond f_{co}; the largest test frequency was 1 GHz. For some of the configurations several high frequency lobes of the response magnitude (greater than two) were investigated. All of the measured response curves followed the functional form of the magnitude predicted by Eq. (5-4) and plotted in Fig. 5-1.

The frequency response of coil #4 listed in Table 5-1 is shown in Fig. 5-2. The dashed curve is generated from Eq. (5-4) using the estimated parameters for the fiber ($n = 1.46$ at $\lambda = 633$ nm) and coil only. Although the curve shape is generally correct, it represents a poor fit to the experimental values. Discrepancies are due somewhat to the uncertainty in determining coil geometry and the optical fiber refractive index but mostly to neglect of the fiber coil leads in the response computation. When the coil was inserted into the coaxial test cell, the input and output fiber leads were arranged so that each lead exited the coil in opposite directions. This effectively adds an extra half turn to the value of N. (This configuration is not a requirement for current sensor coils and some of the tested coils did have a different lead configuration.) The added fiber length then

contributes to a reduced bandwidth since the passing magnetic wave also produces a Faraday rotation in the leads.

An extended model that addresses fiber lead effects is presented in Appendix B. An exact mathematical description is derived for the Faraday rotation in two possible lead configurations: fiber entering and exiting from the same side, and the configuration used for coil #4, leads exiting in opposite directions. When the lead effects are accounted for in the response of the coil, the solid curve in Fig. 5-2 is produced. This predicted response agrees well with the measured data points, especially at the nulls in the curve. Not surprising is the fact that the solid curve in Fig. 5-2 can be duplicated almost precisely by using N = 10.5 as a coil parameter in the magnitude prediction from

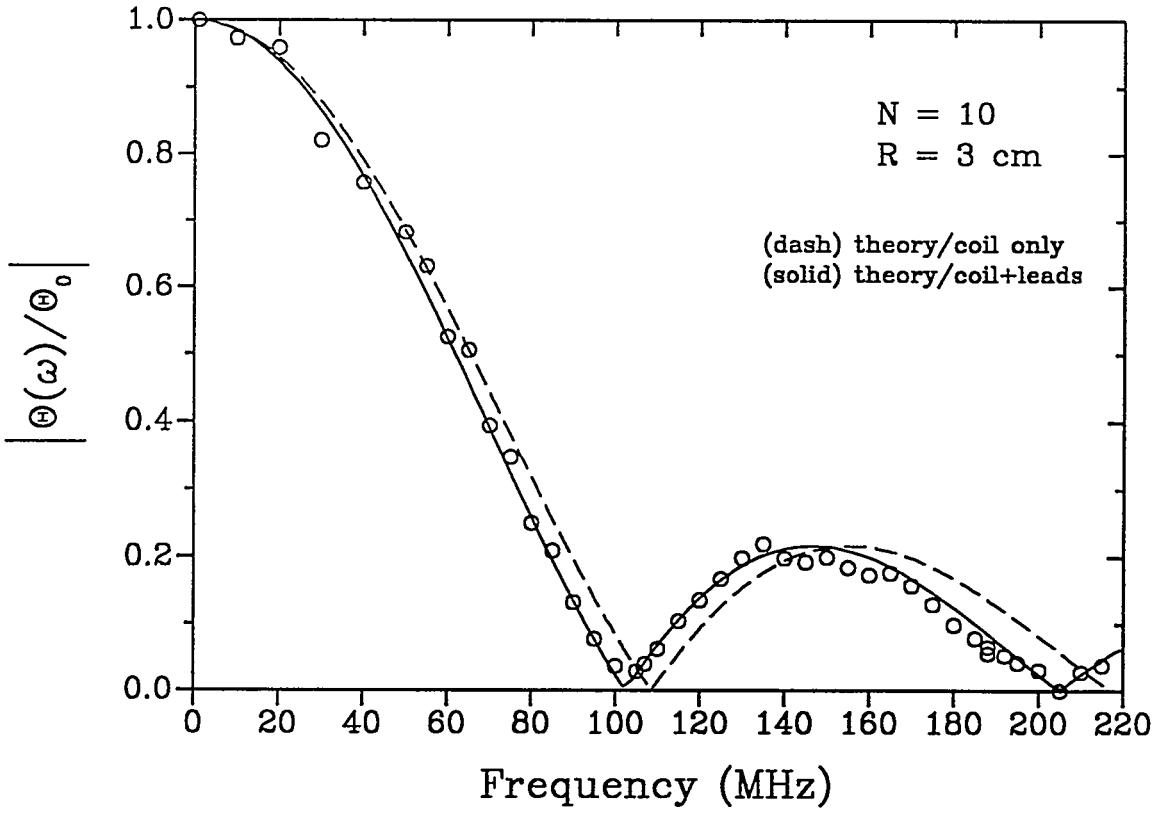

Fig. 5-2. Measured and theoretical Faraday rotation relative response magnitudes versus frequency for a 10 turn, 6 cm diameter current sensor coil.

Eq. (5-4).

Figure 5-3 is a plot of the relative magnitude of the high frequency Faraday response for the annealed fiber coil sensor (coil #6 in Table 5-1). The sensor bandwidth is estimated to be 229 MHz and the cutoff frequency 517 MHz. The dashed curve in Fig. 5-3 is a best fit to the measured values using the function given by Eq. (5-4) and varying the argument, $\omega\tau/2 = 2\pi^2 fRN(n/c)$. This fitted curve is quite accurate and thus can be used to enhance the evaluation of the sensor response. Since relative measurement errors are typically ±1 dB, exact determination of response parameters is difficult using only the measured values. For example, the 3 dB bandwidth is extracted from the experimental

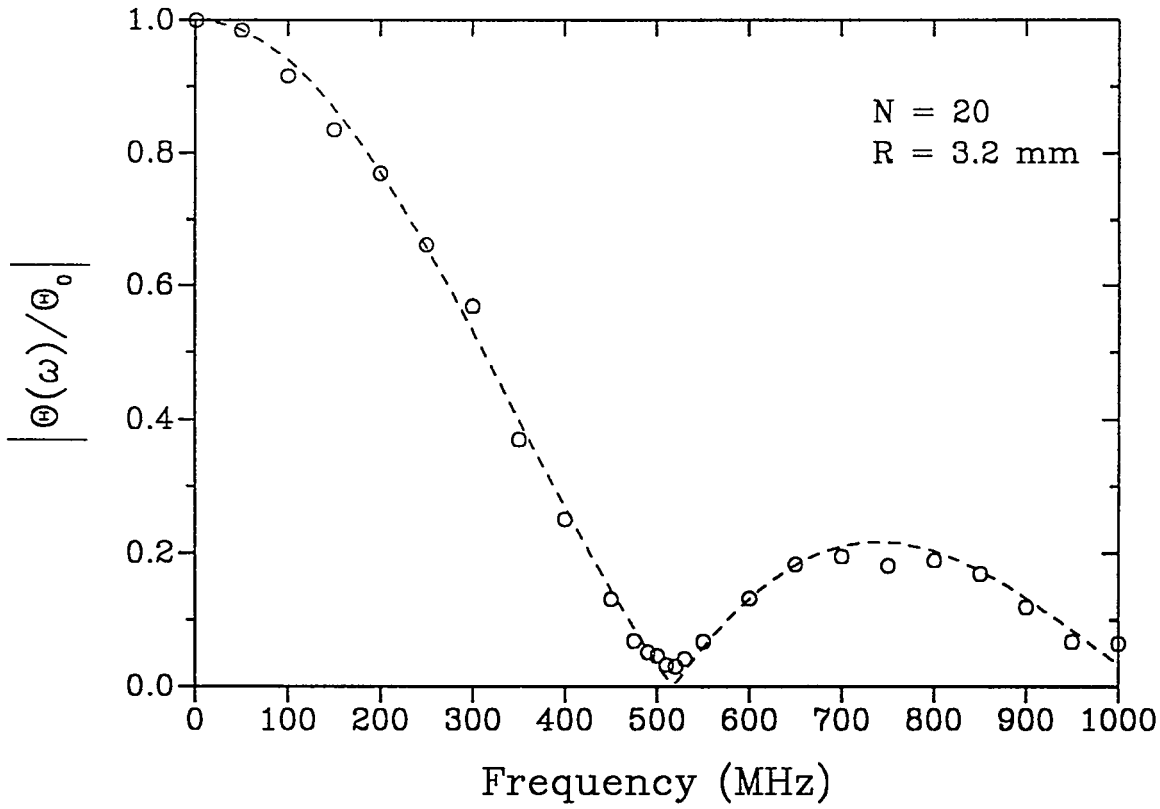

Fig. 5-3. The measured Faraday rotation relative magnitude versus frequency for a 20 turn, 6.4 mm diameter annealed fiber current sensor coil. The dashed curve is a best fit functional response to the experimental data.

data by first performing a functional curve fit, taking care to properly match the response nulls since absolute measurement error is small in these frequency regions, and then interpolating the frequency at a relative magnitude of 0.707. All of the measured bandwidths for sensors presented in Table 5-1 were determined using this procedure.

Fits to the experimental response data are also useful in estimating other fiber and coil parameters. The dashed curve in Fig. 5-3 was used to estimate the mean diameter of the annealed fiber sensor coil. In manufacturing the coil, an annealing fixture with a coil channel 5 mm to 8 mm in diameter is used to confine the fiber. The resulting coil has turns of slightly varying diameter. From the results presented in Fig. 5-3, a light transit time is estimated for the entire coil which then corresponds to a mean coil diameter of approximately 6.4 mm.

The annealed fiber coil represents a first attempt at producing a current sensor with a very wide bandwidth. Its testing is also a first attempt at characterizing the response of a fiber current sensor into the microwave region (> 500 MHz). The estimated 3 dB bandwidth of 229 MHz is almost a factor of five greater than that for any of the other coils characterized in this study. Since the measured Faraday rotations were approximately of the same magnitude for the annealed coil as for all the other test coils, there appears to be no degradation in sensor performance due to fiber annealing. Hence, the annealing process only serves to enhance the capabilities for high frequency current sensing by extending the sensitivity-bandwidth product. The estimated SBP for this sensor is 1.34×10^4 Hz-rad/A or 0.77 MHz-°/A.

The signal and noise spectrum of the annealed fiber current measurement test system is shown in Fig. 5-4. Maximum signals at the low frequencies correspond to measured rms rotations of approximately 41.4 μrad. Diode-laser carrier noise (closed circles in Fig. 5-4) is the limiting factor in sensor performance; it increases in magnitude about 10 dB as the frequency increases from its lower values to 1 GHz. Over the sensor 3 dB bandwidth, a S/N $\approx$ 32 dB is maintained for a spectrum analyzer bandwidth of 10

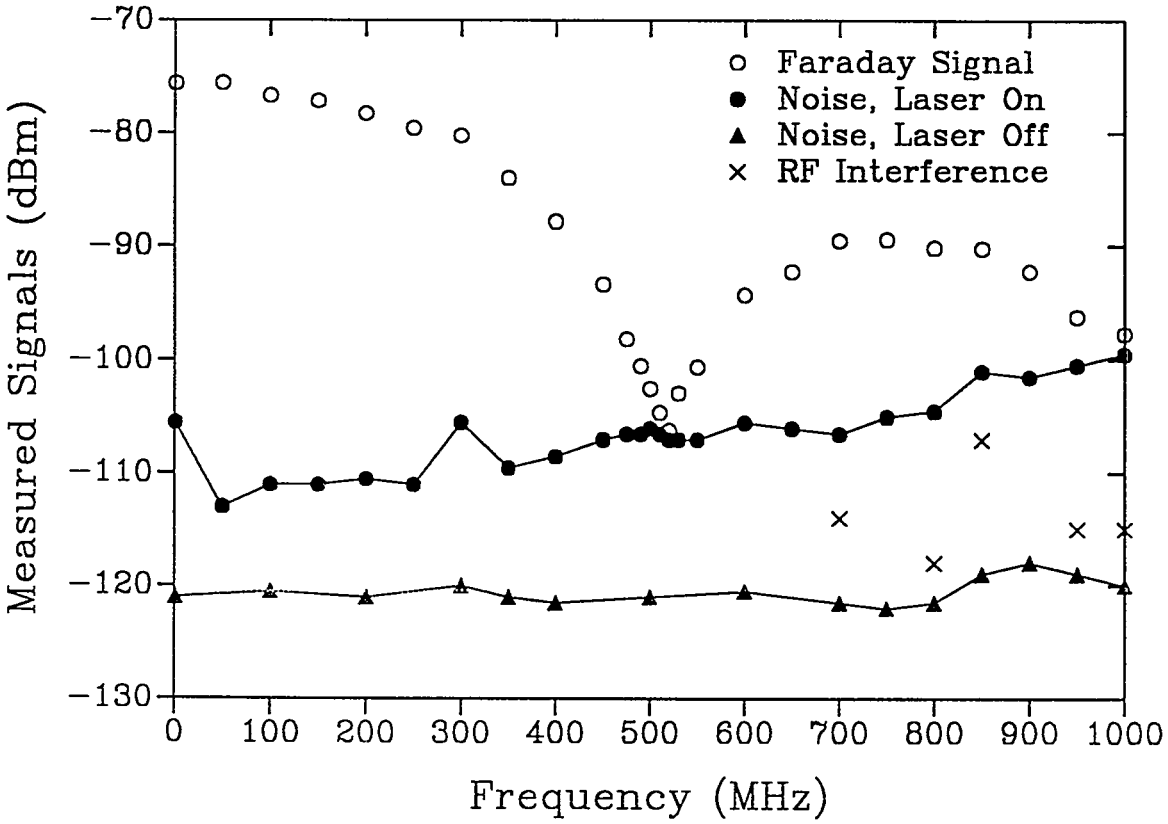

Fig. 5-4. The measured signal and noise responses versus frequency for the annealed fiber current sensing system.

Hz. Based on experimental parameters and measured noise characteristics, the projected noise equivalent rms current (NEI) sensitivity for this annealed coil sensor is 3.6 mA/$\sqrt{\text{Hz}}$, or if the number of fiber turns in the coil is removed, 71.5 mA/$\sqrt{\text{Hz}}$/ turn. Over the full sensor 3 dB bandwidth, the minimum detectable rms current would then be 54 A.

As a comparison, the published NEI sensitivity for a 1 cm diameter, 188 turn annealed-coil sensor system is ~ 100 μA /$\sqrt{\text{Hz}}$ or 18.8 mA /$\sqrt{\text{Hz}}$/ turn [54]. This noise figure is a factor of four better than that determined for the wideband annealed coil system studied here. However, the 3 dB bandwidth for the sensor in Ref. 54 is only 15.5 MHz, almost a factor of 15 smaller. The differences in NEI performance can be rectified

by comparing the detection systems used in each study. In Ref. 54, the sensor sensitivity is based on a shot-noise-limited detection of two, complimentary polarization-state signals (see Eq. (2-10) and Fig. 2-5). Wideband sensing systems as used in the present measurements require 50 Ω or low impedance circuitry to be compatible with RF instrumentation. Thus, detector noise levels are dominated by thermal properties and not shot noise. Thermal noise levels in these systems will typically be 10 dB or greater than detector shot noise. The detector thermal noise measurements for the annealed coil used here are given in Fig. 5-4 as the closed triangles. If this system was limited by thermal noise instead of laser carrier noise (which is frequency dependent), the NEI sensitivity would rival that of the systems presented in Ref. 54. In fact, the dual detector system used in Ref. 54 allows for removal of laser noise common in the two channels.

In most of the measurements on the sensor systems summarized in Table 5-1, a He-Ne laser was used as the source. Performances were then limited by detector thermal noise and not laser carrier noise as seen in Fig. 5-4. This leads to larger signal-to-noise ratios and smaller broadband NEIs. The largest measured S/N values were for coil #8. Over its 3 dB bandwidth of 46.7 MHz, S/N is greater than 40 dB, and the system rms NEI is 1.4 mA /$\sqrt{\text{Hz}}$ or 30 mA /$\sqrt{\text{Hz}}$/ turn. This sensor has a relatively narrow bandwidth compared to that of the annealed coil sensor used in this study, and thus the minimum detectable rms current at full bandwidth is significantly smaller, 3.1 A. It is obvious that complex tradeoffs exist between sensitivity and bandwidth in these high frequency systems. An estimated theoretical limit for the ultimate noise performance in a fiber current sensor system utilizing the dual shot-noise-limited detectors was briefly presented in Chapter 2 and is given as 1 mA /$\sqrt{\text{Hz}}$/ turn [45,59]. It must be remembered that this estimate is based on low frequency signals and assembling such a system for wide bandwidth current monitoring may not be possible.

The maximum measurement frequency for each of the fiber current sensor coils is listed in the last column of Table 5-1. Characterizations were performed at frequencies

that extend well beyond the cutoff frequency. In general, the measured magnitudes for the second lobes of the response functions show excellent agreement with the theoretical predictions. This can be seen in the response plots of Figs. 5-2 and 5-3. For some of the coil systems, several of the higher frequency response lobes were measured, and magnitudes always agreed with the predictions. (One such response curve, for coil #7, is shown in Fig. 6-6a and covers 12 frequency lobes.) The purpose of measuring current sensor frequency response beyond f_{co} is to produce a full understanding of the relative Faraday rotation magnitude as described in Eq. (5-3). By performing fits to the measured magnitude data, an accurate value for $\omega\tau/2$ can be extracted for a given sensor coil. This then gives additional information about the sensor phase frequency response, Eq. (5-5), since the phase angle is much more difficult to measure experimentally. It is postulated that with enough knowledge of the high frequency response magnitude and phase, these Faraday effect current sensor coils could be used as wideband monitoring devices to frequencies above their 3 dB bandwidth. Near f_{co}, however, the sensor response would eventually be limited by system S/N.

CHAPTER 6

NONCENTERED CURRENT SENSOR COILS

Fiber current sensor coils cannot always be properly aligned to have the coil and conductor axes coincident. In some applications, it may not be possible or even desirable. The high frequency Faraday response has been investigated for circular current sensor coils whose axis has a linear radial displacement with respect to the conductor. A model has been developed that predicts the frequency dependent Faraday rotation for such sensors. Experiments have verified the model for specific cases. In general, the radial displacement can assume any value, even those where the conductor lies outside of the coil cross section. The entry point of the light into the fiber coil relative to the conductor also plays an important role in coils with one or a few turns. Both theory and experiment indicate high frequency resonant responses for these noncentered coils. The magnitude of these resonances is dependent on several properties of the coil-conductor system.

Noncentered Coil Model

A noncentered current sensor coil is modeled using the geometry displayed in Fig. 6-1. The coil and field parameters are identical to those identified previously for the centered coil model, except here, the conductor axis is radially displaced from the coil axis by a distance X_1. This displacement means that light propagating around the fiber loop will experience a spatially-dependent magnitude variation in the passing magnetic field. Light enters and exits the coil at a single point designated by the angle, α_o, from the conductor position. Coil leads are neglected in this model. The current conductor is again treated as a filament of moving charge with point cross section. This allows for modeling of the specific configuration $X_1 = R$ or where the conductor is at the fiber.

From Fig. 6-1, the radial distance, r, between the conductor and the propagating light element, dl, on the fiber coil is given by the law of cosines:

$$r^2 = R^2 + X_1^2 - 2RX_1\cos(\alpha+\alpha_0) \quad . \tag{6-1}$$

The angle γ between the magnetic flux density and the light element is also determined from the law of cosines. The relationship is rearranged to give

$$\cos\gamma = \frac{R^2 + r^2 - X_1^2}{2Rr} \quad . \tag{6-2}$$

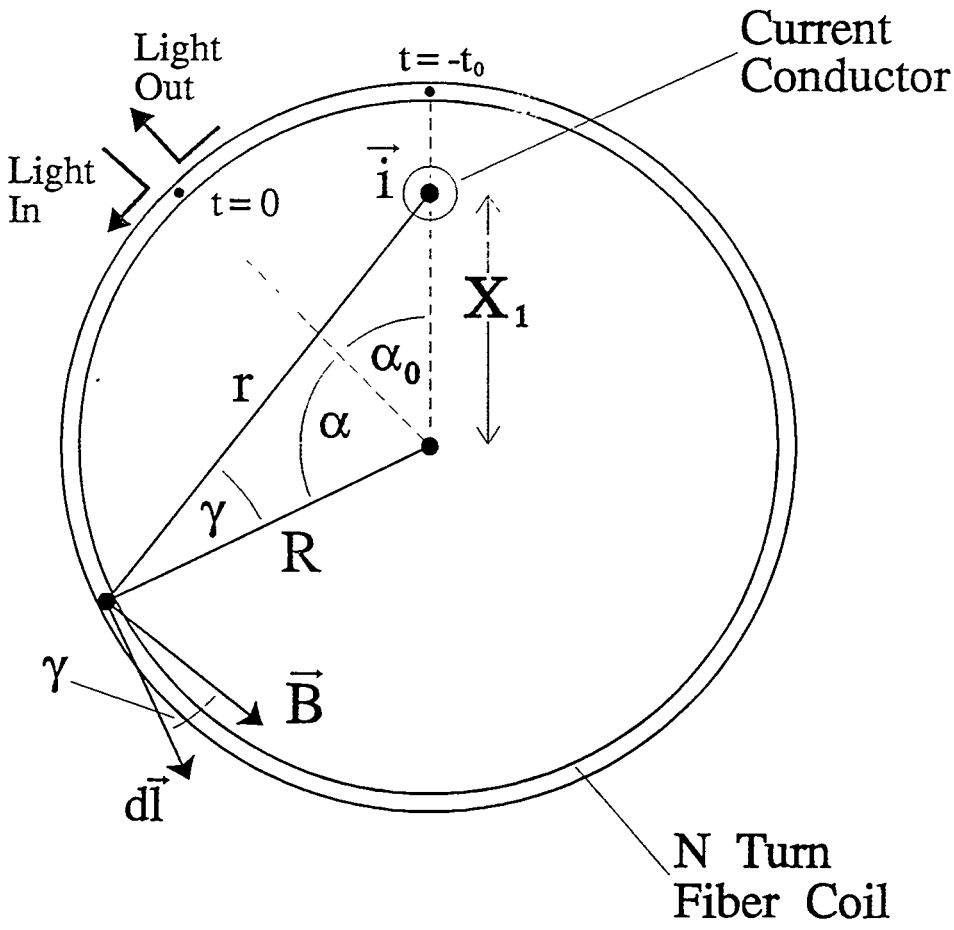

Fig. 6-1. A geometrical model of a fiber current sensor coil with the conductor displaced from the coil axis.

Combining Eqs. (6-1) and (6-2) yields the following expression for substitution into the integrand of Eq. (3-8):

$$\frac{\cos\gamma}{r} = \frac{1}{R}\left[\frac{1 - \left(X_1/R\right)\cos(\alpha+\alpha_0)}{1 + \left(X_1/R\right)^2 - 2\left(X_1/R\right)\cos(\alpha+\alpha_0)}\right] . \qquad (6\text{-}3)$$

The required time dependence of γ and r in Eq. (6-3) is provided by the rotating angle, α. As the light in the fiber propagates, this angle changes as

$$\alpha(t) = \frac{c}{nR}\, t . \qquad (6\text{-}4)$$

The reference starting angle is then given by $\alpha_0 = (c/nR)\, t_0$.

Equation (6-3) can be transformed into an infinite series by using simple long division:

$$\frac{\cos\gamma}{r} = \frac{1}{R}\sum_{m=0}^{\infty}\left(\frac{X_1}{R}\right)^m \cos\left[m(\alpha+\alpha_0)\right] . \qquad (6\text{-}5)$$

Since the cosine function oscillates between 1 and -1, this series converges only when $X_1 < R$. Substituting Eq. (6-5) into Eq. (3-8) provides the integral expression for the frequency dependent Faraday rotation,

$$\Theta(\omega) = \Theta_0 \frac{1}{\tau}\sum_{m=0}^{\infty}\left(\frac{X_1}{R}\right)^m \int_0^{\tau} \cos\left[m\frac{c}{nR}(t+t_0)\right] e^{-j\omega t}\, dt , \qquad (6\text{-}6)$$

where $\tau = (n/c)L = (n/c)\, 2\pi NR$ is used in the factor preceding the summation. In

Eq. (6-6) the summation and integration have been interchanged under the assumption that the series is absolutely convergent. The integration proceeds by rewriting the cosine function in its exponential form,

$$\frac{1}{2}\left[e^{j\frac{mc}{nR}(t+t_0)} + e^{-j\frac{mc}{nR}(t+t_0)} \right] ,$$

and rearranging to get

$$\Theta(\omega) = \Theta_0 \frac{1}{\tau} \sum_{m=0}^{\infty} \left(\frac{X_1}{R}\right)^m \left(\frac{1}{2}\right) \left[e^{j\frac{mc}{nR}t_0} \int_0^{\tau} e^{-j\left(\frac{mc}{nR} - \omega\right)t} dt + e^{-j\frac{mc}{nR}t_0} \int_0^{\tau} e^{-j\left(\frac{mc}{nR} + \omega\right)t} dt \right] . \tag{6-7}$$

Continuing with the integration leads to

$$\Theta(\omega) = \Theta_0 e^{-j\omega\tau/2} \left(\frac{1}{2}\right) \sum_{m=0}^{\infty} \left(\frac{X_1}{R}\right)^m \left[\frac{\sin\left[\left(\omega - \frac{mc}{nR}\right)\frac{\tau}{2}\right]}{\left[\left(\omega - \frac{mc}{nR}\right)\frac{\tau}{2}\right]} e^{j\frac{mc}{nR}\left(t_0+\tau/2\right)} + \frac{\sin\left[\left(\omega + \frac{mc}{nR}\right)\frac{\tau}{2}\right]}{\left[\left(\omega + \frac{mc}{nR}\right)\frac{\tau}{2}\right]} e^{-j\frac{mc}{nR}\left(t_0+\tau/2\right)} \right] . \tag{6-8}$$

The expression for the light transit time, τ, in the N-turn circular coil can be rewritten in the form

$$\frac{mc}{2nR}\tau = mN\pi \ . \tag{6-9}$$

Equation (6-9) is substituted throughout Eq. (6-8). The phase factors for each term in the brackets of Eq. (6-8) further reduce to

$$e^{\pm jmN\pi\left(2t_0/\tau+1\right)} = (-1)^{mN\left(2t_0/\tau+1\right)} , \qquad (6\text{-}10)$$

since $e^{-j\pi} = e^{j\pi} = -1$. In this model both m and N are always integers. The time delay, t_0, is unique only for values between zero and the transit time of light through a single loop of the coil, $\tau_1 = \tau/N$. It is appropriate then to redefine t_0 as a fraction of τ_1 by

$$t_0 = \xi\tau_1 = \xi\frac{\tau}{N} , \qquad (6\text{-}11)$$

where ξ is the fractional multiplier having values $0 \le \xi < 1$. A simplified expression for the noncentered sensor coil response is then

$$\Theta(\omega) = \Theta_0\, e^{-j\omega\tau/2}\left(\frac{1}{2}\right)\sum_{m=0}^{\infty}(-1)^{m(N+2\xi)}\left(\frac{X_1}{R}\right)^m\left[\frac{\sin\left(\omega\tau/2 - mN\pi\right)}{\left(\omega\tau/2 - mN\pi\right)} + \frac{\sin\left(\omega\tau/2 + mN\pi\right)}{\left(\omega\tau/2 + mN\pi\right)}\right]. \qquad (6\text{-}12)$$

Equation (6-12) can be further simplified by combining the two terms in the bracket. First, a common denominator is found for this factor to yield

$$\left[\frac{\left(\omega\tau/2\right)\left[\sin\left(\omega\tau/2 - mN\pi\right) + \sin\left(\omega\tau/2 + mN\pi\right)\right] + \left(mN\pi\right)\left[\sin\left(\omega\tau/2 - mN\pi\right) + \sin\left(\omega\tau/2 + mN\pi\right)\right]}{\left(\omega\tau/2\right)^2 - \left(mN\pi\right)^2}\right].$$

The trigonometric identities for the sum and difference of two angles are then applied to reduce this factor to

$$\left[\frac{\left(\omega\tau/2\right)2\sin\left(\omega\tau/2\right)\cos\left(mN\pi\right)}{\left(\omega\tau/2\right)^2 - \left(mN\pi\right)^2}\right] = (-1)^{mN}\frac{2\sin\left(\omega\tau/2\right)}{\left(\omega\tau/2\right)}\left[1 - \left(\frac{mN\pi}{\omega\tau/2}\right)^2\right]^{-1}, \qquad (6\text{-}13)$$

where $\cos(mN\pi)$ has become $(-1)^{mN}$. Substitution of Eq. (6-13) into Eq. (6-12) leads to a final expression for the Faraday rotation in a noncentered sensor coil:

$$\Theta(\omega) = \Theta_0 \left[\frac{\sin(\omega\tau/2)}{(\omega\tau/2)}\right] e^{-j\omega\tau/2} \sum_{m=0}^{\infty} (-1)^{2m\xi} \left(\frac{X_1}{R}\right)^m \left[1 - \left(\frac{mN\pi}{\omega\tau/2}\right)^2\right]^{-1} . \quad (6\text{-}14)$$

Equation (6-14) can be compared to Eq. (5-3) for the centered coil; obvious similarities exist. If X_1 is set to zero in Eq. (6-14), only a single term in the series will exist, that being $m = 0$. Then the frequency dependent rotation reduces to Eq. (5-3) as required.

The low frequency response for the noncentered coil sensor can also be evaluated. This is more easily accomplished using Eq. (6-12) instead of Eq. (6-14). If $\omega = 0$, Eq. (6-12) becomes

$$\Theta(0) = \Theta_0 \left(\frac{1}{2}\right) \sum_{m=0}^{\infty} (-1)^{m(N+2\xi)} \left(\frac{X_1}{R}\right)^m \frac{2\sin(mN\pi)}{mN\pi} . \quad (6\text{-}15)$$

But $\sin(mN\pi)/(mN\pi)$ is non-zero only for $m = 0$. Then for any value of X_1/R, $\Theta(0) = \Theta_0$ as expected.

The response for the noncentered, circular coil given by Eq. (6-14) shows a dependence on the entry point for light propagation in the coil, the relative displacement of the coil axis, and the number of coil turns. The starting point for light in the fiber coil influences the response because of the series sign factor $(-1)^{2m\xi}$. This factor has a diminished effect when $N >> \xi$, or when the number of turns becomes large. Resonances will occur in the frequency response when $\omega\tau/2$ is equal to integer multiples of $N\pi$ ($\omega\tau/2 = m'N\pi$, for $m' = 1, 2, 3, \ldots$). At each resonant frequency, ω_R, the series in Eq. (6-14) has only one term where $m' = m \neq 0$. (Note that $m' = 0$ produces the low frequency response.) The response given by Eq. (6-14) then becomes

$$\Theta(\omega_R) = \Theta_0 \left(\frac{1}{2}\right)(-1)^{2m'\xi}\left(\frac{X_1}{R}\right)^{m'} , \qquad (6\text{-}16)$$

which has a relative magnitude of

$$\left|\frac{\Theta(\omega_R)}{\Theta_0}\right| = \frac{1}{2}\left(\frac{X_1}{R}\right)^{m'} . \qquad (6\text{-}17)$$

With $X_1 < R$, each successively higher resonance will have a diminishing magnitude. The maximum relative response will be ½ in the limiting case.

Model Predictions

Equation (6-14) is evaluated for several different current sensor configurations to illustrate the effects of a noncentered coil on the high frequency Faraday response. Of particular interest are coils consisting of one turn for which conductor displacement effects are most pronounced. In Fig. 6-2 the relative magnitude of the Faraday rotation is plotted as a function of the normalized frequency, $\omega\tau/2$, for single turn sensor coils. The displayed curves result from varying the relative displacement of the conductor, X_1/R, for two different entry points of light into the coil, $\xi = 0.5$ in Fig. 6-2a and $\xi = 0$ in Fig. 6-2b. These light entry points correspond to the respective angular positions $\alpha_0 = \pi$ and $\alpha_0 = 0$ in Fig. 6-1.

In Fig. 6-2, curves are plotted where the conductor has a displacement of $X_1 = R$. This particular configuration is not physically realizable since the conductor and the fiber cannot occupy the same location in space. Also, when $X_1 = R$, the series convergence criterion established for Eq. (6-5) is violated and a singularity is produced in Eq. (6-3). However, finite solutions to Eq. (6-14) do exist when $X_1 = R$, Eq. (6-16) being evidence of such. Predictions are consistent with others in the noncentered coil model and represent the limiting response as X_1 approaches R. Under these assumptions, the

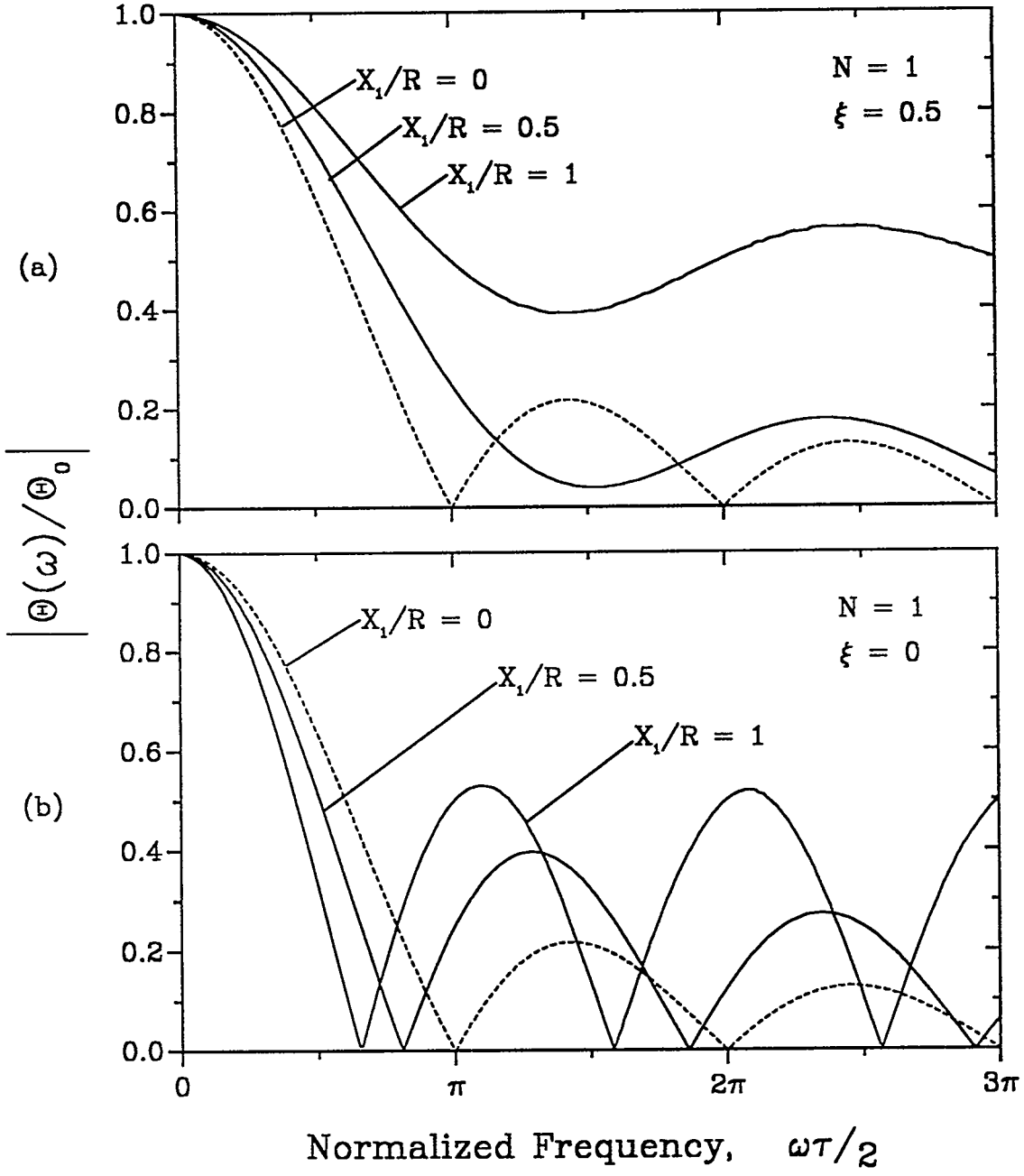

Fig. 6-2. The frequency dependent Faraday rotation response magnitude of a single turn, noncentered current sensor coil. The effects of relative displacement (X_1/R) between the conductor and the coil axis are illustrated for (a) light entry into the coil farthest from the displaced conductor, $\xi = 0.5$, and (b) light entry into the coil nearest to the conductor, $\xi = 0$.

theoretical high frequency response at the $X_1 = R$ limit are included in this study as a means of illustrating extreme effects.

For both plots of Fig. 6-2, the 3 dB bandwidth is changed significantly as the coil and conductor axes become less concentric. In Fig. 6-2a the light enters and exits the single fiber loop at a point farthest from the conductor, $\xi = 0.5$, and ΔB increases with increasing X_1/R. Also, the nulls in the response curve disappear, and the higher frequency response lobes change shape, becoming less pronounced. Under these conditions the Faraday rotation does not have a defined cutoff frequency. In contrast, in Fig. 6-2b the light enters and exits the sensor coil nearest to the conductor, $\xi = 0$, and ΔB decreases with increasing X_1/R. The value of f_{co} decreases proportionally with ΔB, while the response magnitudes in the high frequency lobes increase with X_1/R. Large response magnitudes appear at frequencies where previously there were nulls. In the limiting cases where $X_1 = R$, ΔB has decreased to approximately 0.7 times that of the centered coil sensor when $\xi = 0$ (Fig. 6-2b) and has increased to approximately 1.5 times that of the centered coil when $\xi = 0.5$ (Fig. 6-2a).

The dependence of the single turn coil response on ξ can be explained qualitatively. When the conductor is displaced in the coil cross section, the magnetic field strength is increased at those points of light in the fiber closest to the conductor; the Faraday rotation becomes concentrated in a shorter length of fiber. If the position of the conductor within the coil cross section is away from the light entry point, only one light pass is made through the enhanced region. The decreased effective interaction length naturally leads to an increased response bandwidth. On the other hand, if the conductor is now positioned toward the light entry point in the coil, the light must twice pass close to the conductor as it propagates around the single loop of fiber. Two regions of strong Faraday interaction are created, and the response is largest when these resonate with the field modulation. This resonance effect is best observed at $\omega\tau/2 = \pi$ in Fig. 6-2b for the curve with $X_1/R = 1$. Because of the phasing of the magnetic field with the propagating

light in the coil, an antiresonance must also occur between each of the resonance peaks. The first antiresonance in the Faraday response occurs somewhere between the frequencies $\omega\tau/2 = 0$ and $\omega\tau/2 = \pi$. As a result the 3 dB bandwidth is decreased.

The changes in frequency response for the noncentered single turn coil compared to the centered coil are most pronounced for $\xi = 0$ and $\xi = 0.5$. For other values of ξ, an intermediate response deviation is predicted. In Fig. 6-3 several Faraday response curves are shown for different ξ, all with maximum conductor displacement, $X_1 = R$. A comparison can be made with the response for the centered coil, $X_1/R = 0$, which is also plotted in Fig. 6-3. For values of $\xi > 0.5$, symmetry exists in the response predicted by

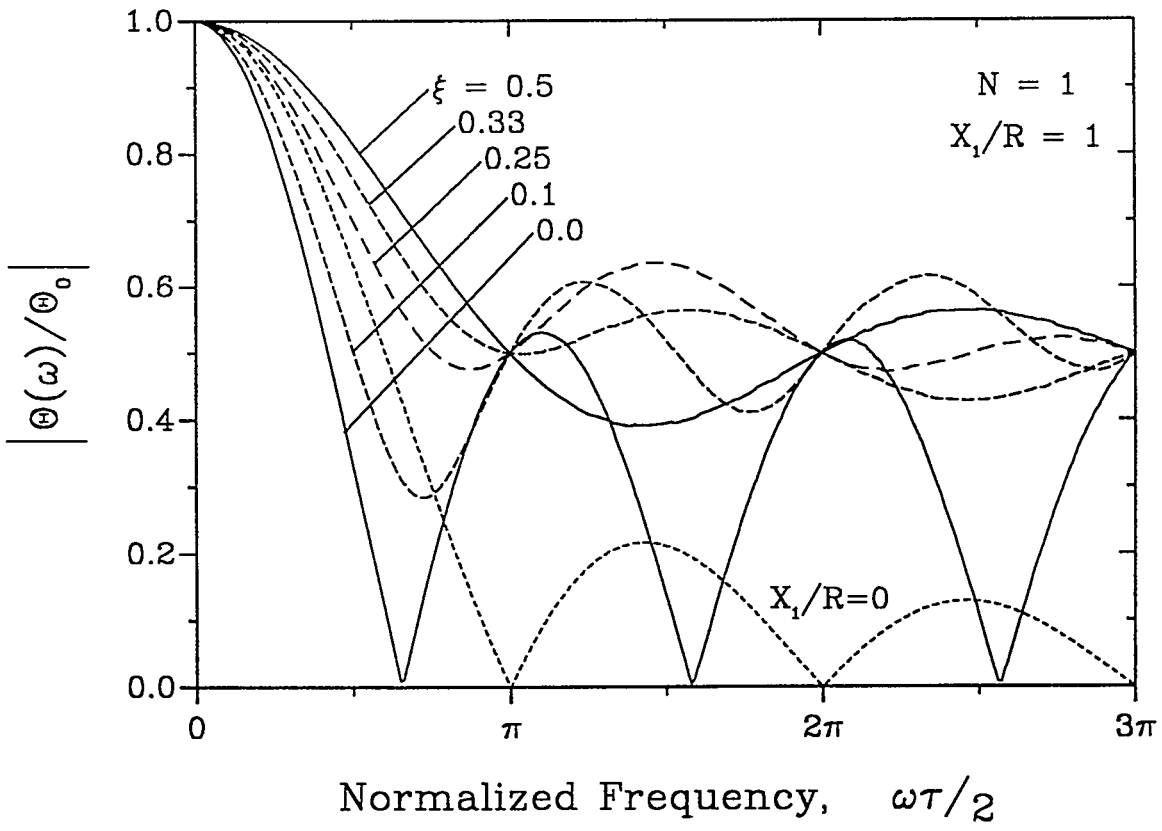

Fig. 6-3. The effects of the light entry point (ξ) in the coil on the frequency response for a single turn noncentered, circular coil with maximum conductor displacement ($X_1/R = 1$). The dotted curve is a reference for a centered, circular coil.

Eq. (6-14): $\Theta(\omega,\xi) = \Theta(\omega, 1-\xi)$ for $0.5 < \xi \leq 1$.

Few current sensor applications call for a fiber coil with only one turn; most require multiple turns for increased measurement sensitivity. When $N > 1$ in Eq. (6-14), many of the anomalous features observed in the Faraday response for a single turn are no longer present. Fig. 6-4 shows the predicted relative magnitude of the Faraday rotation for a five turn sensor coil. Notice the cutoff frequency for the noncentered coils, both for $\xi = 0$ and $\xi = 0.5$, fall at the same frequency as that for the centered coil. This characteristic is seen in the response for all coils with two or more turns; only the single turn noncentered coils have a shifting f_{co}.

In Fig. 6-4 resonant responses occur at frequencies where $\omega\tau/2$ is an integer multiple of 5π. Here, the five turns in the coil, or the number of close passes between the propagating light in the fiber and the strong field from the conductor dictate the resonant conditions. Also, these resonances occur for the noncentered coil at frequencies where nulls exist in the response for the centered coil. The relative magnitudes for the resonance peaks are consistent with the predictions given by Eq. (6-17). For $X_1/R < 1$, each higher frequency resonance has a smaller magnitude than the previous one. When $X_1/R = 1$, the peak magnitudes are approximately ½. Close inspection of the plots in Fig. 6-4 shows that ΔB for the higher frequency resonance lobes is the same as that for the low frequency response lobe.

In Fig. 6-4 the main lobe 3 dB bandwidth is indistinguishable from that of the centered coil response regardless of the X_1/R or ξ value. This is quite different from that predicted for the single turn coil where significant bandwidth deviations occur. In general, for a fixed ξ, ΔB changes as X_1/R increases (the sign of the deviation in ΔB depends on ξ), and for a fixed X_1/R, ΔB increases as ξ increases from 0 to 0.5. The change in ΔB from that of a centered coil diminishes rapidly as N increases. These bandwidth features are shown in Fig. 6-5 for sensor coils with $N = 1$, 2, and 3; the curves are plotted only for $\omega\tau/2 \leq \pi$ to emphasize the main lobe response. The percent

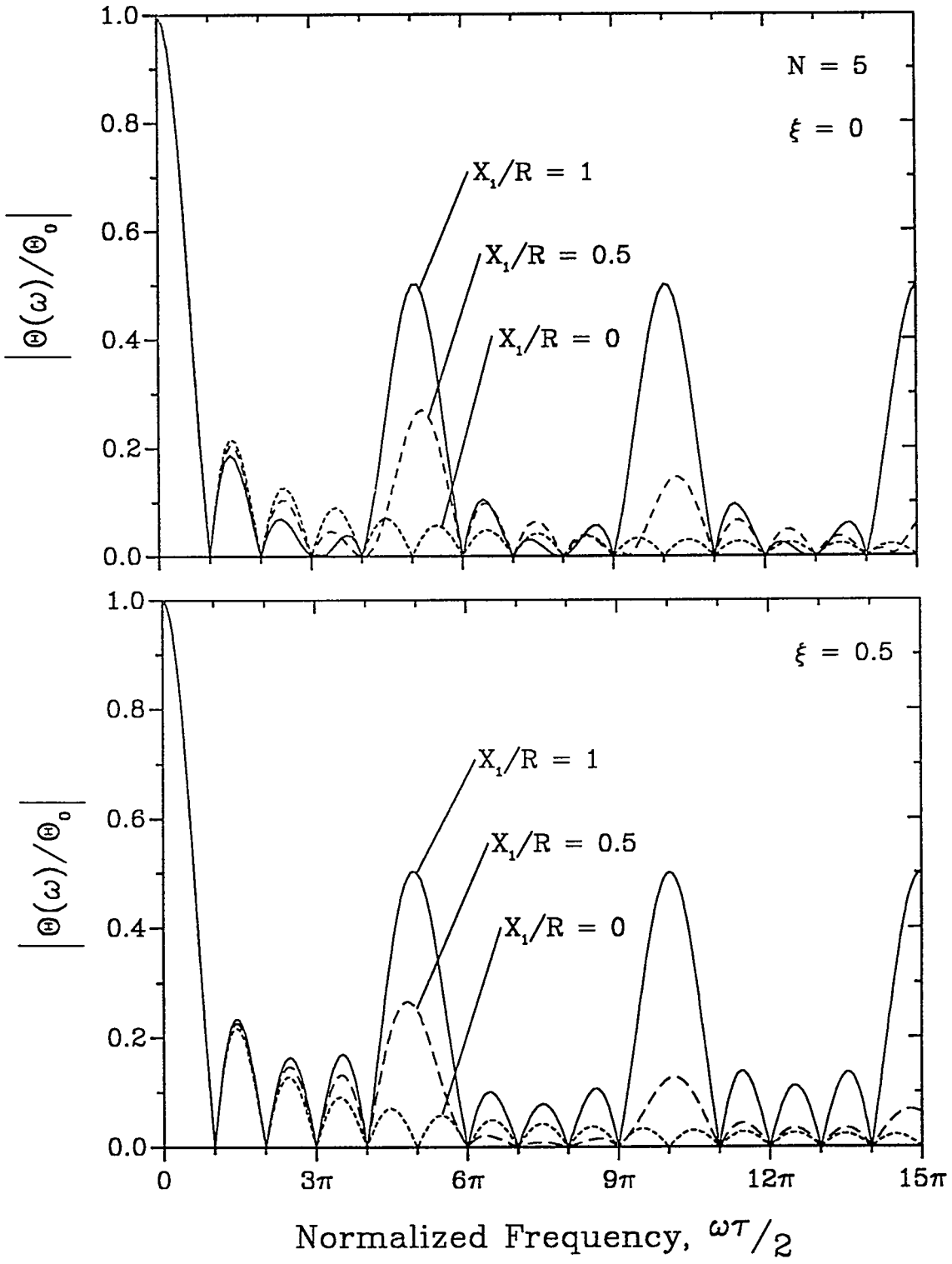

Fig. 6-4. The frequency dependent Faraday response for a five turn circular current sensor coil with varying relative axes displacement. Light enters the coil closest to the conductor (top) and farthest from the conductor (bottom).

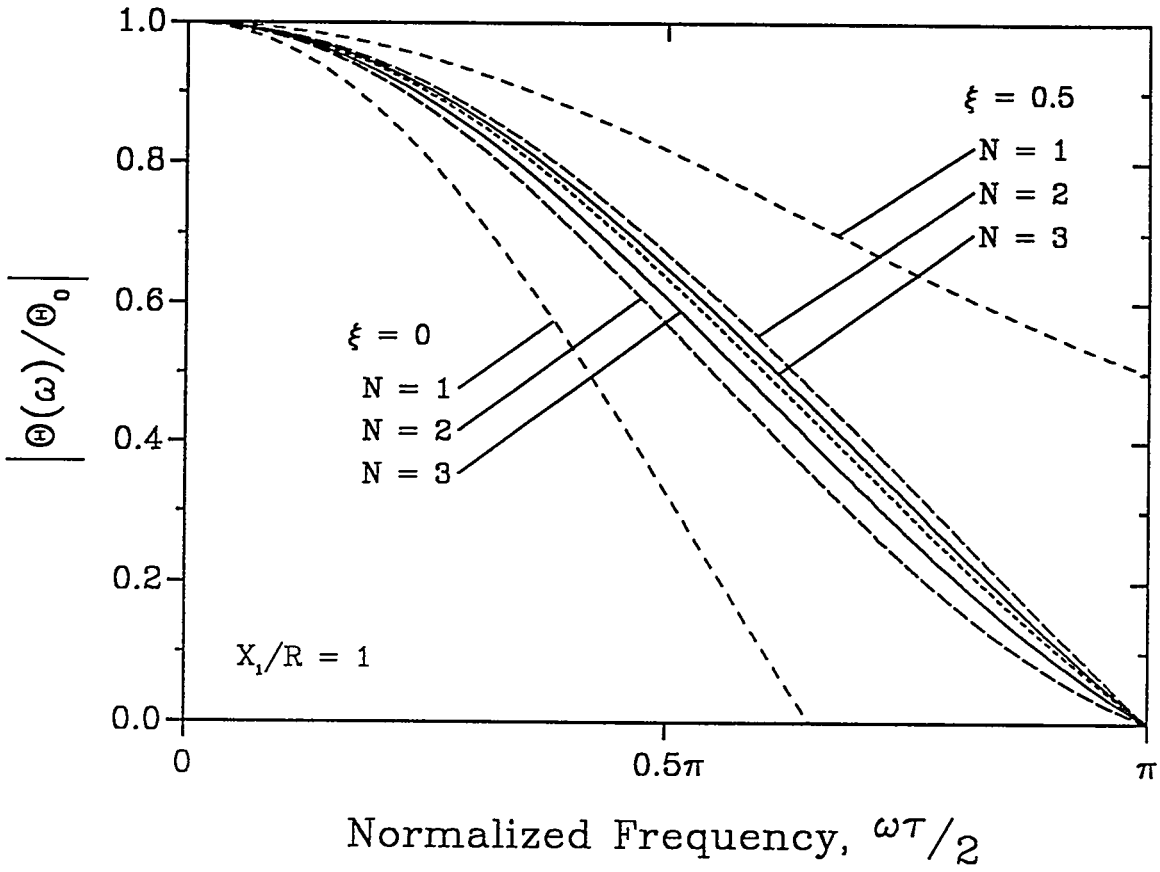

Fig. 6-5. The effects of the number of coil turns and the light entry point on the bandwidth of a noncentered sensor coil with maximum conductor displacement. The dotted reference curve is for a centered, circular coil, $X_1 = 0$. The curve for $\xi = 0$ with $N = 1$ is truncated for frequencies above the first null for plot clarity.

deviations in bandwidth are also given in Table 6-1 for noncentered coil responses with $X_1/R = 1$, $\xi = 0$ and 0.5, and for N between 1 and 10. When $\xi = 0$, bandwidths are smaller than those for the centered coils, while with $\xi = 0.5$, bandwidths are larger. For a coil with ten turns, the bandwidth deviation is insignificant; ΔB can then be estimated using Eq. (5-7) or (5-8) for the centered, circular coil. This indicates that for multiturn current sensor coils ($N \geq 10$), alignment of the coil axis with that of the conductor is not necessary if the range of interest is those frequencies below cutoff.

The frequency response of the noncentered coil is quite similar to that of a recirculating tapped fiber delay line [64,65]. As mentioned previously, the magnetic

Table 6-1.

Changes in the 3 dB Bandwidth for Noncentered Fiber Current Sensor Coils ($X_1/R = 1$) Compared to Centered Coils ($X_1/R = 0$).

N	With $\xi = 0.0$	With $\xi = 0.5$
1	-29.1 %	+50.1%
2	-9.2%	+5.8%
3	-4.6%	+2.5%
5	-1.9%	+0.8%
10	-0.4%	< +0.1%

fields are largest at points on the fiber coil that are closest to the conductor, and as light propagates in the fiber, it experiences greater Faraday rotation in these regions. Once during each turn this Faraday rotation enhancement occurs; when the frequency of the oscillating field is in phase with this process, a resonant response is observed. This phenomenon is much like the extraction of light on each turn in the tapped delay line. Resonant response is observed in Eq. (6-14) when $\omega\tau/2 = m'N\pi$. Then the resonant frequencies are $\omega_R = 2\pi m' (N/\tau)$ or

$$f_R = m' \frac{1}{\tau_1} \quad , \tag{6-18}$$

where $\tau_1 = \tau/N$ has been previously defined as the transit time of light through one coil turn. This resonance frequency relationship has been observed for all Faraday responses predicted for the noncentered coil sensors. An exception is the response with N = 1 and

ξ = 0.5; increased responses are observed at the correct higher frequencies, only the antiresonance nulls are missing.

Three responses are plotted in Fig. 6-6 for $X_1/R = 1$ but now as a function of a new normalized frequency, $\omega\tau_1/2$. With this abscissa, all the higher frequency resonances coincide for sensor coils with varying numbers of turns. The sensor bandwidth still decreases with added fiber turns as expected. This type of behavior has been measured for the tapped fiber delay line with response dependent on the number of fiber taps and the propagation delay between taps [65].

From Eq. (6-17) and Fig. 6-6, the peak magnitudes of the frequency response

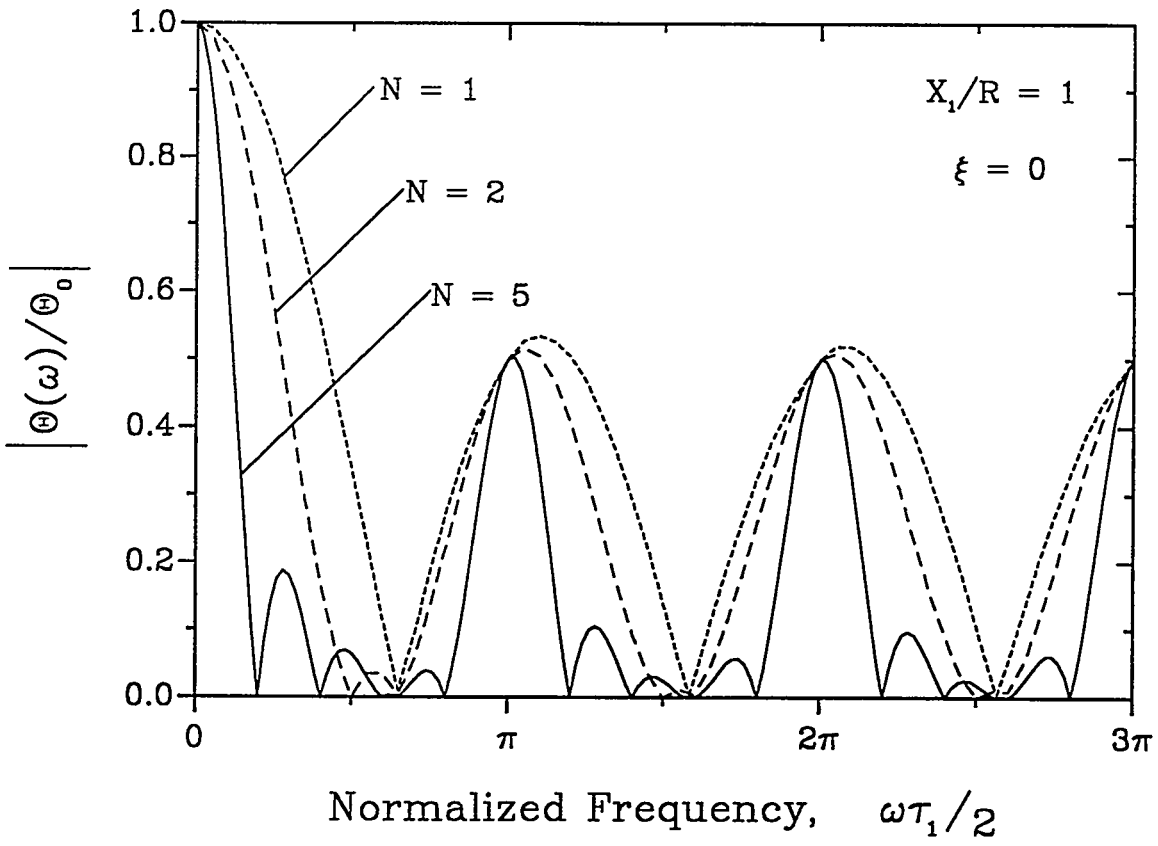

Fig. 6-6. The relative Faraday response for noncentered current sensor coils versus a frequency that has been normalized by the number of turns. Resonances are observed for all three coils at frequencies determined by light transit time in a single fiber turn.

resonances are predicted to have a maximum value of approximately ½ when the conductor is displaced to the very edge of the coil. This indicates that complete phase matching between the magnetic field propagating along with the conducted current and the light propagating in the fiber does not occur. Enhancements in the Faraday rotation that do occur as the light passes near the conductor once during each revolution around the circular coil are partially negated by out-of-phase interactions that occur when the same propagating light segment is further from the conductor and the magnetic field swings to opposite polarity. Complete phase matching can only occur for true point interactions between the magnetic field and the light, resulting in resonances with relative magnitudes of one. This type of Faraday effect current sensor is described in the next chapter of this document.

Equation (6-14) has been used extensively to predict the magnitudes of the Faraday response for noncentered, circular coils, but it can also be used to determine phase angles. In general, the Faraday rotation should have a frequency dependent phase as expressed in Eq. (5-5) for the centered coil; the phase is a simple function only of the total fiber length, τ. However, the series sign factor $(-1)^{2m\xi}$ in Eq. (6-14) can introduce other phase deviations into the response of the displaced coil. If $\xi = 0$ or 0.5, the sign factor is real only, and no deviations occur. But if ξ has other values, the sign factor is complex. The resultant phase shifts are frequency dependent, increasing with X_1/R, decreasing with N, and obtaining a maximum when $\xi = 0.25$, $N = 1$ and $X_1/R = 1$. A plot of the frequency dependent phase for this maximum deviation configuration is shown in Fig. 6-7. Throughout the plotted frequency range ($\omega\tau/2 \leq 3\pi$), the phase angle is slightly nonlinear and has a period approximately $^2/_3$ that for the centered coil.

It is not apparent whether the predicted phase anomalies are real — and observable in measurement systems — or are the result of deficiencies in the model developed to describe the noncentered coil frequency response. A frequency dependent phase shift other than that described by Eq. (5-5) was not anticipated in final

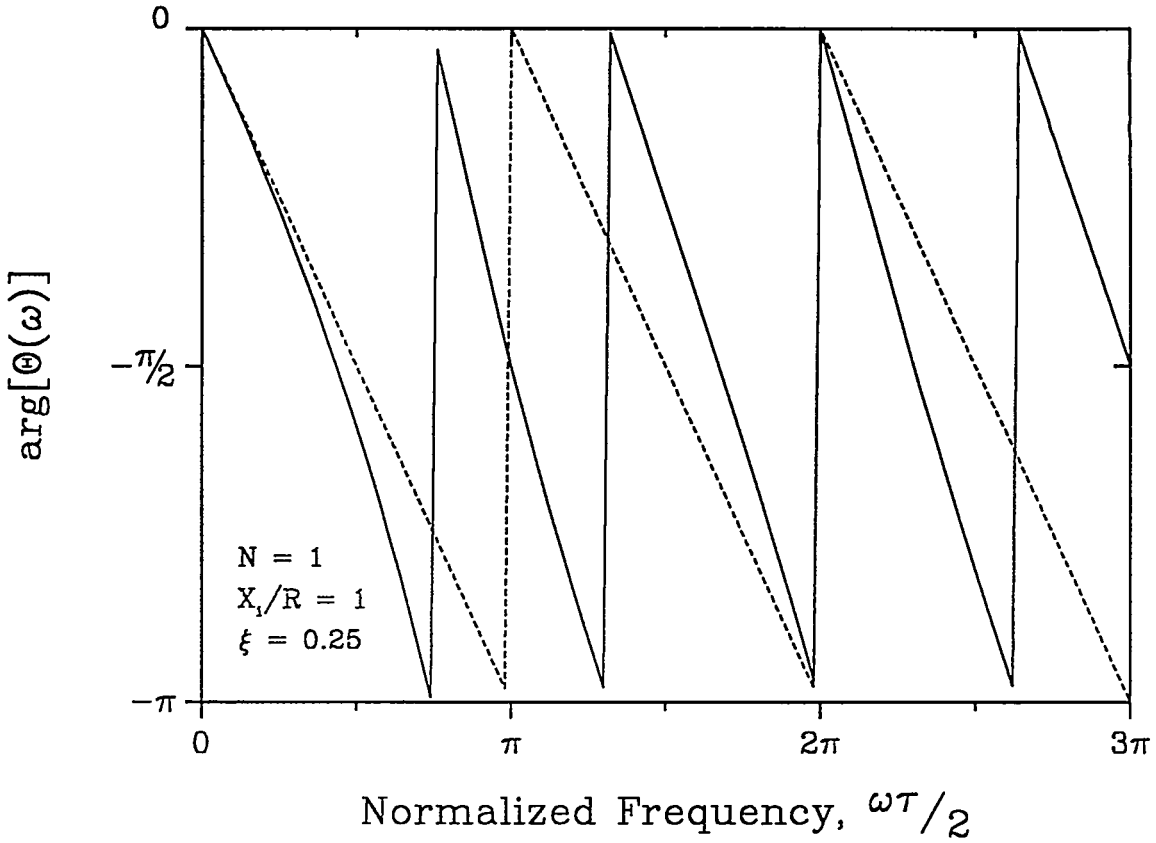

Fig. 6-7. The Faraday rotation phase shift for a single turn coil with maximum conductor displacement and with the light entry point at 90° to the conductor offset direction. The dotted reference curve is the response phase shift in a centered coil.

computations. A check on the model was conducted by substituting cos(γ)/r given by Eq. (6-3) directly into Eq. (3-8) and integrating numerically to determine both magnitude and phase. Results identical to those predicted by Eq. (6-14) were obtained. If the model is in error, it exists in a more fundamental assumption. Obviously, more investigations are needed here. In the meantime, these uncertainties limit the capability of the noncentered coil model to predict complete sensor high frequency response functions.

Nonetheless, radially displacing the fiber coil axis from that of the conductor does offer some potential for increased measurement bandwidth and the measurement of currents at higher banded frequencies. Using a single turn coil, significantly increased

bandwidth and higher frequency response can be achieved by proper placement of the loop. The biggest gain for fiber current sensor applications may be in exploiting the increased response at the higher frequency resonances. In designing such systems, the center frequency of the band is selected by the radius of the coil according to Eq. (6-18). Constraints on minimum radius must be observed to avoid bend birefringence problems. The Faraday sensitivity of the sensor is then determined by the number of fiber turns in the coil and the maximum amount of displacement that can be achieved. As observed from the model predictions of Eq. (6-14), the larger the offset, the greater the relative response magnitude in the high frequency band. Response bandwidth is then found from the total fiber length. ΔB must be traded off with sensitivity as established by the sensitivity-bandwidth product in Eq. (5-10).

Noncentered Coil Measurements

In order to verify some of the predictions of the noncentered coil model, a specific set of parameters was chosen for a coil design and used in the experimental configuration shown in Fig. 4-1. The 1-GHz coaxial airline test cell was selected to generate the appropriate currents. Because of the space constraints in the working volume (outer conductor diameter of 13.3 cm and inner conductor diameter of 5.8 cm), only a limited range of coil diameters and relative displacement factors can be achieved in this cell. An experimental investigation of the high frequency response predicted for the single turn current sensor was desired, however, the small signal-to-noise ratio and the limited dynamic range for a one-turn coil in the assembled measurement configuration precluded such a test. A 10 turn coil with a 9.6 cm diameter was selected. Parameters of this coil appear as #7 in Table 5-1. The diameter of the fiber coil was optimized so that one edge touched the cell outer conductor while the opposite edge just wrapped around and touched the cell center conductor. This coil position gave the maximum-achievable displacement, $X_1/R = 0.38$, measured from the axis of the center

conductor. The coil was configured so that fiber leads entered and exited from the same side and then was arranged inside the test cell so $\xi = 0$.

The measured frequency response magnitudes for the sensor coil in both the centered and displaced position are shown in Figs. 6-8a and 6-8b, along with the appropriate model-predicted curves. In both plots, experiment and theory agree quite well. The predicted sensor bandwidth is 30 MHz and the cutoff frequency is 67 MHz. For the noncentered or displaced coil (Fig. 6-8b), a peak resonance first occurs near 675 MHz, approximately where the tenth null exists for the centered coil frequency response. All the experimental response function peaks and nulls occur at the frequencies predicted.

In Fig. 6-8b, the measured relative magnitude of the resonance peak near 675 MHz is noticeably smaller than expected from the model. The predicted magnitude is 0.19, but both experimental data sets indicate a reduced value. This discrepancy could be caused by one or more of the following factors. (1) Data scatter is significant near the resonance peak as seen for the plotted values in Fig. 6-8b. (2) The model neglects the presence of the fiber coil leads, which could be significant in determining frequency response near the resonances. And (3) the model treats the conductor as a filament of moving charge, while in reality the cell conductor has a large diameter and the current tends to concentrate in the outer skin at these high frequencies.

Other key features predicted by the model and shown in Fig. 6-8b are verified by the experiments. One in particular is the missing response lobe just below 600 MHz. Also, the ratio of the peak magnitudes for the enhanced responses at 675 MHz and 765 MHz is quite precise. The absolute magnitudes of the peaks do not agree well with predictions, however, the ratio does. Measurements above 800 MHz were attempted, but these were limited by RF interference in the detection equipment. Fortunately, response information at those high frequencies offers little to the understanding of the model.

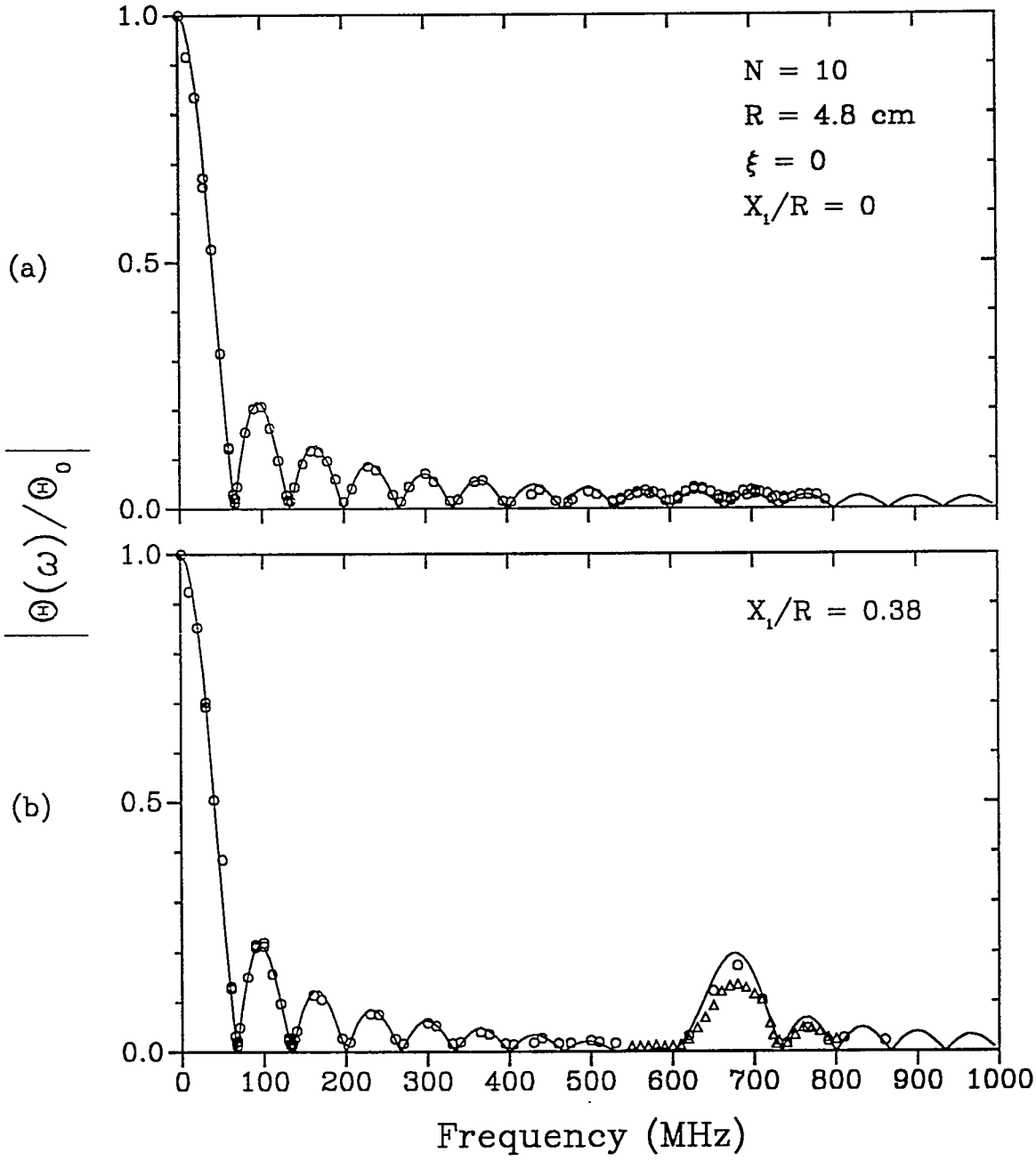

Fig. 6-8. Theoretical and measured frequency response magnitudes for a 10 turn, 9.6 cm diameter fiber current sensor coil. (a) Measured (points) and predicted (solid curve) responses for the centered sensor coil. (b) Measured (two point curves shown) and predicted (solid curve) responses for the noncentered sensor coil.

Conductor Outside the Coil

Ampere's law given by Eq. (2-2) equates the current in a conductor with the magnetic field strength integrated around any loop enclosing that conductor. For a fiber Faraday current sensor, no response is anticipated at low frequencies when the current conductor does not pass through the coil cross section. At the higher frequencies, though, a response does occur and is addressed here in a brief theoretical discussion.

In the previous model for the noncentered coil, the relative displacement factor was taken to be less than one. However, the expression given by Eq. (6-3) remains valid even for X_1/R greater than one. Using this as a starting point, the series expansion is modified and results in

$$\frac{\cos\gamma}{r} = -\frac{1}{R}\sum_{m=1}^{\infty}\left(\frac{R}{X_1}\right)^m \cos\left[m(\alpha+\alpha_0)\right] , \tag{6-19}$$

or

$$\frac{\cos\gamma}{r} = \frac{1}{R}\left[1 - \sum_{m=0}^{\infty}\left(\frac{R}{X_1}\right)^m \cos\left[m(\alpha+\alpha_0)\right]\right] . \tag{6-20}$$

These series are complementary to Eq. (6-5) and converge for $X_1 > R$. When Eq. (6-19) is substituted into Eq. (3-8) and integrated over the transit time through the total fiber, the frequency dependent Faraday rotation is found to be

$$\Theta(\omega) = \Theta_0\left[\frac{\sin(\omega\tau/2)}{(\omega\tau/2)}\right]e^{-j\omega\tau/2}\sum_{m=1}^{\infty}(-1)^{2m\xi}\left(\frac{R}{X_1}\right)^m\left[1-\left(\frac{mN\pi}{\omega\tau/2}\right)^2\right]^{-1} . \tag{6-21}$$

This expression for the rotation is very similar to Eq. (6-14). Resonant responses occur at the same higher frequencies. One major difference is the absence of the m = 0 term in the series of Eq. (6-21); this previously was found to be a necessary condition for the

existence of the low frequency response. Thus when $\omega \approx 0$, $\Theta(0) = 0$ for all N as expected.

The relative magnitude determined from Eq. (6-21) is plotted versus the normalized frequency, $\omega\tau/2$, in Fig. 6-9 for two current sensor coil configurations: (a) a single turn with $\xi = 0.5$ and (b) five turns with $\xi = 0$. For both configurations no responses occur at zero frequency, but secondary lobes and resonant peaks are present at the higher frequencies. As the sensor coils are moved further away from the conductor, the response magnitudes decrease at all frequencies as expected. Eventually as X_1/R grows larger, the conductor and coil are separated by such a large distance that magnetic fields are too small to induce any significant Faraday rotation in the fiber.

In Fig. 6-9a the effects of the light entering and exiting the fiber coil farthest from the conductor ($\xi = 0.5$) are again illustrated. As discussed previously in conjunction with Fig. 6-2b (conductor inside the coil), a single turn coil will exhibit a continuous and enhanced higher frequency response with the proper positioning of the conductor and the coil. The Faraday response magnitude for the solid ($X_1/R = 1$) and dashed curves in Fig. 6-9a are symmetric about the magnitude ½. The frequency response with the conductor just outside the coil is simply one minus that response when the conductor is just inside the coil. This phenomenon is the result of the sign change that occurs in $\mathbf{B} \cdot d\mathbf{l}$ for that fiber section just adjacent to the conductor. It is also evident in the frequency dependent angle/distance relationships, Eqs. (6-5) and (6-20), which are simple complements when $X_1 = R$.

In Fig. 6-9b, the characteristic resonance responses for the noncentered coils are again observed. The center frequencies of the resonant bands fall at $\omega\tau/2 = m'N\pi$, exactly the same as those predicted for a coil with $X_1 < R$. Resonance bandwidths are again determined by the total fiber length. If $X_1/R = 1$, the peak relative magnitudes are all approximately ½, but when $X_1/R > 1$, each successively higher frequency resonance is weaker than the previous one.

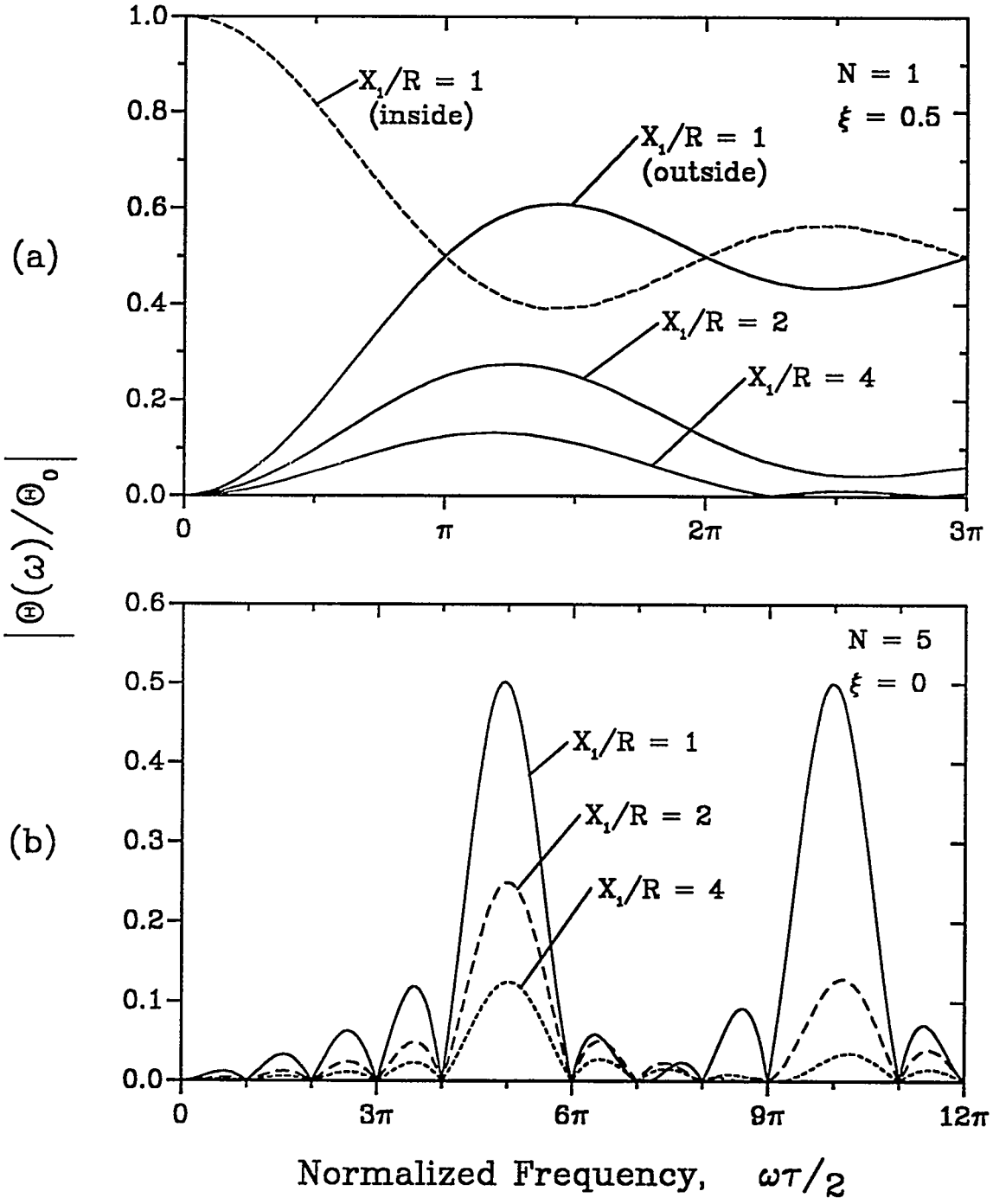

Fig. 6-9. The theoretical high frequency Faraday rotation relative magnitude for fiber current sensor coils with the conductor outside the coil cross section ($X_1/R \geq 1$). (a) A single turn coil with light entering farthest from the conductor, and (b) a five turn coil with light entering nearest the conductor.

This model of a conductor external to the fiber sensor coil was not verified experimentally. The frequency range for the TEM mode in the 50 Ω coaxial airline test cells is not compatible with the expected first resonance frequency or other significant features predicted by the model. Experimentation may be possible in a modified test cell, but for now this concept remains a theoretical curiosity.

CHAPTER 7

COILS WITH NONCIRCULAR CROSS SECTION

The shape of the planar coil cross section can produce changes in the high frequency Faraday response much like the resonant enhancements created by displacement of the coil and conductor axes. In this chapter, the Faraday rotation is investigated for coils with noncircular cross section, and the effects at the higher frequencies are observed. Coils with two particular geometries are studied: (1) those with a highly elongated cross section and the current conductor fully displaced to one edge of the fiber coil, and (2) those with a rectangular cross section and the conductor either centered or displaced within the coil. The first geometry represents a unique situation since the magnetic field interacts only with a small segment of the fiber in each turn. Essentially complete phase matching can occur for this interaction; and the resulting "delta function" Faraday response produces higher frequency resonances with peaks approaching relative magnitudes of one. This response is in contrast to the magnitude limit of approximately ½ for the noncentered, circular cross section coil discussed in the previous chapter. The rectangular coil geometry provides a simple framework for investigating frequency responses for all configurations of coils, those with centered or displaced conductors and those with varying degrees of cross section eccentricity. Also, predictions from the rectangular coil models are easily extrapolated to other coils of arbitrary cross section. Only theoretical studies were possible for the rectangular coils, but experimental verifications of the delta function interaction were performed using two specific coil implementations.

Delta Function Response Model

A highly elongated fiber sensor coil is shown in Fig. 7-1a. In the limit, the conductor can be treated as a point source with the fiber loop making a tight bend just

around the conductor. Realistically, this configuration is impossible since mechanical limitations prohibit such bends and the bend-induced birefringence would be extremely large. But theoretically, this coil cross section is ideal: Faraday rotation occurs only for light in that segment of the fiber adjacent to the conductor. At all other points on the fiber coil, the magnetic field is orthogonal to the light propagation and zero response is recorded. Because this interaction occurs in a small spatial region, TEM mode constraints on the current-produced field can be relaxed; but for the purpose of extending the results of this model to more practical coil configurations, the fields along the conductor are assumed to be planar.

Figure 7-1b illustrates the ideal path followed by the light propagating in the fiber. When the fiber passes near the conductor, it is assumed to make a tight,

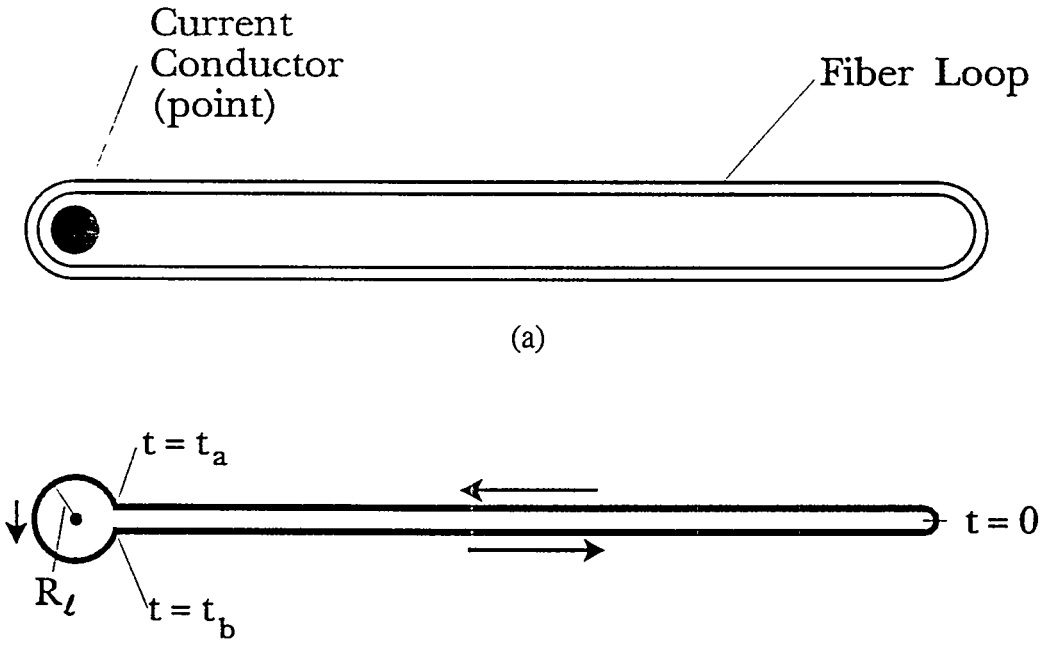

Fig. 7-1. The delta function response fiber current sensing model. (a) The current conductor is fully displaced inside a highly elongated fiber coil cross section. (b) The mathematical treatment of the light path.

approximately circular loop at a constant radial distance R_ℓ from the point conductor. The magnetic flux density in this short segment of fiber is then given by Eq. (3-1) with $r = R_\ell$ and $\mathbf{k} \bullet \mathbf{l} = 0$. The field is assumed always to be codirectional with the propagating light in the fiber loop, so that the local interaction is described by

$$\mathbf{B} \bullet d\mathbf{l} = \mu_f i \, e^{-j\omega t} \, \frac{dl}{2\pi R_\ell} \quad . \tag{7-1}$$

At points along the straight segments of the fiber coil (away from the circular bend) shown in Fig. 7-1b, the general field-light interaction is described by

$$\mathbf{B} \bullet d\mathbf{l} = B \cos(\gamma) \, dl \quad , \tag{7-2}$$

which is Eq. (3-2) with $\psi = \pi/2$. In these straight segments, however, γ is always taken to be $\pi/2$, and $\mathbf{B} \bullet d\mathbf{l} = 0$. Then, substituting Eq. (7-1) into Eq. (2-1) and converting to time-dependent integration yields

$$\Theta(\omega) = \frac{\mu_f V i}{2\pi R_\ell} \left(\frac{c}{n}\right) \int_{t_a}^{t_b} e^{-j\omega t} \, dt \quad , \tag{7-3}$$

which describes the frequency dependent Faraday rotation in a single turn of the elongated fiber current sensor. The integration times, t_a and t_b, are as indicated in Fig. 7-1b. In a multiturn coil, the fiber will make N passes by the conductor. The total Faraday rotation then becomes the sum of that for each individual interaction. Also, during each pass the integration times must be appropriately delayed to account for variations in the oscillating magnetic field. In general, $t_a = m\tau_1 + \xi\tau_1 - \tau_\ell/2$ and $t_b = m\tau_1 + \xi\tau_1 + \tau_\ell/2$ for m = 0 to N - 1; $\tau_\ell = 2\pi R_\ell \, (n/c)$ is the transit time of the light through

each small, circular segment, and $\xi\tau_1$ is an arbitrary time delay from the entry point of the light in the fiber (identical to that introduced in Eq. (6-11)). The Faraday rotation for the N-turn elongated coil is given by

$$\Theta(\omega) = \frac{\mu_f V i}{2\pi R_\ell}\left(\frac{c}{n}\right)\sum_{m=0}^{N-1}\int_{m\tau_1+\xi\tau_1-\frac{\tau_\ell}{2}}^{m\tau_1+\xi\tau_1+\frac{\tau_\ell}{2}} e^{-j\omega t}\,dt \quad . \tag{7-4}$$

Proceeding with the integration leads to

$$\Theta(\omega) = \frac{\mu_f V i}{\tau_\ell}\sum_{m=0}^{N-1}\frac{e^{-j\omega\left(m\tau_1+\xi\tau_1+\frac{\tau_\ell}{2}\right)} - e^{-j\omega\left(m\tau_1+\xi\tau_1-\frac{\tau_\ell}{2}\right)}}{j\omega} \quad , \tag{7-5}$$

and a final solution of

$$\Theta(\omega) = \frac{\Theta_0}{N}\,e^{-j\omega\xi\tau_1}\,\frac{\sin\left(\omega\tau_\ell/2\right)}{\left(\omega\tau_\ell/2\right)}\sum_{m=0}^{N-1} e^{-j\omega m\tau_1} \quad . \tag{7-6}$$

The low frequency response, $\Theta_0(\omega)$ for the entire coil is given by Eq. (2-3).

The concept of a point interaction between the magnetic field and the propagating light is now introduced by allowing $\tau_\ell \rightarrow 0$. The factor $\sin(\omega\tau_\ell/2)/(\omega\tau_\ell/2)$ in Eq. (7-6) becomes unity, and an expression for the "delta function" Faraday response results:

$$\Theta_\delta(\omega) = \Theta_0\,e^{-j\omega\xi\tau_1}\,\frac{1}{N}\sum_{m=0}^{N-1} e^{-j\omega m\tau_1} \quad . \tag{7-7}$$

The time delay created by the light entry point produces only a phase delay in the final

rotation, which, in this model, has no impact on the magnitude of the Faraday rotation. In fact, the arbitrary light entry point is significant only if it occurs exactly at the conductor so that N + 1 interactions are produced for N loops in the coil. This is quite different from the delay introduced in the noncentered, circular coil model where the light entry point had a large impact on the magnitude of the Faraday response for all values of ξ. In order to avoid the confusion in this delta function model between the number of close passes the light makes by the conductor and the number of turns in the coil, the light is assumed to enter at or near the zero location indicated in Fig. 7-1b. Then N will represent both quantities. Consequently, $\xi = ½$ in Eq. (7-7), and

$$\Theta_\delta(\omega) = \Theta_0 \, e^{-j\omega\tau_1/2} \, \frac{1}{N} \sum_{m=0}^{N-1} e^{-j\omega m \tau_1} \quad . \tag{7-8}$$

Or, since $\tau_1 = \tau/N$,

$$\Theta_\delta(\omega) = \Theta_0 \, e^{-j\omega\tau/2N} \, \frac{1}{N} \sum_{m=0}^{N-1} e^{-jm\,\omega\tau/N} \quad . \tag{7-9}$$

These expressions for the frequency dependent Faraday rotation can also be derived by simply treating the field-light interaction as a series of delta functions separated in time by the transit time of the light through a single coil turn, τ_1, and delayed in time by $\xi\tau_1$:

$$\mathbf{B} \cdot d\mathbf{l} = \mu_f \, i \, e^{-j\omega t} \sum_{m=0}^{N-1} \delta(t - m\tau_1 - \xi\tau_1) \, dt \quad . \tag{7-10}$$

When Eq. (7-10) is substituted into Eq. (2-1), the equivalent time integral becomes

$$\Theta_\delta(\omega) = \Theta_0 \frac{1}{N} \sum_{m=0}^{N-1} \int_0^{\tau} \delta(t - m\tau_1 - \xi\tau_1)\, e^{-j\omega t}\, dt \quad . \tag{7-11}$$

Completing the integration yields Eq. (7-7). This treatment is much simpler, however, it is less elegant than the initial approach and lacks the generality needed for later developments.

If a fiber current sensor makes only a single pass by the conductor, the magnitude of the Faraday response from Eq. (7-9) is $|\Theta_\delta(\omega)| = |\Theta_0|$, and an infinite bandwidth results. This prediction is expected from the definition of the delta function interaction. For two passes by the conductor,

$$\Theta_\delta(\omega) = \Theta_0 \cos\left(\frac{\omega\tau}{4}\right) e^{-j\omega\tau/2} \quad . \tag{7-12}$$

For a coil with N loops, a general expression for the response magnitude is

$$|\Theta_\delta(\omega)| = |\Theta_0| \frac{1}{N} \sqrt{\left[\sum_{m=0}^{N-1} \cos\left(\frac{m\omega\tau}{N}\right)\right]^2 + \left[\sum_{m=0}^{N-1} \sin\left(\frac{m\omega\tau}{N}\right)\right]^2} \quad , \tag{7-13}$$

and the phase angle is

$$\phi = -\tan^{-1}\left[\frac{\sum_{m=0}^{N-1} \sin\left[\left(m+\frac{1}{2}\right)\frac{\omega\tau}{N}\right]}{\sum_{m=0}^{N-1} \cos\left[\left(m+\frac{1}{2}\right)\frac{\omega\tau}{N}\right]}\right] . \tag{7-14}$$

Equation (7-13) is plotted in Fig. 7-2 for N = 2 and N = 5. The plot abscissa is the normalized frequency, $\omega\tau/2$. Response resonances occur when $\omega\tau/2$ equals a multiple

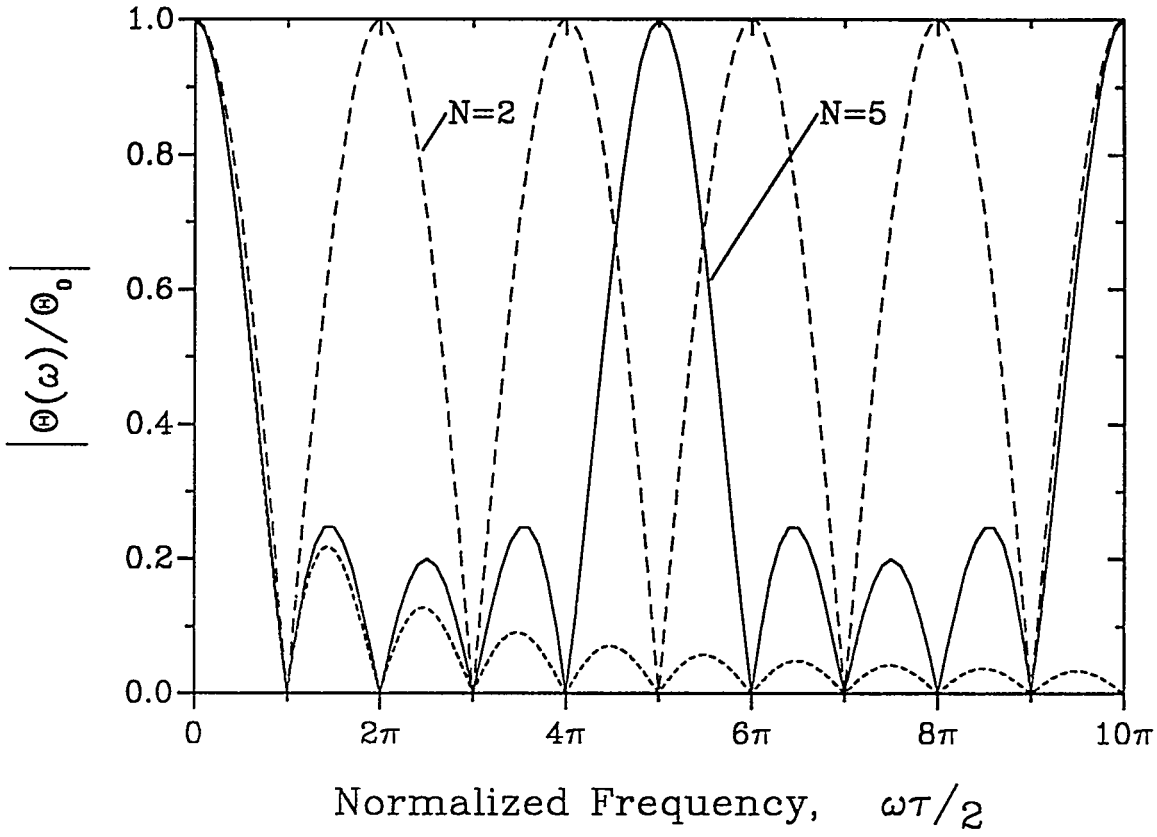

Fig. 7-2. The Faraday rotation relative magnitude versus normalized frequency for delta function current sensor coils with two and five turns. The dotted reference curve is the response for a centered, circular coil.

of Nπ, with the number of intervening nulls equal to N - 1. The response magnitudes in Fig. 7-2 for N = 5 resemble those for the noncentered, circular coil, Fig. 6-4, except higher frequency resonances now have a unity relative magnitude instead of ½. This unity magnitude results from complete phase matching between the magnetic field and the propagating light at each of the single-point interactions. As light in the fiber propagates away from the conductor, it experiences no further out-of-phase rotations that reduce the resonance magnitude as in the noncentered, circular coil. Also observed in Fig. 7-2 that is not seen in Fig. 6-4 is the complete frequency symmetry of the lobes and nulls about each resonance — each rising and falling frequency edge is symmetric about

the lobe/resonance center frequency. The bandwidths of the main response lobe and each of the higher frequency resonance lobes are also equal.

Equation (7-13) can also be plotted with the normalized frequency $\omega\tau_1/2$ as the abscissa; such a plot appears in Fig. 7-3. The similarities between Figs. 6-6 and 7-3 are obvious. The responses illustrated in Fig. 7-3 are identical to those previously discussed for the tapped fiber delay line for N fiber taps (see Chapter 6). Comparisons can be made to similar figures in Ref. 65.

The Faraday response bandwidths for coils configured for a delta function interaction can be significantly larger than those for the centered, circular coils made

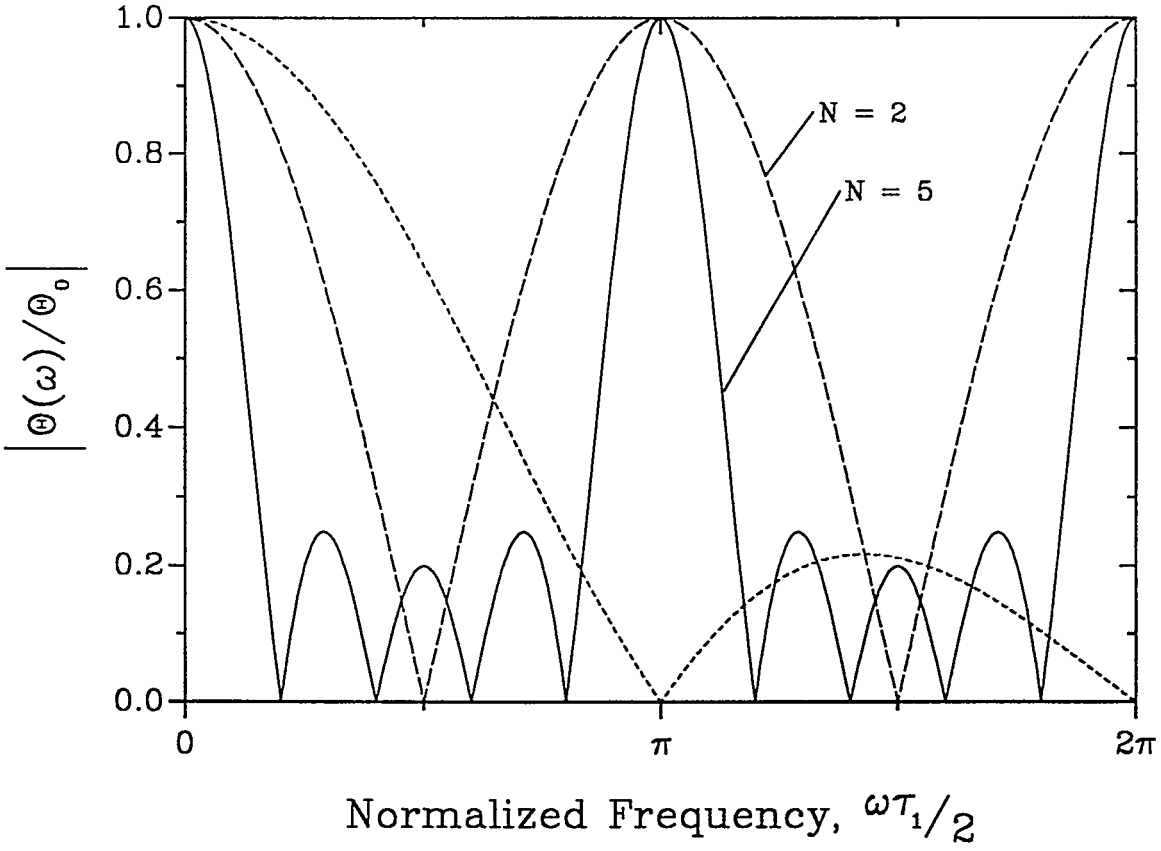

Fig. 7-3. The relative magnitude of the Faraday rotation from Fig. 7-2 replotted versus the normalized frequency $\omega\tau_1/2$. The dotted reference curve is the response for a centered, circular coil.

with the same length of fiber. This is obvious for a single loop coil which produces a theoretically infinite bandwidth. In Fig. 7-2, a notable difference in bandwidth is observed for the N = 2 curve compared to the centered, circular coil response even though the cutoff frequency for the two curves is identical. Using Eq. (7-12), the 3 dB response point for N = 2 will occur when

$$\cos\left(\frac{\omega_u \tau}{4}\right) = \frac{1}{\sqrt{2}} \quad . \tag{7-15}$$

Then

$$\Delta B = \frac{c}{4\pi R\, n\, N} \quad , \tag{7-16}$$

which is larger than the bandwidth for the centered, circular coil, Eq. (5-7), by 12.8%. As N increases the bandwidth for the delta function coil quickly approaches that for the centered, circular coil. Extracting data from the numerical computations of Eq. (7-13), the bandwidth increases are 5.1% for N = 3, 1.3% for N = 5 and negligible when $N \geq 7$. These bandwidth deviations can be compared to those of the noncentered, circular coil in Table 6-1 for the same value of N; larger response bandwidths result from the point interactions.

Based on the predictions from this delta function model, as well as those from the noncentered coil model, a general statement can be made about fiber current sensor coil configurations: for sensors with large numbers of fiber turns, the Faraday response in the low frequency main lobe is unaffected by displacement or coil cross-sectional shape; only sensor response at the higher frequencies is modified.

Although it is not obvious from a first look, the response phase given by Eq. (7-14) can be reduced to $-\omega\tau/2$ for all values of N. This is easily identified for N = 2 by inspecting Eq. (7-12). As a further example, if N = 3, Eq. (7-14) is rewritten as

$$\phi = -\tan^{-1}\left[\frac{\sin\left(\frac{\omega\tau}{6}\right)+\sin\left(\frac{\omega\tau}{2}\right)+\sin\left(\frac{5\omega\tau}{6}\right)}{\cos\left(\frac{\omega\tau}{6}\right)+\cos\left(\frac{\omega\tau}{2}\right)+\cos\left(\frac{5\omega\tau}{6}\right)}\right] . \qquad (7\text{-}17)$$

The sine functions are expanded into

$$\sin\left(\frac{\omega\tau}{6}\right) = \sin\left(\frac{\omega\tau}{2}-\frac{\omega\tau}{3}\right) = \sin\left(\frac{\omega\tau}{2}\right)\cos\left(\frac{\omega\tau}{3}\right)-\cos\left(\frac{\omega\tau}{2}\right)\sin\left(\frac{\omega\tau}{3}\right)$$

and

$$\sin\left(\frac{5\omega\tau}{6}\right) = \sin\left(\frac{\omega\tau}{2}+\frac{\omega\tau}{3}\right) = \sin\left(\frac{\omega\tau}{2}\right)\cos\left(\frac{\omega\tau}{3}\right)+\cos\left(\frac{\omega\tau}{2}\right)\sin\left(\frac{\omega\tau}{3}\right) .$$

Then Eq. (7-17) becomes

$$\phi = -\tan^{-1}\left[\frac{2\sin\left(\frac{\omega\tau}{2}\right)\cos\left(\frac{\omega\tau}{3}\right)+\sin\left(\frac{\omega\tau}{2}\right)}{2\cos\left(\frac{\omega\tau}{2}\right)\cos\left(\frac{\omega\tau}{2}\right)+\cos\left(\frac{\omega\tau}{2}\right)}\right] = -\tan^{-1}\left[\frac{\sin\left(\frac{\omega\tau}{2}\right)\left[1+2\cos\left(\frac{\omega\tau}{3}\right)\right]}{\cos\left(\frac{\omega\tau}{2}\right)\left[1+2\cos\left(\frac{\omega\tau}{3}\right)\right]}\right]$$

$$= -\tan^{-1}\left[\tan\left(\frac{\omega\tau}{2}\right)\right] = -\frac{\omega\tau}{2} . \qquad (7\text{-}18)$$

Determining the phase in this mathematical fashion for larger N quickly becomes unwieldy, but the solution is always the same, $\phi = -\omega\tau/2$. This phase is identical to Eq. (5-5) for the centered, circular coil indicating that phase in this sensor configuration is also dependent only on the total light transit time or the total fiber length.

The Complete Response Model

Based solely on the delta function interaction, the Faraday response resonances displayed in Fig. 7-2 would extend unattenuated (at unity) to infinite frequency. Such a

system, of course is not physically realizable, and the previous presentation of the delta function response model must be considered only for its conceptual value. A more realistic model is constructed by recognizing that $\Theta_\delta(\omega)$ in Eq. (7-9) is the transfer function for an ideal fiber current sensor having N point interactions. The transfer function is then used to construct complete frequency response functions for physical systems. In general, for each pass of the fiber near the conductor, the interaction length between the magnetic field and the propagating light in the fiber may be small but is finite. The two propagating electromagnetic signals become convolved over this short interaction length. Then in the frequency domain, the Faraday response for the coil system is nothing more than the transfer function, Eq. (7-9), multiplied by the expected frequency response for the short fiber length while making a single pass.

If the short interaction length is given as ℓ, the function $\Theta_\ell(\omega)$ describes the response for a single interaction. The complete frequency dependent Faraday rotation, which depends on the number of passes N, is then the product of two functions,

$$\Theta(\omega) = \Theta_\delta(\omega) \cdot \Theta_\ell(\omega) \quad . \tag{7-19}$$

The function $\Theta_\ell(\omega)$ can be labeled an envelope function, since in the frequency domain, it bounds the resonant response due to $\Theta_\delta(\omega)$ alone. If a functional form for $\Theta_\ell(\omega)$ can be identified or computed for a single pass of the fiber by the conductor, then the rolloff in the magnitudes of the higher frequency resonance peaks can be established.

By inspecting Eq. (7-6) and comparing it to Eq. (7-19), one functional form for the envelope function, $\Theta_\ell(\omega)$, can be determined. The function $\sin(\omega\tau_\ell/2)/(\omega\tau_\ell/2)$ is a direct result of using a short circular fiber loop in the derivation of the model for the highly elongated coil. And as would be expected, this function is equivalent to Eq. (5-3), less the phase factor, when the appropriate transit time $\tau_\ell = (n/c)\ell$ is used. Approximating the short interaction length with a circular loop is often a good estimate

for many fiber current measurement systems. In particular, such a description allows for quick computations of the magnitudes of the resonance peaks since they fall under a well-defined enveloping function.

Using Eq. (7-19), the frequency characteristics of the complete response function for a multiturn coil in a delta function configuration are determined by three separate parameters of the fiber current sensor coil. All of these parameters are related to well-defined lengths of different fiber sections and can be used in the design of optimum sensor coils. (1) The resonance peaks in the response function occur at higher frequencies (see Eq. (6-14)) related to propagation through one loop of the coil, $L_1 = (c/n)\tau_1$. (2) The bandwidth of the main response lobe and the bandwidths of all the unattenuated higher frequency resonance peaks are found from the total length of fiber in the coil, L. And (3) the enveloping magnitude of the resonance peaks is determined by the short interaction length, ℓ, of a single pass of the fiber by the conductor. For most applications that exploit the advantages of the delta function response model, the relationship between these three lengths will be $\ell \ll L_1 \leq L$.

Interesting phenomena result from use of the complete response function in Eq. (7-19) when ℓ is not small compared to L_1. A trivial result occurs for N = 1 in $\Theta_\delta(\omega)$; $\Theta(\omega) = \Theta_\ell(\omega)\, e^{-j\omega\tau/2}$ as expected, regardless of the value of ℓ. But if N > 1, the formulation of Eq. (7-19) provides a shortcut for determining the frequency response for more complicated coil systems, especially those that use double-pass/reflective geometries or series of identical coils. As an example, assume a multiturn, circular coil is used and one lead is terminated such that the light is reflected back through the coil. Light injection and detection are both accomplished at the nonreflecting lead. Such a current sensor coil configuration is used in high sensitivity systems to reduce the effects due to reciprocal interactions such as stress or temperature-induced birefringence changes. If the coil is centered about the conductor, $\Theta_\ell(\omega)$ is simply $\sin(\omega\tau_\ell/2)/(\omega\tau_\ell/2)$, for $\tau_\ell = 2\pi R_\ell N_c (n/c)$ the one pass transit time through the entire coil, N_c turns. The delta

function response accounts for phase delays in the light propagation. Here N_δ (number of light passes) = 2 and $\Theta_\delta(\omega)$ is given by Eq. (7-7) with $\xi = 0$ and $\tau_1 = \tau_d$, the time required for light to propagate from the middle of the coil, $\ell/2$, to the reflection point and back. By definition, $\tau_d \geq \tau_\ell$. The complete Faraday response is then

$$\Theta(\omega) = \Theta_0 \left[\frac{\sin\left(\omega\tau_\ell/2\right)}{\left(\omega\tau_\ell/2\right)} \right] \cos\left(\frac{\omega\tau_d}{2}\right) e^{-j\left(\omega\tau_d/2\right)} \quad . \qquad (7\text{-}20)$$

Similar descriptions of the Faraday response can be derived for other sensor systems.

Demonstration of the Model

The delta function response model was verified using the two fiber coil configurations shown in Fig. 7-4. Both experimental systems used the coaxial test cell #2 listed in Table A-1. This cell has an inner conductor diameter of 2.5 cm, an outer conductor diameter of 5.75 cm, and a HOM cutoff frequency of 2.3 GHz [34]. All coils had 10 loops of fiber with each loop being approximately two meters in length and with a small portion of each loop passing through the cell. The Faraday response is then limited to the interactions with light in those short segments of fiber inside the cell; outside the cell, no field exists and the propagating light experiences no induced rotation. In the first configuration (Fig. 7-4a), the fiber made a short turn around the cell center conductor entering and exiting the cell at the same point. This simulates very closely the light path illustrated in Fig. 7-1b. In the second configuration (Fig. 7-4b), a straight fiber section passed near the center conductor with the fiber entering and exiting on opposite sides of the cell. The various lengths in the fiber coil were chosen to achieve a narrow response bandwidth and to place several of the resonance peaks at frequencies that were within the measurement range of the experimental instrumentation.

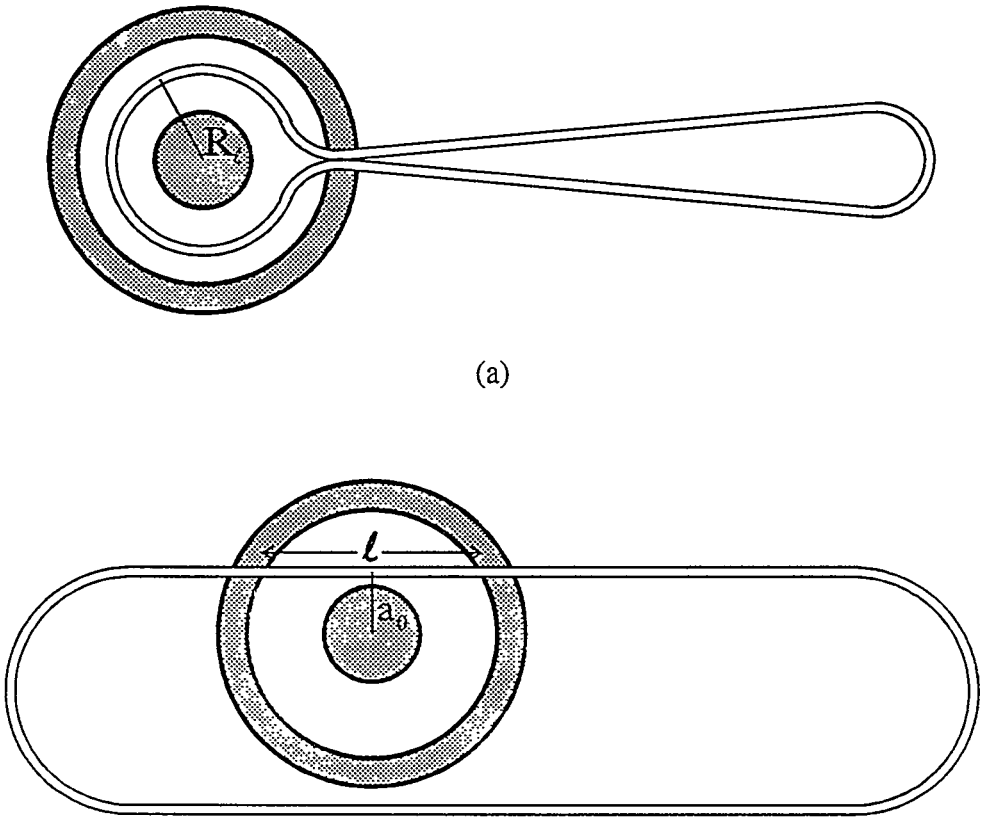

Fig. 7-4. Two fiber coil configurations used to demonstrate the delta function response model.

The relative magnitude of the Faraday rotation measured using the first experimental configuration is shown in the two graphs of Fig. 7-5. In Fig. 7-5a the model response, depicted by a solid curve, and the experimental results, shown as the open circles, are plotted for the lower frequencies. The resonance peaks are spaced about 101 MHz apart, the bandwidths are approximately 4.5 MHz and the cutoff frequency occurs at 10.1 MHz. Although the model and experimental curves in Fig. 7-5a agree well for the frequencies near resonance, the responses at the intervening frequencies do not agree at all. The secondary lobe magnitudes and the null frequencies do not match. Symmetry of the measured values about the resonance frequencies, however, is preserved.

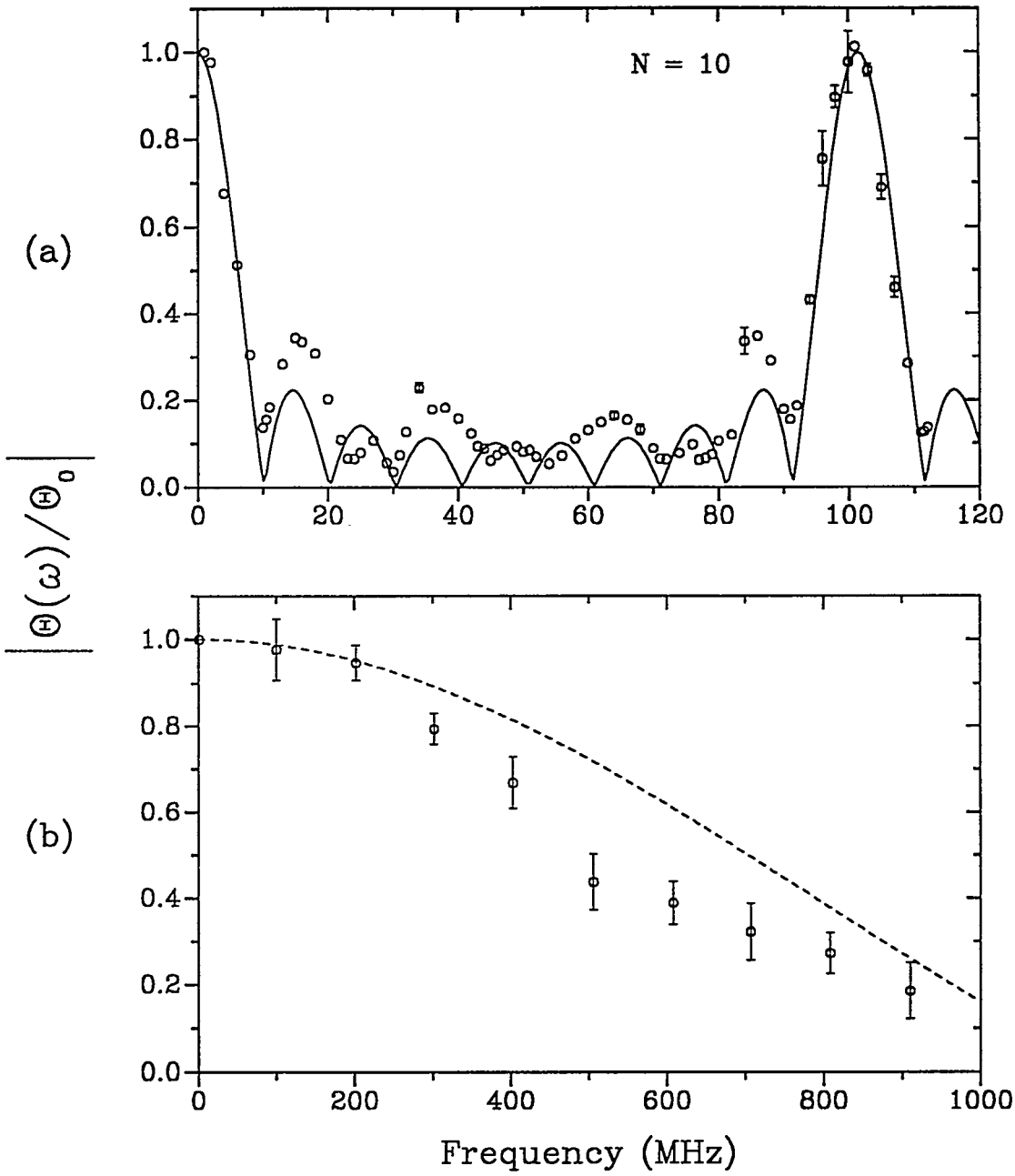

Fig. 7-5. The measured (open circles) and predicted Faraday response at low frequencies (a) and higher frequencies (b) for a 10 turn test coil with short tight loops around the conductor. The solid curve in (a) represents the theoretical behavior near and below the first higher frequency resonance. In (b), the dashed curve is an estimate of the response of an enveloping function for the short fiber length interaction, and the plotted points are measured values only at frequencies near the resonance peaks. Error bars represent total scatter in the measured values.

Much of this disagreement between measurement and model is attributed to bend-induced linear birefringence created by the tight turns as the fiber loops around the cell center conductor. This coil was prepared using the twisted and rejacketed fiber with 40 twists/m [29], which should have been adequate for testing at this diameter; but apparently when tight bends are introduced, the fiber jacket breaks free from the glass and the twist relaxes. By modifying the bend radius of the loops within the cell, significant changes were noted in the frequency response. The curves plotted in Fig. 7-5 represent the best agreement between the model and the experiment. Although the presence of linear birefringence in the fiber is believed to produce perturbations in the frequency response of the Faraday rotation, a detailed investigation of this phenomenon goes beyond the present scope of this study.

The finite interaction length of the short fiber loop inside the test cell causes a rolloff of the resonance peak magnitudes at the higher frequencies. This feature is seen in Fig. 7-5b. The experimental data are plotted only at the peaks of each resonance. The dotted curve is a rough estimate of the envelope function computed using the magnitude $|\sin(\omega\tau_\ell/2)/(\omega\tau_\ell/2)|$ from Eq. (7-6). Although the 10 loops of fiber inside the cell are not circular in cross section, an average length is estimated for these fiber segments and used to determine a value for τ_ℓ. As seen in Fig. 7-5b, the experimental data are bound by relatively large error bars, especially at the higher frequencies. These uncertainties, coupled with some residual linear birefringence effects in the fiber and the imprecise estimates used for the model envelope function, make quantitative comparisons of the curves in Fig. 7-5b difficult. The general trend in the measured data, however, follows the prediction.

The second experimental configuration (Fig. 7-4b) was designed to remove the interfering effects from bend-induced linear birefringence. This was achieved by using only short, straight fiber segments passing through the cell without any bending. Results from measurements using this arrangement are shown in Fig. 7-6 along with the model

predictions. The measured and calculated responses near the resonance frequencies agree well, just as they did for the first configuration. In this case, however, the measured secondary lobe magnitudes and the null frequencies between the resonances are much closer to those predicted by the model. Exact identification of the nulls was difficult with this type of current monitor since a 10 dB loss in sensitivity occurs. This sensitivity loss results from having only a partial turn of optical fiber inside the cell acting as the sensor, whereas in the first configuration, a full sensor turn around the center conductor existed.

A nice feature of this second experimental configuration is that it lends itself to a relatively simple computation of the complete response function. Each of the ten straight sections of singlemode fiber passing through the cell will experience a rotation given by

$$\Theta_\ell(\omega) = \frac{\Theta_0}{\tau_\ell} a_0 \int_0^{\tau_\ell} \frac{e^{-j\omega t}}{a_0^2 + \left(\frac{c}{n}\right)^2 \left(\frac{\tau_\ell}{2} - t\right)^2} dt \ , \qquad (7\text{-}21)$$

where $\tau_\ell = (n/c)\ell$ is the transit time of light through the straight section and a_0 is the distance of closest approach the fiber makes with the axis of the cell center conductor. Here $\Theta_0 = VB_0\ell$, where B_0 is an arbitrary static flux density created by the current at unit distance from the conductor. Equation (7-21) must be normalized to the low frequency response to remove the dependence on B_0 and other geometric parameters. Integrating for $\omega = 0$ results in

$$\Theta_\ell(0) = 2 \frac{\Theta_0}{\tau_\ell} \left(\frac{n}{c}\right) \tan^{-1}\left(\frac{c\,\tau_\ell}{2\,n\,a_0}\right) \ . \qquad (7\text{-}22)$$

The normalized Eq. (7-21) is integrated numerically to produce the envelope function,

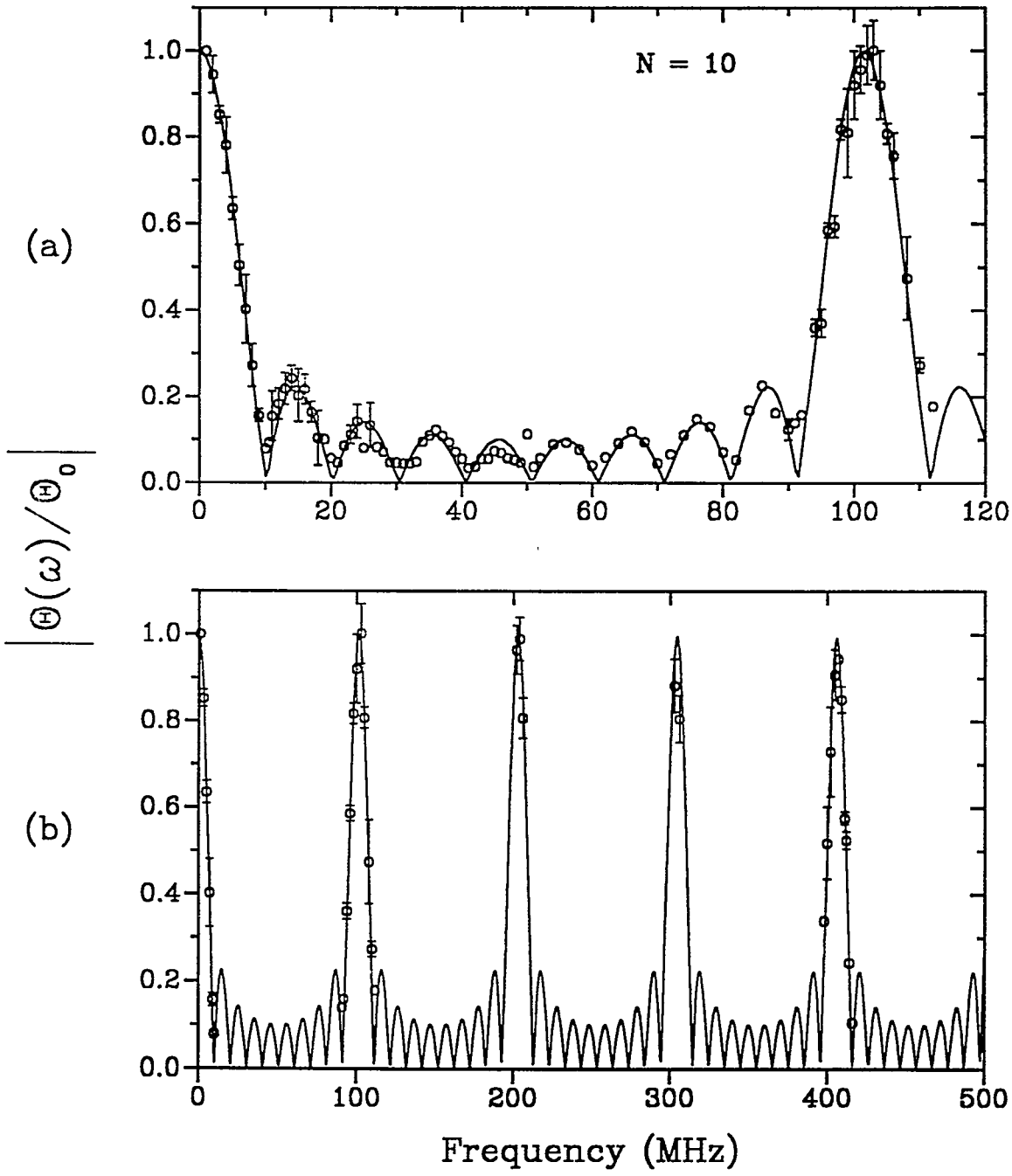

Fig. 7-6. The measured (open circles) and predicted (solid curves) Faraday response at low (a) and higher (b) frequencies for a test coil with short straight segments passing near the conductor. Only measured values near the resonance peaks are plotted in (b). Error bars on the measured values represent total data scatter.

and then substituted into Eq. (7-19). The resulting high frequency model response is used to generate the solid curves in Fig. 7-6. Resonance frequencies, bandwidths and cutoff frequencies predicted by this model are identical to those of the first experimental coil configuration. These features are expected since they depend only on τ and τ_1 (or equivalently on L and L_1) which are identical for both coils. The high frequency rolloff of the resonance peak magnitudes, however, is dependent on τ_ℓ and a_0 in Eq. (7-21). Here, $a_0 = 1.52$ cm and $\ell = 4.85$ cm. The transit time of the light through the short fiber section inside the cell is $\tau_\ell = 0.24$ ns, producing an envelope function with 3 dB bandwidth and cutoff frequency of 1.87 GHz and 4.2 GHz. The resonance peaks in Fig. 7-6b are plotted only to approximately 400 MHz. Unfortunately, RF interference in the measurement instrumentation (peculiar to this experimental configuration only) precluded data recording to nearer the 3 dB bandwidth of the envelope function.

Rectangular Coils

Fiber current sensors coils with rectangular cross sections (though not practical to implement because of the sharp corners) are excellent for the theoretical study of high frequency effects in the Faraday response. This particular geometry is chosen for modeling because (1) it represents a coil cross section that is noncircular in all respects, thus exhibiting several unique high frequency features; and (2) it lends itself to a simple analytical description for predicting centered, noncentered and highly elongated coil frequency responses. Ideally, a model of an elliptically-shaped coil is desired to represent a realistic fiber current sensor coil that might have a displaced conductor or a compressed cross section; however, the mathematical treatment is quite complicated, and the resulting model begins to break down as the coil becomes very eccentric. The rectangular coil model provides a good compromise for this study.

The Faraday response model is constructed using the geometry shown in Fig. 7-7. Expressions similar to Eq. (7-21) are used to determine the rotation in each segment of

the rectangular cross section. The rectangle has dimensions 2w (width) by 2h (height). Light enters the coil at the location marked by t_0 in Fig. 7-7. One complete loop around the rectangle requires light travel through five fiber segments; the total number of fiber segments in the coil is then 5N. The Faraday rotation in the first segment is

$$\Theta_1(\omega) = VB_0\left(\frac{c}{n}\right)(w + X_1)\int_{m\tau_1}^{m\tau_1 + t_1} \frac{e^{-j\omega t}}{(w + X_1)^2 + \left(\frac{c}{n}\right)^2 (m\tau_1 - t)^2}\, dt \quad , (7\text{-}23)$$

where m is the turn counter, 0 to N - 1, $\tau_1 = 2(w + h)(n/c)$ is the light transit time through one complete fiber loop. and $t_1 = h(n/c)$. In the second segment (top horizontal),

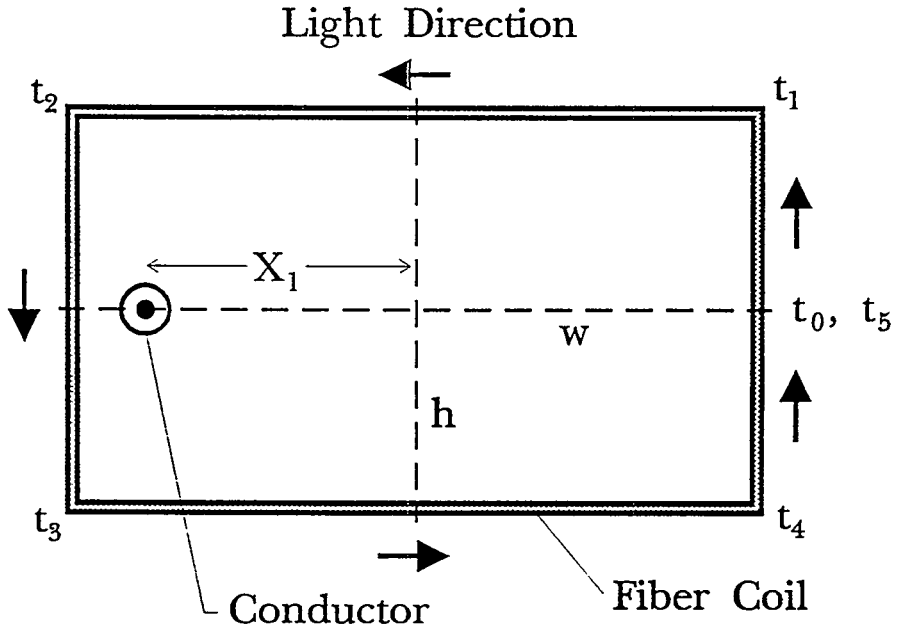

Fig. 7-7. The geometrical layout for the rectangular coil model. The conductor is displaced in the coil cross section, and the coil shape is allowed to vary.

$$\Theta_2(\omega) = VB_0\left(\frac{c}{n}\right)h \int_{m\tau_1 + t_1}^{m\tau_1 + t_2} \frac{e^{-j\omega t}}{h^2 + \left(\frac{c}{n}\right)^2\left[m\tau_1 + t_1 + \frac{n}{c}(w + X_1) - t\right]^2}\, dt \ , \tag{7-24}$$

where $t_2 = t_1 + 2w(n/c)$. The third segment (left vertical) produces a rotation given by

$$\Theta_3(\omega) = VB_0\left(\frac{c}{n}\right)(w - X_1) \int_{m\tau_1 + t_2}^{m\tau_1 + t_3} \frac{e^{-j\omega t}}{(w - X_1)^2 + \left(\frac{c}{n}\right)^2\left[m\tau_1 + t_2 + \frac{n}{c}h - t\right]^2}\, dt \ , \tag{7-25}$$

where $t_3 = t_2 + 2t_1$. An expression for $\Theta_4(\omega)$ for the lower horizontal segment is similar to Eq. (7-24) with appropriate changes in the time; and the final rectangular segment has a rotation, $\Theta_5(\omega)$, similar to Eq. (7-23). The total response is computed by summing the individual rotations, then normalizing to the zero frequency rotation.

$$\frac{\Theta(\omega)}{\Theta_0} = \frac{\sum_{m=0}^{N-1} \left[\Theta_1(\omega) + \Theta_2(\omega) + \Theta_3(\omega) + \Theta_4(\omega) + \Theta_5(\omega)\right]}{2NVB_0\left[\tan^{-1}\left(\frac{h}{w + X_1}\right) + \tan^{-1}\left(\frac{h}{w - X_1}\right) + \tan^{-1}\left(\frac{w + X_1}{h}\right) + \tan^{-1}\left(\frac{w - X_1}{h}\right)\right]} . \tag{7-26}$$

Equation (7-26) is evaluated numerically to determine the total Faraday rotation. Throughout the computations, the rectangle geometries will vary, but the perimeter of the rectangle is held constant so that total transit time, τ, is the same as that in an equivalent circular coil. The light entry point into the fiber can also be varied by letting $X_1 > 0$ to simulate $\xi = 0.5$ and setting $X_1 < 0$ for $\xi = 0$.

The frequency response of the Faraday rotation for the rectangular coil models are plotted in Fig. 7-8. In the models leading to these two plots, the conductor is allowed

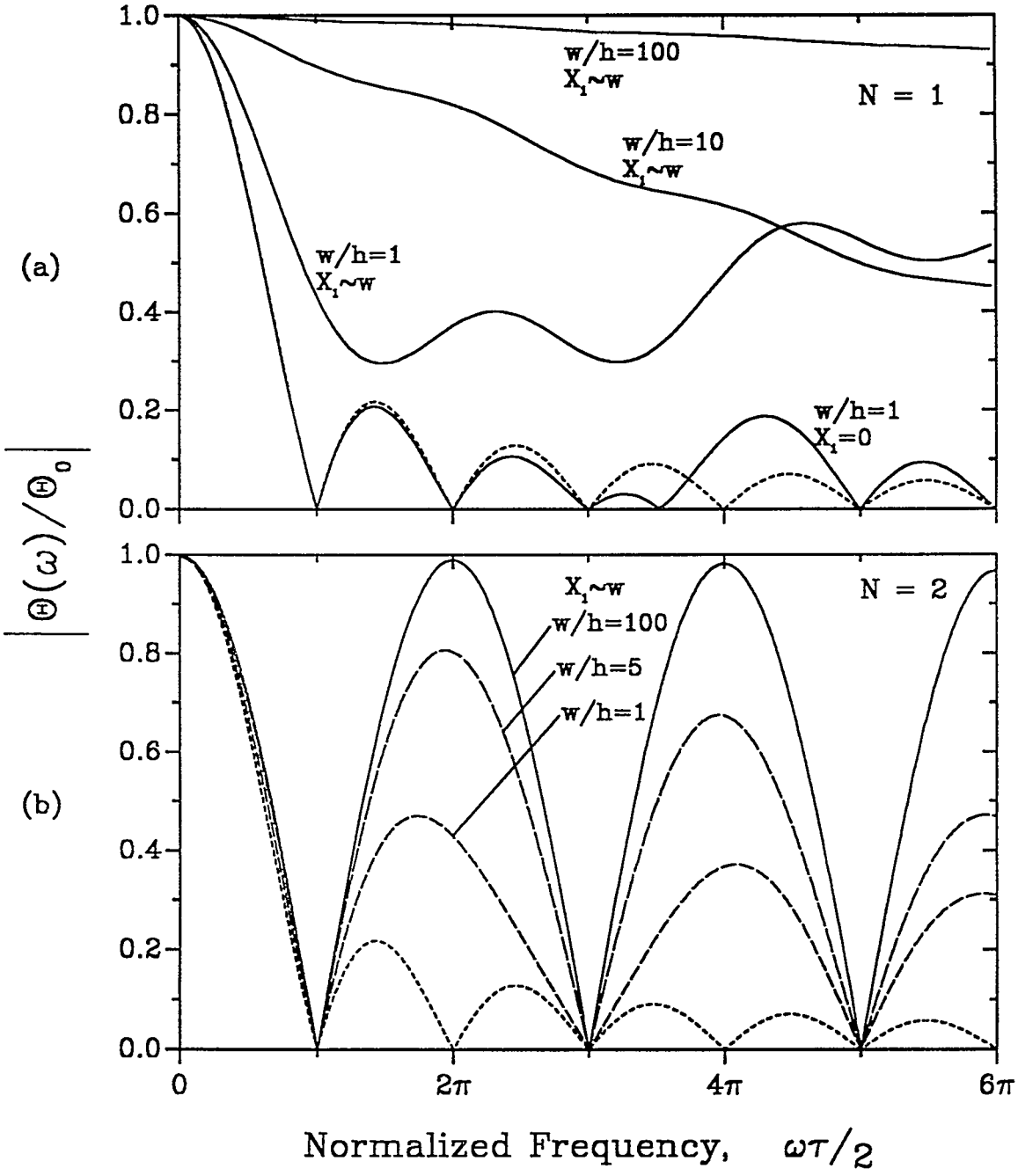

Fig. 7-8. Model predictions for a Faraday effect fiber current sensor coil with a varying rectangular cross section. (a) A single turn coil with the conductor centered in a square cross section and with the conductor displaced to the coil edge in a direction away from the light entry point. The rectangular cross section is varied with the conductor displaced. (b) A two turn coil with the conductor displaced to the coil edge. The dotted curve in each plot is the reference for an equivalent centered, circular coil.

to move toward the fiber coil ($X_1 > 0$) and the rectangular cross section is varied. The dotted curves in both Figs. 7-8a and 7-8b are the response for a centered circular coil which has a circumference equal to the perimeter, 4(w + h). In Fig. 7-8a, the response for a single turn square coil (width/height = 1) is shown. This response has identical main lobe bandwidth and cutoff frequency as that for the centered, circular coil. However, a noticeable deviation in the curves occurs near $\omega\tau/2 = 4\pi$. This is due to the four-fold symmetry created by the four identical coil sides. As might be expected, the exact shape of this small response enhancement near $\omega\tau/2 = 4\pi$ will depend on the choice of light entry point in the square coil. Also shown in Fig. 7-8a is the effect of displacing the conductor to the edge of the square coil (w/h = 1, $X_1 \sim$ w) in a direction away from the light entry point (equivalent to $X_1/R \sim 1$ and $\xi = 0.5$ in the circular coil). This curve shows an increased bandwidth in the low frequency lobe and higher frequency oscillations that result from both two-fold and four-fold symmetries. This curve can be compared directly to its counterpart for the circular coil in Fig. 6-2a. Noted similarities are the lack of response nulls at the higher frequencies and relative response magnitudes near ½.

With the conductor fully displaced, the rectangular coil cross section is compressed to a highly elongated state. Response curves are shown in Fig. 7-8a for an intermediate compression state (w/h = 10) and near total compression (w/h = 100). The frequency response for the coil with large eccentricity and near-maximum conductor displacement approaches that of the delta function model for a single turn coil. This response exhibits a near-infinite bandwidth.

In Fig. 7-8b the Faraday response is shown for a two-turn coil, again with the conductor displaced almost fully to the edge of the coil; the cross section of the rectangle is allowed to vary in shape. For the square coil, resonant responses are observed near the frequencies defined by $\omega\tau/2 = 2m'\pi$. This resonant behavior is very similar to that of the two-turn circular coil with displaced conductor. The relative magnitude of the first

higher frequency resonance peak for the square coil in Fig. 7-8b is near ½, and the magnitudes of subsequent higher frequency peaks diminish. If the model were to allow the limiting case of $X_1 = w$ without producing a singularity, the magnitude of all the higher frequency resonances would be ½ as demonstrated for the circular coil in Chapter 6. As the cross section of the rectangular coil is compressed, the relative magnitude of the resonance peaks in Fig. 7-8b increases. When w/h = 100, the predicted Faraday response approaches that of the delta function model shown in Fig. 7-2 for N = 2. The bandwidth increase in the main lobe is noted, and the magnitudes of the higher frequency resonances are very near one.

The curves in Fig. 7-8 are presented to help visualize the frequency responses for coils that are in intermediate states between a symmetric (i.e., circular) coil with fully displaced conductor and a highly elongated coil with fully displaced conductor. During the transition of coil cross section between these two states, the magnitude of the resonance response peaks (see Fig. 7-8b) progresses from approximately ½ to very near unity. It is expected that coils that initially have a circular cross section will exhibit similar high frequency responses as the cross section is compressed.

Many general high frequency characteristics of fiber current sensors can be investigated theoretically using the rectangular coil model. One good example is a single turn coil with the conductor placed at the center and the coil cross section compressed. Modeling the initial shape as a square, the frequency response begins as that seen in Fig. 7-8a for the curve with w/h = 1 and $X_1 = 0$. After compression, the response is much like the curve in Fig. 7-8b for w/h = 100. The current sensor response will resemble that of a "double delta function", since in the highly elongated state, the light in the fiber makes two close approaches to the conductor for a single coil turn. The frequency spacing between resonances is determined from the transit time of light through half a coil turn, $\tau_1/2$, resulting in $\omega_R\tau/2 = 2m'\pi$, which is exactly that shown in Fig. 7-8b for the two-turn coil.

The resonance phenomenon just described is observable in the frequency response of almost any fiber coil with arbitrary cross section. If the conductor is centered in the coil cross section, then the sensor main lobe bandwidth and frequency response will closely approximate that of the centered, circular coil. Deviations in the higher frequency response will result from symmetries peculiar to the chosen coil geometry and the choice of the light entry point. Then in the highly elongated state, the response will approach that predicted by the delta function model. Also, it is easily envisioned that specific features in the responses for coils with displaced conductors in arbitrary cross sections can be predicted using information already generated from the delta function and rectangular coil models. In general, it appears that predicting the Faraday frequency response for many coil geometries is possible through use of the framework developed here for the noncircular current sensor coils.

CHAPTER 8

TRAVELLING WAVE FIBER CURRENT SENSORS: BASIC CONCEPTS AND THEORY

Manipulation of the fiber current sensor coil cross section and the position of the conductor relative to the coil changes the higher frequency characteristics of the Faraday response, but has limited effects on the sensor bandwidth, especially for multiturn coils. Bandwidth can be enhanced in the transit time limited fiber sensors by deviating from the planar coil structure and expanding the fiber into a helix. In this geometry the electromagnetic wave propagating along the conductor experiences partial phase matching with the light propagating in the fiber. This travelling wave configuration enhances the Faraday rotation at the higher frequencies, and thereby increases the bandwidth.

The travelling wave concept has been used extensively in electro-optic modulators [62], and integrated optic devices with bandwidths well beyond 10 GHz have been fabricated [66]. In these modulators, however, the Pockel's effect (interaction between the light and the electric field) is used, and the two interacting signals propagate codirectionally and in the same dielectric medium. In a fiber current sensor, the magnetic field is generally orthogonal to the direction of current propagation, while the Faraday rotation is dictated by $\mathbf{B} \bullet d\mathbf{l}$ and is maximized when the field and light are codirectional. Implementing a Faraday effect travelling wave concept is thus much more difficult since both **B** and **k** cannot simultaneously be directional with the light. The helical coil geometry allows for partial phase matching, but further enhancement of the Faraday signal requires slowing the propagation of the electromagnetic wave.

Travelling Wave Fiber Current Sensor Model

A basic travelling wave fiber current sensor is shown schematically in Fig. 8-1.

The helical singlemode fiber coil is immersed in the dielectric of a coaxial transmission line. If the frequency of operation is limited to a range where only a TEM mode exists in the transmission line and the fiber coil is centered about the coax center conductor, then Eq. (3-9) describes the Faraday response for the system. It is possible for the coil to assume any position relative to the center conductor, which then requires use of Eq. (3-7) to fully describe the frequency dependent Faraday interaction. This added complexity is addressed briefly in Chapter 12; however, for most of this study of travelling wave fiber current sensors, the coil is taken to be coaxial with the conductor. Two further simplifications are introduced into the model: the fiber helix consists of N complete turns with a constant pitch, x_0 and the coax line dielectric is free of magnetic materials, $\mu_r = 1$. Using these assumptions, the angle ψ is no longer time dependent,

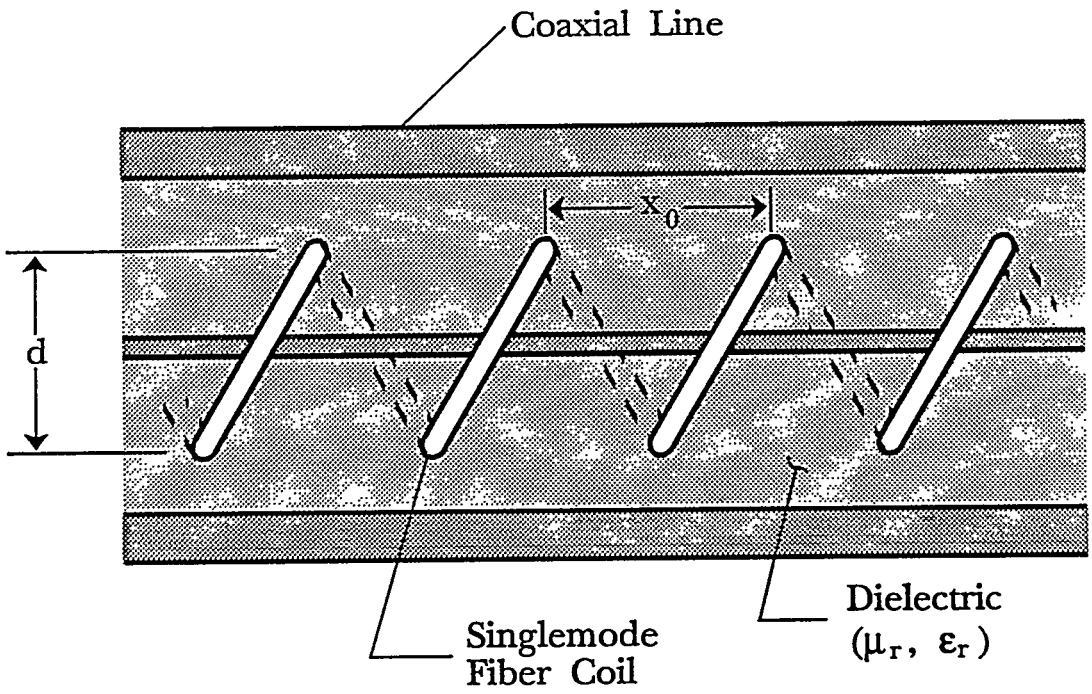

Fig. 8-1. A travelling wave fiber current sensor constructed of a helical singlemode fiber coil immersed in the dielectric of a coaxial transmission line.

$$\cos\psi = \frac{Nx_0}{L} \quad , \tag{8-1a}$$

and

$$\sin\psi = \frac{N\pi d}{L} \quad , \tag{8-1b}$$

where L is the total fiber length in the coil helix and d is the mean diameter of the coil measured radially from the conductor axis. Substituting Eqs. (8-1) into Eq. (3-9) results in a general expression for the Faraday rotation of the simplified travelling wave sensor:

$$\Theta(\omega) = \Theta_0 \frac{1}{\tau} \int_0^{\tau} e^{-j\omega t\left[1-\frac{\sqrt{\varepsilon_r}}{n}\frac{Nx_0}{L}\right]} dt \quad . \tag{8-2}$$

In Eq. (8-2) $\tau = (n/c)2\pi RN/\sin\psi$, which differs from that for the planar coil by $(\sin\psi)^{-1}$. This factor arises because the helical coil requires a longer fiber length for a given coil diameter, d. The actual length of the fiber is given by

$$L = N\sqrt{(\pi d)^2 + x_0^2} \quad , \tag{8-3}$$

which when substituted into Eq. (8-2) results in a final integral expression for the Faraday response:

$$\Theta(\omega) = \Theta_0 \frac{1}{\tau} \int_0^{\tau} e^{-j\omega t\left[1-\frac{\sqrt{\varepsilon_r}}{n\pi\sqrt{\left(d/x_0\right)^2 + 1/\pi^2}}\right]} dt \quad . \tag{8-4}$$

If the material relative permittivity is considered constant (independent of

frequency), Eq. (8-4) can be solved in manner similar to Eq. (5-1) for the centered, circular (and planar) coil. The solution becomes

$$\Theta(\omega) = \Theta_0 \left[\frac{\sin(\zeta)}{\zeta}\right] e^{-j\zeta} \quad , \tag{8-5a}$$

where

$$\zeta = \frac{\omega\tau}{2}\left(1 - \frac{\sqrt{\varepsilon_r}}{n\pi\sqrt{\left(d/x_0\right)^2 + 1/\pi^2}}\right) \quad . \tag{8-5b}$$

At the low frequencies, $\omega \rightarrow 0$, ζ becomes zero and Eq. (8-5a) reduces to Eq. (2-3) as expected. If the coil pitch, x_0, becomes small, the contribution from the second term in the parenthesis of Eq. (8-5b) is diminished. If $x_0 = 0$, then Eq. (8-5a) is identical to Eq. (5-3) for the planar coil. The relative magnitude of the Faraday response in Eqs. (8-5) has a form similar to Eq. (5-4):

$$\left|\frac{\Theta(\omega)}{\Theta_0}\right| = \left|\frac{\sin(\zeta)}{\zeta}\right| \quad . \tag{8-6}$$

The 3 dB bandwidth occurs when $\zeta \approx \sqrt{2}$ which leads to [60]

$$\Delta B \approx \frac{\sqrt{2}\,c}{\pi^2\, n\, N\, x_0}\left[\sqrt{\left(d/x_0\right)^2 + \frac{1}{\pi^2}} - \frac{\sqrt{\varepsilon_r}}{n\pi}\right]^{-1} \quad . \tag{8-7}$$

The travelling wave sensor bandwidth now shows a dependence on the coaxial line relative permittivity and the fiber coil diameter-to-pitch ratio, d/x_0 .

The bracketed factor in Eq. (8-7) can be equal to zero, which theoretically gives

an infinite bandwidth. This condition arises from perfect phase matching between the two interacting electromagnetic signals. When Eq. (8-6) for the travelling wave coil configuration is compared to Eq. (5-4) for the planar coil geometry (the baseline configuration), an enhancement factor equivalent to

$$F = \frac{1}{1 - \frac{v_f}{v_{ph}}} \quad , \tag{8-8}$$

is extracted [62]. The travelling wave enhancement is determined by the relative phasing between the light in the fiber, $v_f = (c/n)\cos\psi$ (in the direction of $\mathbf{k}$) and the velocity of the TEM wave, v_{ph}, as given by Eq. (3-6). When the relative phase velocities are identical, the enhancement is infinite.

The relative magnitude of the Faraday rotation from Eq. (8-6) is plotted versus the normalized frequency, $\omega\tau/2$, in Fig. 8-2. Also plotted is a reference curve taken from Eq. (5-4). In the example in Fig. 8-2, a travelling wave enhancement of slightly larger than two is used for illustration.

The Bandwidth Enhancement Factor

A bandwidth enhancement factor (BEF) is determined by the ratio of the travelling wave sensor bandwidth to the planar coil bandwidth:

$$\text{BEF} \equiv \frac{\Delta B \text{ (travelling wave)}}{\Delta B \text{ (planar)}} \quad . \tag{8-9}$$

Upon substitution of Eqs. (8-7) and (5-8) [60],

$$\text{BEF} = \left(\frac{d}{x_0}\right)\left[\sqrt{\left(\frac{d}{x_0}\right)^2 + \frac{1}{\pi^2}} - \frac{\sqrt{\varepsilon_r}}{n\pi}\right]^{-1} . \qquad (8\text{-}10)$$

In defining the BEF, the number of fiber turns and the coil diameter remain fixed for the two coils being compared. This means the low frequency Faraday sensitivity is unchanged from that described by Eq. (2-3). Thus, the BEF can be used as a figure of merit to give a quantifiable estimate of sensor performance improvement for travelling wave configurations. The BEF can also be used directly to compute the increase in the sensitivity-bandwidth product over that for the planar coil given in Eq. (5-10).

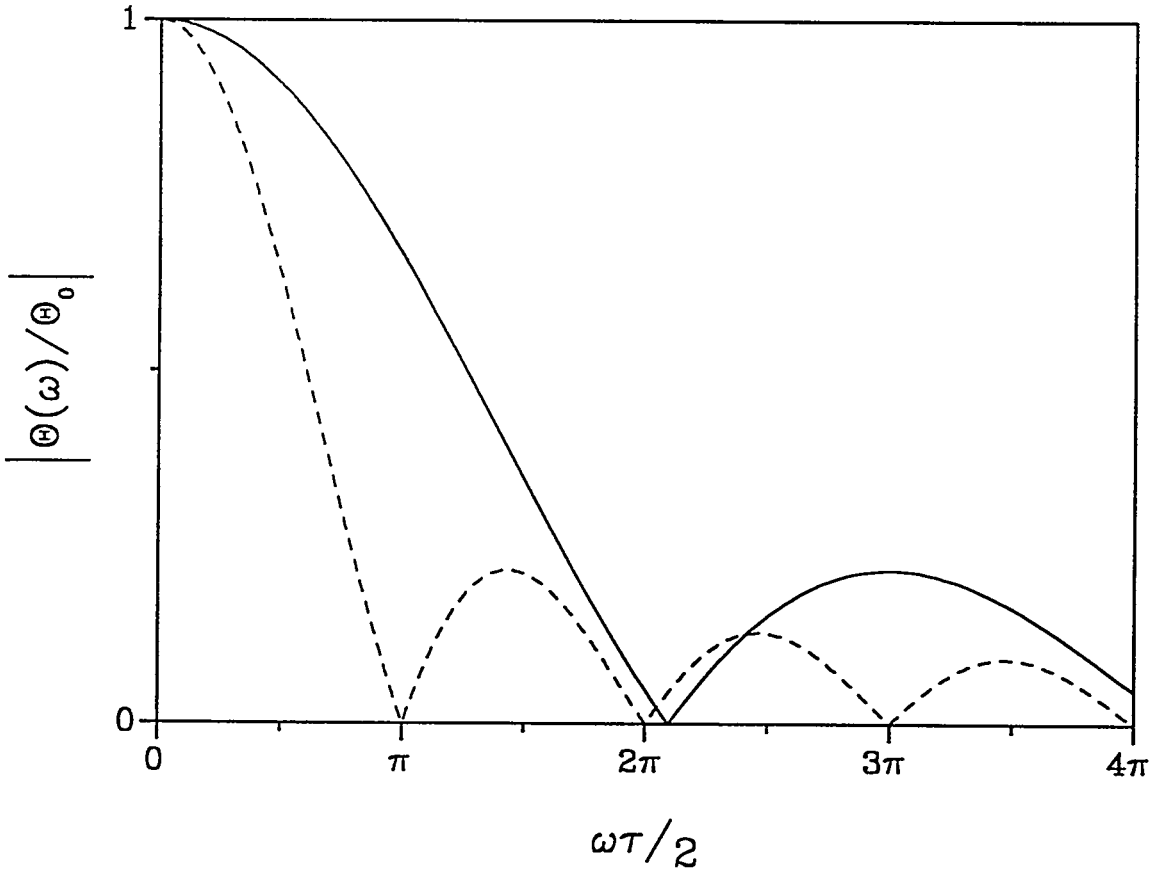

Fig. 8-2. A typical Faraday response curve for a travelling wave fiber current sensor. The dotted reference curve is the response for an equivalent sensor coil with coplanar turns.

Equation (8-10) is very similar to the enhancement factor given by Eq. (8-8) when the respective velocities are substituted. The only difference is the added fiber length,

$$\Delta L = \sqrt{1 + \left(x_0/\pi d\right)^2} \quad , \tag{8-11}$$

that must be used in the helical coil in order to maintain a fixed diameter. Equation (8-8) is a generic expression for any travelling wave structure that accounts only for the relative phase velocity mismatches; Eq. (8-10) is specific to this fiber configuration.

The BEF is strongly dependent on the diameter-to-pitch ratio of the travelling wave fiber sensor coil and the relative permittivity of the slow-wave structure (the coaxial line). Figure 8-3 is a plot of the BEF, Eq. (8-10), for several values of ε_r using d/x_0 as the independent variable. The fiber refractive index is assumed to have a nominal value of 1.46. For any ε_r a value of d/x_0 exists for which a maximum BEF occurs. If $\varepsilon_r > n^2$, the maximum BEF approaches infinity. This complete phase matching condition (the travelling wave condition) occurs when the bracketed factor in Eq. (8-10) equals zero, or when

$$\frac{d}{x_0} = \frac{1}{\pi}\sqrt{\frac{\varepsilon_r}{n^2} - 1} \quad . \tag{8-12}$$

In Fig. 8-4, the values of ε_r and d/x_0 are plotted for which the travelling wave condition, Eq. (8-12) are met. It is obvious from Fig. 8-4 that slow-wave structures with larger relative permittivities are needed if the fiber helix has a small pitch.

In Fig. 8-3, if $\varepsilon_r < n^2$, the maximum BEF remains finite. For $\varepsilon_r = 2$, the BEF attains a peak value of ~ 4.0 at $d/x_0 = 0.083$; and for $\varepsilon_r = 1$, an air or vacuum dielectric, the BEF peaks at 1.37 when $d/x_0 = 0.33$. Thus, merely expanding the fiber coil into a

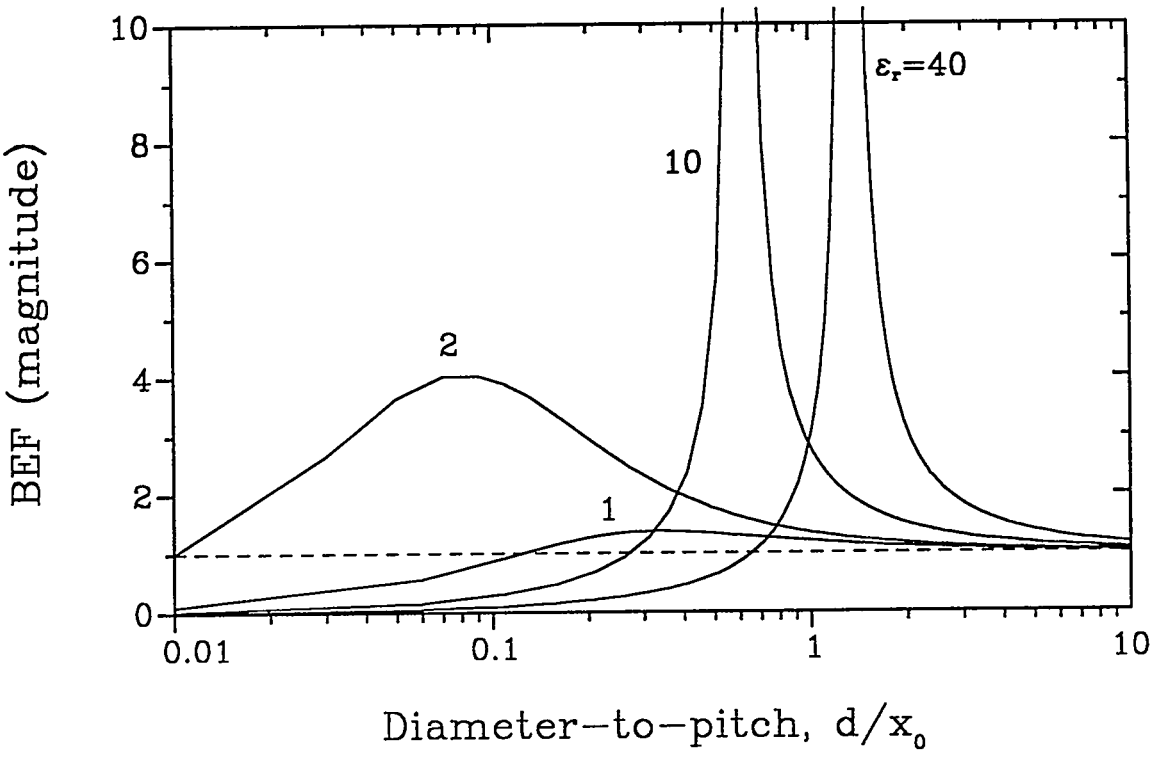

Fig. 8-3. The magnitude of the bandwidth enhancement factor as a function of the travelling wave coil diameter-to-pitch ratio. Curves are plotted for a wide range of relative permittivity values.

helix does not provide much improvement in the sensor bandwidth. The propagation of the magnetic wave must also be slowed, preferably by using a dielectric with a large relative permittivity.

Two other features are noted in the curves in Fig. 8-3. As $d/x_0 \rightarrow \infty$, or the coil pitch becomes small, the BEF approaches one for all values of ε_r (no enhancement occurs as expected). But as $d/x_0 \rightarrow 0$ ($x_0 \rightarrow \infty$, infinite pitch), the BEF approaches zero for all ε_r. This feature results from the chosen definition for the BEF. If the coil diameter must remain constant, then as x_0 increases so does the total fiber length according to Eq. (8-3). Eventually, the transit time of the light through this fiber length becomes prohibitively long and the bandwidth for the sensor decreases to zero. In order to keep the travelling

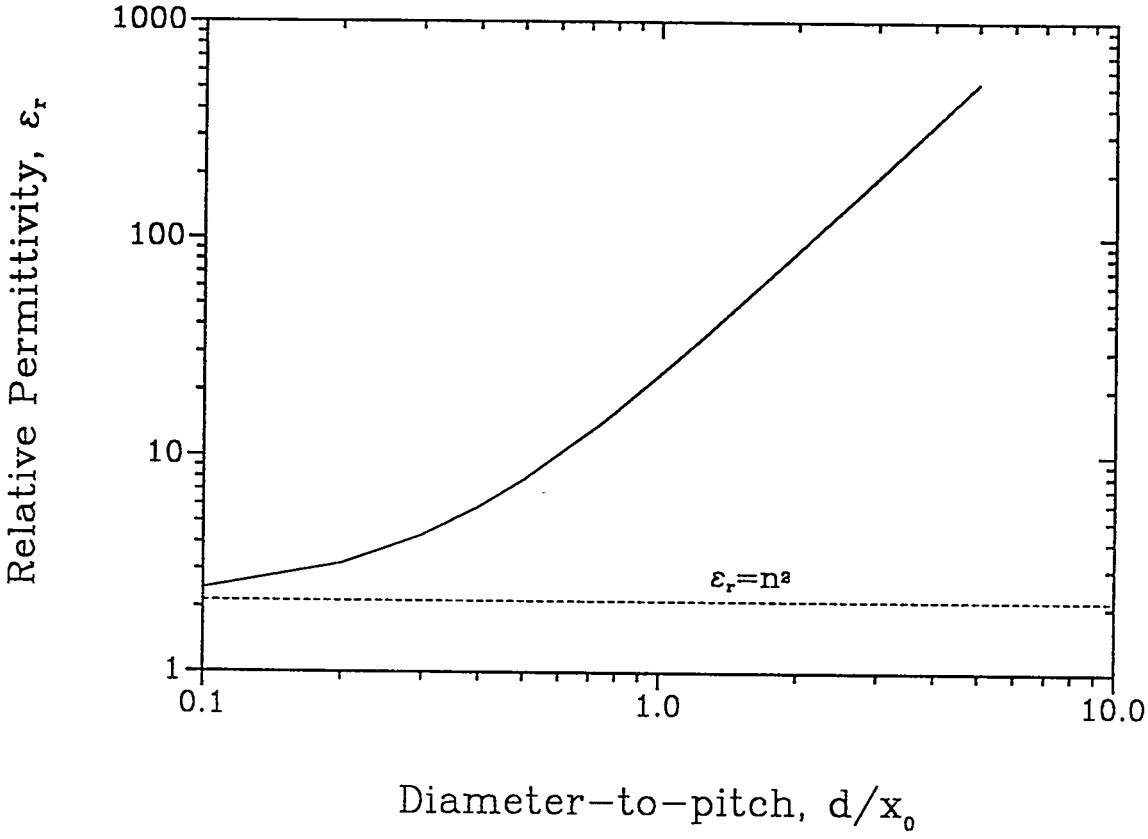

Fig. 8-4. A plot of the relative permittivity of the dielectric medium required for maximum Faraday response bandwidth versus the sensing fiber diameter-to-pitch ratio. For the ideal travelling wave sensor with $\varepsilon_r > n^2$, the theoretical maximum bandwidth approaches infinity.

wave sensor at a practical length and yet produce as large a BEF as possible, emphasis is again placed on using the high relative permittivity materials.

CHAPTER 9

TRAVELLING WAVE TRANSMISSION CELLS

The travelling wave fiber current sensor shown in Fig. 8-1 was implemented using coaxial transmission cells with helical fiber coils mounted in the cell working volume [34]. Two basic cell configurations were used: one with an air dielectric, the other with liquid dielectrics of varying relative permittivity. The airline provided a baseline measurement for Faraday current sensor response when only a helically-shaped coil was used. Liquids were chosen as coaxial line dielectrics for the second configuration because they have large ε_r, they are readily available in a wide range of permittivities, and they can easily assume the shape of the cell interior and fill the large volumes required.

The fiber coils were constructed from low birefringence singlemode fiber with an 80 μm cladding diameter. Fibers were twisted at a rate of ~30 turns/meter and wound on 3 cm diameter mandrels. The selected twist rate was adequate for the circular birefringence bias to overcome the bend-induced birefringence at the chosen coil diameter. Faraday responses then could be measured directly from relative changes in the light intensity as described in Chapter 4. The coil diameter was held constant for all test designs, but the pitch of the helical coil varied between 1.5 and 3.0 cm; several values of d/x_0 were used. In some configurations, the coils were quite long; however, the total number of turns was limited so that coils never exceeded 45 cm in axial length. The number of coil turns varied from 10 to 20.

A single coaxial cell outer structure was used for all travelling wave experiments. The outer conductor diameter was 5.75 cm. In order to maintain a 50 Ω nominal impedance on the transmission line, the inner conductor diameter varied according to Eq. (A-11) for the appropriate value of ε_r. Properties of the travelling wave transmission cells — SWR, impedance and transmission magnitude — were determined using ANA

measurements and Eqs. (A-25) and (A-26). These properties were important in assessing the useful operating frequency range for the liquid cells and necessary in developing accurate response models that accounted for all the liquid parameters.

The transmission cells were positioned as shown in the experimental arrangement of Fig. 4-1. A photograph of the bench-top hardware for this configuration is shown in Fig. 9-1. All remaining instrumentation and procedures for the measurements of the travelling wave current sensor response were as outlined in Chapter 4.

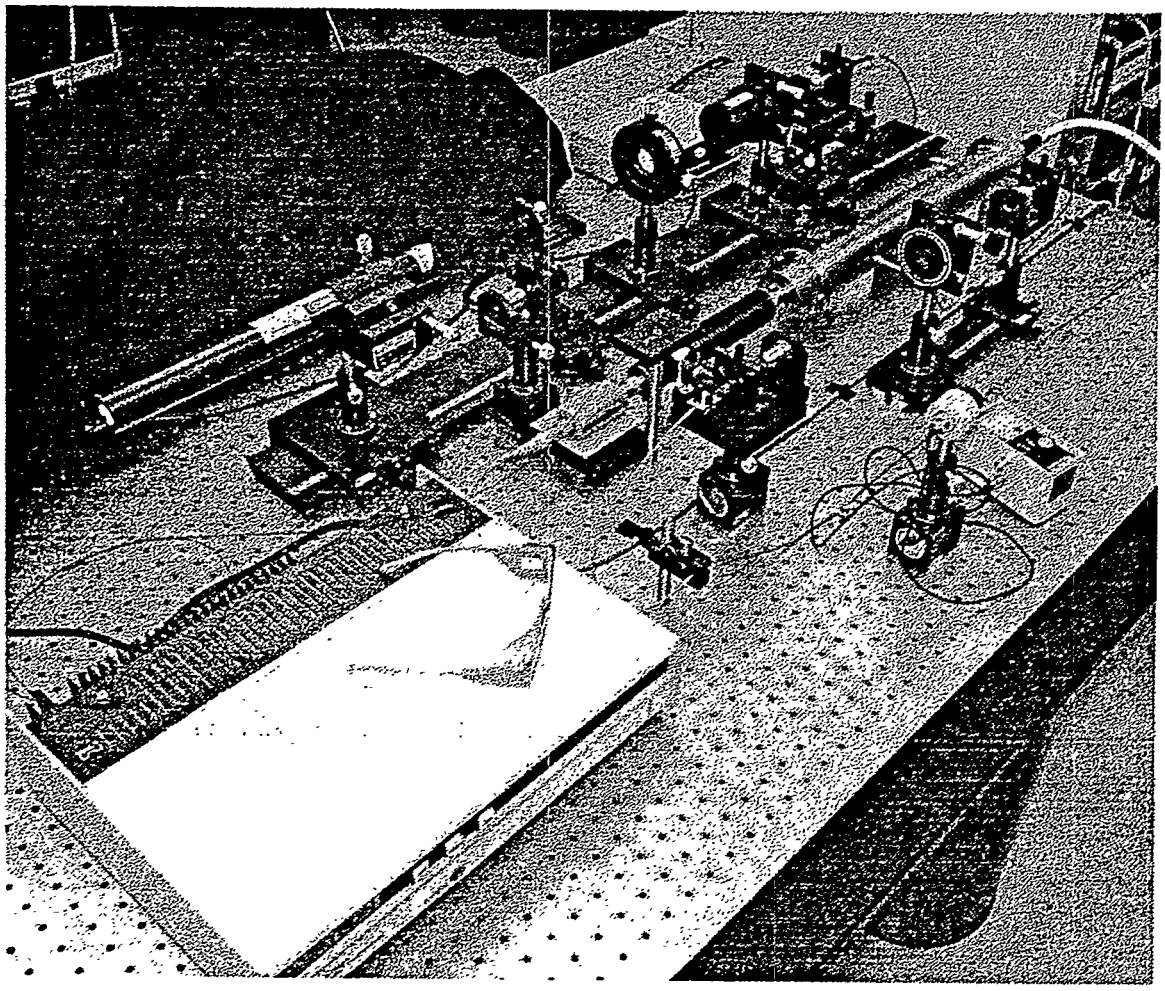

Fig. 9-1. A bench-top photograph of the experimental hardware used during testing of the travelling wave fiber current sensors.

Airline Cell

The coaxial airline travelling wave test cell is described as Cell #2 in Table A-1 of Appendix A. The cell center conductor diameter is 2.49 cm (for 50 Ω characteristic impedance), and the working volume length is 45.7 cm. The fiber sensor coil consisted of 10 turns wound on a polyurethane foam mandrel of 3.0 cm diameter. This coil support then fit directly over the cell center conductor. A view of the disassembled airline is shown in the photograph, Fig. 9-2. Tapered end sections of both inner and outer conductors can be seen at the left of the photo. The ends of the fiber coil are secured to the foam mandrel by first sewing several thread loops around the fiber and through the foam; then a dab of UV-curing epoxy is hardened at the fiber-thread interface. The twist is locked into the fiber turns, and the coil leads are allowed to dangle (untwisted) so they may be fed through the wall of the cell outer conductor section.

The electromagnetic performance characteristics of the airline travelling wave cell were quite good. SWR and impedance magnitude of the cell are plotted versus frequency in Fig. 9-3. The cell SWR never exceeds 1.23 and the impedance varies

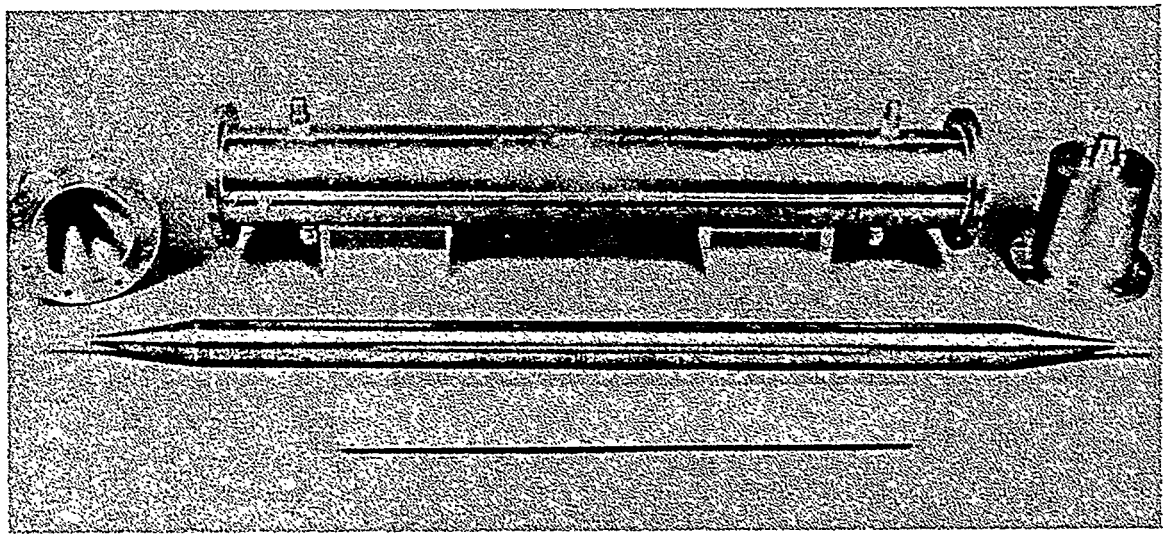

Fig. 9-2. Photograph of the disassembled travelling wave airline cell. A 10-turn, helical fiber coil on a foam mandrel is located at the bottom of the photo.

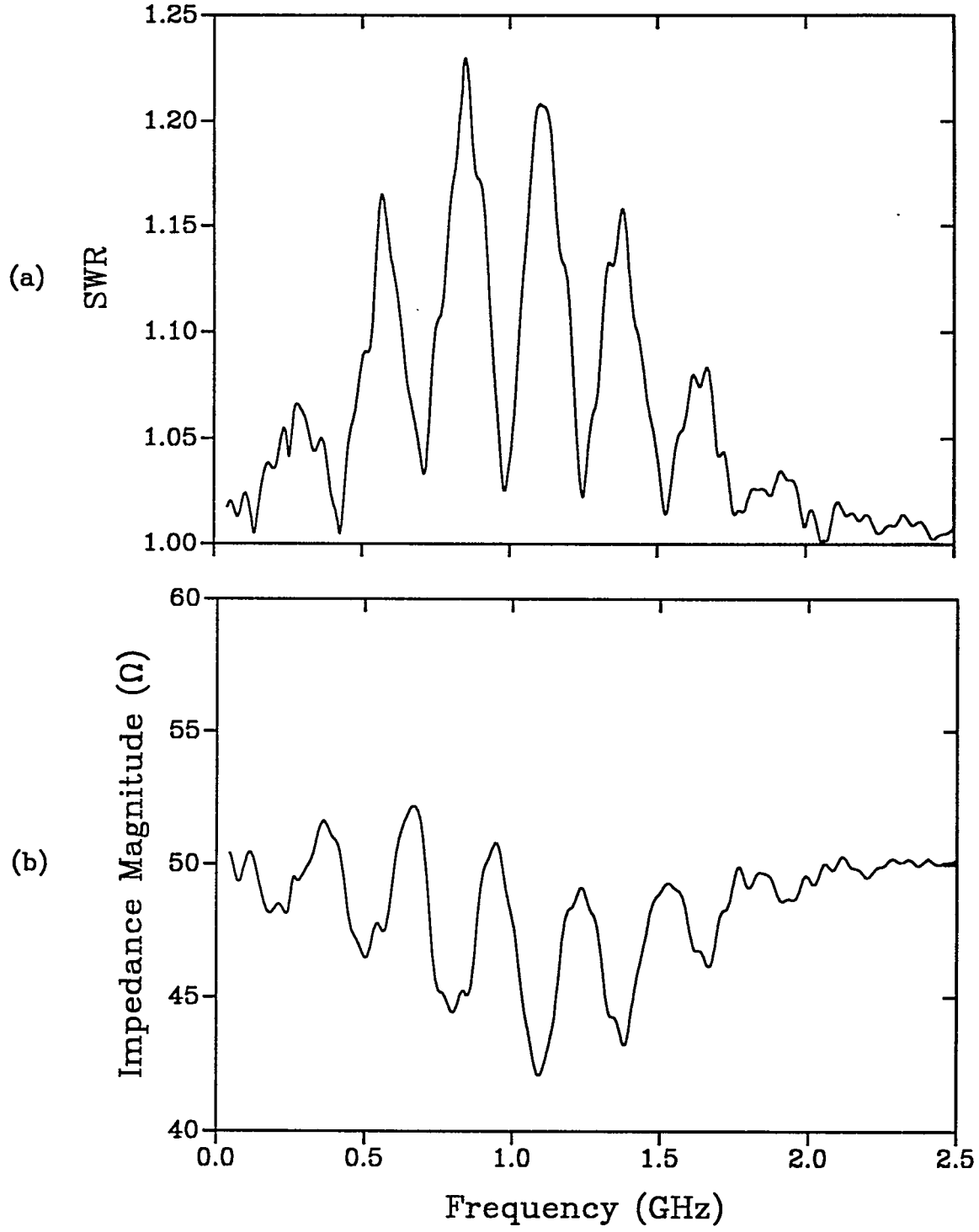

Fig. 9-3. The measured SWR (a) and the impedance magnitude (b) of the travelling wave airline cell with the optical fiber sensor inside.

between 42.5 and 52 Ω. Frequency spacing between the larger oscillations in both the SWR and the impedance is approximately 260 MHz. This corresponds to resonant reflections at the transitions from the RF connectors into the cell air space. The fiber coil and foam mandrel do not create noticeable perturbations in the electromagnetic characteristics. The useful operating frequency range of the airline cell extends beyond 2.3 GHz, which is the cutoff frequency for cell higher order modes. Such a high test frequency, however, is not needed since the fiber current sensor Faraday response is limited to much lower values.

Liquid Cells

Many organic and inorganic liquids with large relative permittivities [67], $\varepsilon_r > 10$, were considered during design of the travelling wave sensors. Three — 1-propanol, methanol, and water — were chosen for testing because they spanned a wide range of ε_r values and were relatively nonhazardous in the small volumes used. The static or low frequency relative permittivity of these three liquids is 20.1, 32.63, and 78.54, respectively, at 25°C. One disadvantage of using liquid dielectrics in the travelling wave cell is the temperature dependence of ε_r. Selected values of the relative permittivity for the three test liquids are given in Tables 9-1 and 9-2. Near ambient temperature in the laboratory, values for ε_r vary only slightly. Thus, no temperature control was deemed necessary, but a monitor was provided to indicate liquid temperature. This sensor, a Fluoroptic™ thermometer [68] from Luxtron, is seen in Fig. 9-1.

Figure 9-4 is a close-up view of the fully assembled liquid travelling wave cell. (This cell is also seen in the experimental setup of Fig. 9-1.) Inlet and vent ports for liquid filling are visible on the top of the cell. Exit holes for the fiber sensor required sealing to prevent liquid leakage. The optical fiber test coil is supported in the liquid medium by a teflon tube. A helical groove with a semicircular cross section was machined in the outside surface of the tube as a guide for the twisted fiber. The fiber

Table 9-1.

Relative Permittivity of the Test Liquids at Selected Temperatures [67].

Temperature (°C)	1-Propanol	Methanol	Water
-113	—	64.0	—
-80	38.0	54.0	—
-34	29.0	—	—
-20	—	40.0	—
20	—	33.62	80.37
25	20.1	32.63	78.54
200	—	—	34.5

was anchored to the mandrel using the same thread-and-epoxy technique as used for the airline coil. Several mandrel tubes were used, each with a different helical pitch. The teflon mandrel was aligned coaxially in the cell using several teflon support rings. These rings are seen in the end-view photograph of the opened liquid cell in Fig. 9-5a. The support rings also aligned the center conductor coaxially in the cell. Because of the large relative permittivity of the liquid, the center conductor diameter required to maintain a 50 Ω characteristic impedance in the cell was often very small. Thus, external support was needed.

Barely visible in Fig. 9-5a is the optical fiber spooling off the end of the teflon mandrel and exiting the cell. This section of fiber was untwisted, and care was taken to not stress it during cell assembly. Figure 9-5b shows the disassembled travelling wave cell. The O-rings used to seal the cell outer conductor components are visible on the two endcap sections. Also, short teflon extension tubes are seen in the endcaps; these help

Table 9-2.

Relative Permittivity of Water.

Temperature (°C)	ε [Ref. 69]	ε [Ref. 70]
0	87.74	87.90
5	85.76	85.90
10	83.83	83.95
15	81.95	82.04
20	80.10	80.18
25	78.30	78.36
30	76.55	76.58
35	74.83	74.85
40	73.15	73.15
45	71.51	71.50
50	69.91	69.88
55	68.34	68.30
60	66.81	66.76
65	65.32	65.25
70	63.86	63.78
75	62.43	62.34
80	61.03	60.93
85	59.66	59.55
90	58.32	58.20
95	57.01	56.88
100	55.72	55.58

maintain radial dielectric continuity throughout the entire length of the cell interior.

The presence of the teflon support structures inside the cells often created numerous points for reflection of the electromagnetic waves. Teflon was chosen as a support material because it is impervious to all liquids considered as potential dielectric materials. However, the teflon has a relative permittivity of 2.0, which differs significantly from that of any of the liquids. Impedance mismatches could occur at many

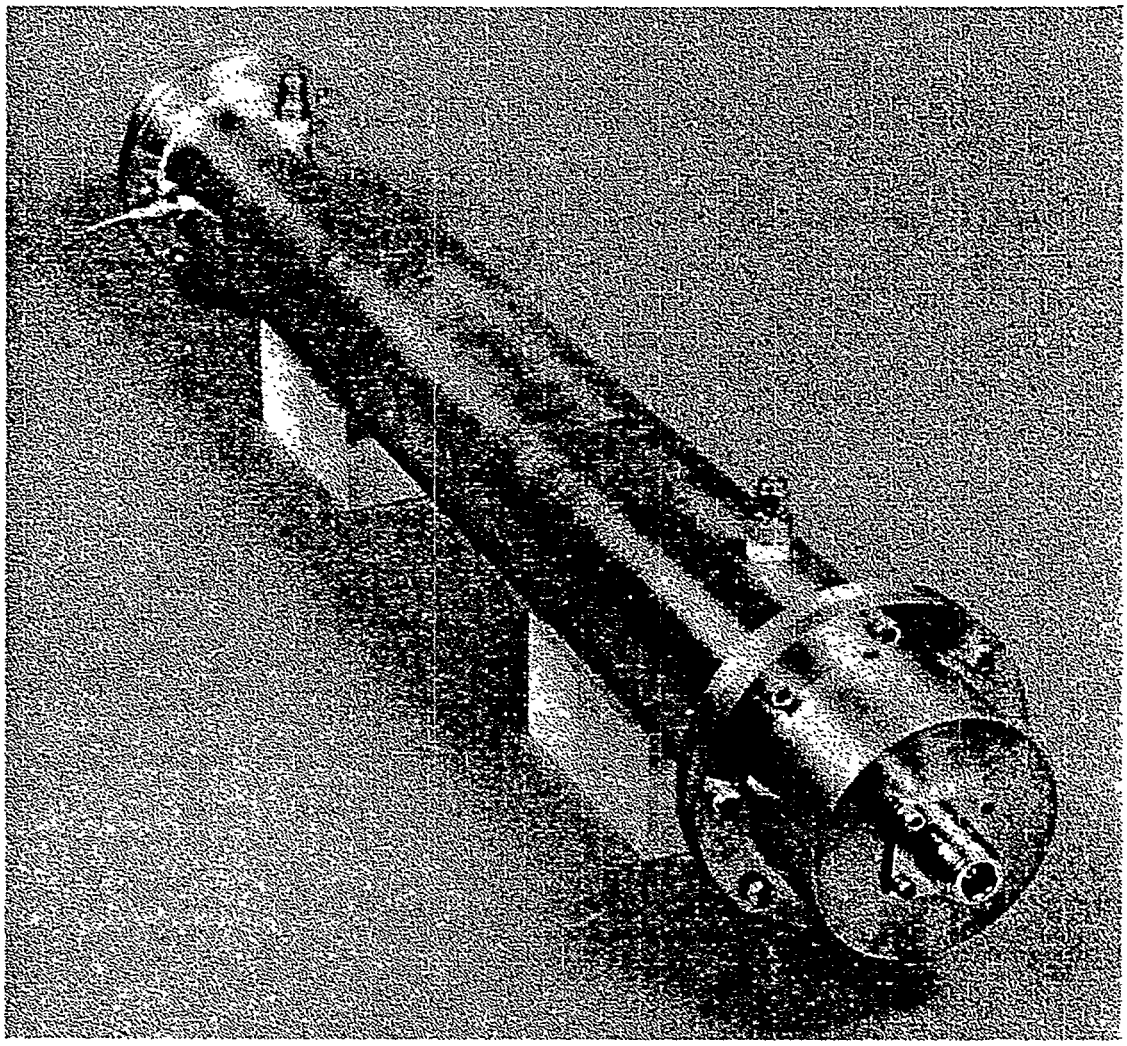

Fig. 9-4. Photograph of the liquid travelling wave transmission cell. Optical fiber leads exit the cell through sealed holes in the cell outer conductor. Fill and vent holes for the liquid are located on top of the cell.

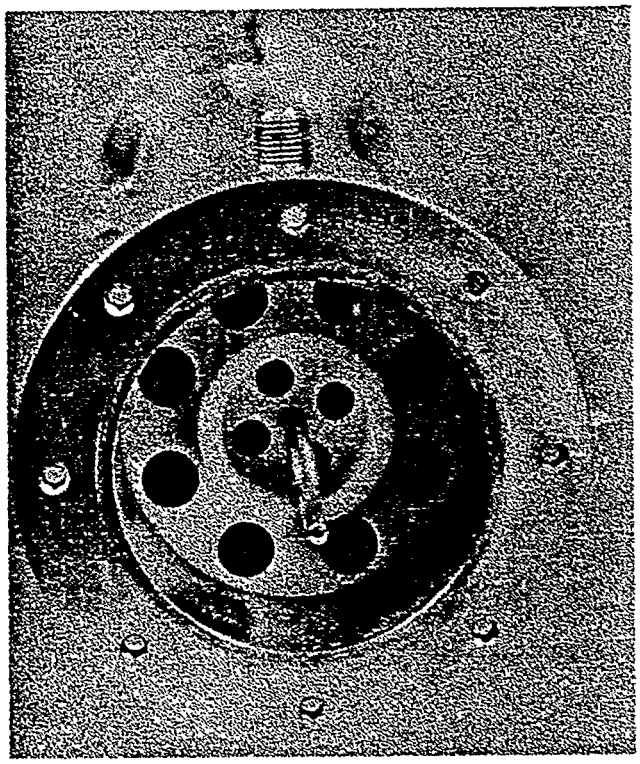

(a)

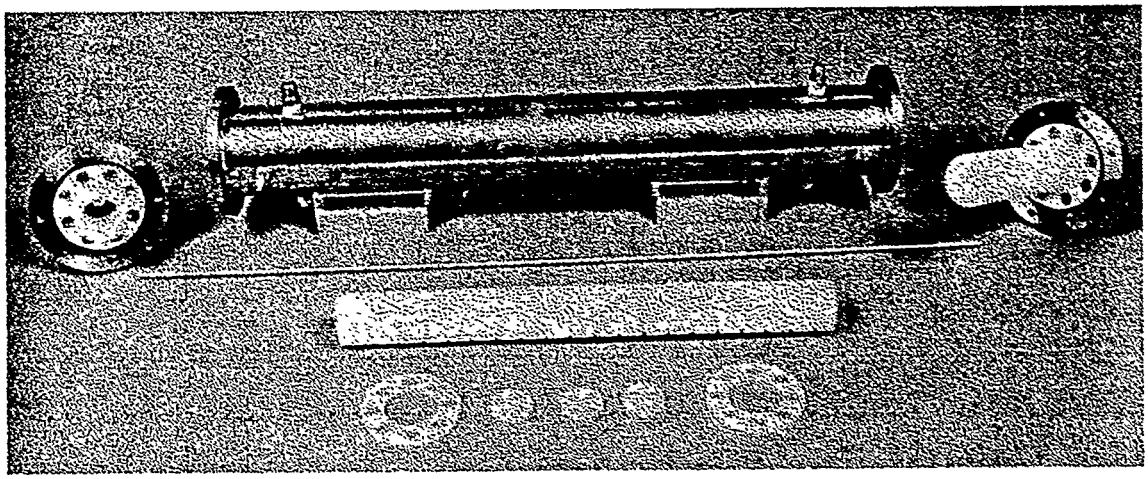

(b)

Fig. 9-5. Photographs of the liquid travelling wave transmission cell. (a) End view showing the inside of the cell, and (b) the fully disassembled cell.

locations inside the cell. Also, the geometric transition from the RF connectors to the inside of the cell was difficult to design considering the large permittivity steps, the varying size of the small diameter center conductor, and the presence of the support structures. As a result, the SWR of many of the cell configurations was not good.

The measured SWRs for a propanol-filled cell and a water-filled cell are shown in Figs. 9-6 and 9-7. For the propanol cell, the SWR never exceeds 1.31 below 500 MHz. These low-level reflections are attributed to the good impedance matching achieved in

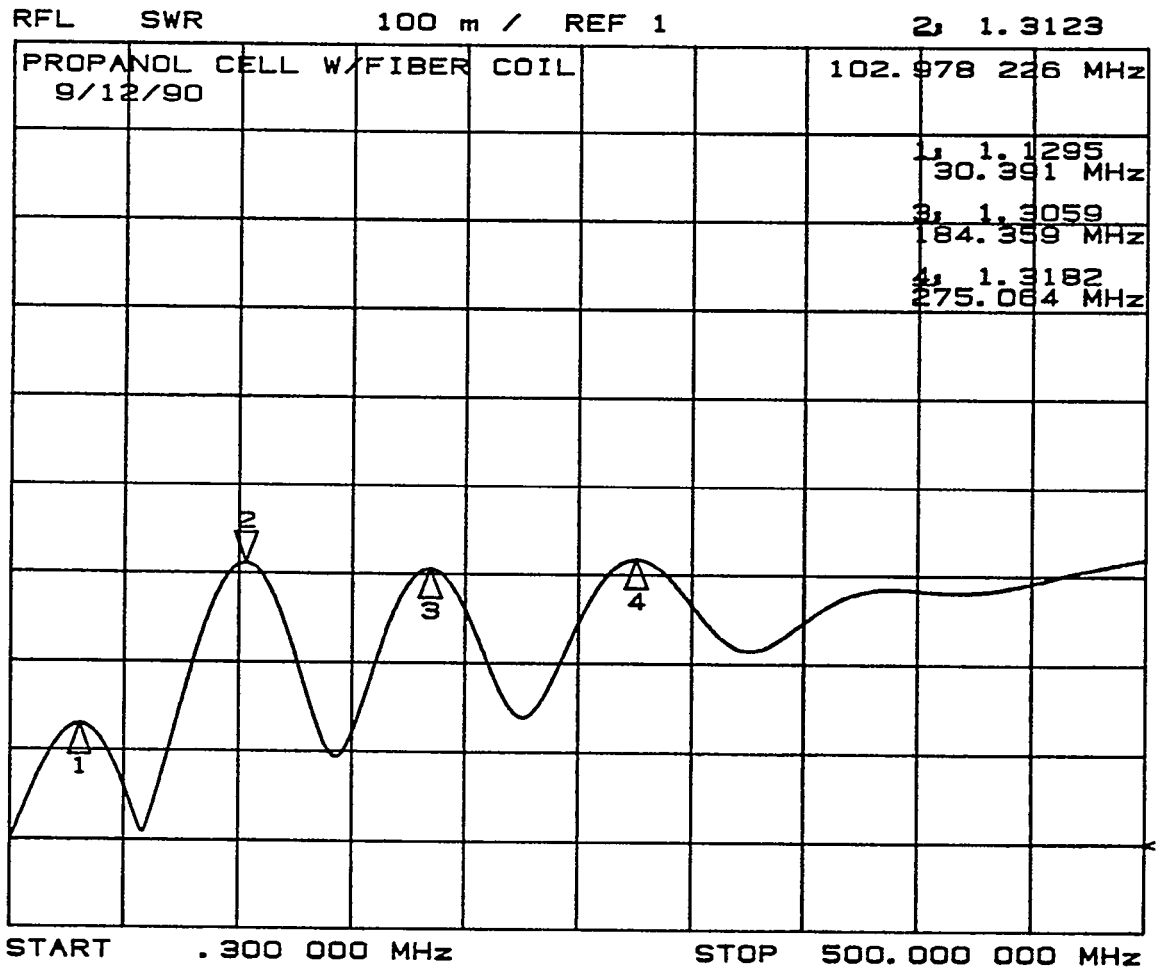

Fig. 9-6. The SWR for the propanol-filled transmission test cell for frequencies up to 500 MHz.

the cell when using a relatively low ε_r liquid material. The impedance magnitudes corresponding to data in Fig. 9-6 vary between 38 Ω and 52 Ω, which represents a maximum deviation of only 1.2 dB from the nominally 50 Ω design.

In contrast, the SWR for the water cell, Fig. 9-7, is as high as 15 for frequencies below 1 GHz. This cell is burdened with large reflections due to the high ε_r of the water. Corresponding impedance magnitudes vary from ~3.5 Ω to ~109 Ω, a 11 dB deviation from 50 Ω. Some configurations of the water cells had better electromagnetic

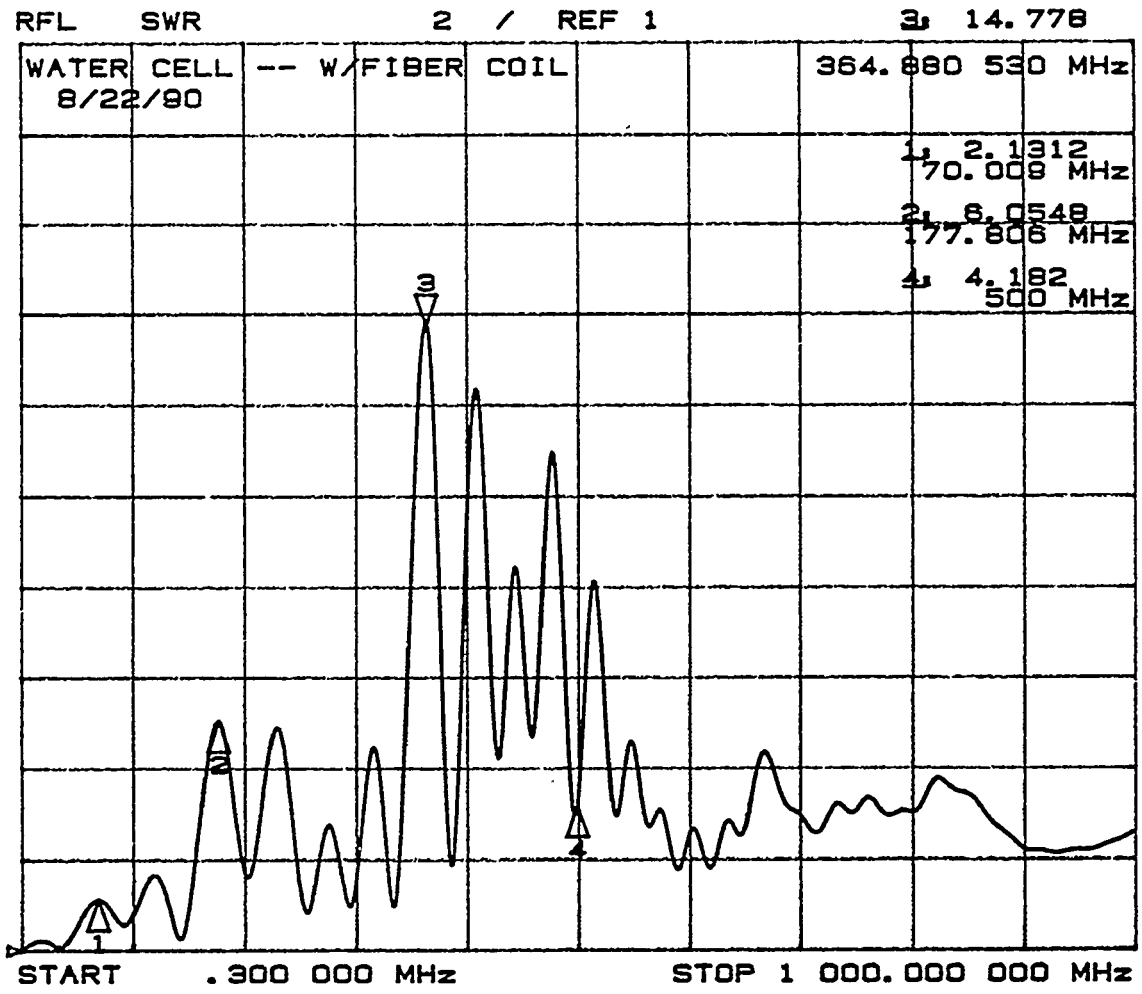

Fig. 9-7. The SWR for the water-filled transmission test cell for frequencies up to 1 GHz.

characteristics than those shown in Fig 9-7, but all had SWRs greater than 5.0. Even with the large mismatches, however, the water-filled cell proved useful in travelling wave current sensor testing. It is postulated that energy, once coupled into the cell, propagates with a wave impedance that closely approximates that of a TEM wave and with a well-established phase velocity that can be estimated by Eq. (3-6). Further details on the construction and characterization of the liquid travelling wave cells are found in Ref. 34.

CHAPTER 10

EXTENDED MODELS FOR LIQUID CELL TRAVELLING WAVE SENSORS

The theory for the travelling wave current sensor presented in Chapter 8 assumes all parameters of the fiber coil, the transmission cell, and the dielectric medium are ideal (i.e., they are independent of frequency). In reality, however, several factors contribute to perturbations of the basic travelling wave Faraday response, Eqs. (8-5), all which reduce the predicted bandwidth enhancement given by Eq. (8-10). Infinite bandwidths are certainly not possible, even under the best matching of parameters, but the perturbations do not preclude achieving large bandwidths in many practical devices.

Five mechanisms have been identified that affect the Faraday response in the experimental travelling wave structures and limit the system bandwidth. First is the presence of the fiber coil leads. In the cell configurations discussed in the previous chapter, the fiber is allowed to spool off the end of the support mandrel and exit the cell through the outer conductor wall. In most cases the fiber leads do not conform to the prescribed helical pitch of the coil proper and merely increase in radial distance along a path that is perpendicular to the conductor. Thus, the leads do not "travel" like the remainder of the fiber and contribute to a minor bandwidth reduction. The deviation in response created by the fiber coil leads is discussed in detail in Appendix B for the planar coil configuration. Since the fiber leads used with the travelling wave coils do not differ significantly from those of the planar coil, the theory presented in Appendix B is adequate to describe all Faraday responses. Also, the Faraday response in the leads is independent of the value of ε_r because of the chosen configuration, and thus, both the airline and the liquid cell travelling wave sensor systems experience some bandwidth reductions.

The second limiting mechanism is the modal structure of the coaxial transmission line. All response models, especially those for the travelling wave sensors, are based on

TEM wave propagation, and more importantly, on the magnetic field component being perpendicular to the direction of wave propagation. Higher order modes begin propagating in the cells at frequencies defined by Eq. (A-13) in Appendix A. This prediction assumes that an ideal dielectric is present in the coaxial waveguide. For the cell configurations described in Chapter 9, the onset of the higher order modes will occur at 2.32 GHz for ε_r = 1 (air dielectric), 517 MHz for ε_r = 20.1 (the static value for propanol at 25 °C), 406 MHz for ε_r = 32.6 (methanol), and 262 MHz for ε_r = 78.5 (water). The first higher order mode in the ideal coaxial line is TE_{11}, which means the magnetic field will have a component in the direction of propagation — along the direction of the conducted current. This could enhance the Faraday response in the travelling wave coil at the higher frequencies since the light and field vectors might align more readily. But an exact mathematical description of this interaction is difficult since the contribution of both the TEM and the TE_{11} mode must be considered and each has a separate propagation constant that varies differently with the frequency. Consequently, the wave phase velocity varies with frequency, and this quantity is the determining factor in the degree of phase matching that occurs in the travelling wave sensor. As more higher order modes are added in the waveguide volume, the situation becomes even more complicated. Thus, operation of the travelling wave current sensors is targeted for a frequency range in which a single dominant waveguide mode exists, limiting the useful bandwidth of the system.

A third perturbation arises from the presence of the teflon fiber support mandrel used in the liquid cell. The relative permittivity of the teflon is ~ 2.0 which is much smaller than that of any of the liquids. This modifies the wave propagation in the coaxial line and produces an effective relative permittivity (at low frequencies) for the composite dielectric structure. The effective relative permittivity is smaller than the ε_r of the immersing liquid. The fourth mechanism is liquid dispersion and absorption. Polar molecules that necessarily give rise to the large relative permittivities must reorient in the

oscillating fields. At higher frequencies the liquid molecule cannot keep up with the changing field polarization, resulting in absorption of the RF power and a subsequent loss in current detection sensitivity. Finally, a fifth mechanism is described by a combination of those effects just discussed for the second, third and fourth mechanisms above. This response perturbation is due to the waveguide modal structure in multilayer, dispersive dielectric media.

A detailed description of these last three mechanisms is warranted given their significant affect on the Faraday response of the travelling wave fiber current sensor. Each is treated separately in the following sections. A complete computational model for predicting responses of the liquid travelling wave sensors is offered at the end of this chapter.

Effective Relative Permittivities

The relative permittivity of the dielectric medium in the coaxial transmission line establishes the phase velocity of the propagating magnetic wave according to Eq. (3-6). Consequently, the response, Eqs. (8-5), and the bandwidth, Eq. (8-7), of the travelling wave fiber current sensor are dependent on the value of ε_r. In all of the previous theoretical developments, it is assumed that ε_r is single-valued and equal to that of the dielectric medium, here, the liquid. However, in the liquid cell configurations, it is necessary to support the helical fiber coil at a given diameter and position relative to the coax center conductor. When the teflon mandrel tube is submersed in the liquid, the field spatial distribution is perturbed from that of the liquid alone, and the EM properties of the cell are changed. The propagating wave in the transmission line then has a phase velocity determined by an apparent or effective relative permittivity which is intermediate to the liquid ($\varepsilon_r > 20$) and the mandrel ($\varepsilon_r \sim 2$). For the purpose of computing cell geometric parameters and estimating sensor responses, this effective relative permittivity, ε_{eff}, is treated as a single-valued quantity.

With the fiber mandrel present, the lowest-order mode in the coaxial cell is no longer TEM, but TM_{01}. This follows from the waveguide modal solutions for the multilayer dielectric which is treated later in this chapter. In the static or low frequency case, however, the TM_{01} mode can be considered "quasi-TEM," and the electric field has a $1/\rho$ dependency in the cell volume between the conductors. The derivation of an effective relative permittivity for a coaxial cell with two dielectric media, one submersed in the other, is performed in detail in Appendix C. The solution is given as

$$\varepsilon_{eff} = \varepsilon_1 \left[1 + \left(\frac{\varepsilon_1}{\varepsilon_2} - 1 \right) \frac{\ln\left(r_2/r_1\right)}{\ln\left(b/a\right)} \right]^{-1} , \qquad (10\text{-}1)$$

where ε_1 is the relative permittivity of the liquid, ε_2 is the relative permittivity of the mandrel material (the teflon), r_1 and r_2 are the inner and outer radii of the mandrel tube, and 'a' and 'b' are the center and outer conductor radii of the coaxial line.

Fixed values were designed for three of the radii in the travelling wave liquid cell: $r_1 = 0.475$ in. (1.20 cm), $r_2 = 0.625$ in. (1.59 cm), and b = 1.13 in. (2.87 cm). The value of 'a' varies with each liquid. When the fixed radii values and the relative permittivity of the teflon mandrel are substituted into Eq. (10-1), the effective relative permittivity becomes

$$\varepsilon_{eff} = \frac{\varepsilon_1}{1 + \left(0.5\varepsilon_1 - 1\right) \dfrac{0.27}{\ln\left(1.13/a\right)}} , \qquad (10\text{-}2)$$

where 'a' has the units of inches. Figure 10-1 is a plot of Eq. (10-2) for each of the three test liquids used in the cell and with the cell center conductor diameter, 2a, as the abscissa. A wide range of values for 2a are plotted. For the small conductor sizes, the

effective relative permittivity is greatest, but it is still significantly less than that of the liquid alone. For large conductor sizes, the three curves begin to converge, attaining values of ε_{eff} between 5 and 6 at the maximum center conductor diameter, $a = r_1$.

The large effect of the teflon fiber mandrel tube on the relative permittivity of the liquid cell can be interpreted by examining the boundary conditions at the dielectric interfaces. From Eq. (C-5), $E_2 = (\varepsilon_1/\varepsilon_2)E_1$ at both r_1 and r_2. This requires the electric field in the volume occupied by the mandrel to be at least 10 times larger (since $\varepsilon_1 > 20$ and $\varepsilon_2 = 2$) than the field in the equivalent volume occupied by the liquid alone. If the relative permittivity of the fiber support material more closely matched that of the

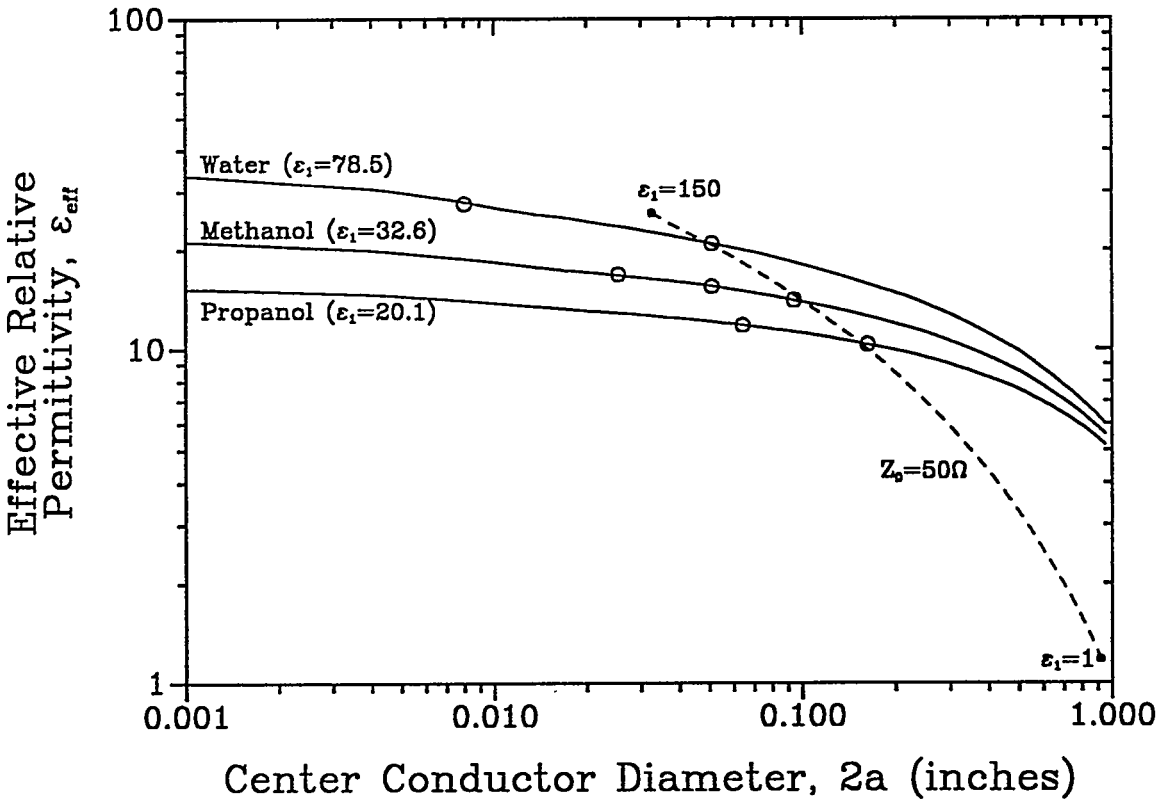

Fig. 10-1. The static, or low frequency, effective relative permittivity versus center conductor diameter for the three liquid travelling wave test cells. The dashed curve represents the appropriate ε_{eff} for a coaxial cell with a fixed 50 Ω characteristic impedance. Open circles are parameters for actual experimental cell configurations.

liquids, the perturbation would not be so great. Fortunately, a second boundary condition, $H_{\phi 1} = H_{\phi 2}$, requires the magnetic field component to be uniformly continuous along the cell radius between the two conductors, extending through the teflon. Since the desired current measurements depend only on the interaction of this magnetic field component with the light in the fiber, no deviations will occur in the low frequency Faraday response magnitude even with the fiber at the outer surface of the support mandrel. Thus, the properties of the travelling wave sensor must be adjusted to account only for the faster wave phase velocity created by changes in the relative permittivity.

The low frequency characteristic impedance, Z_0, of the liquid travelling wave cell can be computed by substituting ε_{eff} from Eq. (10-1) for ε_r in Eq. (A- 11):

$$Z_0 = 60 \sqrt{\frac{1 + \left(\frac{\varepsilon_1}{\varepsilon_2} - 1\right)\frac{\ln\left(r_2/r_1\right)}{\ln\left(b/a\right)}}{\varepsilon_1}}\ \ln\left(\frac{b}{a}\right) . \qquad (10\text{-}3)$$

The relationship between impedance and relative conductor radii is now much more complicated. If all the cell geometric parameters and the material relative permittivities are known, the characteristic impedance can be computed. However, it is often desirable to identify an impedance, then design the coaxial cell for given dielectric materials. Rearranging Eq. (10-3) gives an expression for the ratio of the conductor radii as a function of the remaining parameters,

$$\ln\left(\frac{b}{a}\right) = \frac{1}{2}\left(1 - \frac{\varepsilon_1}{\varepsilon_2}\right)\ln\left(\frac{r_2}{r_1}\right) + \sqrt{\frac{1}{4}\left(\frac{\varepsilon_1}{\varepsilon_2} - 1\right)^2\left[\ln\left(\frac{r_2}{r_1}\right)\right]^2 + \varepsilon_1\left(\frac{Z_0}{60}\right)^2} \quad . (10\text{-}4)$$

For a cell matched to 50 Ω and with the teflon mandrel and cell outer conductor

geometries as given previously, Eq. (10-4) reduces to

$$a = 1.13 \times \exp\left[0.14\left(0.5\varepsilon_1 - 1\right) - \sqrt{0.02\left(0.5\varepsilon_1 - 1\right)^2 + 0.7\varepsilon_1}\right] . \quad (10\text{-}5)$$

This expression can be used to uniquely determine the size of the center conductor required for a 50 Ω test cell for a given liquid. For the three test liquids selected for use in the travelling wave sensors, the center conductor diameters are 0.15 in. (0.39 cm) for propanol, 0.1 in. (0.26 cm) for methanol, and 0.05 in. (0.13 cm) for water. If these values are appropriately substituted into Eq. (10-2), the effective relative permittivities for the 50 Ω cells are 10.5 for the propanol cell, 13.9 for the methanol cell, and 21.1 for the water cell.

In Fig. 10-1, a dashed curve is plotted that represents the values of ε_{eff} as a function of 2a for all possible liquids used in our 50 Ω cell. This curve is generated by first selecting a liquid relative permittivity, ε_1, and using Eq. (10-5) to find 'a'. The values for ε_1 and 'a' are then substituted into Eq. (10-2) to find a unique ε_{eff}. Liquid relative permittivities cover the continuum from $\varepsilon_1 = 1$ to 150. These extreme values for ε_1 are shown as the endpoints for the dashed curve in Fig. 10-1. The intersections of the dashed curve with the three solid curves identify the values of the effective relative permittivity for the 50 Ω cells for the selected test liquids. These three values were stated in the preceding paragraph. Also plotted in Fig. 10-1 (as the open circles) are the parameters of the actual travelling wave sensor experimental configurations. As can be seen, for each test liquid a configuration near 50 Ω characteristic impedance was used. Other cell configurations with different impedances were also implemented.

Equation (10-1) can also be used to compute the effective relative permittivity of the dielectric in the airline travelling wave test cell. This cell used a polyurethane foam ($\varepsilon_r < 1.2$) mandrel to support the helical optical fiber. As might be expected, the foam

represents only a minimal perturbation on the cell dielectric properties: $\varepsilon_{eff} = 0.98$ if $\varepsilon_2 = 1.1$, and $\varepsilon_{eff} = 0.96$ if ε_2 is as large as 1.2. Since the transmission line characteristic impedance follows as $(\varepsilon_{eff})^{-½}$, insignificant changes in the wave properties occur due to the presence of the foam fiber mandrel.

Liquid Dispersion

One of the greatest concerns with liquid as a dielectric medium is the dispersion that occurs at high frequencies. The EM wave propagating in the medium causes oscillations of the liquid molecule. At high frequencies, these molecules cannot reorient fast enough to move synchronously with the field. A phase delay occurs between the wave and the molecule resulting in apparent deviations of the real component of the relative permittivity and significant increases in the imaginary component. The latter effect gives rise to dielectric absorption. The complex relative permittivity is expressed by Eq. (A-16). A Debye relaxation model is used to describe the real and imaginary components in terms of the molecular properties [71]:

$$\varepsilon_r = \left(1 + \frac{4\pi\alpha_s N_d}{1 + \omega^2 T_R^2}\right) + j\left(\frac{4\pi\alpha_s N_d}{1 + \omega^2 T_R^2}\omega T_R\right), \qquad (10\text{-}6)$$

where α_s is the static polarizability of the molecule, N_d is the molecular density, and T_R is the molecular reorientation time. T_R is closely related to the material viscosity and the size of the molecule [71]. Small liquid molecules with low viscosity, such as water, will produce large absorption only at the highest frequencies; however, dielectrics with large molecules will exhibit significant dispersion.

Figure 10-2 shows the frequency characteristics of the real (ε') and imaginary (ε'') parts of Eq. (10-6) for a typical dielectric medium. When the frequency is equal to $1/T_R$, the imaginary component is maximum (indicating peak absorption) and the real

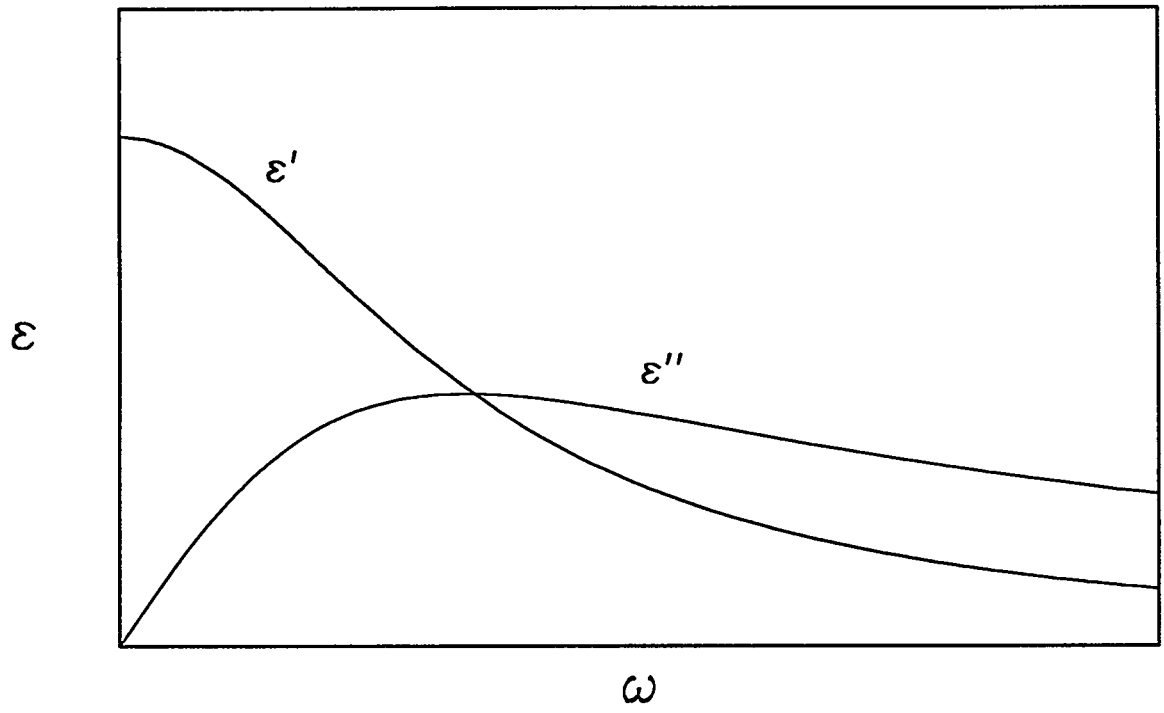

Fig. 10-2. The real and imaginary components of the relative permittivity for a dispersive medium.

component is reduced to approximately one-half the difference between the low frequency and the high frequency relative permittivity. As an example, the peak absorption for water occurs near 16 GHz at 25 °C which equates to a molecular reorientation time of $T_R \sim 10^{-11}$ seconds [72]. The values of the reorientation time for the other two liquids used in the experimental travelling wave sensor cells are approximately 3.6×10^{-10} sec for propanol and 7×10^{-11} sec for methanol. These two liquids have much larger molecules than water, consequently, the longer reorientation times. In many materials, several higher frequency absorption bands will also occur. Each of these will have relative permittivity characteristics as shown in Fig. 10-2, only with progressively lower starting values for ε'. For the purpose of describing dispersion in the liquid dielectrics used in this study, however, only the first absorption is of interest.

The static or low frequency value for the relative permittivity, ε_s, is found from

Eq. (10-6) when $\omega = 0$:

$$\varepsilon_s = 1 + 4\pi\alpha_s N_d \quad . \tag{10-7}$$

Static values for materials are usually those published in the handbook tables. If a constant parameter, κ, is defined as $\kappa \equiv 4\pi\alpha_s N_d$, then $\kappa = \varepsilon_s - 1$. The two material dielectric parameters, κ and T_R, are all that is needed to fully describe the frequency dependence of the relative permittivity given by Eq. (10-6).

The amplitude of the propagating EM wave in the coaxial transmission line is given by

$$A(z) = A_0 e^{-\beta z} = A_0 e^{-j\frac{\omega}{c}\sqrt{\varepsilon_r} z} \quad , \tag{10-8}$$

where A_0 is the initial wave amplitude, β is the waveguide propagation constant, and z is the direction of propagation. The attenuation or absorption coefficient is determined from the real component of the exponential factor, or

$$\alpha_D = \frac{\omega}{c} \mathrm{Im}\left(\sqrt{\varepsilon' + j\varepsilon''}\right) \quad . \tag{10-9}$$

If attenuation is small, the dielectric has a loss that is described by Eq. (A-18). For the liquids at higher frequencies, larger attenuation occurs and Eq. (10-9) must be used directly to determine losses. Figure 10-3a shows the transmission magnitude measured for the travelling wave sensor cell filled with propanol. The dashed curve is a prediction of the frequency-dependent absorption using the waveguide model discussed in the following section of this chapter. Absorption is quite large in this configuration, approximately 30 dB at 500 MHz. The Faraday response sensitivity for the travelling

(a)

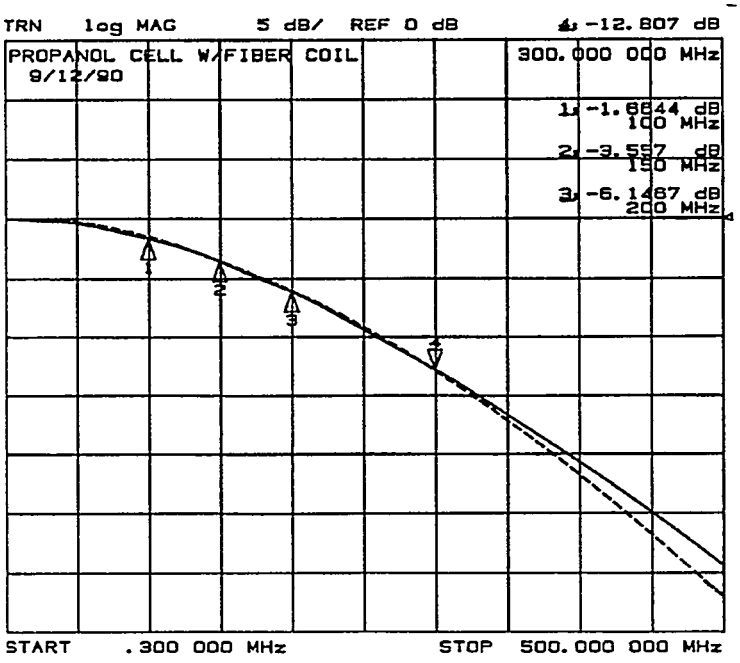

(b)

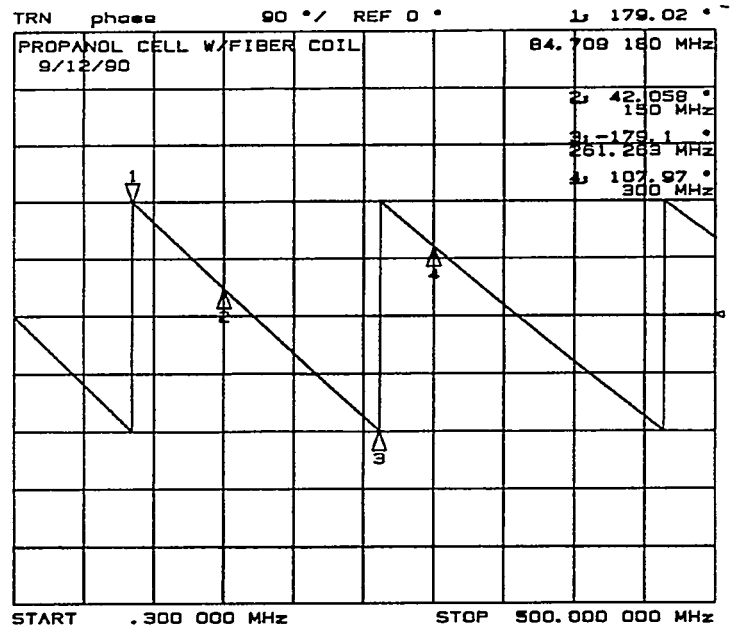

Fig. 10-3. The transmission magnitude (a) and phase angle (b) for the propanol-filled liquid test cell used as a travelling wave sensor. The dashed curve in (a) is a computation of the cell attenuation produced by absorption in the propanol with an estimated molecular reorientation time of 3.6×10^{-10} sec. In (b) the liquid dispersion creates a noticeable phase lag.

wave sensor is significantly diminished under these large attenuation conditions. In fact, it is determined that only ~ 20 dB of loss can be accommodated before measurement signal-to-noise ratios become too small. This limitation then establishes a higher frequency bound on each travelling wave sensor configuration. For the propanol-filled cell, this upper frequency limit is approximately 380 MHz. For the methanol cell, the limit is ~ 650 MHz, and for the water cell, ~ 825 MHz. Because of other limitations in the Faraday current sensor response, none of the cells could be used up to this absorption frequency bound.

Absorption of the RF power by the liquid dielectrics limits the maximum energy that can be injected into the transmission cells. The heat generated by the absorbed power elevates the liquid temperature, thus lowering the relative permittivity (see Tables 9-1 and 9-2). No attempts were made during experimentation to control the liquid temperature, but a monitor was used and the temperature was continuously recorded. The controller for the fiber optic temperature sensor, a Luxtron Model 1000A, can be seen in the lower left of the photo in Fig. 9-1. Liquid temperatures were not allowed to deviate greater than 5 °C during all tests. This ensured a reasonably stable relative permittivity and cell impedance, and negated the need for any corrections to the measured sensor responses.

In addition to absorption, dispersion in the liquid relative permittivity also perturbs the waveguide propagation parameter. At the higher frequencies, changes in both ε' and ε'' produce deviations in the imaginary component of the exponential factor in Eq. (10-8). This factor is critical in establishing the wave phase velocity in the travelling wave sensor configuration. In liquids that exhibit large absorption, large increases in phase velocity also occur. In Fig. 10-3b, the transmission phase angle for the propanol-filled cell is plotted. A noticeable phase lag is observed, which results from the relative permittivity steadily decreasing as the frequency increases. This indicates that the EM wave in the cell is gaining speed with frequency. In a current sensing system this leads

to a gradually increasing phase mismatch with the light in the optical fiber. Faraday response will obviously decrease at the higher frequencies.

The Liquid Coaxial Waveguide

An exact determination of the electromagnetic properties for the liquid travelling wave sensor cells requires a detailed analysis of the actual and complete waveguide. This analysis must include the relative permittivity perturbations caused by the presence of the fiber mandrel tube, the dispersion in the liquid dielectric, and the waveguide dispersion created by modes at the higher frequencies. The general problem that must be solved is finding the modal structure in the transmission line dielectric volume for a multilayer coaxial dielectric with complex relative permittivities. Maxwell's equations (the wave equations) are solved subject to the appropriate coaxial boundary conditions. From these solutions, a complex relative permittivity is determined that can be substituted into Eq. (8-4) to give an expression for the frequency-dependent Faraday response in the travelling wave current sensor.

A complete, detailed solution to the general waveguide problem is quite involved; it must assume that all spatially-orthogonal components of the magnetic and electric field exist inside the transmission line dielectric volume. The approach of reducing the computations to TM and TE modes as taken for the ideal coaxial line (see Appendix A) may not be appropriate. Coupled modes must initially be considered. Fortunately, the implementation of the travelling wave sensors only requires knowledge of the lowest order mode propagating in the cells. This can be achieved by simplifying the problem from the outset: assume a limited modal structure and a limited frequency range of operation. Previously, the lowest order mode in the liquid-filled cells was assumed to have quasi-TEM characteristics. Then, a reasonable assumption is that this mode possesses azimuthal symmetry. With no ϕ dependencies, the field components in the multilayer dielectric become uncoupled (transverse field components are no longer a

superposition of E_z and H_z) [73], and the modal problem can again be simplified mathematically into TE and TM groupings. The problem is further simplified by identifying the approximate cutoff frequency of the first higher order azimuthally symmetric mode, then bounding sensor operation to the assumed single mode region below this frequency. As verified by the experimental data, the above assumptions have proved quite accurate in treatment of the travelling wave fiber sensor response.

The eigenvalue equations for the TE_{0n} and TM_{0n} modes in the liquid-filled transmission cells are developed in Appendix D. Modal solutions to these equations are approached, and eventually displayed, from the perspective of an effective relative permittivity, ε_{eff}. The effective relative permittivity is related to the waveguide propagation constant through the expression

$$\beta = j\frac{\omega}{c}\sqrt{\varepsilon_{eff}} \quad . \tag{10-10}$$

It is more common to determine the modes in the coaxial transmission line by simply finding β as a function of frequency. Such a treatment is used in Appendix A. However, the relative permittivity representation continues from earlier discussions of the travelling wave sensor systems and allows for greater insight into dielectric properties, especially dispersion. The use of an ε_{eff} in the mathematical treatment is consistent with other waveguide properties.

Throughout the waveguide modal analysis, it is assumed that computed values for ε_{eff} will be representative of a homogenous dielectric medium between the conductors in the coaxial line. Then the effective relative permittivity can be used to estimate impedances, propagating-wave phase velocities, and ultimately, the travelling wave sensor responses. In the waveguide computations, the liquid relative permittivity is treated as complex, thus the resulting ε_{eff} is complex. This allows for treatment of both the wave dispersion and attenuation.

An iterative computer algorithm [34] was used to compute the solutions to the modal eigenvalue equations, Eq. (D-15) for the TM_{0n} modes and Eq. (D-27) for the TE_{0n} modes. The code initially estimates a value for ε_{eff} (complex components where appropriate) at a given frequency and then computes the waveguide propagation constant, β, using Eq. (10-10). The complex value of k_1 (from Eqs. (A-4) and (10-6)) for the liquid dielectric is combined with β to determine the parameter u_1 from Eq. (D-2). Similarly, u_2 is determined from β and k_2, for a nondispersive relative permittivity for the teflon fiber mandrel. Arguments for the Bessel functions are then generated from the geometric dimensions, and trial solutions to the eigenvalue equations are computed. Iterations of ε_{eff} occur until satisfactory solutions are found. Because u_1 and u_2 can assume any complex value, it is necessary to utilize Bessel function routines that allow complex arguments. These functions were provided by D. E. Amos as a complete Fortran subroutine package [74].

Modes within the multilayer dielectric transmission line are first identified by treating the liquids as lossless or nondispersive. Then the effective relative permittivities introduced into Eqs. (10-10) and (A-4) are real only. The lowest order mode for all the multilayer dielectric configurations is TM_{01}. A TEM mode cannot exist. Guided modes in the cell require that $\varepsilon_2 \leq \varepsilon_{eff} < \varepsilon_1$ for propagation to occur; modes fall below cutoff if $\varepsilon_{eff} < \varepsilon_2$. This implies the phase velocity of the propagating wave is faster than the speed of light in the liquid medium. Such anomalous phase velocities are not unusual in guided wave structures. The maximum phase velocity in the multilayer dielectric is limited by the speed of light in the teflon.

Figure 10-4 is a plot of ε_{eff} versus frequency for several TM and TE modes in a lossless coaxial transmission cell filled with water. At zero frequency, the static value of ε_{eff} for the TM_{01} mode agrees exactly with that determined by Eq. (10-2) from the theory developed in Appendix C. This validates the assumption that at low frequencies a quasi-TEM mode exists in the cell. In Fig. 10-4 the modal values for ε_{eff} are bound by ε_1 on

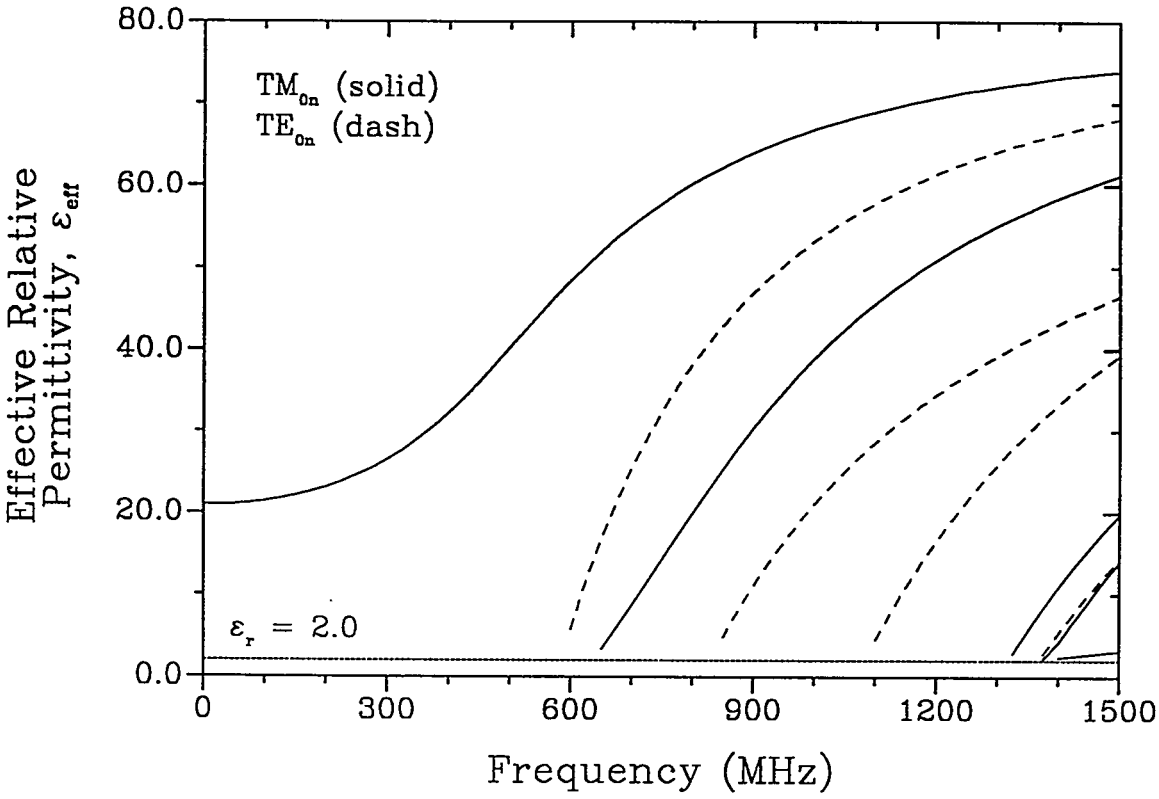

Fig. 10-4. The effective relative permittivity versus frequency for the azimuthally symmetric TM_{0n} and TE_{0n} modes in a multilayer dielectric coaxial waveguide containing water. Liquid dispersion is neglected.

the high side and ε_2 on the low side. The transmission cell becomes highly multimoded as the frequency approaches 1.5 GHz; several additional modes, that are not azimuthally symmetric, are expected to appear among the TM_{0n} and TE_{0n} modes at the higher frequencies. The first higher order azimuthally symmetric mode in Fig. 10-4 is the TE_{01} mode which begins propagating near 600 MHz. This cutoff establishes an approximate upper frequency bound for single mode operation in a water-filled travelling wave cell. For travelling wave cells filled with propanol and methanol, the TE_{01} mode is also the first higher order mode in the multilayer dielectric waveguide assuming nondispersive liquids. The cutoff frequency for this mode is approximately 1220 MHz in the propanol cell and approximately 940 MHz in the methanol cell.

Portions of the lower frequency ε_{eff} for the TM_{01} mode in the lossless liquids propanol, methanol and water are plotted as the dotted reference curves in Figs. 10-5 through 10-7. All three curves show a static value for ε_{eff} that agrees with the previously determined quasi-TEM calculations. Also, each curve shows a waveguide dispersion in the effective relative permittivity that is independent of the liquid dispersion. Below 500 MHz, the waveguide dispersion for the propanol-filled cell is quite small (see Fig. 10-5), but values for the methanol cell and especially the water cell are quite significant (see Figs. 10-6 and 10-7). This waveguide dispersion arises from the large disparity between the relative permittivities of the liquid and the teflon tube, and subsequently, from the large disparity between the static ε_{eff} value and the static liquid ε_r.

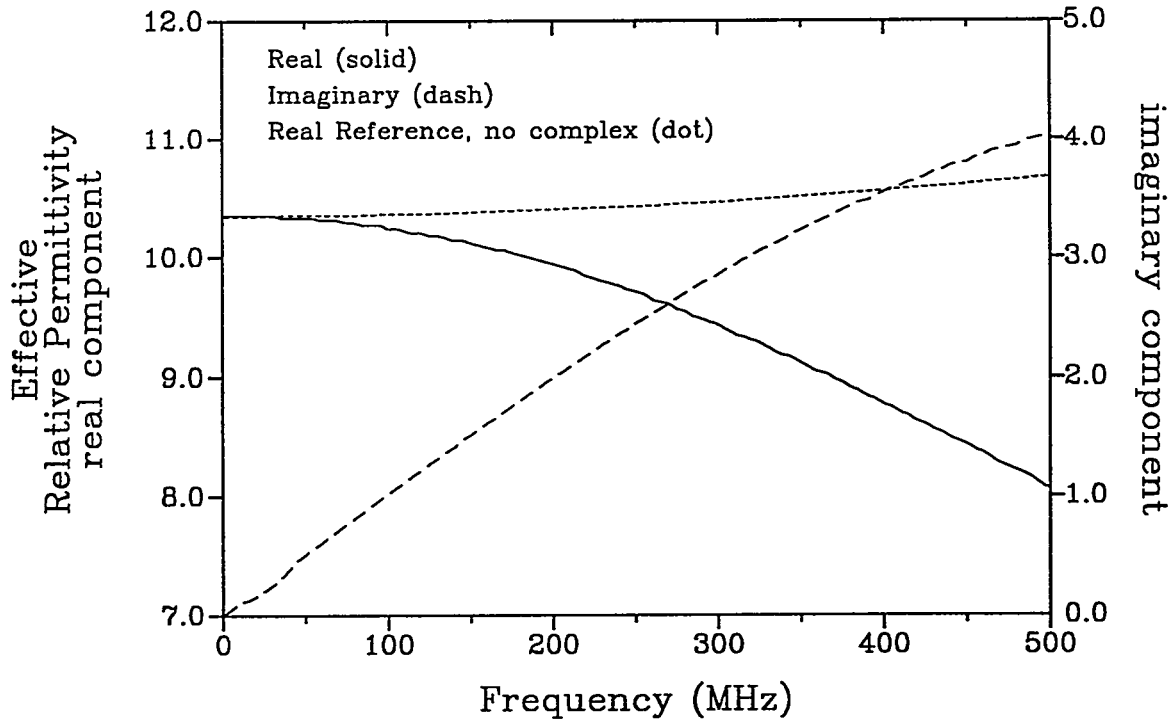

Fig. 10-5. The complex effective relative permittivity versus frequency for the TM_{01} mode in a propanol-filled travelling wave transmission cell. The dotted reference curve is produced from the waveguide model neglecting liquid dispersion.

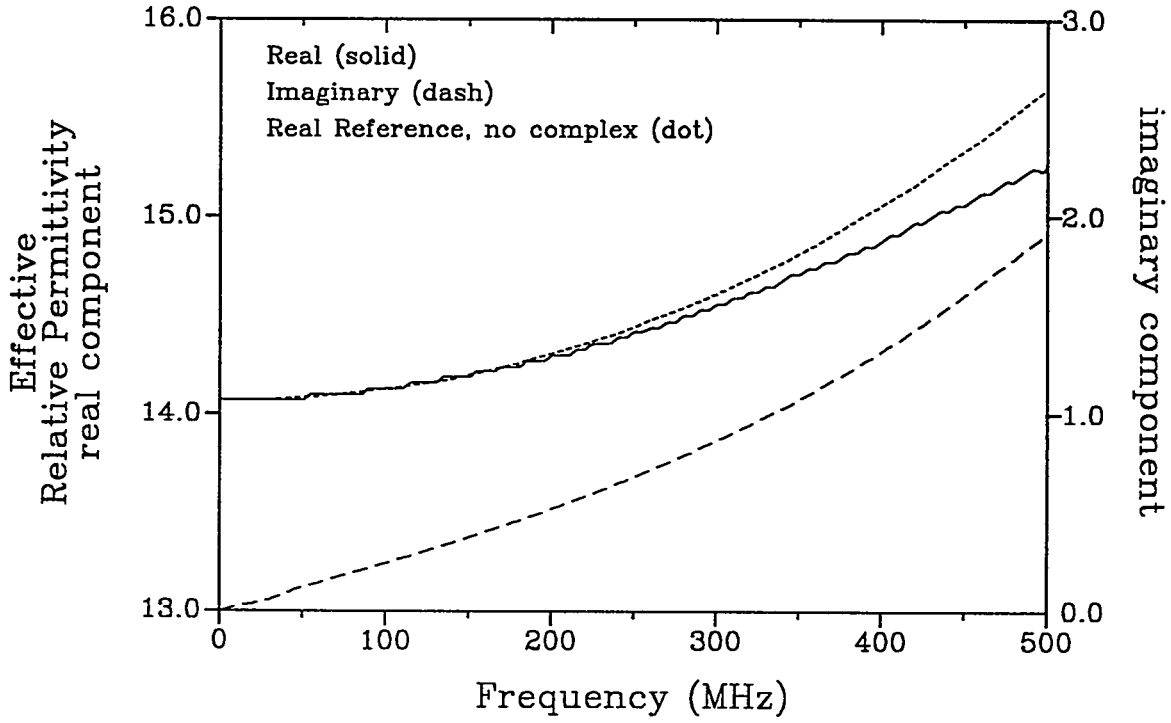

Fig. 10-6. The complex effective relative permittivity versus frequency for the TM_{01} mode in a methanol-filled travelling wave transmission cell. The dotted reference curve is produced from the waveguide model neglecting liquid dispersion.

When liquid dispersion is included in the multilayer waveguide computations, complex solutions for ε_{eff} are generated. Only the TM_{01} mode is investigated for these dispersion calculations, and the frequency range is limited to 500 MHz for the propanol and methanol-filled cells and to 600 MHz for the water-filled cell. Cell absorption is included as part of the computations so that comparisons can be made directly to measured transmission (or loss) values. The molecular reorientation time, T_R, is treated as a variable input parameter in the model. The complex relative permittivity of the liquid, Eq. (10-6), is then used to determine k and u for use in the waveguide eigenvalue equations. Differences between computed and measured attenuation values determine the correctness of the chosen value of T_R. Figure 10-3a is one such comparison of cell transmission values for the propanol-filled coaxial line. The dashed curve in Fig. 10-3a

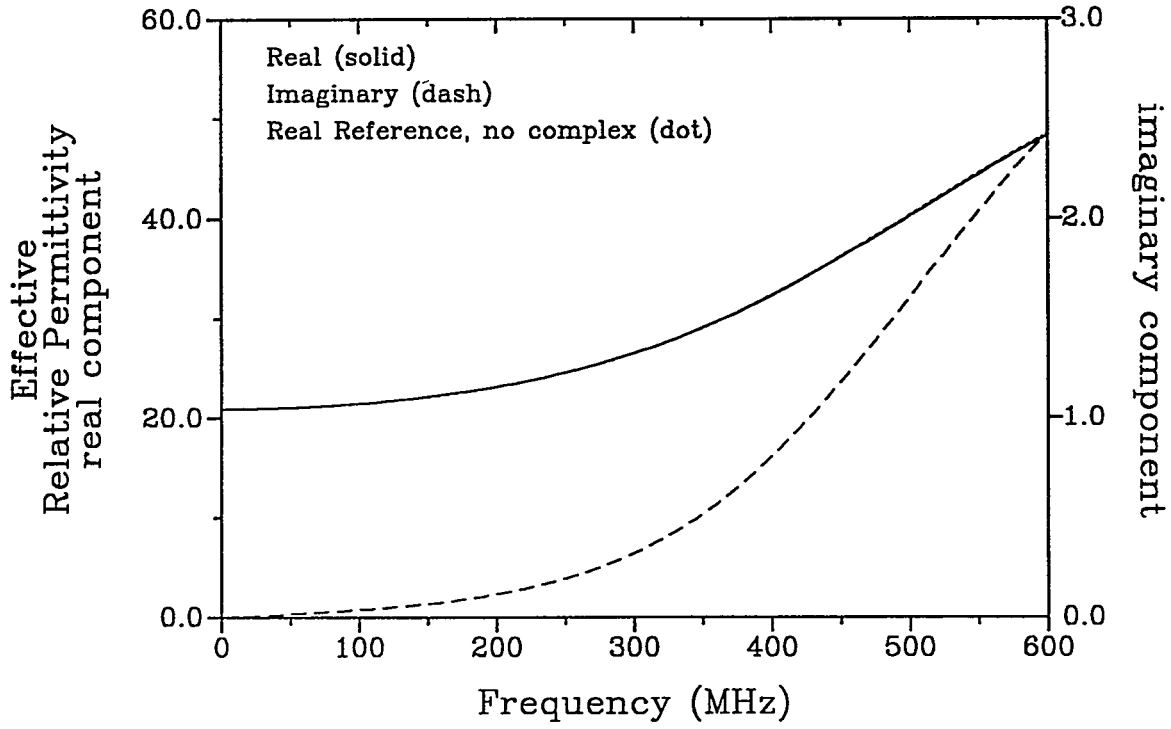

Fig. 10-7. The complex effective relative permittivity versus frequency for the TM_{01} mode in a water-filled travelling wave transmission cell. The dotted reference curve, which is almost hidden behind the solid curve, is produced from the waveguide model neglecting liquid dispersion.

is generated by the multilayer waveguide model for T_R = 3.6 x 10^{-10} sec. Good agreement with the network analyzer curve is observed, especially below 350 MHz. All estimated values for T_R for the three test liquids were determined using this technique .

The complex effective relative permittivities versus frequency for the three liquids are plotted in Figs. 10-5 through 10-7. The real and imaginary components of ε_{eff} are plotted as separate curves in each figure. In the propanol-filled cell, Fig. 10-5, absorption dominates. The imaginary part of ε_{eff} increases rapidly with increasing frequency. The dispersion in the real part of ε_{eff} is dramatic; liquid dispersion dominates the waveguide dispersion which is observed by comparing the solid and dotted curves in Fig. 10-5. In the methanol-filled cell, Fig. 10-6, the absorption is much smaller below

500 MHz. Waveguide dispersion is slightly greater than the liquid dispersion, as the real componen. of ε_{eff} increases only 8% over the frequency range plotted. Because of the fast reorientation time for the water molecules, little liquid absorption occurs in this travelling wave cell. In Fig. 10-7, the real component of ε_{eff} below 600 MHz is almost identical to ε_{eff} computed for the lossless liquid (the dotted curve). Waveguide dispersion, however, produces more than a two-fold increase in the value of ε_{eff}. This leads to dramatic effects in the wave propagation characteristics for the water cell.

The complex effective relative permittivity for each liquid is used to compute the wave impedance, using Eq. (A-9), for the TM_{01} mode in the multilayer dielectric transmission line. The TM_{01} mode is considered quasi-TEM at the low frequencies, which means that over some frequency range the wave impedance can be considered constant. For a pure TEM mode, the wave impedance does not change with frequency.

Figure 10-8 shows a plot of the wave impedance magnitude for the travelling wave cells filled with the three test liquids. This parameter deviates with frequency in much the same manner as the real components of ε_{eff} plotted in Figs. 10-5 through 10-7. For methanol in the liquid-filled cell, Fig. 10-8 shows almost a constant wave impedance magnitude up to 500 MHz. Waveguide characteristics for this cell configuration are obviously quite good, indicating that travelling wave sensors using methanol as a liquid dielectric are useful up to the liquid absorption frequency limit, approximately 650 MHz. For propanol, the wave impedance magnitude shown in Fig. 10-8 deviates somewhat greater (and with opposite slope) than methanol with increasing frequency. If a 10% deviation from the static value is allowed in considering the frequency range over which the wave impedance is "essentially constant", then travelling wave sensors using propanol can operate to ~ 375 MHz. This frequency is about the same as that established by the liquid absorption limit. Waveguide dispersion in the water-filled cell creates large deviations in the wave impedance magnitude as seen in Fig. 10-8. Greater than 10% increases from the static η value are observed for frequencies above 315 MHz. This is

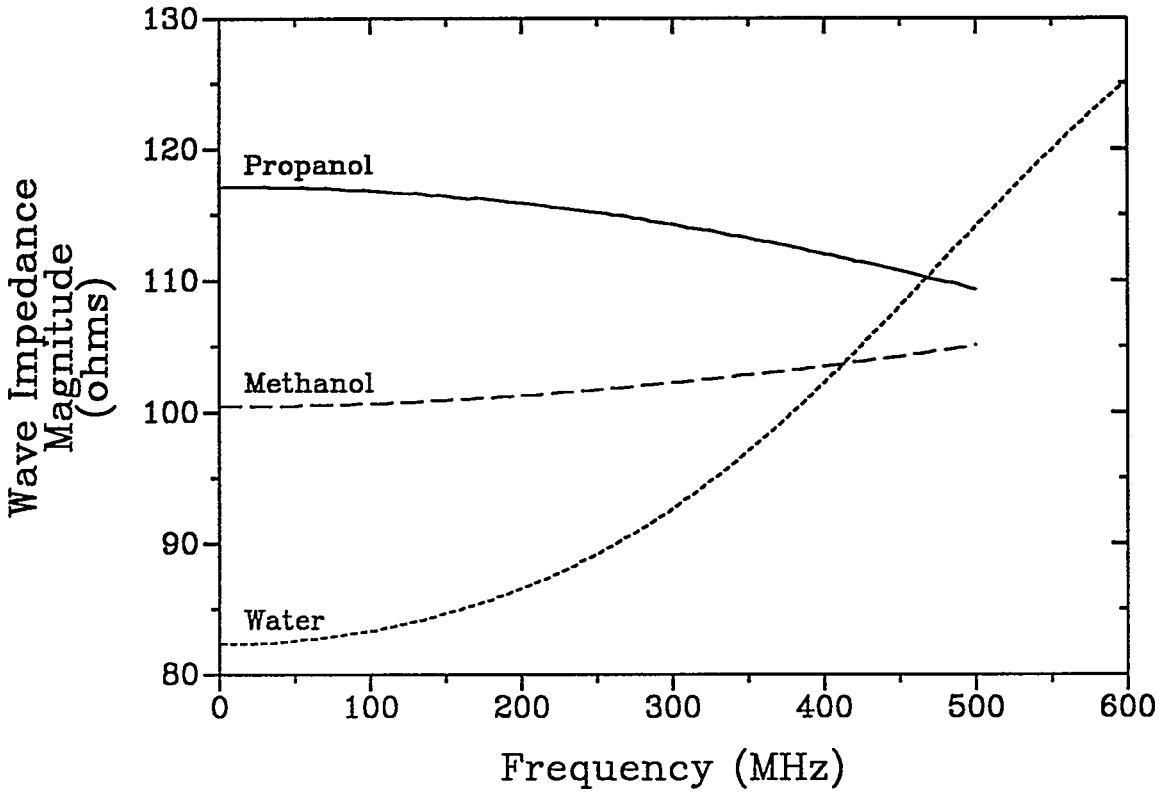

Fig. 10-8. The computed wave impedance magnitude for the TM_{01} mode in liquid-filled travelling wave cells for each of the three test liquids.

easily the most dominant factor in configuring a single mode cell with water dielectric for use as a travelling wave sensor.

The Complete Sensor Model

The mechanisms discussed in the previous sections of this chapter significantly alter the electromagnetic properties of the travelling wave sensor cells and, thus, can have a profound effect on the response of the fiber sensor. The relative permittivity of the coaxial dielectric medium cannot be treated as a constant over all the frequencies of interest, and in many cases it deviates largely from its static value and its liquid-only value. Thus, only when dealing with ideal or severely confined configurations can the response function given by Eq. (8-5) be used to describe the frequency dependent

Faraday rotation. In all other cases, Eq. (8-4) must be used directly to predict responses. A suitable expression for the relative permittivity is identified and substituted for ε_r in Eq. (8-4); integration then follows to determine the response. For the most complete description, the liquid multilayer coaxial waveguide model discussed in the previous section and in Appendix D is used to generate a table of values for ε_{eff} at discrete frequencies for a given sensor cell configuration. These values are used in Eq. (8-4) to predict Faraday rotation at those discrete frequencies. In addition, the lead effects for the complete sensor system can be included by using the developments of Appendix B; the responses just described for the travelling wave coil proper are used as $\Theta_3(\omega)$ in Eq. (B-17). Such a comprehensive model [75] is used to predict the behavior of all the travelling wave sensor experimental configurations and to evaluate responses for a broader range of possible sensors.

Figure 10-9 shows model predictions for several different travelling wave sensor example configurations. In the examples, a coaxial transmission cell with methanol as the liquid dielectric is used. All fiber coils have 20 turns, a mean diameter of 3 cm, and a constant helical pitch of 2.4 cm. This fixes the diameter-to-pitch ratio at $d/x_0 = 1.25$. Curve (a) in Fig. 10-9 is the relative magnitude of the Faraday rotation for the reference coil having planar turns (zero pitch). The bandwidth for this sensor coil is 48.3 MHz. Curve (b) is the sensor response for a travelling wave coil system with $\varepsilon_r = 32.6$. The helical fiber coil is assumed self supporting in the liquid medium, and the methanol is treated as nondispersive. Equation (8-6) describes the response for curve (b), which is very close to having the maximum bandwidth for a travelling wave sensor. The travelling wave condition, Eq. (8-12), for this dielectric is met when $d/x_0 \approx 1.20$. A very wide bandwidth, 1.34 GHz, is predicted for this near-ideal sensor configuration. If liquid dispersion is considered in the model, the Faraday response is given by curve (c) in Fig. 10-9. Absorption by the methanol damps the response at the higher frequencies; the bandwidth is reduced by a factor of 5.5 from that of curve (b). Liquid dispersion also

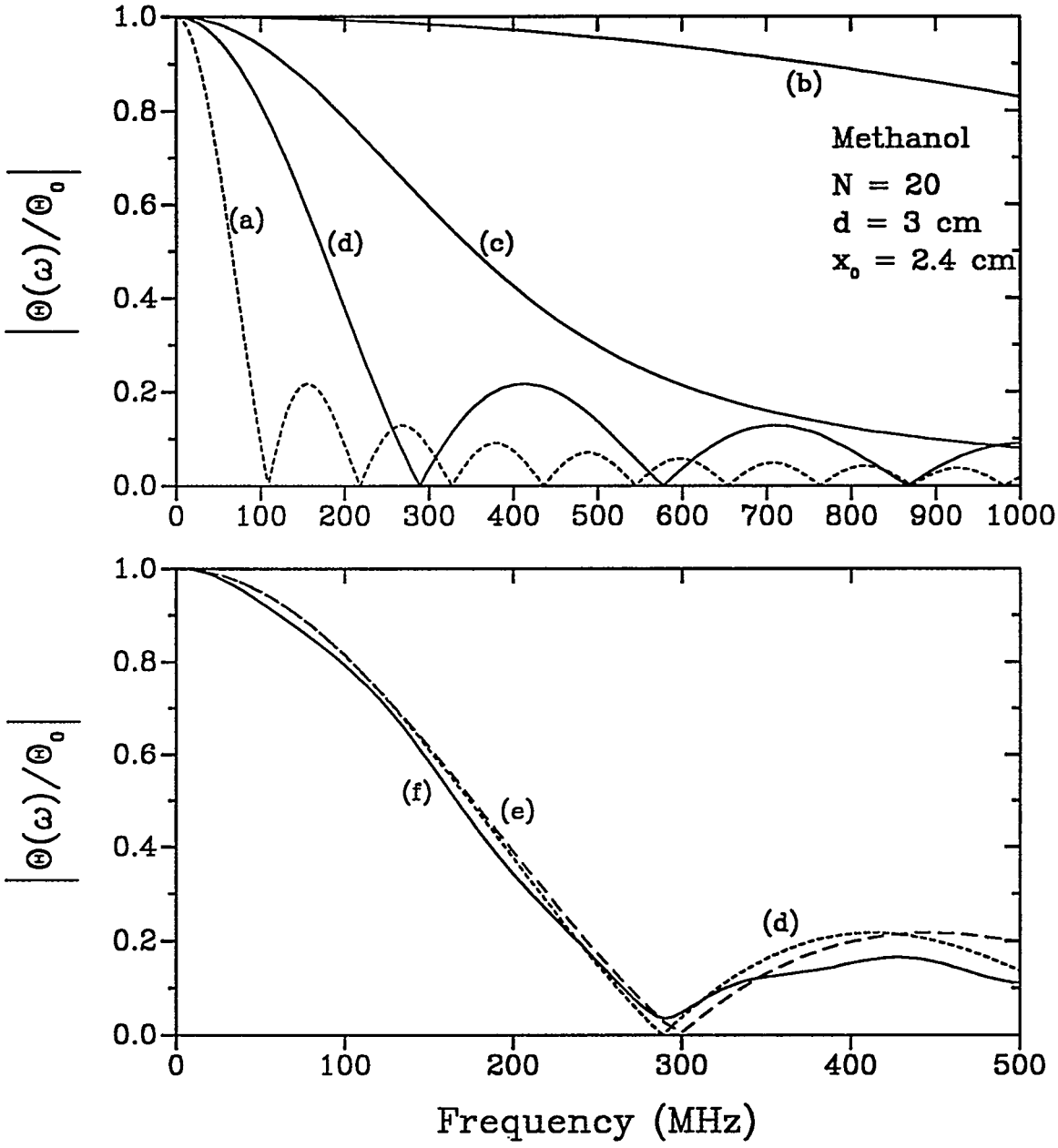

Fig. 10-9. Model predictions of the relative magnitude of the Faraday rotation for a travelling wave fiber current sensor with methanol as the dielectric. (a) Planar coil only; (b) helical coil, no dispersions; (c) helical coil, liquid dispersion only; (d) helical coil, ε_{eff} due to the teflon, no dispersions; (e) helical coil, ε_{eff}, waveguide dispersion only; and (f) helical coil, ε_{eff}, liquid and waveguide dispersion, and fiber lead effects.

eliminates the nulls from the sensor response, meaning the magnitude never drops completely to zero. This is an argument for potential utilization of fiber sensors well beyond their 3 dB bandwidth or the expected cutoff frequency.

In practical travelling wave systems, the presence of the fiber support mandrel was shown to perturb the transmission line relative permittivity. If this effect is considered in our example model, curve (d) in Fig. 10-9 results. In generating this response, a teflon support tube (ε_r = 2.0) having inner and outer diameters of 2.4 and 3.18 cm was used, and the coaxial transmission cell had center and outer conductor diameters of 0.52 and 5.75 cm. These dimensions are exactly those used for all the experimental configurations in this study. An effective relative permittivity of 14.07 is computed for the methanol-teflon dielectric system. Once again, the liquid is assumed nondispersive in generating the response curve (d). The 3 dB bandwidth for this curve, computed using Eq. (8-7), is 127.9 MHz.

In the lower half of Fig. 10-9, the perturbations in the Faraday response due to the addition of waveguide dispersion, liquid dispersion and lead effects are shown. Curve (e) adds the waveguide dispersion but treats the liquid medium as lossless. The ε_{eff} values from the dotted reference curve in Fig. 10-6 were used to generate this response. Since the effective relative permittivity of the methanol increases with frequency, the phase matching between the electromagnetic signals actually improves as the frequency increases. This leads to a slightly larger bandwidth for curve (e) when compared to curve (d) in Fig. 10-9. Significant increases in response are seen in the second lobe near 500 MHz. This increased travelling wave performance is even more pronounced for other liquids, such as water, since the waveguide dispersion for the TM_{01} mode is much greater (see Fig. 10-7).

All travelling wave sensor effects, including the fiber coil lead effects, were considered in generating the response curve (f) in Fig. 10-9. Leads are assumed to have a length defined in Appendix B by X = R and be oriented perpendicular to the planar

magnetic wave, having no travelling wave characteristics. This lead configuration describes precisely that used in the experimental sensor cells. Both absorption in the methanol and increased propagation time in the fiber leads lower the sensor bandwidth in curve (f) of Fig. 10-9. Lead effects are not as pronounced in this model description since N = 20. As might be expected, coils with fewer numbers of turns exhibit further reductions in bandwidth due to the lead effects. Even when accounting for the many effects that spoil the original near-ideal travelling wave condition, the predicted sensor response still shows a bandwidth enhancement of greater than 2.5 compared to the planar coil sensor configuration. And this occurs without a loss in Faraday sensitivity.

In Fig. 10-9, two other features of curve (f) are noted. First, the response never drops to zero. One explanation for this phenomenon, the liquid dispersion effects, was given earlier when describing curve (c). Missing nulls in the response curve can also be created by the fiber leads, since they are arranged in a non-travelling wave configuration. For curve (f) in Fig. 10-9, a combination of both liquid dispersion and lead effects contribute to the non-zero response near 300 MHz and also to the loss in higher frequency response in the second lobe. The second noted feature in curve (f) is the presence of a weak modulation over the entire response. This is entirely due to the fiber leads and appears to have a modulation frequency which very closely follows that for the planar coil shown in curve (a). This result is somewhat expected, since the leads are configured in a planar layout and contribute additional length to the coil proper (as described in Appendix B). In travelling wave coil configurations that have fewer turns, the lead effects are more dominant, and the modulation is more pronounced.

The Faraday rotation phase also undergoes various transformations as the effects of the liquid travelling wave cell configurations are compounded. Some of these are illustrated in Fig. 10-10. Shown are phase response curves that correspond to the magnitudes in the lower half of Fig. 10-9; the curve letter indicators remain the same. Curve (d) gives the expected response for a sensor whose frequency dependent phase is

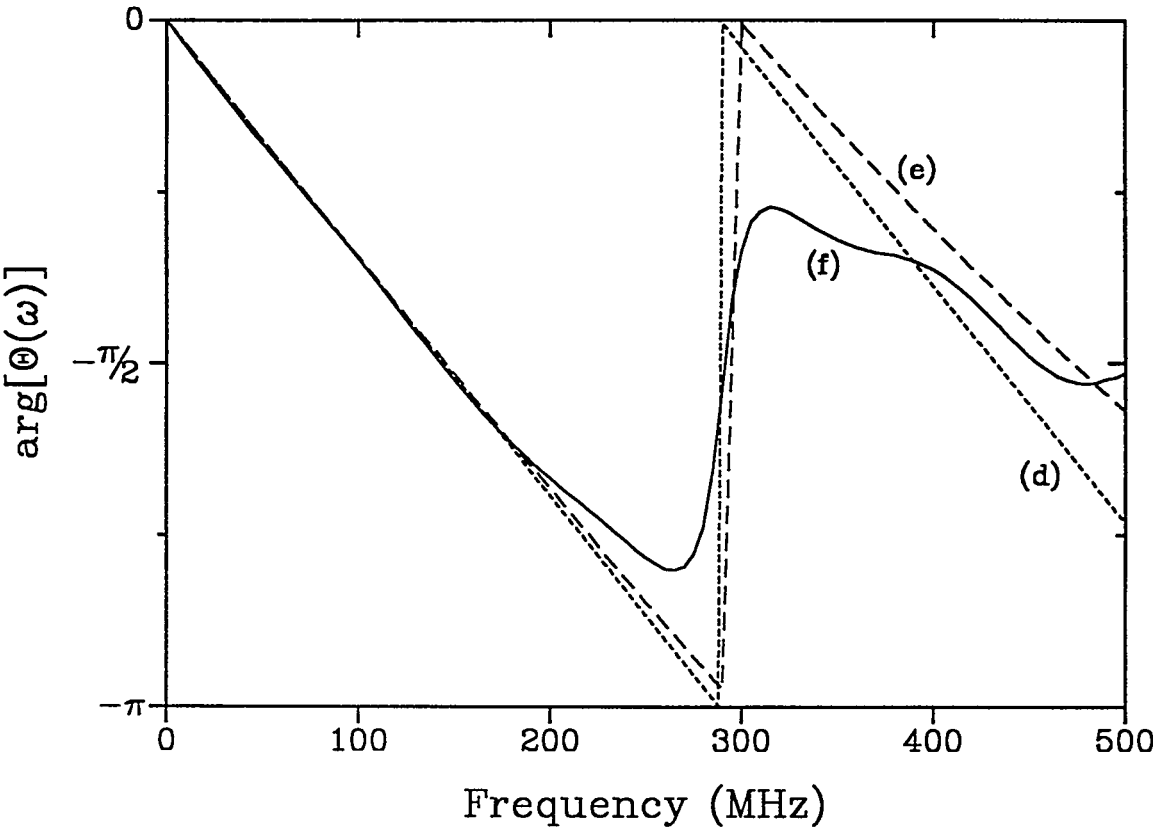

Fig. 10-10. Model predictions of the Faraday rotation phase for a methanol-filled travelling wave current sensor. The sensor parameters and the curve designators correspond to Fig. 10-9.

determined by the total interaction time, $\phi \propto \omega$. The "apparent" interaction time for a travelling wave sensor decreases as the phase matching increases, when in reality, the actual interaction time lengthens. The decrease in interaction time is given by the factor in parenthesis in Eq. (8-5b). In fact, Eq. (8-5b) describes the phase angle (less the sign change) for the travelling wave sensor used to generate curve (d) in Fig. 10-10. Curve (e) shows the increasing phase angle with frequency created by the constantly increasing value of ε_{eff} for the lossless methanol model. The phase is a nonlinear function of frequency, giving rise to the less-abrupt phase flip near 300 MHz and the lag in phase angle as frequency increases.

The most noticeable phase deviations occur in curve (f) in Fig. 10-10. Flattening and diminution of the phase angle curve near the transition frequency is what contributes to the missing nulls in the magnitude curve. From previous discussions of the Faraday response for fiber sensor coils (see Eq. (5-5) and Fig. 5-1), the zero response magnitude occurs at frequencies where the phase is an integer multiple of $-\pi$. For curve (f) in Fig. 10-10, the phase never achieves this value, and thus, the corresponding magnitude in Fig. 10-9 never drops to zero. Also noticeable in the phase curve (f) is the weak modulation due to the fiber coil leads and the increased phase flattening at the highest frequencies due to absorption in the methanol.

Many of the mechanisms discussed earlier in this chapter, and illustrated in Fig. 10-9, lead to reduced bandwidths for practical travelling wave fiber current sensors. In particular, the waveguide and liquid dispersion in the travelling wave transmission cells and the presence of the non-travelling wave configuration of the fiber coil leads preclude achieving the near-infinite bandwidth enhancement factors described in Chapter 8 for the ideal configurations. These limitations are illustrated in Fig. 10-11 where predicted magnitudes of the bandwidth enhancement factor are plotted for several configurations of the methanol example model. The diameter of the helical coil is again fixed at 3 cm and the pitch is varied to allow for a changing d/x_0 in the plot abscissa. Curve (a) is the BEF magnitude for the nondispersive, travelling wave sensor; one point on this BEF curve comes from curve (b) in Fig. 10-9. The BEF magnitude is generated from Eq. (8-10) with $\varepsilon_r = 32.6$. At $d/x_0 = 1.2$, the BEF approaches infinity. If the model now includes liquid dispersion in the methanol, curve (b) in Fig. 10-11 results. For this curve, the BEF is generated directly from Eq. (8-9) with ΔB (travelling wave) extracted from numerical computations. The peak BEF in curve (b) is limited to ~ 5.04 and occurs at $d/x_0 \approx 1.23$. Although the maximum-achievable bandwidth enhancement is significantly reduced due to the absorption, the design parameters for the best travelling wave sensor performance remain essentially the same (peak BEF is approximated by Fig. 8-4). From further

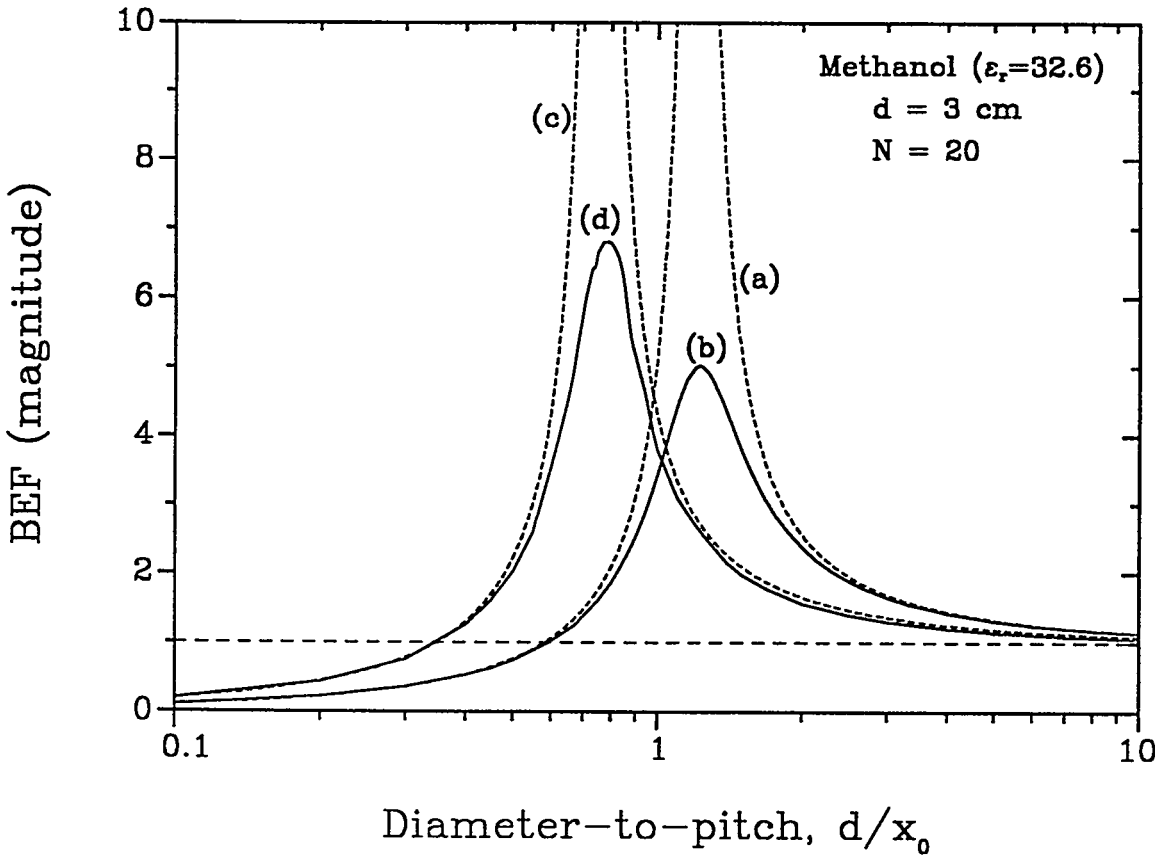

Fig. 10-11. The bandwidth enhancement factor as a function of the diameter-to-pitch ratio for travelling wave current sensors using a methanol dielectric. (a) Helical coil only, $\varepsilon_r = 32.6$; (b) helical coil, liquid dispersion only; (c) helical coil only, $\varepsilon_{eff} = 14.07$; and (d) helical coil, ε_{eff}, all effects included.

investigations using the extended models, it appears that the larger the liquid absorption, the greater the reduction in the maximum BEF. This prediction is not surprising.

Curve (c) in Fig. 10-11 is the BEF magnitude for the travelling wave current sensor including effects produced by the teflon fiber support tube but neglecting dispersion in the methanol medium. The BEF curve, computed using Eq. (8-10), is now shifted to smaller d/x_0 values to account for the effective relative permittivity, $\varepsilon_{eff} = 14.07$. Because of the nondispersive medium, a BEF approaching infinity occurs for $d/x_0 \approx 0.753$. Curve (d) is generated for the comprehensive travelling wave model

including all perturbing effects. The peak BEF magnitude is ~ 6.82 and occurs when $d/x_0 \approx 0.785$. Again this maximum BEF, though attenuated, appears at nearly the same d/x_0 value as that for the ideal travelling wave sensor. The peak BEF magnitude for curve (d) is noticeably larger than that for curve (b). This appears to solely depend on the static value of the ε_{eff} for the transmission cell dielectric medium; the smaller the value of ε_{eff}, the greater the degree of phase matching and the larger the maximum-achievable BEF. The inclusion of lead effects in the model used to generate curve (d) in Fig. 10-11 reduces the peak BEF by only 3%. This small reduction is obviously due to the large number of turns (N = 20) used in the model fiber coil. When fewer turns are used, more pronounced reductions in the maximum BEF are predicted. Also noticeable in curve (d) is the weak modulation effects produced by the fiber coil leads.

The complete extended models describing the liquid travelling wave current sensors predict that large bandwidth enhancements are possible for many configurations. In the previous example for a sensor containing methanol as a dielectric, BEFs greater than 6.0 were predicted. However, the model predicts that BEFs will always be below 10 for most configurations using methanol. For other liquid dielectrics, larger bandwidth enhancements may be possible, but for the three test liquids chosen for experimentation, estimates are that BEFs will remain less than 10. Bandwidth enhancement is very much dependent on travelling wave sensor design parameters such as transmission cell geometries, fiber support material and geometry, fiber coil pitch and number of turns, and fiber coil lead length and configuration. The comprehensive models indicate that highly precise estimates of the effective relative permittivity can be made, and that static values for ε_{eff} can be used in Eq. (8-12) to find d/x_0 for maximum performance in the travelling wave sensor design.

CHAPTER 11

TRAVELLING WAVE SENSOR MEASUREMENTS

The relative magnitude of the Faraday rotation was measured for several configurations of the travelling wave fiber current sensors. Relative permittivity was varied through use of air and liquid dielectrics, and diameter-to-pitch ratio was varied in the helical fiber coils. Travelling wave cell configurations are discussed in detail in Chapter 9, and the laboratory experimental instrumentation and hardware are shown in Figs. 4-1 and 9-1. Measurements with the liquid-filled cells were conducted up to a frequency that was limited by loss in response signal-to-noise: a combination of the Faraday rotation high frequency rolloff and the absorption of the transmitted power in the liquid dielectric. Thus, maximum experimental frequencies were 625 MHz. The transmitted power through the coaxial test cells was held constant for most of the high frequency testing so that monitored currents could be related directly to power. However, as absorption increased it was sometimes necessary to accept the reduced transmitted power and correct the data for the relative magnitudes. Also, because of the large impedance mismatches that occurred for some of the travelling wave test cells, corrections to the estimated conducted currents were attempted. This was only necessary in a few extreme cases.

For all the experimental sensor configurations, an increase was observed in response 3 dB bandwidth compared to that for an equivalent planar fiber coil. The travelling wave fiber sensor concept was proven, and quantitative information was acquired on sensor parametric effects. Also, the complete extended current sensor models developed in Chapter 10 predicted quite accurately the magnitude versus frequency response curves for most of the systems. Trends in the measured responses were noted for the others.

Airline Measurements

One configuration of a travelling wave sensor with an air dielectric was tested. The helical fiber coil parameters were N = 10, d = 3 cm, and $d/x_0 = 1.0$. Figure 11-1 shows the Faraday response for that system. Plotted are the measured values of the relative magnitude, shown as the open circles, and the model predictions, the solid curve. Scatter in the measured data is approximately 1 dB around the plotted points. The measured 3 dB bandwidth for the sensor system is ~ 109.5 MHz.

As seen in the Fig. 11-1, agreement is excellent between the experimental and theoretical values. Below 350 MHz, little deviation is observed; however, at the higher frequencies some loss in measured response is seen compared to that predicted by the

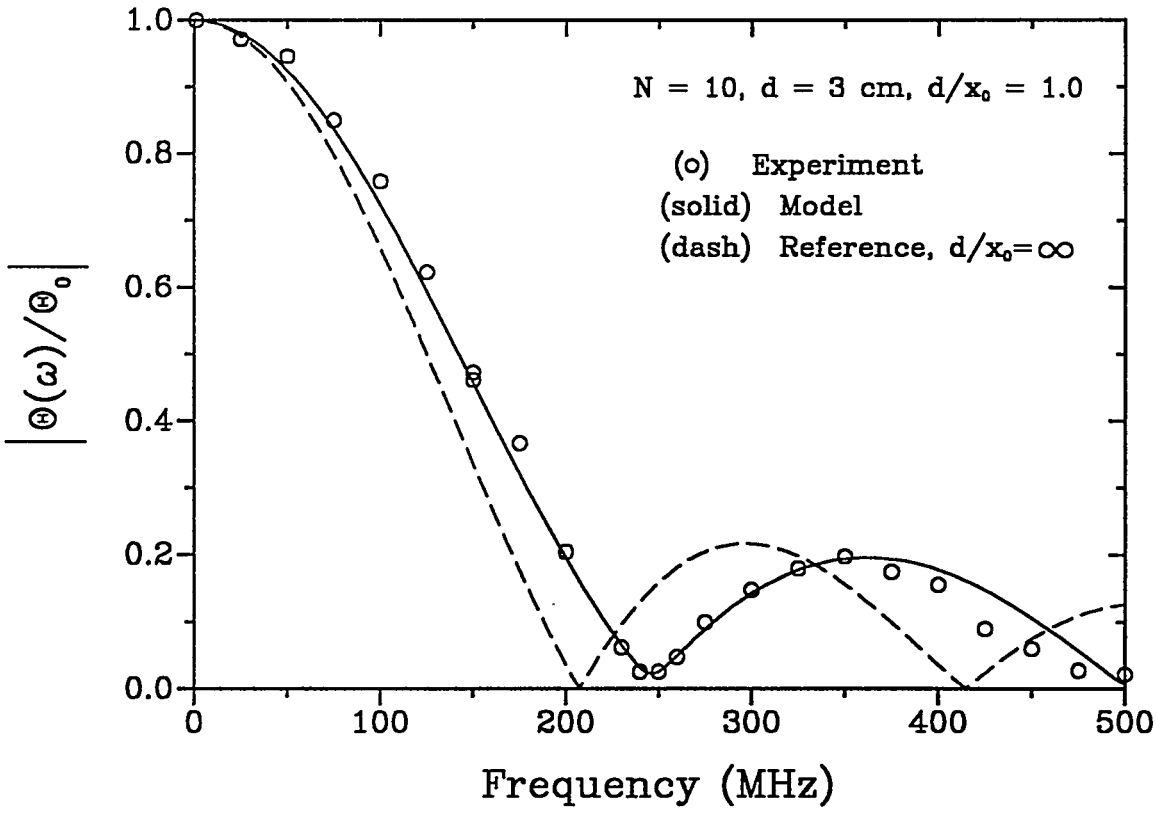

Fig. 11-1. The relative magnitude of the Faraday rotation for a coaxial airline travelling wave fiber current sensor.

model. This high frequency discrepancy between model and experiment is consistent throughout all measurements made for the travelling wave sensors, air or liquid cells, and can only be explained by a deficiency in the model, unaccounted perturbations in the EM properties of the transmission cells, or a combination of the two. The model predicts quite accurately the non-zero response minimum near 245 MHz in Fig. 11-1. This missing null is caused by the fiber leads that enter and exit the coaxial line in a non-travelling wave configuration. The fiber leads are also configured such that they add an equivalent half turn to the fiber coil length (see Appendix B for a further explanation), which reduces the sensor response bandwidth.

Also plotted in Fig. 11-1 is a dashed reference curve for the equivalent planar coil fiber current sensor. This reference sensor also includes fiber leads in the exact configuration as those for the travelling wave coil. The measured values for the travelling sensor show an enhanced high frequency response when compared to that of the reference sensor. The bandwidth enhancement factor (BEF), determined from the ratio of interpolated ΔB values, is approximately 1.19 (ΔB for the reference sensor is ~ 103.4 MHz). This is very close to 1.2, the BEF predicted for $\varepsilon_r = 1$ and $d/x_0 = 1$ by the ideal travelling wave theory presented in Chapter 8. Thus, well within experimental error, the enhanced response of this sensor can be determined from simple theory.

Judging from the predictions shown in Fig. 11-1, the extended models (that account for fiber lead effects) can be used to identify optimum design parameters for general configurations of the airline travelling wave fiber sensor. If the fiber coil parameters N = 10 and d = 3 cm are used in the model and the coil pitch is allowed to vary, the BEF attains a peak value of ~ 1.37 at $d/x_0 = 0.33$. This prediction is essentially identical to that found from Eq. (8-10) and shown in Fig. 8-3 for the idealized travelling wave sensors. The mathematical developments leading to Eq. (8-10) neglect the presence of the fiber leads, both for the planar as well as the travelling wave coil. Obviously, the lead configuration in a 10 turn airline travelling wave coil has little, if

any, effect on the relative bandwidth enhancement. However, it is expected that for coils with fewer turns or for systems with larger high frequency enhancements that lead interactions may be more significant, producing somewhat reduced BEFs.

Regardless, it is obvious from these predictions and the validating measurements on the air dielectric travelling wave current sensor that significant increases in sensing bandwidth cannot be achieved with only the helical fiber structure. Slow-wave mechanisms for improved phase matching are required. In the present travelling wave cell design, this entails use of higher relative permittivity dielectrics.

Liquid Cell Measurements

In addition to the three test liquids used as dielectrics in the coaxial transmission cells, three different fiber coil helical pitches were employed. These were x_0 = 3.0, 2.0, and 1.5 cm, which correspond to d/x_0 values of 1.0, 1.5, and 2.0, respectively, since the mean coil diameter was held constant at d = 3 cm. The number of fiber turns was 20 for the coils with d/x_0 = 1.5 and 2.0, and 14 for the coil with d/x_0 = 1.0. This difference was deemed necessary due to the total length of the cell working volume, approximately 46 cm. A 20 turn coil with the largest coil pitch would have been 60 cm in length. In all, nine different sensing configurations were available for experimentation. Actually a few additional configurations were explored, involving a varied cell center conductor diameter. These variations caused cell impedance to differ from 50 Ω and produced deviations in the dielectric effective relative permittivity (see Eqs. (10-2) and (10-3)), but changes in the measured Faraday responses for the sensors could not be distinguished due to the relatively large experimental errors (~ 1 dB). For this reason, the responses presented for the travelling wave current sensors are identified only by test liquid, the fiber coil d/x_0, and the number of coil turns.

A typical response curve showing the relative magnitude of the Faraday rotation versus frequency is presented in Fig. 11-2 [60]. These data were generated from a

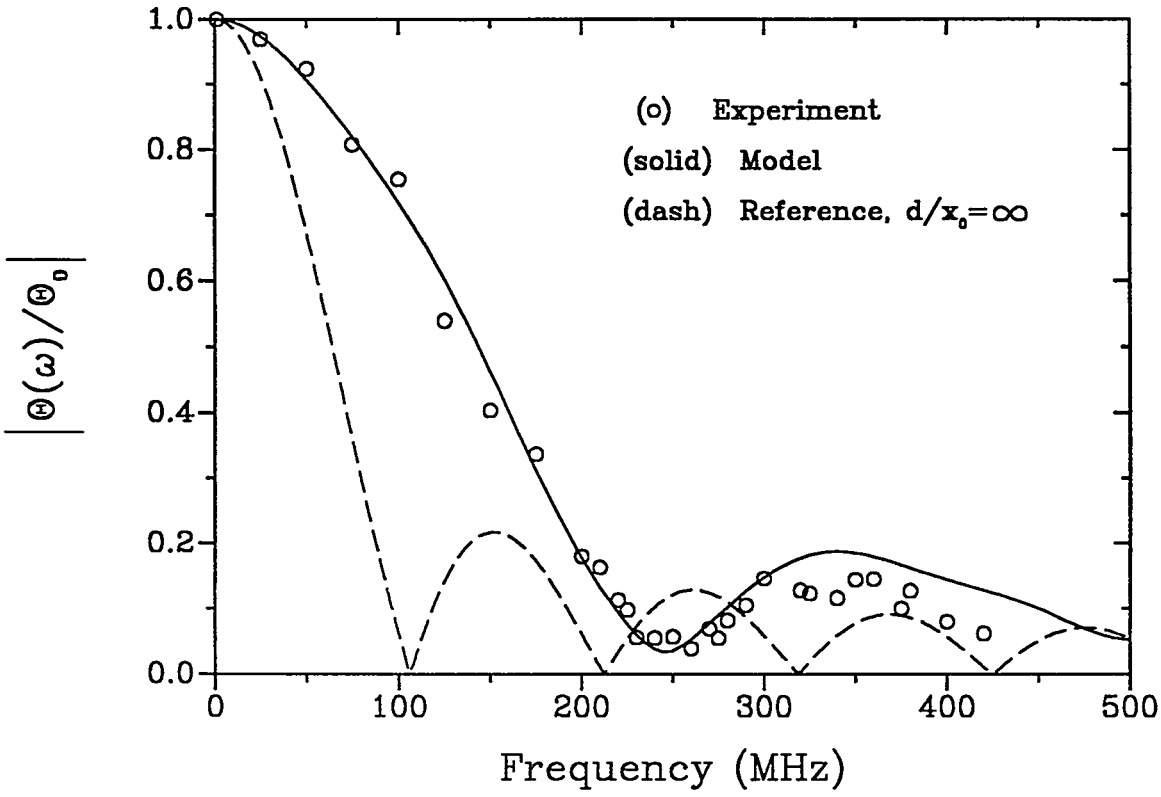

Fig. 11-2. The experimental and theoretical Faraday response for a liquid travelling wave fiber current sensor containing a methanol dielectric. The helical coil has 20 turns, a 3 cm diameter and a diameter-to-pitch ratio of 1.5.

system that used methanol as the cell dielectric and a fiber sensor coil of 20 turns and $d/x_0 = 1.5$. The measured response values (open circles) agree well with the predictions of the sensor model. Deviations between experiment and theory occur only at the higher frequencies, in the second response magnitude lobe. Explanations for this discrepancy are offered in the previous section. Both the measured and predicted response curves show the missing null near 250 MHz in Fig. 11-2 which is the result of liquid dielectric dispersion and fiber coil lead effects.

This travelling wave sensor has a 3 dB bandwidth of approximately 103 MHz and a BEF of ~ 2.2 when compared to the planar sensing coil (dashed response curve in Fig. 11-2). This enhancement is slightly smaller than the BEF of 2.47 predicted by Eq. (8-10)

for a nondispersive dielectric with the effective relative permittivity of the methanol/teflon combination and for a leadless helical coil in the same test configuration. The difference in these two BEFs, 11%, is approximately the same as that illustrated for curves (c) and (d) in Fig. 10-11 when $d/x_0 = 1.5$.

Using a liquid as the dielectric medium in the travelling wave fiber sensor systems provides the slow-wave mechanism needed to enhance high frequency Faraday response. Experimental measurements verified the theoretical predictions that increasing the liquid relative permittivity progressively increases the sensor bandwidth. This point is illustrated in Fig. 11-3, where response curves for each of the test liquids are plotted.

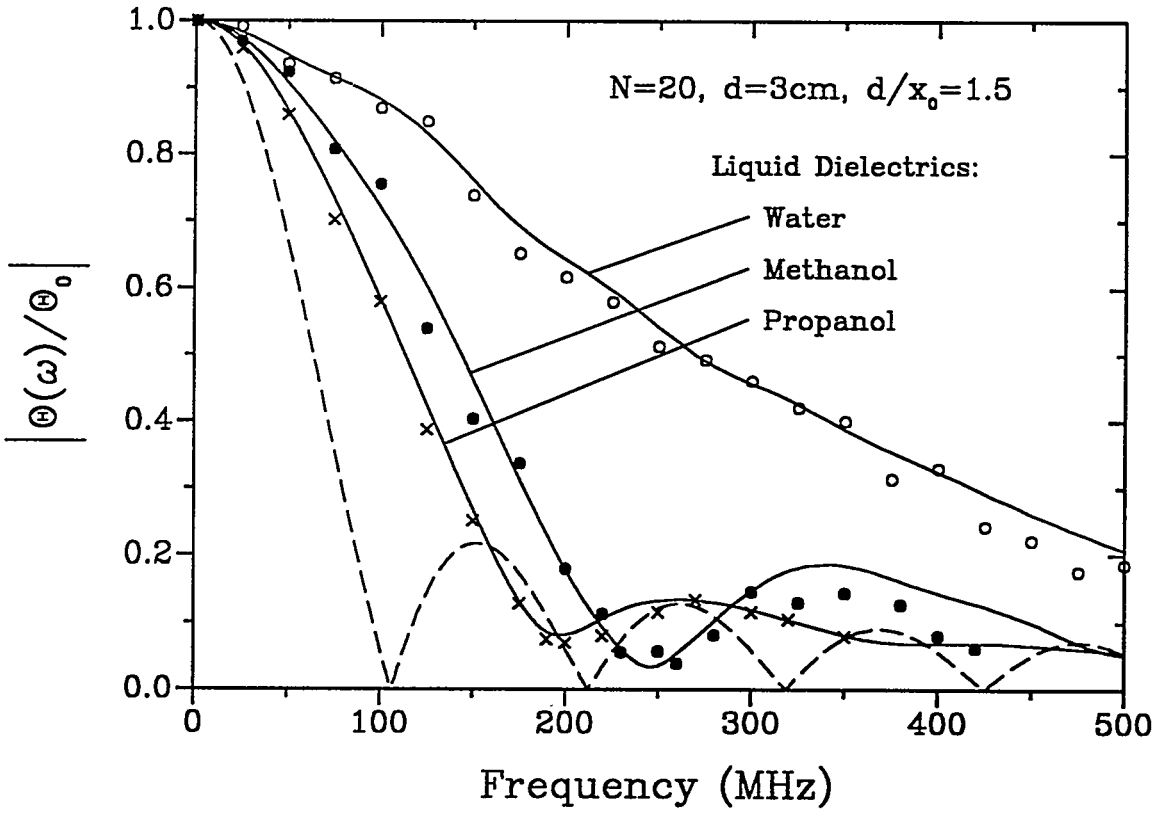

Fig. 11-3. A comparison of the relative Faraday rotation for each of the three test liquids used with the same helical coil. The plotted points are experimental values, and the solid curves are model predictions of response. The dashed curve is the response for an equivalent 20-turn coil with $d/x_0 = \infty$.

The same fiber sensing coil, N = 20 and d/x_0 = 1.5, is used with the three liquids. Effective relative permittivities (static values) for the liquids increase from 10.35 for the propanol, to 14.07 for the methanol, to 20.94 for the water. Sensor bandwidths are approximately 77.4 MHz, 103 MHz, and 159.5 MHz, respectively, for the curves using the three liquids. The corresponding bandwidth enhancement factors are 1.65, 2.2, and 3.4 when compared to the reference curve bandwidth of 46.9 MHz. In Fig. 11-3, both measured data (the plotted points) and model-generated responses (the solid curves) are displayed. For the parameters used in these experimental configurations, the model predictions are shown to be highly accurate.

The other travelling wave sensor parameter that affects the bandwidth enhancement factor is the fiber coil diameter-to-pitch ratio. Experimentation on similar configurations with each test liquid while varying only d/x_0 showed that increasing the coil pitch improved sensor phase matching and increased response bandwidth. In Fig. 11-4, a plot of the relative magnitude of the Faraday rotation versus frequency is given for several methanol liquid cell configurations. Both experimental values and model-generated curves are again plotted for the Faraday response, except for d/x_0 = 1.0, which is represented only by a modeling prediction. As discussed earlier, the fiber coil with d/x_0 = 1.0 had only 14 turns, while the other coils had 20 turns. Since the comprehensive model predictions for the travelling wave fiber current sensors agree quite well with the measured values, liberty was taken to generate the extra curve for the larger coil pitch and appropriately complete the illustrated comparisons. In Fig. 11-4, as d/x_0 decreases (x_0 increasing), the BEF increases. Values of approximately 1.6 (with $\Delta B \approx 75.3$ MHz), 2.2 ($\Delta B \approx 103.5$ MHz), and 3.9 ($\Delta B \approx 183.3$ MHz) are attained for d/x_0 = 2.0, 1.5 and 1.0, respectively. As illustrated previously in Fig. 10-11 for a similar methanol-filled sensor cell, the BEF grows nonlinearly with decreasing d/x_0. When d/x_0 =1.0, the sensor system parameters are very close to meeting the travelling wave condition for maximum phase matching.

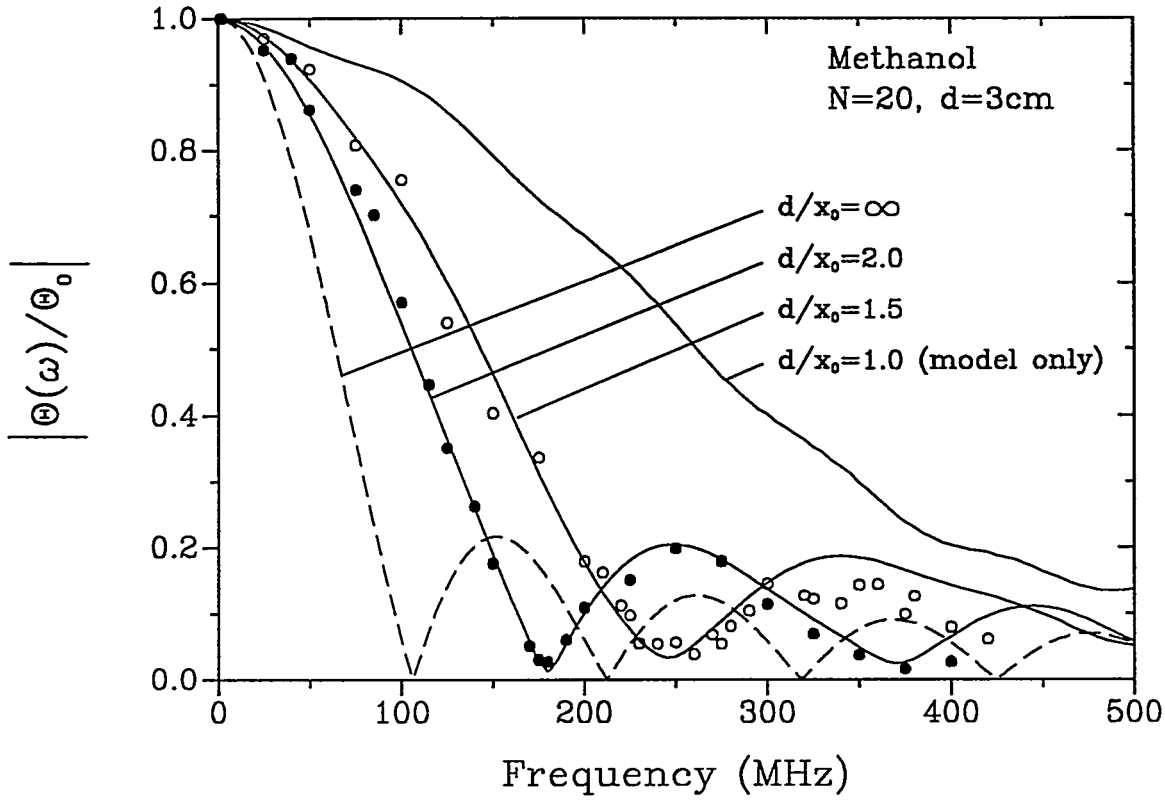

Fig. 11-4. The relative magnitude of the Faraday rotation for a travelling wave current sensor with a 20-turn helical coil in a methanol-filled transmission cell. The diameter-to-pitch ratio is varied to show the correlation with response bandwidth.

The largest bandwidth enhancement achieved during experimentation with the liquid travelling wave sensors was approximately 4.1 for a water-filled test cell using a fiber coil with 14 turns and $d/x_0 = 1.0$ [60]. Figure 11-5 shows the Faraday response curve for this sensor. The measured sensor bandwidth is ~ 300 MHz, which is the largest for any multiturn fiber current sensor reported to date. An estimate of the system sensitivity-bandwidth product (SBP) for this wideband sensor is 1.85×10^{-4} rad/A-s or 1.06 MHz-°/A. This SBP, though much larger than any for a fiber current sensor, is approximately seven times smaller than reported for a bulk optic current sensor using Ga:YIG as the Faraday rotator material [30]. In Fig. 11-5, the rolloff in the response for frequencies above the 3 dB point is quite dramatic, but significant response S/N is seen

for frequencies as high as 400 MHz. For some current monitoring applications, this sensor could be used to these higher frequencies.

At the low frequencies in Fig. 11-5, below 200 MHz, the measured values (open circles) agree well with the model predictions (solid curve). Above 200 MHz, however, the experimental and theoretical values deviate significantly. Here, the quantitative ability of the comprehensive travelling wave model to predict sensor responses breaks down. It is postulated that the electromagnetic properties of the transmission cells are not adequately described in the model since contributions that do not adhere to the quasi-TEM assumption are ignored. The source of such contributions could be large cell

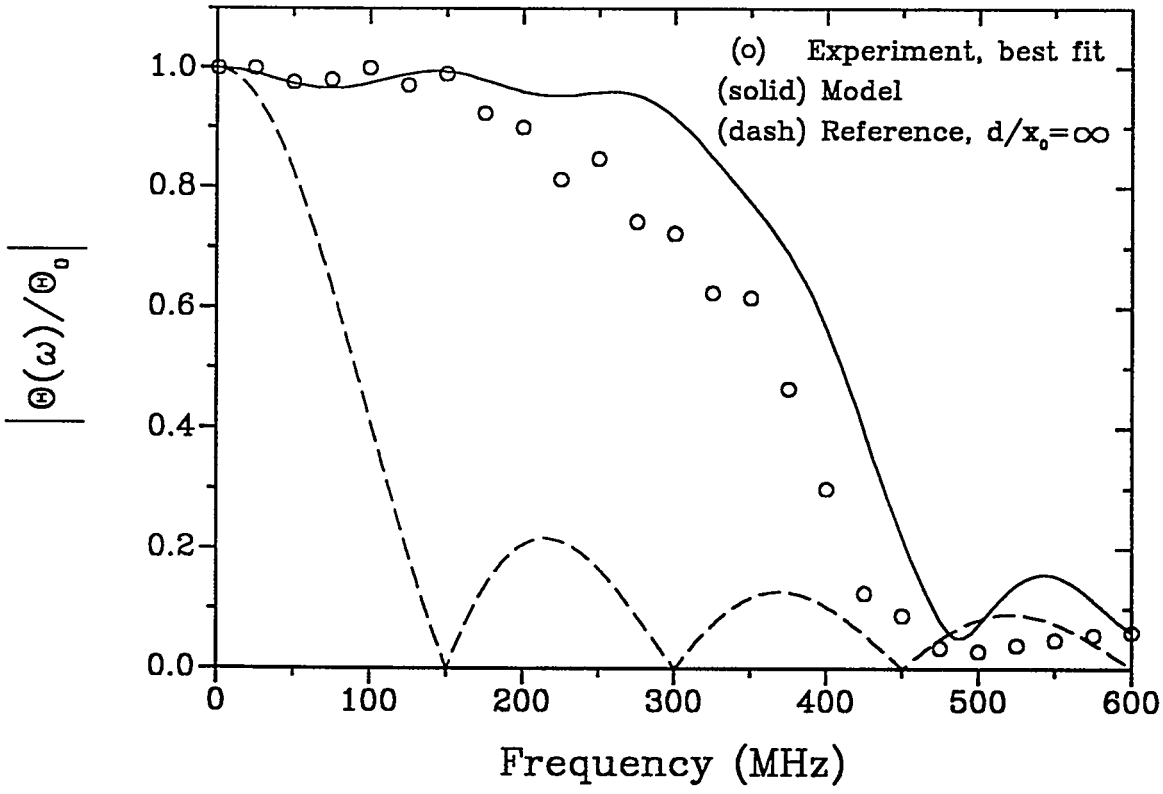

Fig. 11-5. The measured and modeled responses for a travelling wave fiber current sensor using a coil with N = 14, d = 3 cm, and d/x_0 = 1.0 inside a cell containing water. The measured bandwidth for this configuration is approximately 300 MHz, the largest for any of the experimental systems.

reflections, cell multimoding by nonazimuthally-symmetric modes, or a combination of these and other high frequency effects.

In spite of these discrepancies, qualitative trends are observed in the measured response values that are predicted by the model. One of these is the abrupt rolloff of the curves. For the model-generated response, this occurs between 300 and 500 MHz, with magnitudes dropping from approximately 0.95 to near 0.05. A probable explanation for this fast rolloff lies in the rapid increase of the effective relative permittivity for the TM_{01} mode in the water transmission cell. From Fig. 10-7, the value of ε_{eff} increases from ~ 23 at 200 MHz to ~ 40 at 500 MHz; thus, at the higher frequencies, the magnetic wave is travelling much slower. For frequencies below ~ 150 MHz, the wave phase velocity is essentially constant and the Faraday response curve will behave normally with a given travelling wave enhancement. But as ε_{eff} increases rapidly above 200 MHz, the phase matching is also modified, first increasing slightly, then decreasing significantly as the light in the fiber now begins to outrun the progressively slowing magnetic wave. The travelling wave condition for this water cell configuration should occur when $\varepsilon_{eff} \approx 23.5$ according to Eq. (8-12). Thus, at approximately 220 MHz, the phase matching predicted by the model is greatest, and the travelling wave enhancement peaks. As the frequency increases beyond 220 MHz, the enhancement decreases and the response curve quickly drops. At 500 MHz, predictions indicate that travelling wave enhancement has been reduced by nearly a factor of three from its peak value.

The experimentally determined values in Fig. 11-5 show a rapid rolloff at much lower frequencies than predicted by the model. This decreased response at a lower frequency could be caused by the changing wave impedance of the TM_{01} mode in the transmission line. As seen in Fig. 10-8, the wave impedance for the water-filled cells increases significantly, and rapidly, above 150 MHz. Thus, the propagating wave becomes less quasi-TEM with a larger field component along the positive axial direction of the cell. This should produce an enhanced phase matching between the magnetic

wave and the light in the fiber at lower frequencies than predicted by the model (the model does not address the "non-quasi TEM" conditions of the EM wave). A resultant loss in travelling wave enhancement then occurs at somewhat lower frequencies due to the combination of the rapidly increasing ε_{eff} and η. The experimental values in Fig. 11-5 appear to confirm this hypothesis, with essentially flat frequency response below 150 MHz, and rapid decrease above that frequency.

Also seen in Fig. 11-5 is the weak modulation created by the fiber coil lead effects. This modulation is apparent in both the measured and model-generated curves. The depth of modulation is slightly larger for this sensing configuration, primarily due to lead effects having a greater impact on coils with smaller numbers of turns. The largest response perturbations caused by lead effects have also been observed when liquid absorption is minimum and when travelling wave enhancements are near maximum. Both of these conditions apply to this water dielectric current sensor configuration.

The largest sensor bandwidths measured for the propanol and methanol-filled travelling wave cells also occurred for the fiber coils with N = 14 and $d/x_0 = 1.0$. The experimental 3 dB bandwidths for these sensors were approximately 137 MHz and 221 MHz for propanol and methanol liquid dielectrics, respectively. Corresponding BEFs are 2.1 and 3.3 for the given configuration. Figure 11-6 is a plot of the Faraday response curves for the widest bandwidth current sensors using each of the three test liquids. As expected, the bandwidth becomes progressively larger as the liquid relative permittivity increases. But at the higher frequencies, the curve for the water-filled cell has a faster response rolloff and crosses the curve for the methanol cell. This indicates that a travelling wave current sensor using methanol as the dielectric medium may be more useful at the higher frequencies, since the S/N remains quite large to well beyond 500 MHz.

In Fig. 11-6 only the measured values for the three liquid dielectric cells are plotted. For these wide bandwidth sensors, the discrepancies between the measured

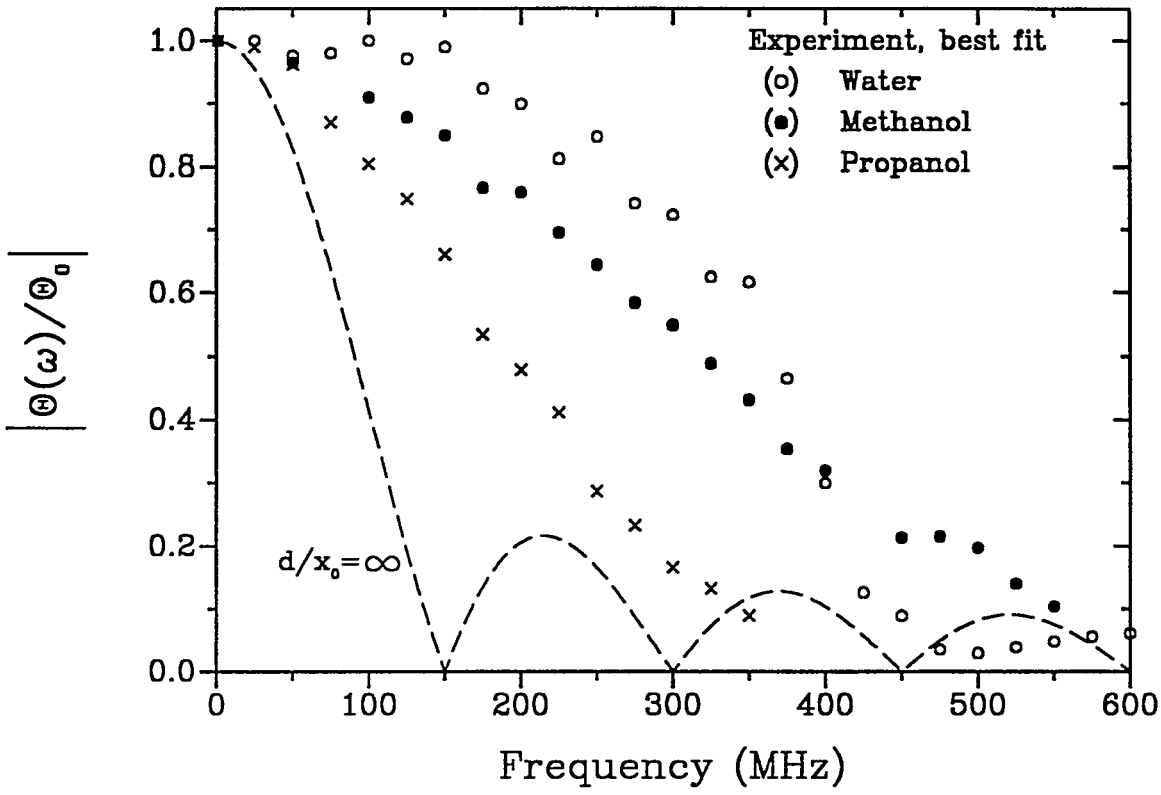

Fig. 11-6. The measured relative magnitude of the Faraday rotation for the largest bandwidth travelling wave sensors using each of the three test liquids. The common coil configuration had N = 14, d = 3 cm, and $d/x_0 = 1.0$.

Faraday responses and the model predictions are noticeable, as seen in Fig. 11-5. It is observed that for sensor configurations with low values of the BEF, the comprehensive travelling wave model predicts quite accurately most features of the response magnitude (as seen in Fig. 11-2); however, for configurations with larger BEFs, the model predictions consistently show a greater relative magnitude at the higher frequencies than the measured values. This occurred for all the liquid cell configurations when $d/x_0 = 1.0$ and N = 14. Although, the theory-experiment discrepancy is much less for the propanol-filled sensor cell (approximately 6.5% at the 3 dB point in the response curve) and the methanol-filled cell (approximately 11%) than for the water-filled cell. These discrepancies become slightly greater at the higher frequencies.

Phase Considerations

Throughout experimentation with the travelling wave fiber current sensors, only response magnitudes were measured. A phase delay measurement is much more difficult to make than a magnitude measurement, and none was attempted as part of this study. However, this characteristic of the sensor systems is needed to provide the complete transfer function for the Faraday interaction. It is hoped that measurements of the Faraday response magnitude presented here along with the well-developed models to predict sensor behavior is adequate to fully describe the wideband transient response. For most of the liquid-cell experimental sensor configurations, the comprehensive travelling wave model was quite accurate in its predictions of the magnitude; it is reasonable to expect that phase delays can be predicted equally as well. Thus, during travelling wave current sensor design, the models presented in Chapter 10 should be useful in describing both Faraday rotation magnitude and phase. Time domain response measurements should follow to finalize and verify sensor characteristics.

CHAPTER 12

OTHER TRAVELLING WAVE CONFIGURATIONS

The liquid travelling wave configurations show enhancements in the bandwidth of Faraday effect fiber current sensors, all without a loss in the sensitivity. Significant increases in sensor bandwidth and sensitivity-bandwidth product have been demonstrated. However, estimates of the maximum BEFs using models of the liquid transmission line sensing structure are limited to less than 10. Further increases in current sensor bandwidth and sensitivity might be possible, but significant deviations from the existing travelling wave structures will most likely be required. In this chapter, several innovative schemes that utilize travelling wave current sensing configurations are discussed. Predictions of the potential response, bandwidths and high frequency characteristics, are made where appropriate.

In the liquid travelling wave sensors, dielectric dispersion is the major bandwidth-limiting factor, while the need to support the fiber helix in the liquid leads to a waveguide dispersion that can also affect higher frequency response. One way of eliminating these factors is to use a solid dielectric as the propagation medium in the slow-wave structure. A very low-loss material at microwave frequencies can be identified so that dielectric dispersion is minimized, and the dielectric alone should be capable of supporting the fiber coil without use of other interfering materials. As part of this study, a travelling wave structure using a ceramic dielectric was designed, and its electromagnetic properties were characterized.

Another disadvantage of the liquid (and air) travelling wave current sensors is size. The liquid test cells were quite large, 6.35 cm diameter and 53.8 cm length, in order to accommodate the 20 turn fiber helical coils. Such large size is tolerable for laboratory development, but practical systems need to be much smaller. Reductions in device size can be accomplished in three ways: (1) using dielectric materials with

extremely large relative permittivities, so that x_0 is minimized for a given bandwidth; (2) decreasing the fiber coil diameter so high-sensitivity coils with many turns are still short; and (3) developing optical fibers with larger Verdet constant materials so high sensitivity is achieved with fewer coil turns. All of these methods have limitations, some of them severe, due to present technology.

Thus, constructing usable travelling wave current sensors will require new technological developments and possibly new materials in new configurations. Fiber coils have been utilized exclusively because of their ease of use, but they may have to give way to other optical waveguide structures. Or the coaxial transmission line with helical light guide must be abandoned altogether. New configurations are postulated here in hopes of stimulating further development of wideband optical current sensors. In addition to the ceramic dielectric transmission line structure, devices that use helical optical waveguides, planar integrated waveguides, and bulk optical materials are discussed. Travelling wave configurations include the use of helical conductor paths as well as looping optical paths. For the sake of completeness, travelling wave designs that utilize combinations of the fiber sensing techniques discussed in the earlier chapters are covered here. The theoretical framework derived for those techniques provides an excellent means for predicting high frequency response, even in non-fiber systems.

Ceramic Dielectric Travelling Wave Sensor

A solid material with a large relative permittivity that is suitable for use in a transmission cell is difficult to find. Typically, polyethylene or teflon is used in coaxial cables because of their flexibility and good microwave characteristics; but they have relative permittivities of less than 2.5. Higher ε_r materials are generally limited to the high-alumina content ceramics and the titanates (barium, strontium, calcium, magnesium and lead) [67]. These materials have very good microwave characteristics, but lack much of the fabrication flexibility afforded by the polyethylene or teflon. With these

properties in mind, a diamonite high alumina (95%) ceramic with a static relative permittivity of 9.6 was chosen as the candidate material for a solid dielectric travelling wave structure. This ceramic does exhibit some dielectric dispersion, as ε_r drops to 9.36 at 10 GHz.

The fabricated coaxial transmission cell with ceramic dielectric is shown in the cross- sectional composite view of Fig. 12-1 [34]. The test cell working volume consists of five ceramic pieces; each were cast and fired separately. The core component is a tube 6 cm long with a 1.3 mm inner diameter and 6 mm outer diameter. Along the outer surface of the tube a 10-turn helical groove is machined approximately 0.75 mm deep. Mating ceramic parts were fabricated so the entire dielectric structure filled the coaxial cell working volume: 10 cm long and 1.59 cm in diameter.

The ceramic pieces were designed to double as an annealing fixture for the 10-turn singlemode fiber coil. Fiber annealing is necessary on this sensor in order to remove the large linear birefringence produced by the small radius turns [21]. Initially,

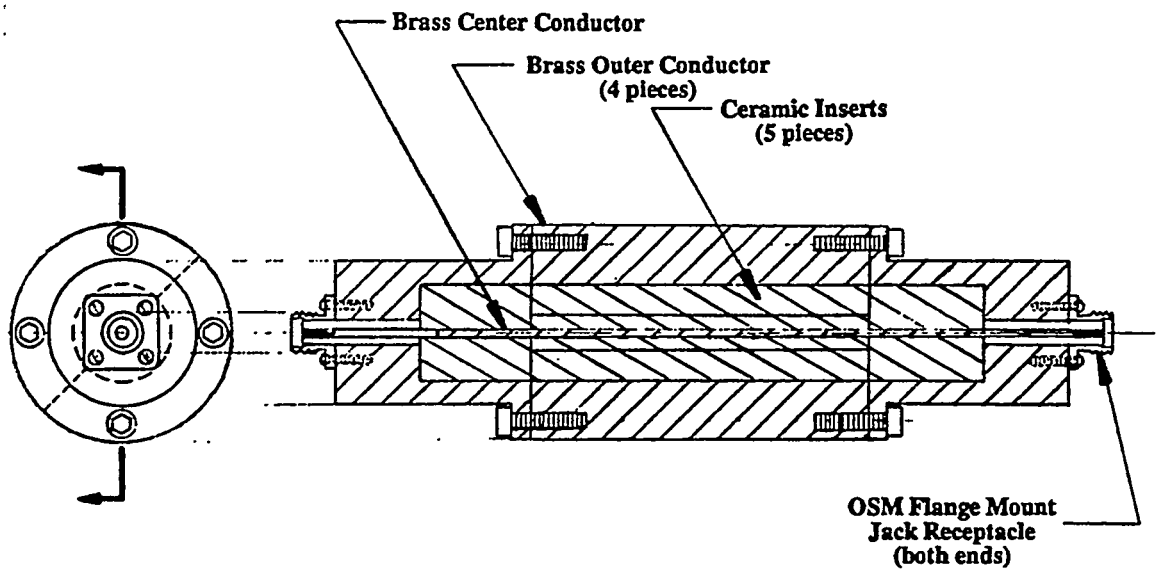

Fig. 12-1. A composite drawing of a travelling wave sensor transmission cell with a ceramic dielectric.

the fiber is wound into the groove of the tube with ample lengths of excess fiber for leads. The remaining ceramic pieces are assembled around the fiber, the transmission line's brass center conductor is passed through the ceramic parts, and the whole structure is taken to a high temperature (~ 850 °C) to perform the annealing process [22]. After annealing, the outer conductive shield of the transmission cell is assembled around the dielectric containing the fiber coil. Cutaway and disassembled views of the travelling wave transmission cell (less the optical fiber) are shown in the photographs of Fig. 12-2.

Annealing of the helical fiber coil, final assembly of the sensor, and measurement of the Faraday response have yet to be conducted. To date, fiber annealing has only occurred for coils in a planar configuration [22]. Extending this technology to other coil shapes is still a challenge, but likely one with a workable solution. In the annealing process, the singlemode optical fiber with its buffer coating is place in the annealing fixture. Pretreatment of the fiber by soaking in solvent, typically acetone or methylene chloride, allows the buffer to evaporate at a relatively low temperature in the annealing cycle (300 to 400 °C), leaving the bare glass fiber to be annealed [22]. Ideally, a soft ceramic such as Macor™ is used to prevent scratching and fracturing of the fiber. The diamonite ceramic used in the travelling wave sensor design is much harder than Macor™, but it also has a significantly larger relative permittivity. One challenge is to determine if the fiber coil will survive the annealing cycle. A second challenge is to apply a protective coating on the fiber while it remains in the ceramic fixture. Backfilling with a thinned polyurethane or silicone elastomer should provide a soft coat for the fiber.

In the absence of finished hardware and measured responses, the utility of the ceramic-filled travelling wave current sensor can only be evaluated from cell electromagnetic characterization and modeled Faraday responses. Based on cell geometries and the relative permittivity of the ceramic dielectric, the higher order mode cutoff frequency for the transmission line is 3.6 GHz. The impedance of the cell was

(a)

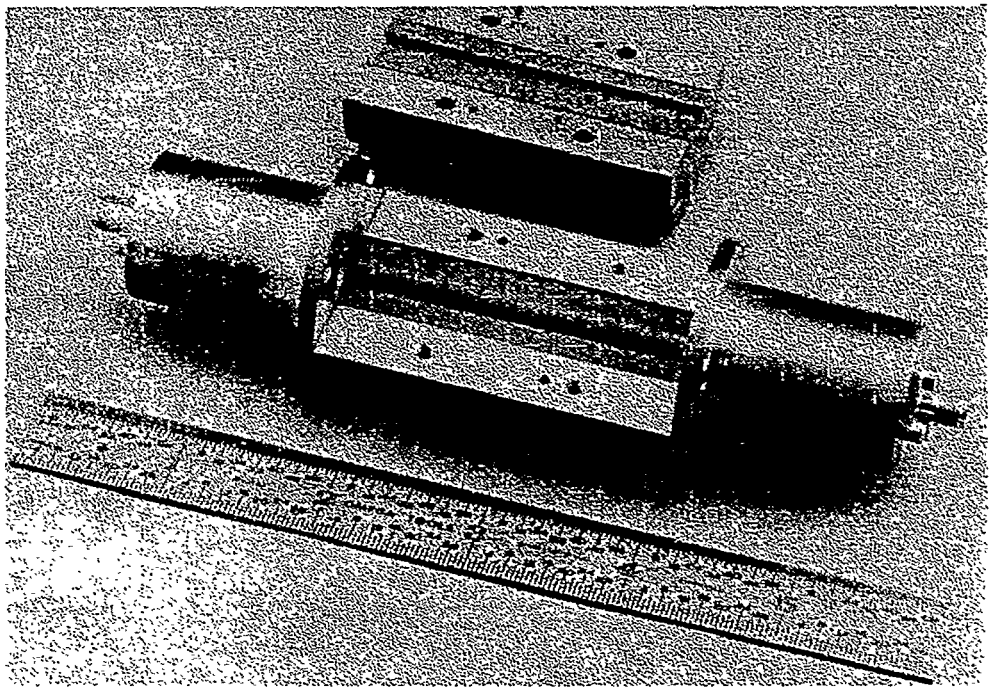

(b)

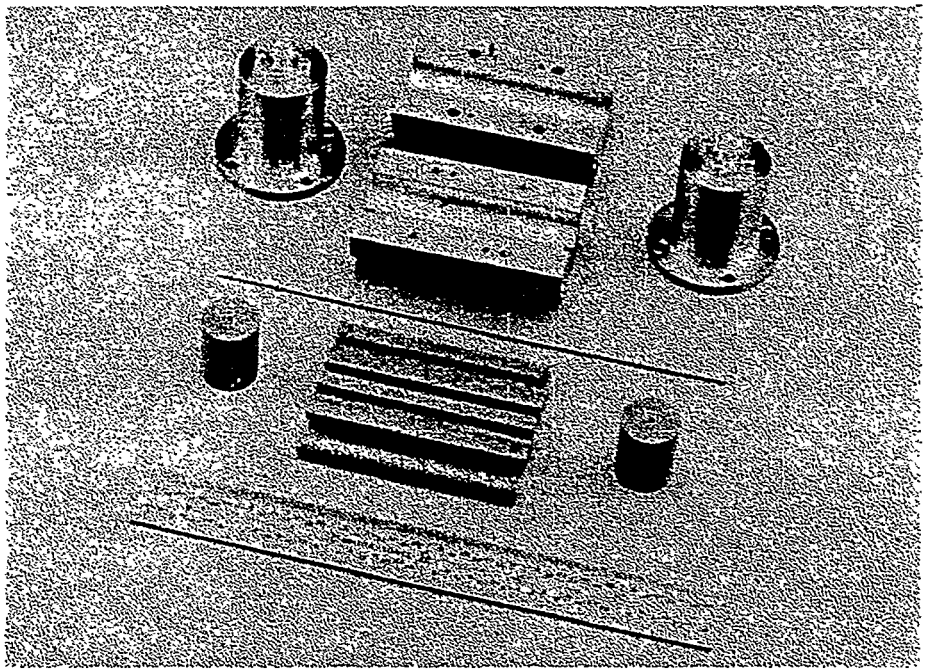

Fig. 12-2. Photographs of the ceramic dielectric travelling wave transmission cell. (a) A cutaway view of the cell showing the fiber mandrel guide: a 10-turn helical groove in the outer surface of the 6-mm ceramic tube. (b) The fully disassembled cell.

characterized for frequencies below 5 GHz. A plot of the impedance magnitude is presented in Fig. 12-3. Oscillations in the impedance are created by reflections at the transition points into the cell dielectric volume. These cause the cell impedance to vary between ~ 20 Ω and ~ 120 Ω for the frequencies below 5 GHz. If the frequency range is limited to 2.5 GHz, a likely cutoff in the Faraday response characterization, impedance deviations about 50 Ω are bound within 1.3 dB. Also, below 2.5 GHz the test cell has a very impressive SWR of 1.4.

The predicted Faraday response for this travelling wave sensor is shown in Fig. 12-4. Plotted are model-generated curves for both the magnitude and the phase. The

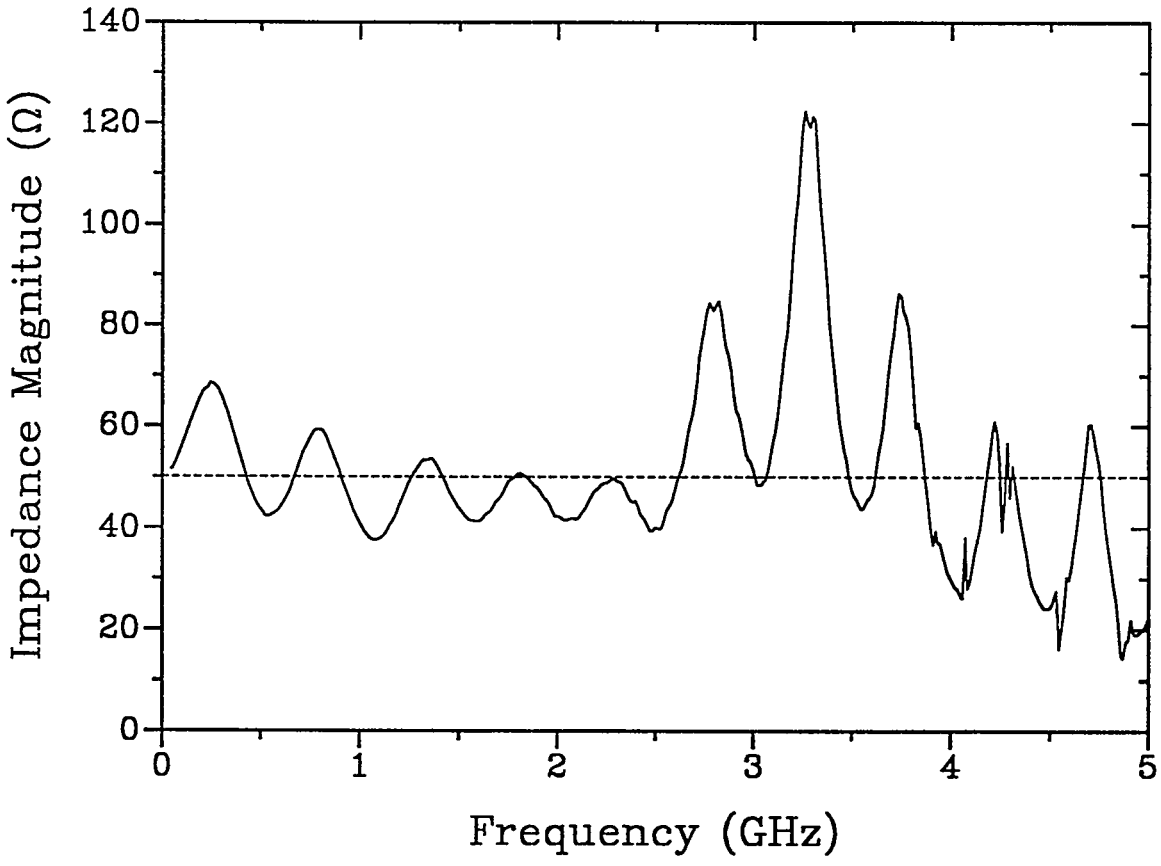

Fig. 12-3. The measured impedance magnitude of the ceramic dielectric transmission cell for frequencies below 5 GHz. The cell HOM cutoff frequency is 3.6 GHz.

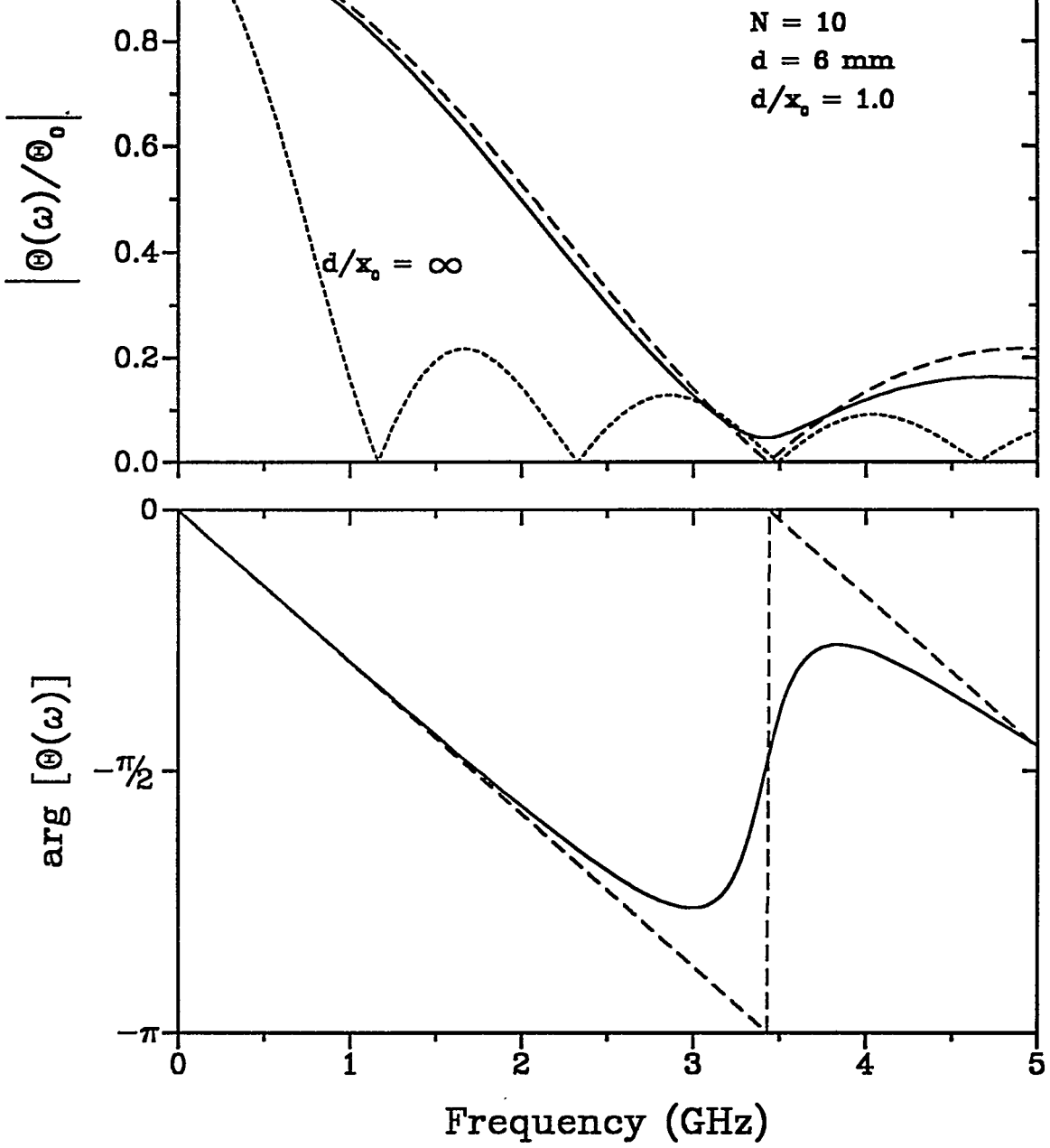

Fig. 12-4. The predicted frequency dependent magnitude (top) and phase (bottom) of the Faraday rotation for a travelling wave current sensor using a ceramic dielectric and an annealed helical fiber coil. The solid curve includes some dielectric dispersion; the dashed curve is for a system with no dielectric dispersion.

solid curves are determined using a model that includes a small amount of dielectric loss in the ceramic. These losses are based on a Debye molecular reorientation model much like the liquid dispersion treated earlier [71]. Typical effects in the Faraday response result from the dielectric dispersion: some loss of bandwidth in the main response lobe, the missing null in the response magnitude, and the lack of maximum phase deviation at the frequency where zero magnitude usually occurs. The fiber coil leads have essentially no affect on the travelling wave sensor response because of their designed configuration. Leads enter and exit the coil from the same direction making the transition to the helical shape over a minimal distance and with a radius of approximately one-half that of the coil. It is intended that the fiber annealing process will adequately remove any linear birefringence in this lead transition region.

The projected sensor bandwidth is approximately 1.45 GHz, with a corresponding bandwidth enhancement factor of 2.8. It appears from Fig. 12-4 that response S/N is large enough at 2.5 GHz that measurements are possible up to this frequency (over the frequency range where the cell has a very good SWR). Estimated value for the sensitivity-bandwidth product for this travelling wave device is 3.85 MHz-°/A, more than three times larger than that of the water-filled travelling wave current sensor. However, this SBP remains a factor of two below that measured for the bulk optic Faraday effect current sensor [30].

Combination Fiber Sensors

It is possible to use the helical fiber coil concept with the noncentered or noncircular, planar fiber coil concept to form a new travelling wave fiber current sensor configuration. The combination allows all of the separately-observed bandwidth and high frequency enhancements for these coil configurations to be utilized in a single sensor. The frequency dependent Faraday response for this combination is found directly from Eq. (3-7). In Chapter 3, two simplifying routes were developed, which led to the

travelling wave coil configurations or the noncentered/noncircular coil configurations. Here no simplifications are made. To illustrate the combination sensor approach, a mathematical model is briefly outlined for a travelling wave fiber coil with a displaced (noncentered) conductor within the coil cross section.

The function [(1/r) cos(γ)] in Eq. (3-7) describes the deviation in the Faraday interaction due to the nonconcentric axes of the current-carrying conductor and the fiber coil. Equation (6-3) for this function is valid for the combination sensor, but with R now representing the mean radial distance from the helical coil axis to any perpendicular point on the fiber, and the time dependence of the angle α now given by

$$\alpha(t) = \frac{c}{n\,R\,\Delta L}\,t \quad , \tag{12-1}$$

where ΔL is defined by Eq. (8-11). Also, the reference angle in Eq. (6-3) is now expressed by $\alpha_0 = c\,t_0 / (n\,R\,\Delta L)$. The phase factor in Eq. (3-7) is modified according to the developments in Chapter 8, leading to the form given in Eq. (8-4). Then an integral expression for the noncentered, travelling wave fiber current sensor is

$$\Theta(\omega) = \Theta_0\,\frac{1}{\tau}\int_0^{\tau}\left[\frac{1 - \left(X_1/R\right)\cos(\alpha+\alpha_0)}{1 + \left(X_1/R\right)^2 - 2\left(X_1/R\right)\cos(\alpha+\alpha_0)}\right] e^{-j\omega t\left[1 - \frac{\sqrt{\varepsilon_r}}{n\pi\sqrt{\left(d/x_0\right)^2 + 1/\pi^2}}\right]}\,dt \quad , \tag{12-2}$$

where τ is now the total transit time of light propagation through the helical fiber coil given by

$$\tau = 2\,\pi R\,N\left(\frac{n}{c}\right)\Delta L \quad . \tag{12-3}$$

The solution to Eq. (12-2) proceeds as followed in Chapter 6 using long division decomposition of the first bracketed factor in the integral. The resulting series is integrated term by term and then simplified to yield an expression similar to Eq. (6-14). The frequency dependent Faraday response for the combination sensor is

$$\Theta(\omega) = \Theta_0 \left[\frac{\sin(\zeta)}{\zeta}\right] e^{-j\zeta} \sum_{m=0}^{\infty} (-1)^{2m\xi} \left(\frac{X_1}{R}\right)^m \left[1 - \left(\frac{mN\pi}{\zeta}\right)^2\right]^{-1}, \quad (12\text{-}4)$$

where ζ is given in Eq. (8-5b) for the travelling wave configurations and ξ is the fraction of the single loop propagation delay taken from Eq. (6-11). Both of these variables are functions of τ as given by Eq. (12-3).

The Faraday response predicted by Eq. (12-4) is simply that determined by Eq. (6-14) for a noncentered, planar coil expanded in the frequency domain to account for the travelling wave interaction. Figure 12-5 shows the predicted response for a two-turn, travelling wave sensor coil with d = 3 cm, $d/x_0 = 1.0$, and $\xi = 0.5$ and with the conductor fully displaced in the coil cross section, $X_1 = R$. The fiber coil is treated as leadless. The displaced conductor creates a response resonance where initially the second null occurs in the centered-coil travelling wave response. This response is identical to the resonant behavior observed for the noncentered, planar coil predictions. The travelling wave characteristics of the sensor coil produce a large bandwidth enhancement (compare the dotted and dashed curves in Fig. 12-5.), and a smaller, but notable, enhancement is created by the nonconcentric axes (dashed and solid curves). From Table 6-1, the BEF of the solid curve should be 5.8% larger. And as discussed in Chapter 6, the small enhancement due to the noncentered coil decreases as the number of fiber turns in the coil increases.

It is obvious from Fig. 12-5 that combining coil manipulation schemes with the travelling wave concept can enhance the high frequency response of the fiber current

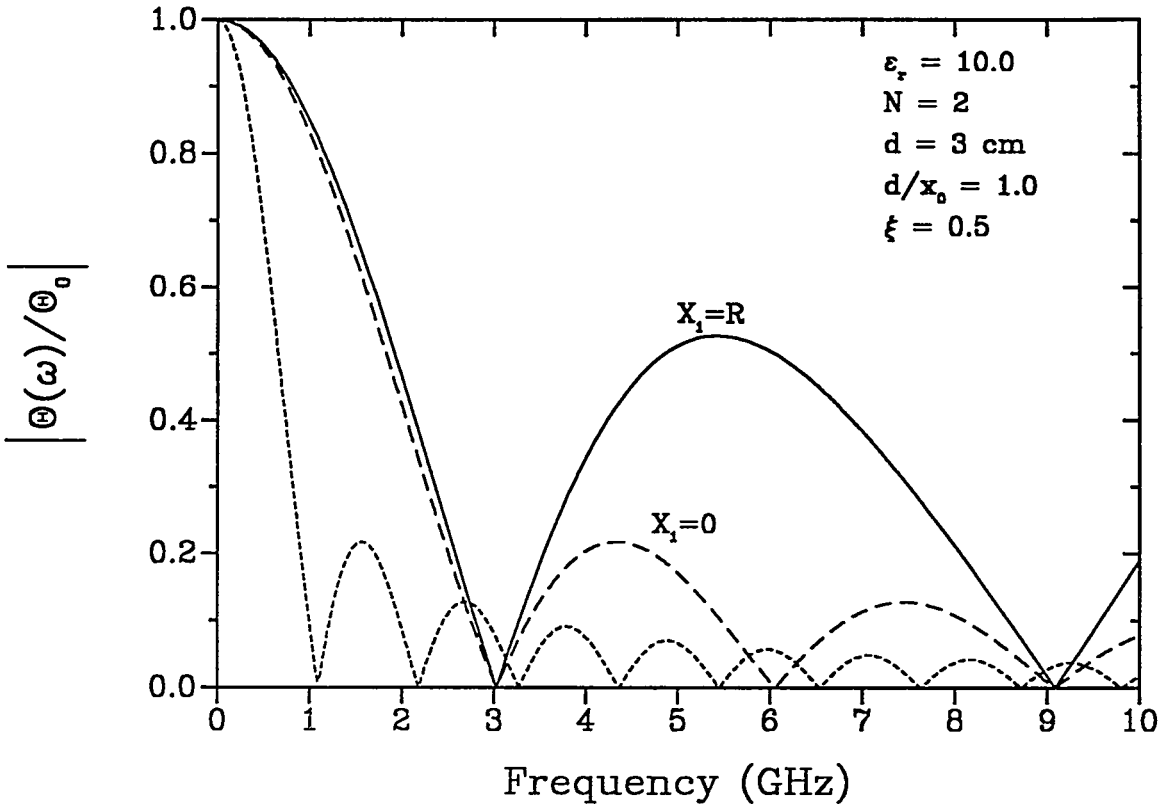

Fig. 12-5. The predicted relative magnitude of the Faraday rotation for a two-turn travelling wave fiber sensor with the current conductor fully displaced in the coil cross section. The dotted curve is the reference response for a centered, planar coil.

sensors. Other combinations of sensing concepts are certainly possible, and mathematical expressions to predict their Faraday response can be developed using the existing theories.

Non-Fiber Configurations

Several travelling wave current sensor configurations that utilize bulk optics or planar waveguides have been formulated. Three of these are discussed here to show options to the helical fiber travelling wave design. Some quantitative information is provided, but most of the discussion is conceptual.

1. Helical Waveguide Sensor

The ceramic dielectric travelling wave current sensor, with an annealed helical coil, offers significant reduction in size and large improvement in the sensitivity-bandwidth product compared to the liquid travelling wave configuration, but absolute Faraday sensitivity still suffers. The only mechanism for improving the static response is to add fiber turns. However, this will increase the length of the transmission cell as further reductions in coil diameter (even using the annealing process) do not appear feasible. A planar waveguide structure fabricated on the surface of a cylindrical substrate could provide the optical propagation medium. Envisioned is a singlemode rib waveguide etched on the surface of a glass or crystal which has a high Verdet constant. Singlemode waveguides are typically a few micrometers in dimension, and such structures have not been demonstrated on other than flat surfaces. A real challenge exists in fabricating such a waveguide, especially in a helical layout. Significant reductions in waveguide helix diameter are possible with this concept.

The terbium-doped borosilicate glass, FR-5, has a Verdet constant that is approximately 20 times larger than that of a silica fiber (see Table 2-1) [39,40]. A waveguide fabricated from this material would significantly improve the Faraday sensitivity of a current sensor. FR-5 glass has a relatively high loss per unit length for a waveguide medium [25], but the total attenuation should be small since the proposed light transit distance is short. If a travelling wave light path is created with a mean diameter of 2 mm, 10 turns and $d/x_0 = 1.0$, the sensor bandwidth is predicted to be ~ 2 GHz. The projected sensitivity-bandwidth product is approximately 106 MHz-°/A. These computations assume a laser wavelength of 633 nm, so that $n = 1.684$ for the FR-5 glass [40], and that the glass medium is the sole dielectric in the coaxial line. An estimate of the relative permittivity of the FR-5 is 5.0 in the 1 MHz to 1 GHz frequency range based on handbook values for similar glasses [76]. If only a thin cylinder of the FR-5 substrate is used along with a higher ε_r ceramic as the remaining dielectric, the

bandwidth can be enhanced even further. Assuming ε_{eff} = 9.0 for the slow-wave structure, the sensor will have a $\Delta B \approx 2.6$ GHz and a SBP = 137.5 MHz-°/A. The waveguide will only be 2 cm long, and the entire device package should not exceed one inch long by half inch in diameter, excluding the RF connectors and the supporting optoelectronics needed for light production and detection.

The challenge of mating miniature lenses, polarizers and optical fiber to the waveguide structure is not addressed here, however, these technologies are becoming quite advanced and should not be a limiting factor. If the complete sensing system can be fabricated and assembled, it would provide milliampere current detection at greater than 100 MHz bandwidth. These figures rival or surpass conventional electrical current monitors [4], with the added advantages afforded by the noninterfering optical techniques.

2. Bulk Optic Sensor

Another prospective travelling wave current sensing technique utilizes a bulk optic Faraday rotator material and reverses the optical and current-carrying paths in the structure. The current passes through a wire solenoid wound around a cylinder of the optical material. Figure 12-6 shows a schematic drawing of the sensor. The magnetic field inside the solenoid is axial and scales linearly with both the current and the number of wire turns. The light is injected along the cylindrical axis of the Faraday material and is codirectional with the magnetic field. Sensitivity of this device can be controlled by varying the wire turns and the choice of optical materials. In this scheme the propagating light will outpace the magnetic field since it travels a shorter path. Bandwidth will depend on phasing between these two signals.

This technique should produce small, yet responsive, current monitors when implemented. As an example, FR-5 glass is selected as the Faraday rotator material and cast in a cylinder 2 mm in diameter and 2 cm long. Forty turns of wire (30 or 32 gauge

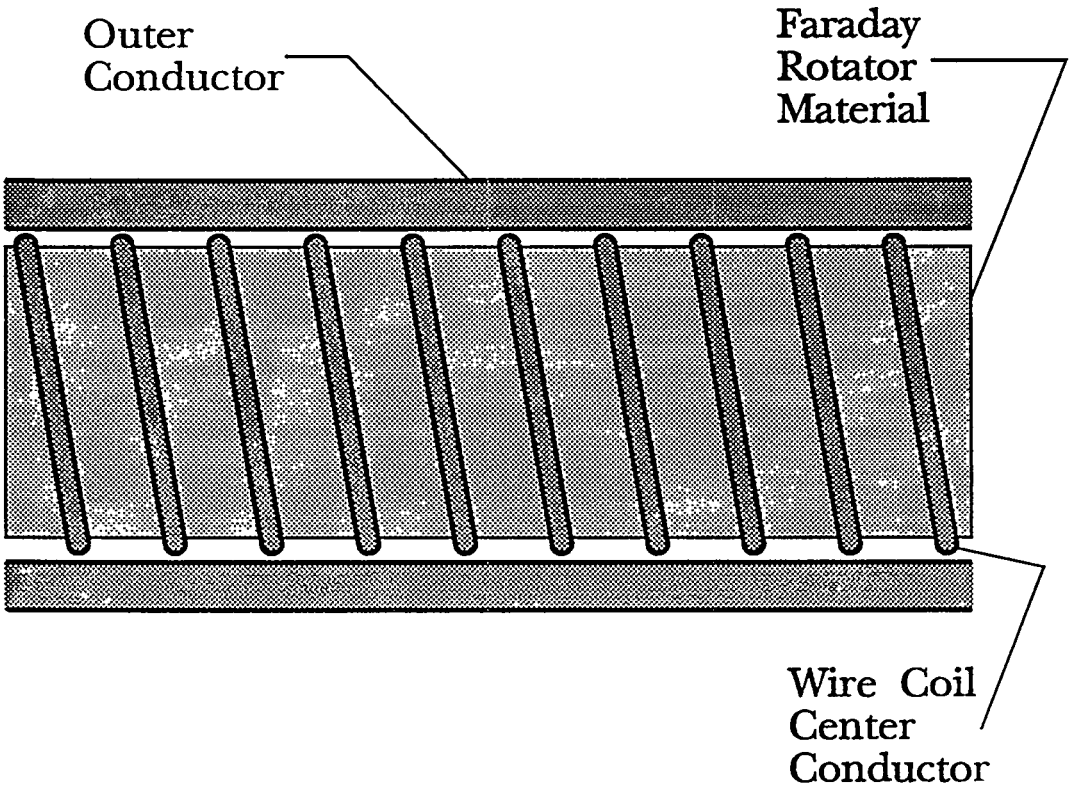

Fig. 12-6. A wideband bulk optic current sensor with a helical wire coil used to generate an axial magnetic field inside a cylindrical piece of Faraday rotator material.

should be small enough, yet capable of handling sufficient current) is wrapped in a helical solenoid around the glass. Because of the helix pitch, 0.5 mm, the magnetic field phase velocity along the solenoid axis is approximately an order of magnitude smaller than that of the propagating light. Consequently, the system 3 dB bandwidth should be limited to approximately 250 MHz. The measurement sensitivity of this device, however, is quite high, with an estimated noise equivalent current at full bandwidth of 0.75 A and a projected sensitivity-bandwidth product of approximately 51 MHz-°/A.

One design difficulty with the wire solenoid is its large reactance at the higher frequencies. Near the sensor 3 dB bandwidth, the inductive reactance exceeds 500 Ω which can limit signal current propagation. By adding distributed capacitance through

use of a transmission line ground plane, this effect is countered [77]. The coaxial line structure shown in Fig. 12-6 is such an implementation. The device characteristic impedance can be returned to 50 Ω by maintaining a spacing of a few mils (~ 0.2 mm) between the solenoid and the outer coaxial conductor. By choosing a thin electrical insulating material such as mylar for the spacer, the relative permittivity is closely matched with that of the FR-5 glass, and the electromagnetic properties of the transmission line are optimized.

3. Planar Waveguide Sensor

A third travelling wave sensor configuration incorporates a serpentine singlemode planar waveguide in the dielectric substrate of an RF stripline. This structure is shown in the schematic of Fig. 12-7. The waveguide is perpendicular as it passes under the RF trace, and the propagating light interacts N times with the magnetic field. Each interaction is over a very short distance so the Faraday response behaves much like that for the delta function interaction described in Chapter 7. Only with this current sensor, the sign of **B**•d**l** changes with each consecutive pass by the conductor. A combination of previously developed techniques and models can be used to predict responses.

The frequency dependent Faraday rotation is determined by introducing the travelling wave phase factor, $\exp[-j\omega t(1 - {}^{v_{light}}/_{v_{ph}})]$ into Eq. (7-4) and accounting for the counter-rotating interactions using $(-1)^m$ in the series. The resulting delta function response has the form

$$\Theta_\delta(\omega) = \Theta_0 \frac{1}{N} \sum_{m=0}^{N-1} (-1)^m e^{-jm\frac{\omega\tau_1}{2}(1-\varsigma')} , \qquad (12\text{-}5)$$

with

$$\tau_1 = \frac{n}{c} L_1 , \qquad (12\text{-}6)$$

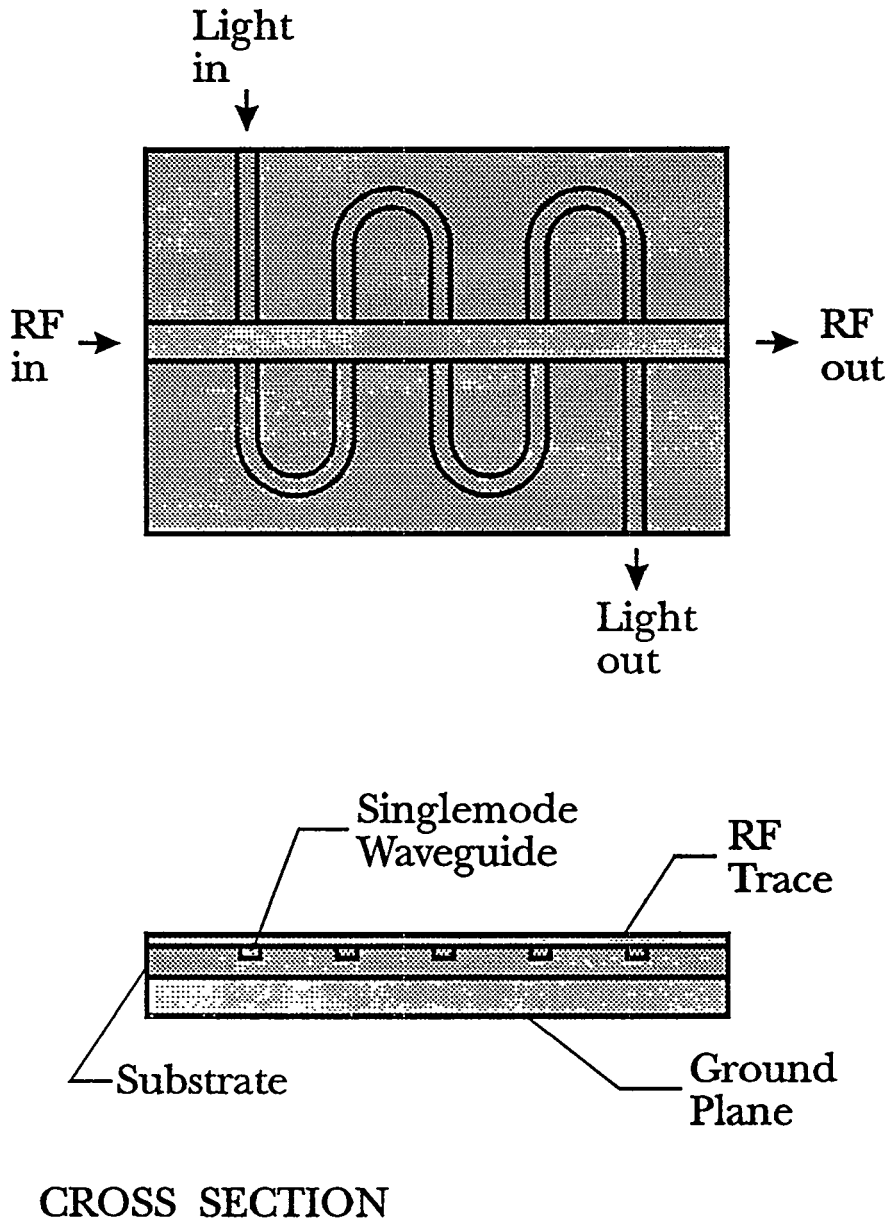

Fig. 12-7. A planar waveguide travelling wave optical current sensor. The waveguide follows a serpentine path that makes several passes by the stripline conductor.

and

$$\varsigma' = \frac{\sqrt{\varepsilon_r}}{n}\frac{x_0}{L_1} \quad , \tag{12-7}$$

where $x_0/2$ is the distance along the stripline between waveguide interactions, and $L_1/2$ is the light propagation distance between interactions. In Eq. (12-5) any arbitrary phase delays between the light and the magnetic field have been ignored.

The response predicted by Eq. (12-5) is unique in that it depends on N being even or odd and the degree of travelling wave phase matching. At the low frequencies, $\omega \rightarrow 0$, the relative response is

$$\frac{\Theta_\delta(0)}{\Theta_0} = \frac{1}{N}\sum_{m=0}^{N-1}(-1)^m = \begin{cases} 0 & \text{if N is even} \\ \dfrac{1}{N} & \text{if N is odd} \end{cases} . \tag{12-8}$$

The maximum relative response, Θ_0, is not attained at the low frequencies (unless N = 1) since every second pass of the light by the conductor negates the response of the previous pass. Maximum response will involve all N interactions and is given by

$$\Theta_0 = N V B \ell \quad , \tag{12-9}$$

where ℓ is the short interaction length between the light and the field as the waveguide passes near the RF conductor.

Equation (12-8) also describes the Faraday response for perfect phase matching between the two propagating signals. When the travelling wave condition is met, $\varsigma' = 1$, and the phase factor in Eq. (12-5) is again equal to one. Thus, under ideal travelling wave conditions and with N odd, the response magnitude is 1/N for all frequencies. This

implies that optimum sensors with near perfect phase matching only require that N = 1.

For less than perfect phase matching, the sensor Faraday response exhibits resonances, as seen previously for the delta function interactions. In Fig. 12-8 the response relative magnitude is plotted versus the normalized frequency, $\omega\tau_1/2$, for a waveguide device making three passes by the conductor. The use of the normalized frequency for the plot abscissa removes structure dimensions from the computations and presents the response in a form consistent with those in Chapter 7. The degree of phase matching is quite important in determining the frequency responses shown in Fig. 12-8.

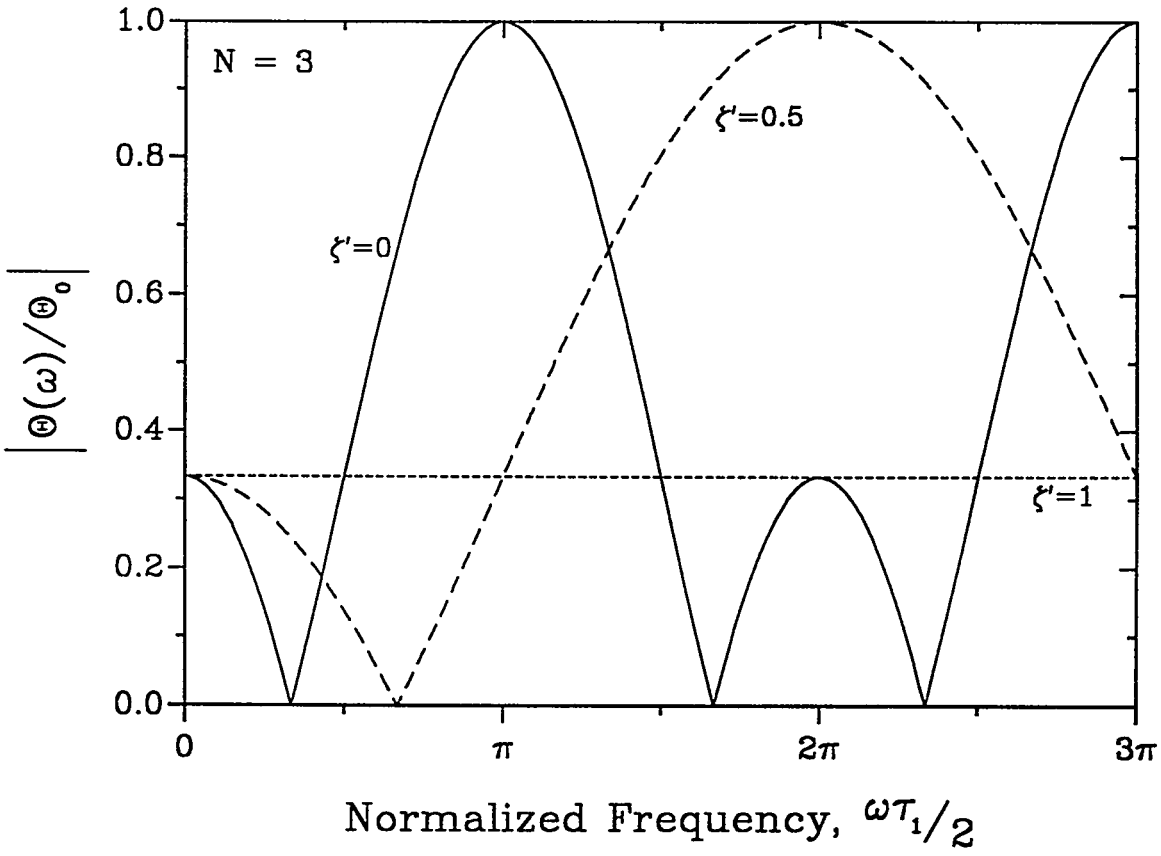

Fig. 12-8. The predicted relative magnitude of the Faraday rotation for the planar waveguide travelling wave current sensor. The waveguide makes three passes under the RF trace. Three phase matching conditions are shown: none ($\varsigma' = 0$), intermediate ($\varsigma' = 0.5$) and perfect ($\varsigma' = 1$).

Resonance maxima occur when

$$\frac{\omega \tau_1}{2}(1 - \varsigma') = (2m' + 1)\pi, \quad m' = 0, 1, 2, \ldots \quad . \tag{12-10}$$

The frequency dependence of the maxima on N is removed since the transit time τ_1 is used. But the number of nulls occurring between the response peaks is N - 1. For frequencies below the first maxima, there are ½(N - 1) nulls if N is odd and $N/2$ nulls (including the one at zero frequency) if N is even. Also, the bandwidth of the high frequency resonances is determined by the total transit time $\tau = N(\tau_1/2)$. If the number of waveguide passes under the stripline gets quite large, $N \rightarrow \infty$, the response becomes concentrated at frequencies near resonance, approaching zero relative magnitude between the maxima.

One of the advantages of this planar waveguide current sensor is its large narrowband, high frequency response. By tailoring the device parameters, these high frequency bands can be utilized. (As discussed in Chapter 7, the resonant response does not continue to infinity but is bound by an enveloping function that depends only on the interaction length ℓ.) As an example, the characteristics of a practical waveguide sensor are estimated. The example device uses a substrate material 0.5 mm thick with a relative permittivity of 5.0. The singlemode waveguide has a refractive index of 1.68 (FR-5 glass) and makes five passes by the conductor, every 1 cm along the light path and every 2.5 mm along the current path ($x_0/L_1 = 0.25$). The 50 Ω stripline has a trace width of ~ 1.7 mm. An estimate of the magnetic flux density along the light path at each interaction point is $B \approx 0.0025$ T/A, which produces a peak Faraday rotation of $\Theta_0 =$ 0.087 °/A. The static rotation is 1/5 this value or 0.017 °/A. Frequency parameters are quite impressive: the first null in the response curve occurs at 2.68 GHz, the first resonance maximum with relative magnitude of one occurs at 13.4 GHz, and the

resonance response bandwidth is 2.37 GHz. The bandwidth of the lowest frequency response lobe is approximately 1.2 GHz. As a comparative measure, the SBP for this device is only 20.4 MHz-°/A at low frequencies, but has an SBP of 204 MHz-°/A, or ten times larger, in the resonance frequency band.

CHAPTER 13

CONCLUSIONS

A thorough investigation has been made of the high frequency response of planar and travelling wave Faraday effect optical fiber current sensors. Several models have been developed that provide excellent response predictions for fiber coils in a variety of sensor configurations. Measurements of the magnitude of the high frequency response for the sensors verify many of the model predictions. Thus, some unique Faraday effect current sensors have been demonstrated and reported for the first time as a result of this study.

Three basic configurations of planar coil fiber current sensors were explored: circular cross section coils with coincident coil and conductor axes; circular coils with the conductor displaced from the coil axis; and noncircular and highly elongated coils with the conductor centered or fully displaced in the coil cross section. Travelling wave current sensors were also explored. They consisted of helical fiber coils with constant diameter immersed in the dielectric of a coaxial transmission line. Both air and liquid dielectrics were used in these transmission lines. Both groups of current sensors, planar and travelling wave, required the development of coaxial transmission test cells [34] to properly characterize the fiber coils at high frequencies (up to 1 GHz).

Planar fiber current sensors with a circular coil cross section and concentric coil/conductor axes have an easily predictable high frequency response determined by light transit time in the fiber. Many measurements were made with coils of varying radii and numbers of turns to demonstrate this concept. All tests extended in frequency beyond the cutoff frequency of the sensors and, in some cases, covered several of the higher frequency response lobes. Of particular interest in this sensor category were measurements using a 20 turn, 6.4 mm diameter coil which had been annealed to remove bend-induced linear birefringence [21,22]. This sensor has a bandwidth of 229 MHz and

a sensitivity-bandwidth product estimated at 0.8 MHz-°/A. The measurements on this sensor verified that the annealing process can successfully be used to manufacture small radii coils with improved sensitivity-bandwidth products and without the detrimental birefringence effects.

Important in the correct modeling of the frequency dependence of fiber current sensors are the effects of leads. They add to the total length of fiber that the light must traverse and can result in reduced detection bandwidths. In some configurations, the fiber leads add an effective half turn to the coil length, which significantly alters high frequency response, especially for coils with small numbers of turns.

Noncentered and noncircular planar coils used as fiber sensors exhibit resonances in their high frequency response. Resonance magnitudes are dependent on the displacement distance between the coil and conductor axes and the eccentricity of the coil cross section. Spacing of the resonance frequencies depends on the length of fiber in a single coil turn. This type of response at the higher frequencies is compared to similar responses that occur in tapped and recirculating fiber delay line devices [64,65]. To aid in the characterization of the high frequency Faraday rotation for a coil with a highly elongated cross section and the conductor at maximum displacement, a delta function model was introduced. This model is based on a point interaction between the magnetic field and the light, and it provides an excellent theoretical framework for building frequency response functions for sensors that exhibit bounded resonant behavior. A rectangular cross section coil model was used to predict the frequency response for sensors with arbitrary coil cross section and with arbitrary placement of the conductor within the coil. A connection between the noncentered, circular coil and the highly elongated coil was provided by the rectangular coil model as it allowed for varying eccentricity of the cross section. One additionally interesting feature is that resonant responses at high frequencies occur for fiber current sensors with the conductor outside the coil cross section, even when such response is prohibited at the low frequencies as

described by Ampere's law.

Single-turn and few-turn planar fiber coils exhibit sensor 3 dB bandwidths that are significantly affected by coil configuration. The maximum bandwidth for these sensors is realized for a highly elongated, one-turn coil (a delta function interaction); ideally the bandwidth approaches infinity. Light entry point into the single-turn, circular coil can create a factor of two difference in response bandwidth when the conductor is fully displaced in the coil cross section. If light enters away from the radial conductor offset, a large (~ 50%) bandwidth increase is observed compared to the centered coil; if light enters nearest the conductor, a significant loss (~ 29%) in bandwidth occurs. Bandwidth increases in single or few-turn coils are further enhanced by increasing the eccentricity of the coil cross section. Using the delta function response model, a two-turn coil will exhibit a 13% increase in bandwidth. These bandwidth deviations become less significant as the number of coil turns increases, regardless of the coil configuration. For multiturn coils with $N \gtrsim 10$, all fiber sensor bandwidths converge to that of the simple circular, centered coil, Eq. (5-7). This simplifies current sensor coil design, especially for those applications where the frequency range of interest lies below the main lobe 3 dB bandwidth.

The travelling wave configurations show that increases in bandwidth are possible for fiber current sensors without a loss in detection sensitivity. By distributing the fiber coil and slowing the propagation of the magnetic wave, improved phase matching occurs. Bandwidth enhancement is a function of the helical coil diameter-to-pitch ratio and the relative permittivity of the transmission line dielectric. Under ideal conditions, a configuration exists where, theoretically, a near-infinite bandwidth could occur. Realistically, such a large bandwidth is not possible, but enhancement factors of approximately 10 (compared to an equivalent planar coil) appear achievable.

Transmission test cells filled with liquid provided the slow-wave structures for travelling wave sensor experimental measurements. Liquids were chosen as coaxial line

dielectrics because they have large relative permittivities and can easily fill the volume of the cell around the fiber sensor. However, liquids also exhibit significant dielectric dispersion at the higher frequencies [71] and require other structures to support the fiber coil within the cell. These properties can severely limit the system bandwidth. Extended mathematical models of the travelling wave current sensor have been developed that account for many of the properties of the transmission cell structures [75]. In addition to liquid dispersion, the models include waveguide dispersion of the lowest-order TM mode in the transmission line, an effective relative permittivity due to the teflon support structures, and effects from excess lead length used in a non-travelling configuration. The models only consider a single EM mode in the coaxial line and assume that mode has quasi-TEM characteristics. In most cases the extended models showed excellent agreement with the experimental results.

Three liquids — 1-propanol, methanol and water — were used in the test cells. Their progressively larger relative permittivities — 20.1, 32.6, and 78.5, respectively at 25°C — created sensor systems with increasingly larger bandwidth for a given helical coil structure. Comparative tests with a helical coil in a coaxial airline indicated that merely distributing the coil provides minimal bandwidth enhancement (maximum of 1.37); slow-wave mechanisms are needed for further phase matching. The largest bandwidth recorded during experimentation was approximately 300 MHz for a water-filled cell and a 14-turn helical fiber coil with 3 cm diameter and 3 cm pitch. This sensor has a bandwidth enhancement factor of ~ 4.1 when compared to a 14-turn, 3 cm planar coil. Its estimated sensitivity-bandwidth product is 1.06 MHz-°/A, the largest SBP measured to date for a fiber current sensor.

Models of the travelling wave fiber sensor configurations predict that high frequency response will be limited in liquid-filled devices. Large bandwidth enhancements or higher frequency operation will require solid dielectric slow-wave structures in combination with annealed fiber coils or helical waveguides. Predictions

for such systems indicate that bandwidths greater than 2 GHz and SBPs greater than 100 MHz-°/A are possible. In addition to enhanced performance, these devices will also significantly reduce sensor size. Other non-fiber travelling wave sensor configurations may ultimately prove to be more sensitive in given current monitoring applications. A proposed planar waveguide travelling wave sensor fabricated in an RF stripline shows excellent response potential. With proper selection of Faraday rotator materials for the waveguide and with optimum serpentine path design, enhanced high frequency operation is predicted well into the microwave region with SBPs as large as 200 MHz-°/A.

In summary, this work has explored the theoretical and experimental high frequency characteristics of Faraday effect fiber current sensors. Detailed quantitative analyses of the frequency responses of planar and travelling wave sensor configurations are now possible. High frequency response functions depend on several properties of the fiber coil and the transmission medium surrounding the coil. Sensor bandwidth can be enhanced through careful travelling wave fiber design or through selected use of few-turn noncentered and elongated fiber coils. Narrowband, high frequency resonant enhancement is produced through proper design with the noncentered or noncircular fiber coils. Measurements have been performed at frequencies that extend into the microwave region with 1 GHz being the maximum used. All of the experiments explore high frequency regions (usually above the 3 dB bandwidth) not previously considered for sensitive, Faraday effect fiber current sensors. Many of the sensors show adequate S/N and characterizable responses in these regions. Models of the sensor systems have allowed further investigations of potential response in these high frequency regions. Thus, it appears feasible to fabricate current sensors from optical fibers (or optical waveguides) that have a wider bandwidth or higher frequency detection capability than conventional current probes.

APPENDIX A

EXPANDED COAXIAL TRANSMISSION CELLS

Expanded coaxial transmission cells have been developed to provide a known electromagnetic environment for the testing of optical fiber current sensor coils [34]. These structures are the coaxial analog to the rectangular transverse electromagnetic (TEM) cells that are used extensively in RF testing [78,79]. Large working volumes are characteristic of the transmission cells, able to contain sizable test objects with minimal perturbation of the impinging TEM wave. The coaxial cell geometry is ideal for experimentation with optical fiber coils that measure conducted RF currents; the known modal properties and impedances make it easy to relate current to power at frequencies well into the microwave region.

Coaxial Line Properties

The waveguide theory for an ideal coaxial cable is well developed [73,80], but it is repeated in a brief format here to highlight some of the useful properties and to provide a reference for later theoretical developments.

The fields inside the dielectric medium of a coaxial line (see Fig. A-1) with center conductor radius $\rho = a$ and outer conductor radius $\rho = b$ can be divided into transverse magnetic (TM) and transverse electric (TE) components. The TM components of the electric and magnetic field are given by

$$E_z = u^2 \left[A J_m(u\rho) + B Y_m(u\rho) \right] \cos(m\phi) \quad , \tag{A-1a}$$

$$H_\phi = \frac{j\omega\varepsilon}{\beta} E_\rho = -\frac{jk^2}{\mu\omega} \left[A \frac{\partial}{\partial\rho} J_m(u\rho) + B \frac{\partial}{\partial\rho} Y_m(u\rho) \right] \cos(m\phi) \quad , \tag{A-1b}$$

and

$$E_\phi = -\frac{j\omega\varepsilon}{\beta}H_\rho = \frac{m\beta}{\rho}\left[A\,J_m(u\rho) + B\,Y_m(u\rho)\right]\sin(m\phi) \quad . \qquad \text{(A-1c)}$$

The TE field components are given by

$$H_z = u^2\left[C\,J_m(u\rho) + D\,Y_m(u\rho)\right]\cos(m\phi) \quad , \qquad \text{(A-2a)}$$

$$E_\phi = -\frac{j\omega\mu}{\beta}H_\rho = j\mu\omega\left[C\frac{\partial}{\partial\rho}J_m(u\rho) + D\frac{\partial}{\partial\rho}Y_m(u\rho)\right]\cos(m\phi) \quad , \qquad \text{(A-2b)}$$

and

$$H_\phi = \frac{j\omega\mu}{\beta}E_\rho = \frac{m\beta}{\rho}\left[C\,J_m(u\rho) + D\,Y_m(u\rho)\right]\sin(m\phi) \quad . \qquad \text{(A-2c)}$$

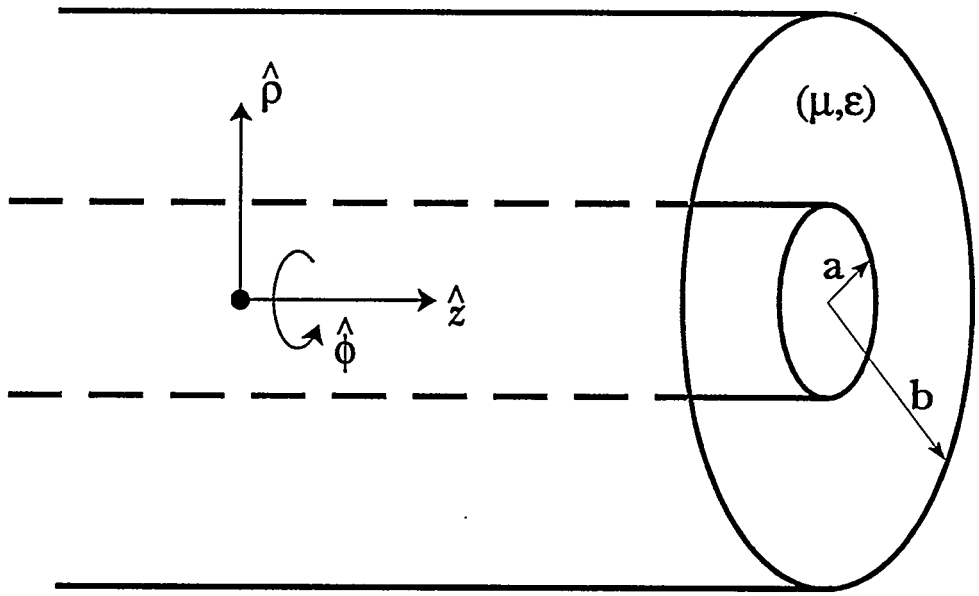

Fig. A-1. The geometry of a coaxial transmission line. A dielectric medium with permeability μ and permittivity ε fills the volume between cylindrical conductors of radius a and b. The cylindrical coordinates (ρ, ϕ, z) as indicated are used for computations.

For brevity, the common phase factor $e^{-\beta z + j\omega t}$ is omitted from all the components in Eqs. (A-1) and (A-2). Here

$$u^2 = k^2 + \beta^2 \quad , \tag{A-3}$$

with

$$k^2 = \mu\varepsilon\omega^2 \, , \tag{A-4}$$

and β the wave propagation constant. The coefficients A, B, C, and D are arbitrary constants, and $J_m(u\rho)$ and $Y_m(u\rho)$ are Bessel functions of order m of the first and second kind, respectively. If the coax has infinitely conducting walls, the tangential components of the electric field vanish at both $\rho = a$ and $\rho = b$. This leads to two eigenvalue equations describing the TM and TE modes:

$$\frac{Y_m(ua)}{J_m(ua)} = \frac{Y_m(ub)}{J_m(ub)} \quad , \tag{A-5}$$

for the TM modes, and

$$\frac{Y'_m(ua)}{J'_m(ua)} = \frac{Y'_m(ub)}{J'_m(ub)} \quad , \tag{A-6}$$

for the TE modes. The primes in Eq. (A-6) denote differentiation with respect to ρ.

The lowest order mode in the ideal coaxial line is both TE and TM or TEM; this requires that $E_z = H_z = 0$ for all ρ. Using Eqs. (A-1a) and (A-2a), these conditions are satisfied only if $u^2 = 0$. Then $\beta = jk$, and the TEM wave propagates with a phase velocity given by

$$v_{ph} = \frac{\omega}{k} = \frac{1}{\sqrt{\mu\varepsilon}} \quad , \tag{A-7}$$

which is the speed of light in the dielectric medium. The TEM mode is azimuthally symmetric (m = 0), and its two transverse field components can be derived from Eq. (A-1b). They are given by

$$H_\phi = \frac{E_\rho}{\eta} = \frac{i}{2\pi\rho} \quad , \tag{A-8}$$

where

$$\eta = \sqrt{\frac{\mu}{\varepsilon}} \tag{A-9}$$

is the wave impedance and i is the conducted current. The characteristic impedance of the TEM mode is

$$Z_0 = \frac{\eta}{2\pi} \ln\left(b/a\right) \quad . \tag{A-10}$$

For a dielectric medium containing no magnetic materials, $\mu = \mu_0$, and with a relative permittivity, $\varepsilon_r = \varepsilon/\varepsilon_0$, Eq. (A-10) becomes

$$Z_0 \approx \frac{60}{\sqrt{\varepsilon_r}} \ln\left(b/a\right) \quad . \tag{A-11}$$

Equations (A-5) and (A-6) provide for an infinite number of real solutions for u for a given order m of the Bessel functions. The propagation constants identifying these modes are given by

$$\beta_{mn} = j\sqrt{k^2 - u_{mn}^2} \quad , \quad m = 0,1,2,\ldots \quad , \quad n = 1,2,3,\ldots \quad . \tag{A-12}$$

These satisfy the condition that $\beta^2 < 0$ for all propagating modes within the coaxial line.

The second lowest mode in the typical ideal coaxial line is the TE_{11} mode. It has an approximate cutoff frequency described by [80]

$$f_c \approx \frac{c}{\pi(a + b)\sqrt{\varepsilon_r}} \quad , \tag{A-13}$$

for a dielectric with $\mu = \mu_0$. Equation (A-13) approximates the cutoff at a point where the modulation half-wavelength equals the circumference of a circle midway between $\rho = a$ and $\rho = b$.

Coaxial transmission lines experience some attenuation due to conductor and dielectric losses. Contrary to the boundary condition originally stated, the metal coax walls are not infinitely conducting, but have a conductivity, σ. The propagating wave penetrates into the conductors as defined by the skin depth

$$\delta' = \sqrt{\frac{2}{\omega\sigma\mu}} \quad . \tag{A-14}$$

The conductor losses of the coaxial line given in dB per unit length are [80]

$$\alpha_c = 13.6 \frac{\delta'\mu}{\lambda} \frac{1}{b} \left(1 + \frac{b}{a}\right) \frac{\sqrt{\varepsilon_r}}{\ln\left(b/a\right)} \quad , \tag{A-15}$$

where λ is the free space wavelength.

Dielectric losses arise from the finite time of molecular reorientation in the insulating materials [71]. Absorption is treated mathematically by assuming a complex relative permittivity

$$\varepsilon_r = \varepsilon' + j\varepsilon'' \quad . \tag{A-16}$$

Since the waveguide propagation constant is expressed as

$$\beta = jk = j\omega\sqrt{\mu\varepsilon} \quad , \tag{A-17}$$

an attenuation factor results from the imaginary part of k, while the real component gives rise to the material dispersion. An expression for the dielectric loss given in dB per unit length is [80]

$$\alpha_D = 27.3\frac{\sqrt{\varepsilon_r}}{\lambda}\tan\delta \quad , \tag{A-18}$$

where

$$\tan\delta = \frac{\varepsilon''}{\varepsilon'} \tag{A-19}$$

is the loss tangent published in the handbooks for many dielectric materials.

Another useful property of coaxial lines is the maximum power-handling capability. This property is based on the dielectric standoff or breakdown electric field, E_m. The maximum power, in Watts, is given by

$$P_{max} = \frac{E_m^2\, b^2}{60}\frac{\ln\left(b/a\right)}{\left(b/a\right)^2} \quad . \tag{A-20}$$

As a reference, the breakdown electric field for air is ~ 30 kV/cm.

Coaxial Airlines

The design of expanded coaxial airlines is straightforward; most are intended for use with 50 Ω RF test instrumentation. If $Z_0 = 50$ is substituted into Eq. (A-11), the airline design requires that b/a = 2.301. Equation (A-13) for the higher order mode

(HOM) cutoff frequency then simplifies to $f_c \approx 2.89/a$ GHz, if the center conductor radius is given in cm. For a desired HOM cutoff frequency in the cell design, the remaining geometric parameters can be determined. If a given working volume size is desired for testing a fiber coil, the TEM mode parameters can be computed.

A transition region in the cells is necessary to expand the radial dimensions from the input and output connectors to a reasonably large working volume. This is accomplished using tapered conical conducting sections. Conical launchers for coaxial transmission lines are common, and the impedance and field matching conditions required for geometrical transitions have been well studied [81]. The characteristic line impedance for the TEM mode in the tapered section is given by

$$Z_0 = \frac{\eta}{2\pi} \ln\left[\frac{\tan\left(\theta_2/2\right)}{\tan\left(\theta_1/2\right)}\right] , \qquad \text{(A-21)}$$

where θ_1 and θ_2 are the taper angles of the center and outer conductors. If the angles are kept small, Eq. (A-21) reduces to Eq. (A-10) for a coaxial line of the appropriate geometry. Subsequently, cell design can be simplified by allowing the conductor radii ratio to be 2.3 throughout the cell length, even in the conical region. For an airline, this cylindrical-geometry-only approach can be used quite effectively to large taper angles. If θ_2 does not exceed 45°, the characteristic impedance of the conical transition deviates less than 5% from 50 Ω.

Long tapered transition regions for the coaxial cells ensure good impedance matching in the lines; however, all field disturbances cannot be avoided at the geometrical discontinuities. At the discontinuities, the spherical wavefront of the conical section must make the transition to the cylindrical wavefront (planar) of the coax section [81]. Cell higher order modes are excited at the discontinuities, but they are

evanescent, carrying no energy and dying out rapidly. Attenuation to HOM propagation at the frequencies, f, near cutoff is given in dB per unit length by [80]

$$\alpha_m = 54.6 \frac{f_c}{c} \sqrt{1 - \left(f/f_c\right)^2} \quad . \tag{A-22}$$

The effective cell bandwidths and the proximity of the fiber optic test coils in the working volume to the transition discontinuities can be determined from Eq. (A-22).

Three expanded airlines were designed and fabricated for testing of fiber current sensor coils. Table A-1 gives the dimensions and the HOM cutoff frequency for each airline. Each cell was machined from brass because of its workability, high electrical conductivity, and its relatively high chemical resistance. The cells were disassembled at mating joints for ease of placement of the fiber coils in the working volume. Polyurethane foam was used for all supports inside the cells, including most of the mandrels onto which the optical fiber coils were wound. The relative permittivity of the foam is ~ 1.15, which can perturb the cell impedance as much as 4.5 Ω from its nominally 50 Ω value. Use of the foam supports was thus limited to absolute minimum for operation.

All losses in the coaxial airlines are quite small: dielectric loss is insignificant, and the conductor loss for the brass in dB per unit length is

$$\alpha_c = 2.25 \times 10^{-8} \frac{\sqrt{f}}{b} \quad . \tag{A-23}$$

For a frequency of 1 GHz and a minimum value of b = 0.49 cm at the cell connector transitions, this attenuation is only 0.0015 dB/cm. The maximum power handling capability of the airlines is $P_{max} \approx 2.36\ b^2$ Megawatts if b is expressed in cm. Again for the minimum value of b at the connector transitions, $P_{max} > 500$ kW.

The airline cell working volumes are of sufficient length to allow HOMs created at the transition discontinuities to be well damped. For the existing designs, Eq. (A-22)

Table A-1.

Expanded Coaxial Airline Cells

Cell Property	Cell #1	Cell #2	Cell #3
	[dimensions given in inches and (cm)]		
Cell outer dimensions			
Total length	18.000 (45.72)	24.000 (60.96)	6.000 (15.24)
Cell Diameter	5.500 (13.97)	2.500 (6.35)	1.300 (3.30)
Outer conductor dimensions			
Center section length	6.000 (15.24)	18.000 (45.72)	4.820 (12.24)
Center section diameter	5.240 (13.31)	2.260 (5.74)	0.384 (0.98)
End section length	5.410 (13.74)	2.410 (6.12)	——
End section diameter at connector	0.384 (0.98)	0.384 (0.98)	——
End section taper angle	26.86 °	23.63 °	no taper
Inner conductor dimensions			
Center section length	6.000 (15.24)	18.000 (45.72)	4.820 (12.24)
Center section diameter	2.280 (5.79)	0.980 (2.49)	0.167 (0.42)
End section length	5.410 (13.74)	2.410 (6.12)	——
End section diameter at connector	0.167 (0.42)	0.167 (0.42)	——
End section taper angle	12.28 °	10.64 °	no taper
HOM cutoff frequency	1.00 GHz	2.32 GHz	13.65 GHz

becomes

$$\alpha_m = \frac{12.1}{b}\sqrt{1 - \left(\frac{f}{f_c}\right)^2} \quad , \tag{A-24}$$

with dimensions of dB per unit length. For the largest outer conductor radius, b = 6.66 cm, evanescent modes are attenuated 1.2 dB/cm at a frequency, f = 0.75 f_c. Depending on the perturbations created by the fiber coils inside the cell, operations to greater than 80% of the HOM cutoff frequency are predicted for all airlines.

The exact, useful operating ranges are established through experimental performance verification. Part of the evaluation criteria comes through measurement of basic properties of the cell using automatic network analysis. The transmission (S_{21}) and reflection (S_{11}) scattering parameters, both magnitude and phase, are collected for the cells in their final configurations. Along with these parameters the standing wave ratio (SWR) and the device impedance are computed from

$$SWR = \frac{1 + |S_{11}|}{1 - |S_{11}|} \quad , \tag{A-25}$$

and

$$Z = Z_0 \frac{1 + S_{11}}{1 - S_{11}} \quad , \tag{A-26}$$

where Z, Z_0, and S_{11} are complex quantities. Ample information is provided from these electromagnetic characterizations to determine the range of useful frequencies for the testing of fiber sensor coils.

APPENDIX B

EXACT TREATMENT OF FIBER COIL LEADS

The fiber leads on a Faraday effect current sensor coil can significantly change the high frequency characteristics of the sensor response function. Each lead adds to the total fiber length in the coil, reducing the sensor bandwidth. More importantly, the position of the fiber leads creates a complex phase interaction between the propagating light in the fiber and the oscillating magnetic field signal. This produces deviations in the Faraday rotation from the simple response function for the centered, circular coil as described by Eq. (5-2).

Lead Effect Model

A simple model for a fiber coil lead is developed to allow for an analytical investigation of the effect on sensor response. As illustrated in Fig. B-1, the coil lead is treated as a constant radius arc of optical fiber originating a distance X from the coil edge and ending at a point on the coil proper tangent to its curvature. Beyond the distance X, the fiber lead is assumed perpendicular to the magnetic field and no Faraday interaction occurs ($\mathbf{B} \cdot d\mathbf{l} = 0$). The formulation in chapter 3 is used to derive the frequency dependent Faraday rotation for the fiber lead, $\Theta_1(\omega)$. Starting with Eq. (3-4), the angle ψ is set to zero and integration occurs only over the fiber lead length, ℓ_1, the distance between points 0 and 1 in Fig. B-1. The Faraday rotation is then

$$\Theta_1(\omega) = V \frac{\mu_f i}{2\pi} \int_0^{\ell_1} \frac{\cos\gamma}{r} \, e^{-j\omega t} \, dl \, . \qquad \text{(B-1)}$$

Since both γ and r depend on the position of the light in the fiber lead, both remain as part of the integrand. Changing the integral to one over time yields the expression

$$\Theta_1(\omega) = V \frac{\mu_f i}{2\pi} \left(\frac{n}{c}\right) \int_0^{t_1} \frac{\cos[\gamma(t)]}{r(t)} \; e^{-j\omega t} \; dt \;, \tag{B-2}$$

where t_1 is the light transit time through the lead section.

From the geometry in Fig. B-1, the following properties are derived:

$$\gamma = \alpha' + \beta' \;, \tag{B-3}$$

$$\sin\alpha' = \frac{R_1}{r} \sin\beta' \;, \tag{B-4}$$

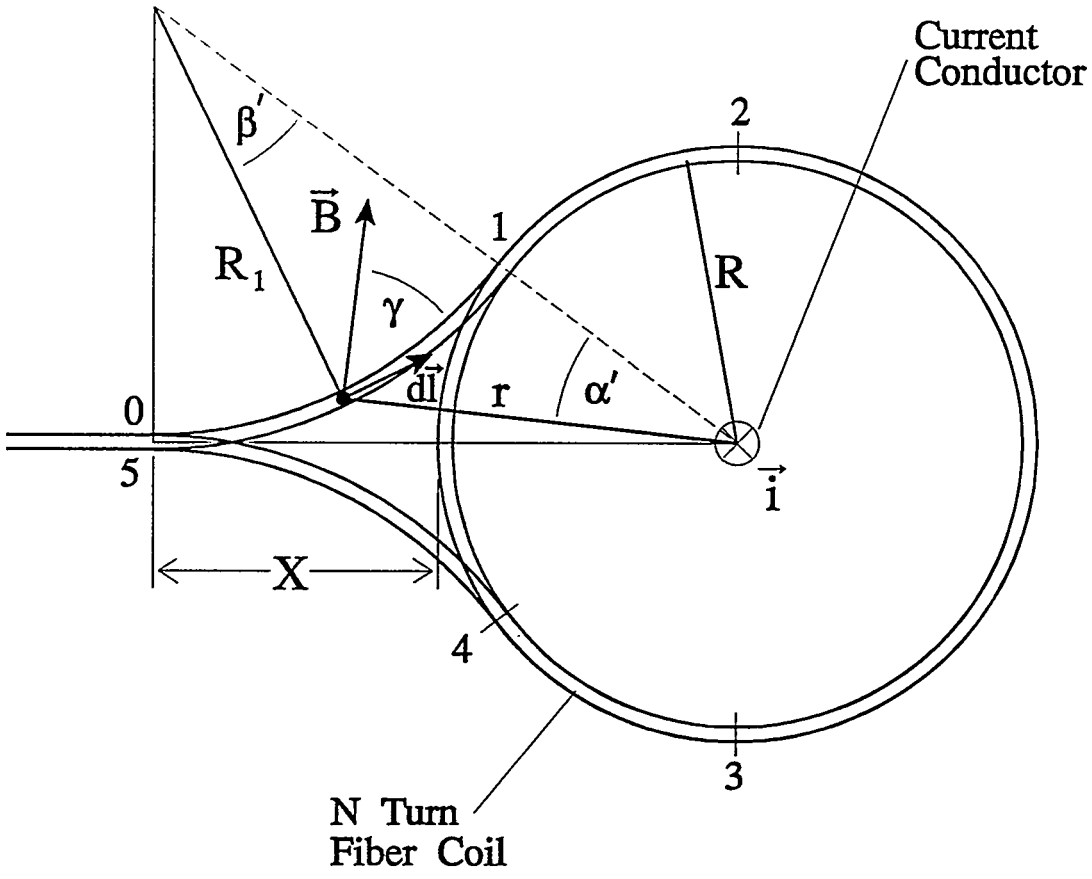

Fig. B-1. A geometrical model of the fiber leads on a current sensor coil.

$$r^2 = (R + R_1)^2 + R_1^2 - 2R_1(R + R_1)\cos\beta' \quad , \tag{B-5}$$

$$R_1 = \frac{X^2}{2R} + X \quad , \tag{B-6}$$

and

$$\beta'_{max} = \tan^{-1}\left(\frac{1 + R/X}{1 + X/2R}\right) \quad . \tag{B-7}$$

The relationships between the angles and the light propagation times are

$$t_1 = \frac{nR_1}{c}\,\beta'_{max} \quad , \tag{B-8}$$

and

$$\beta'(t) = \frac{c}{nR_1}\,(t_1 - t) \quad . \tag{B-9}$$

A time dependent function for r is constructed from Eqs. (B-5) and (B-9):

$$r(t) = \sqrt{(R + R_1)^2 + R_1^2 - 2R_1(R + R_1)\cos\left[\frac{c}{nR_1}\,(t_1 - t)\right]} \quad . \tag{B-10}$$

A similar expression for γ is derived from Eqs. (B-3), (B-4), (B-5) and (B-9):

$$\gamma(t) = \sin^{-1}\left(\frac{R_1 \sin\left[\frac{c}{nR_1}\,(t_1 - t)\right]}{\sqrt{(R + R_1)^2 + R_1^2 - 2R_1(R + R_1)\cos\left[\frac{c}{nR_1}\,(t_1 - t)\right]}}\right) + \frac{c}{nR_1}\,(t_1 - t) \, . \tag{B-11}$$

The exact coil lead Faraday rotation is found by substituting Eqs. (B-10) and (B-11) into Eq. (B-2). This final expression is

$$\Theta_1(\omega) = V \frac{\mu_f i}{2\pi} \left(\frac{n}{c}\right) \int_0^{t_1} \frac{\cos\left[\sin^{-1}\left(\frac{R_1 \sin\left[\frac{c}{nR_1}(t_1 - t)\right]}{\sqrt{A_1 - A_2 \cos\left[\frac{c}{nR_1}(t_1 - t)\right]}}\right) + \frac{c}{nR_1}(t_1 - t)\right]}{\sqrt{A_1 - A_2 \cos\left[\frac{c}{nR_1}(t_1 - t)\right]}} e^{-j\omega t}\, dt, \tag{B-12a}$$

where

$$A_1 = (R + R_1)^2 + R_1^2 , \tag{B-12b}$$

and

$$A_2 = 2R_1(R + R_1) . \tag{B-12c}$$

Equations (B-12) must be integrated numerically to find the solution.

Input and output leads contribute differently to the Faraday interaction, although each can be treated with similar mathematics. Two fiber coil lead configurations have been used in this study, and both can be visualized using the layout shown in Fig. B-1. In the first configuration, the light in the fiber propagates through the input lead from position 0 to position 1, through an input transition section to position 2, around (N - ½) coil turns to position 3, through an output transition section to position 4, and finally along an output lead to position 5. Light propagation in the second configuration differs only in that it passes through a complete N coil turns between positions 2 and 3. This means that positions 2 and 3 are coincident on the coil and the output fiber lead exits to the right of the coil in Fig. B-1, opposite that of the input lead. The interaction of the magnetic field with the light as it passes through the output transition section and output lead is identical for the two configurations except for a phase delay created by the extra half turn in the second configuration.

In the mathematical model, Eq. (B-12) describes the Faraday rotation for the input lead. A similar expression integrating from t_4 to t_5 (propagation times

corresponding to light at positions 4 and 5 in Fig. B-1) describes the rotation for the output lead:

$$\Theta_5(\omega) = V\frac{\mu_f i}{2\pi}\left(\frac{n}{c}\right)\int_{t_4}^{t_5}\frac{\cos\left[\sin^{-1}\left(\frac{R_1\sin\left[\frac{c}{nR_1}(t-t_4)\right]}{\sqrt{A_1 - A_2\cos\left[\frac{c}{nR_1}(t-t_4)\right]}}\right) + \frac{c}{nR_1}(t-t_4)\right]}{\sqrt{A_1 - A_2\cos\left[\frac{c}{nR_1}(t-t_4)\right]}} e^{-j\omega t}\,dt. \tag{B-13}$$

Between positions 1 and 4, the fiber follows the constant radius path of the coil proper. The expression for the rotation in this coil section then follows directly from Eqs. (5-1) and (5-2) and is given by

$$\Theta_{2,3,4}(\omega) = V\frac{\mu_f i}{2\pi}\left(\frac{n}{c}\right)\frac{(t_4 - t_1)}{R}\left[\frac{\sin\left(\frac{\omega(t_4 - t_1)}{2}\right)}{\left(\frac{\omega(t_4 - t_1)}{2}\right)}\right] e^{-j\omega\frac{(t_4 - t_1)}{2}} e^{-j\omega\left(t_1/2\right)}. \tag{B-14}$$

In general, the rotation expressed in Eq. (B-14) can be treated as a single quantity as shown. However, in some configurations it may be necessary to break out the rotation into constituent components $\Theta_2(\omega)$, $\Theta_3(\omega)$, and $\Theta_4(\omega)$, with corresponding separation in the time intervals $(t_2 - t_1)$, $(t_3 - t_2)$, and $(t_4 - t_3)$. One such configuration is the travelling wave fiber design where the coil proper and the lead transition sections may differ. The critical times corresponding to positions 1 through 4 shown in Fig. B-1 can be found from the associated geometries. These are expressed by

$$t_2 - t_1 = t_4 - t_3 = \frac{nR}{c}\beta'_{max}\ , \tag{B-15}$$

and

$$t_3 - t_2 = 2\pi R \frac{n}{c} \begin{Bmatrix} (N - 1/2) \\ \text{or} \\ N \end{Bmatrix} . \qquad \text{(B-16)}$$

The choice of the coil turn factor (N - ½ or N) in Eq. (B-16) is dependent on the desired coil configuration.

The time dependent expressions Eqs. (B-12), (B-13) and (B-14) are added to determine the total Faraday rotation as the light propagates from one end of the fiber sensor to the other. Since the complete model consists of several integral and nonintegral expressions, each for a distinct section of the coil, care must be taken to properly normalize to the low frequency response. In its final form the description of the relative Faraday rotation for the entire sensor is

$$\frac{\Theta(\omega)}{\Theta_0} = \frac{\Theta_1(\omega) + (\Theta_2(\omega) + \ldots) + \Theta_5(\omega)}{\Theta_1(0) + (\Theta_2(0) + \ldots) + \Theta_5(0)} \qquad \text{(B-17)}$$

Appropriate use of Eq. (B-14) or the constituent rotations is determined by the selected sensor configuration.

Model Results and Comparisons

The effects of fiber leads on the high frequency Faraday response of current sensor coils is dependent on the number of turns in the coil. Perturbations are at a maximum for a single turn coil, with effects diminishing as N becomes larger. Plotted in Fig. B-2 are the relative magnitudes of the Faraday rotation for one turn coils with the two lead configurations described previously. Lead distance is X = R. The resulting lead length is such that its radius of curvature is R_1 = 1.5R, which satisfies a condition that

bends in the lead not produce a linear birefringence per unit length greater than that of the bends in the coil.

Curve (a) in Fig. B-2 is the frequency response for a coil with leads entering and exiting from the same side. This configuration is simply a single loop around the conductor. Its response matches closely that of the one turn leadless, centered and circular coil. The cutoff frequency is identical, but the 3 dB bandwidth is reduced slightly, approximately 1.5%. A noticeable reduction in peak magnitude of the second response lobe (near $\omega\tau/2 = 1.5\pi$) is observed when the lead effects are included. This loss of response becomes more pronounced for each successively higher frequency lobe

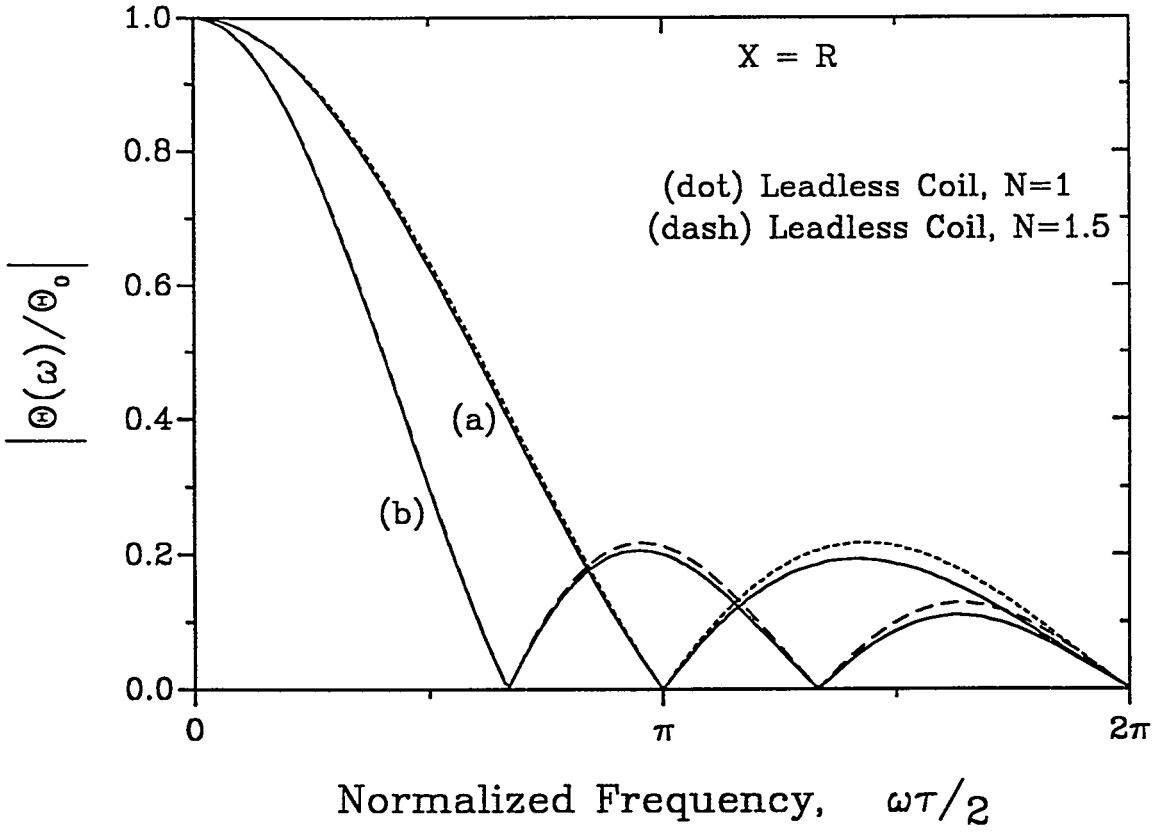

Fig. B-2. The predicted frequency response for a single turn Faraday effect fiber current sensor with (a) input and output leads exiting from the same side of the coil and (b) the input and output leads exiting in opposite directions (equivalent to 1.5 coil turns).

(not displayed in Fig. B-2), indicating that magnetic field phasing with the light propagating in the coil leads becomes much more important as frequency increases. As the number of turns in the coil is increased, the leads are less of a perturbation to the system frequency response. For as few as three coil turns, the bandwidth and secondary lobe magnitudes are predicted to be essentially the same as those for the leadless coil.

Curve (b) in Fig. B-2 is the response for a single loop sensor with the fiber leads exiting the coil in opposite directions. This configuration has an effective 1.5 coil turns, thus making the bandwidth for curve (b) much smaller than for curve (a). The magnitude of the frequency response for curve (b) can be predicted quite well using Eq. (5-3) for a centered, circular coil with N = 1.5 (see the comparison in Fig. B-2). Deviations in response between the leadless coil and the coil with leads occur only near the frequency peaks of the secondary lobes where a loss in magnitude is observed. Again, as the number of coil turns increases, this lead-induced response loss diminishes rapidly. However, it is necessary to include the extra half turn of fiber length when predicting frequency response for coils with this lead configuration remains unless N is an extremely large number. This is evident in comparing the measured and predicted values in Fig. 5-2 where N = 10.

In addition to the magnitude predictions, phase angle deviations are also considered in the lead effect model. For both configurations investigated, the coil leads add some length to the total fiber required in sensor fabrication. Thus, a propagation phase delay, compared to the leadless coil, is produced due to the slightly longer light transit time. This phase delay as a function of frequency follows exactly that given by Eq. (5-4) for the appropriate value of τ.

The actual length of the fiber coil leads can have an impact on the Faraday frequency response. This is shown in Fig. B-3 for a single turn coil with leads exiting from the same side of the coil and with X = 10R. Note that the added fiber length in the leads results in a loss of 3 dB bandwidth, but that the cutoff frequency of the curve is

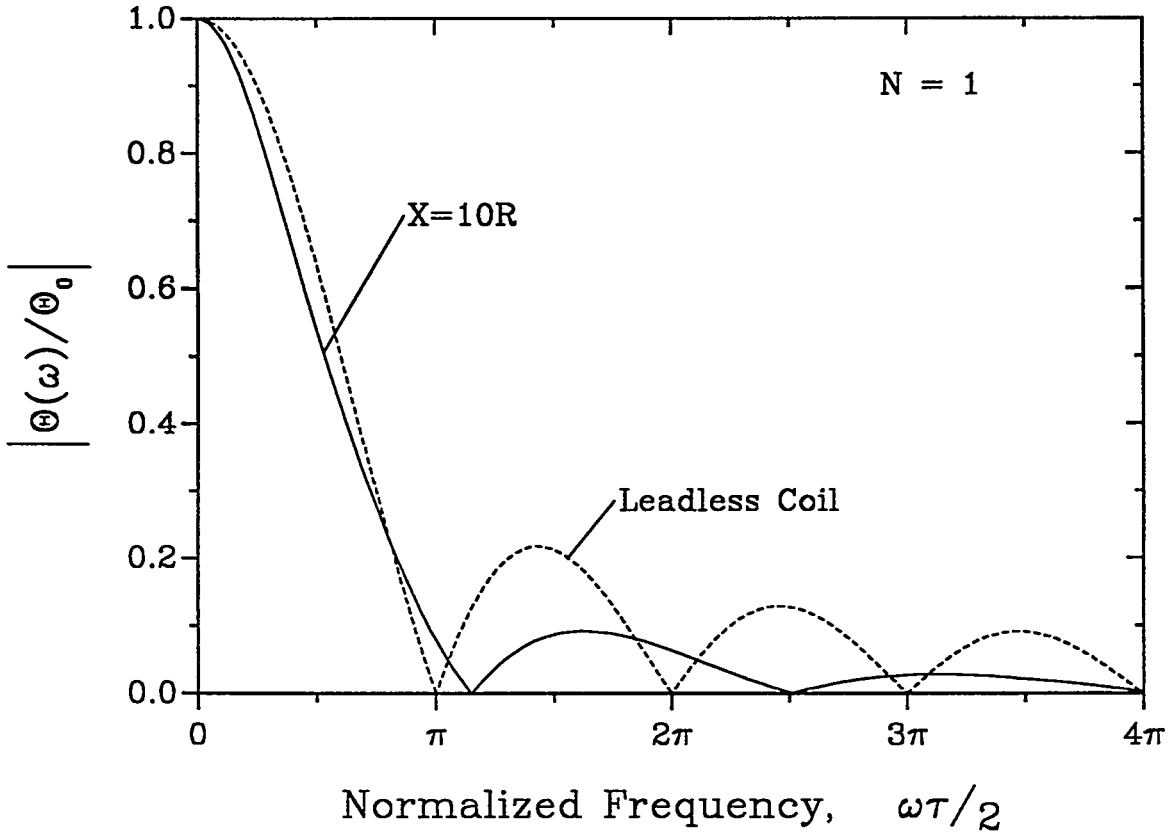

Fig. B-3. The effect of lead length on the relative response magnitude of a single turn fiber current sensor.

shifted to a higher value than that for the leadless coil. This feature occurs because light propagating in the fiber lead experiences a much weaker Faraday interaction — the angle γ is large when X is large — than in the coil proper. At the low frequencies where the magnetic field polarization is changing slowly, the entire fiber length, including the long leads, contributes to the response. But at the higher frequencies ($\omega\tau/2 > 0.6\pi$), where the magnetic field wavelength is approximately the same as the length of the fiber in the leadless coil, the leads contribute less to the total response and an effective shortening of the interaction length results. The decreasing dB and increasing f_{co} continues to occur for the single turn coil as more length is added to the leads. Eventually, the leads become so long that total Faraday interaction in them is comparatively weak. At that point the

model begins to exhibit anomalous results due to the segmented mathematical treatment of the different fiber sections. All of the predicted response then derives from the remaining half-turn of the coil proper, with non-interactive delays due to the leads; a delta function-type response results.

If the model allowed, it would be of theoretical interest to explore more fully the extreme limit, $X \rightarrow \infty$, for the long leads on a single turn fiber current sensor coil. In experimental coils, however, such long lead lengths are simply not practical, especially if the stringent fiber geometries are followed as required by the model. True interaction lengths in the coil leads will always be significantly shorter. Thus, frequency response shifts due to long fiber leads are not expected to be greater than those shown in Fig. B-3 for $X = 10R$. And, as mentioned previously, the lead effects become less pronounced as the number of turns in the fiber coil increases. For $N \geq 10$, the Faraday response can be predicted quite precisely by the leadless coil model, regardless of the fiber coil lead lengths.

APPENDIX C

DERIVATION OF EFFECTIVE RELATIVE PERMITTIVITY

The cross sectional geometry of the multilayer dielectric coaxial line is defined by Fig. C-1. Inner conductor radius is 'a', outer conductor radius is 'b', and the dielectric transitions occur at r_1 and r_2. The relative permittivities at radii ρ are given as ε_1 for $a < \rho < r_1$ and $r_2 < \rho < b$, and ε_2 for $r_1 < \rho < r_2$. At low frequencies, the fields in all the dielectric regions are assumed to be TEM. The radial electric field between a and b then has a $1/\rho$ dependency so that in medium 1, $E_1 = C_1/\rho$, and in medium 2, $E_2 = C_2/\rho$, where

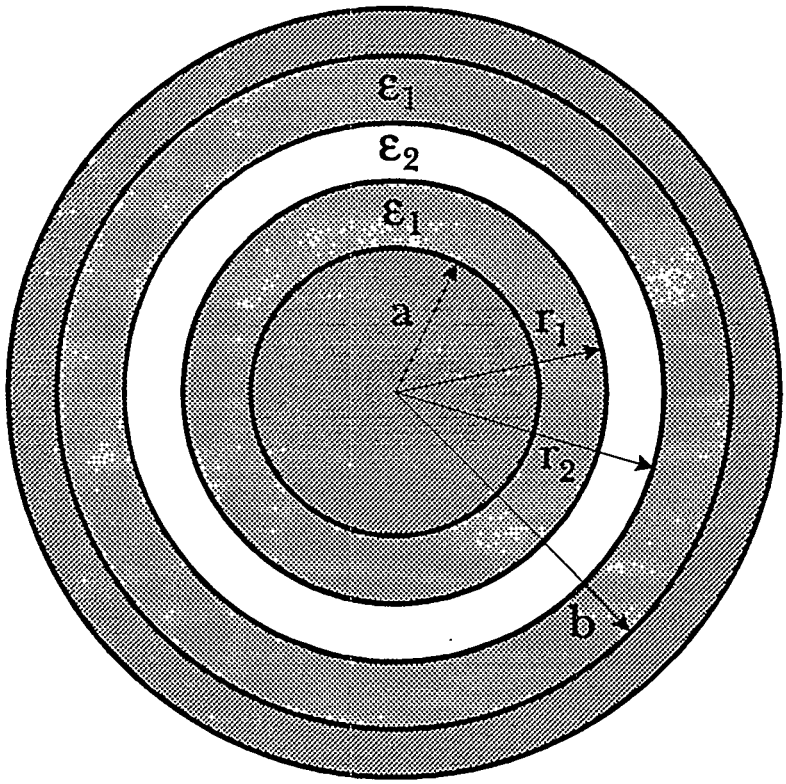

Fig. C-1. Cross section of the multilayer dielectric coaxial line. A medium with relative permittivity ε_2 is surrounded by a medium of relative permittivity ε_1. Coax conductors are defined by inner radius a and outer radius b.

C_1 and C_2 are constants. An equivalent effective (homogeneous) medium is defined throughout the dielectric region such that $E_{eff} = C_{eff}/\rho$ for $a < \rho < b$. The electric field is assumed to vanish at the conductor walls ($\sigma = \infty$), and the boundary condition $\mathbf{D}_1 \bullet \mathbf{n} = \mathbf{D}_2 \bullet \mathbf{n}$ is applied at r_1 and r_2. An effective displacement vector, $\mathbf{D}_{eff}$, is defined so that in the coaxial dielectric volume their exists an equivalent medium with relative permittivity, ε_{eff}, and $\mathbf{D}_{eff} = \varepsilon_{eff}\, \mathbf{E}_{eff}$.

The voltage between the conductors in the coaxial cell is found from the line integral over the radial component of the electric field,

$$V_{ab} = \int_a^b E_\rho \, d\rho \quad . \tag{C-1}$$

It follows then that

$$V_{ab} = \int_a^b \left(E_{eff}\right)_\rho \, d\rho \quad , \tag{C-2}$$

and equivalently

$$V_{ab} = \int_a^{r_1} E_1 \, d\rho + \int_{r_1}^{r_2} E_2 \, d\rho + \int_{r_2}^{b} E_1 \, d\rho \quad . \tag{C-3}$$

Equation (C-2) reduces to

$$V_{ab} = C_{eff} \int_a^b \frac{1}{\rho} d\rho = C_{eff} \ln\left(\frac{b}{a}\right) \quad . \tag{C-4}$$

To solve Eq. (C-3), the boundary condition at the dielectric interface is applied so that

$$E_2 = \frac{\varepsilon_1}{\varepsilon_2} E_1 \quad . \tag{C-5}$$

Then substituting for E_1 and E_2 in Eq. (C-3),

$$V_{ab} = C_1 \left[\int_a^{r_1} \frac{1}{\rho} d\rho + \frac{\varepsilon_1}{\varepsilon_2} \int_{r_1}^{r_2} \frac{1}{\rho} d\rho + \int_{r_2}^{b} \frac{1}{\rho} d\rho \right] . \qquad \text{(C-6)}$$

This integral expression has the solution

$$V_{ab} = C_1 \left[\ln\left(\frac{r_1}{a}\right) + \frac{\varepsilon_1}{\varepsilon_2} \ln\left(\frac{r_2}{r_1}\right) + \ln\left(\frac{b}{r_2}\right) \right] . \qquad \text{(C-7)}$$

Equation (C-7) can be further reduced to

$$V_{ab} = C_1 \left[\ln\left(\frac{b}{a}\right) + \left(\frac{\varepsilon_1}{\varepsilon_2} - 1\right) \ln\left(\frac{r_2}{r_1}\right) \right] . \qquad \text{(C-8)}$$

Combining Eqs. (C-4) and (C-8) gives

$$\frac{C_{eff}}{C_1} = \frac{\left[\ln\left(\frac{b}{a}\right) + \left(\frac{\varepsilon_1}{\varepsilon_2} - 1\right) \ln\left(\frac{r_2}{r_1}\right) \right]}{\ln\left(\frac{b}{a}\right)} , \qquad \text{(C-9)}$$

or

$$\frac{C_{eff}}{C_1} = \left[1 + \left(\frac{\varepsilon_1}{\varepsilon_2} - 1\right) \frac{\ln\left(r_2/r_1\right)}{\ln\left(b/a\right)} \right] . \qquad \text{(C-10)}$$

The energy density in the dielectric of the coaxial line is given by

$$\frac{dW}{dV_o} = \frac{1}{2} (\mathbf{D} \cdot \mathbf{E}) , \qquad \text{(C-11)}$$

which becomes ½ εE^2 for a TEM mode. The total energy per unit length is found by integrating Eq. (C-11) over a given planar surface, S, in the coaxial line dielectric region.

$$\frac{dW}{dz} = \frac{1}{2}\varepsilon \int_S E^2 \, dA \quad . \tag{C-12}$$

Here $dA = \rho \, d\rho \, d\phi$. The electric field for the TEM mode is azimuthally symmetric (no ϕ dependency). Then for a radially dependent electric field in a homogeneous dielectric with an effective relative permittivity, Eq. (C-12) becomes

$$\frac{dW}{dz} = \frac{1}{2}\varepsilon_{eff} C_{eff}^2 \, 2\pi \int_a^b \left(\frac{1}{\rho}\right)^2 \rho \, d\rho \quad , \tag{C-13}$$

which has a solution of

$$\frac{dW}{dz} = \pi \varepsilon_{eff} C_{eff}^2 \ln\left(\frac{b}{a}\right) \quad . \tag{C-14}$$

Equivalently, Eq. (C-12) can be broken into its constituent integrals for each of the three radial dielectric regions:

$$\frac{dW}{dz} = \pi \left[C_1^2 \varepsilon_1 \int_a^{r_1} \left(\frac{1}{\rho}\right)^2 \rho \, d\rho + C_1^2 \varepsilon_2 \int_{r_1}^{r_2} \left(\frac{\varepsilon_1}{\varepsilon_2}\frac{1}{\rho}\right)^2 \rho \, d\rho + C_1^2 \varepsilon_1 \int_{r_2}^{b} \left(\frac{1}{\rho}\right)^2 \rho \, d\rho \right] , \tag{C-15}$$

where Eq. (C-5) has been applied in the second dielectric. Then

$$\frac{dW}{dz} = \pi \varepsilon_1 C_1^2 \left[\ln\left(\frac{r_1}{a}\right) + \frac{\varepsilon_1}{\varepsilon_2} \ln\left(\frac{r_2}{r_1}\right) + \ln\left(\frac{b}{r_2}\right) \right] \quad . \tag{C-16}$$

This further reduces to

$$\frac{dW}{dz} = \pi \varepsilon_1 C_1^2 \left[\ln\left(\frac{b}{a}\right) + \left(\frac{\varepsilon_1}{\varepsilon_2} - 1\right) \ln\left(\frac{r_2}{r_1}\right) \right] . \qquad \text{(C-17)}$$

Combining Eqs. (C-14) and C-17) leads to

$$\frac{\varepsilon_{eff}}{\varepsilon_1} = \left(\frac{C_1}{C_{eff}}\right)^2 \left[1 + \left(\frac{\varepsilon_1}{\varepsilon_2} - 1\right) \frac{\ln\left(r_2/r_1\right)}{\ln\left(b/a\right)} \right] . \qquad \text{(C-18)}$$

Finally, an effective relative permittivity results by substituting C_{eff}/C_1 from Eq. (C-10) into Eq. (C-18). This gives

$$\frac{\varepsilon_{eff}}{\varepsilon_1} = \left[1 + \left(\frac{\varepsilon_1}{\varepsilon_2} - 1\right) \frac{\ln\left(r_2/r_1\right)}{\ln\left(b/a\right)} \right]^{-1} . \qquad \text{(C-19)}$$

The ratio of the effective relative permittivity to the relative permittivity of medium 1 is dependent only on the geometry of the coaxial line and the ratio of the two media relative permittivities. If medium 2 is very thin so that $r_1 \approx r_2$, or if the two dielectrics have approximately the same relative permittivities, $\varepsilon_1 \approx \varepsilon_2$, then $\varepsilon_{eff} \rightarrow \varepsilon_1$ in Eq. (C-19) as expected. And if medium 2 is large so that it nearly fills the entire volume of the coaxial line, then $r_1 \approx a$, $r_2 \approx b$ and $\varepsilon_{eff} \rightarrow \varepsilon_2$.

APPENDIX D

WAVEGUIDE MODES FOR AZIMUTHALLY SYMMETRIC FIELDS IN A MULTILAYER COAXIAL TRANSMISSION LINE WITH COMPLEX RELATIVE PERMITTIVITY

In these discussions the waveguide geometry and material dielectric properties for the coaxial line are taken as described in Appendix C and as illustrated in Fig. C-1. Material wave parameters $k_{1,2} = (\omega/c)\sqrt{\varepsilon_{1,2}}$ and the waveguide propagation constant, β_{mn} as given by Eq. (A-8), are all treated as complex quantities. Due to the added dielectric, medium 2, the electric and magnetic field components in all the coaxial dielectric layers may, in general, be coupled together, and defining strictly TE and TM modes as in the simple (single dielectric) coaxial line is not appropriate. The treatment of this coupled mode problem is quite involved mathematically, and thus a complete description of the transmission cell higher order modes is not attempted here. Instead, azimuthal symmetry ($m = 0$) is assumed, the field components become uncoupled, and TE and TM modes can be derived separately. The waveguide propagation constants, β_{mn}, for each of the modes then takes on the simpler form, β_{0n}. The derivation of the modal eigenvalue equations in the following discussions is adapted from Wait [73].

TM_{0n} Modes

If $m = 0$ in Eqs. (A-1), E_ϕ and H_ρ vanish and the remaining field components E_z, H_ϕ and E_ρ are sufficient to describe the TM fields in each coaxial layer. In the region defined by $a < \rho < r_1$, the TM field components are given by

$$E_{z1} = u_1^2 \left[A_1 J_0(u_1\rho) + B_1 Y_0(u_1\rho) \right] , \qquad \text{(D-1a)}$$

$$H_{\phi 1} = -\frac{jk_1^2}{\mu\omega}\left[A_1 \frac{\partial}{\partial\rho} J_0(u_1\rho) + B_1 \frac{\partial}{\partial\rho} Y_0(u_1\rho)\right] , \qquad \text{(D-1b)}$$

and

$$E_{\rho 1} = -\beta\left[A_1 \frac{\partial}{\partial\rho} J_0(u_1\rho) + B_1 \frac{\partial}{\partial\rho} Y_0(u_1\rho)\right] . \qquad \text{(D-1c)}$$

Here

$$u_1^2 = k_1^2 + \beta^2 . \qquad \text{(D-2)}$$

In Eqs. (D-1) and (D-2), u_1 and β are both multivalued parameters — $u_{1,0n}$ and β_{0n} for n = 1, 2, 3... — due to the waveguide modal structure. For simplicity in these derivations, the modal subscripts '0n' are dropped from u and β, and the remaining numerical subscripts refer only to the dielectric region they represent.

In the region defined by $r_2 < \rho < b$, the field components E_{z3}, $H_{\phi 3}$ and $E_{\rho 3}$ will be identical to those described in Eqs. (D-1) only with A_1 and B_1 replaced with A_3 and B_3. For $r_1 < \rho < r_2$, the TM field components are

$$E_{z2} = u_2^2\left[A_2 J_0(u_2\rho) + B_2 Y_0(u_2\rho)\right] , \qquad \text{(D-3a)}$$

$$H_{\phi 2} = -\frac{jk_2^2}{\mu\omega}\left[A_2 \frac{\partial}{\partial\rho} J_0(u_2\rho) + B_2 \frac{\partial}{\partial\rho} Y_0(u_2\rho)\right] , \qquad \text{(D-3b)}$$

and

$$E_{\rho 2} = -\beta\left[A_2 \frac{\partial}{\partial\rho} J_0(u_2\rho) + B_2 \frac{\partial}{\partial\rho} Y_0(u_2\rho)\right] , \qquad \text{(D-3c)}$$

with

$$u_2^2 = k_2^2 + \beta^2 . \qquad \text{(D-4)}$$

The metal walls of the coaxial line are considered to be infinitely conducting so that E_z vanishes at $\rho = a$ and $\rho = b$. Then

$$\frac{A_1}{B_1} = -\frac{Y_0(u_1 a)}{J_0(u_1 a)} \quad , \tag{D-5}$$

and

$$\frac{A_3}{B_3} = -\frac{Y_0(u_1 b)}{J_0(u_1 b)} \quad . \tag{D-6}$$

At the dielectric interfaces $\rho = r_1$ and $\rho = r_2$, the tangential components, E_z and H_ϕ are continuous. At $\rho = r_1$, this leads to

$$u_1^2 B_1 \left[\left(\frac{A_1}{B_1}\right) J_0(u_1 r_1) + Y_0(u_1 r_1)\right] = u_2^2 B_2 \left[\left(\frac{A_2}{B_2}\right) J_0(u_2 r_1) + Y_0(u_2 r_1)\right] , \tag{D-7}$$

and

$$k_1^2 u_1 B_1 \left[\left(\frac{A_1}{B_1}\right) J_1(u_1 r_1) + Y_1(u_1 r_1)\right] = k_2^2 u_2 B_2 \left[\left(\frac{A_2}{B_2}\right) J_1(u_2 r_1) + Y_1(u_2 r_1)\right] . \tag{D-8}$$

In Eq. (D-8), the property of the Bessel function

$$\frac{\partial}{\partial \rho} J_0(u\rho) = -u J_1(u\rho) \tag{D-9}$$

has been applied. Equation (D-8) is divided by Eq. (D-7), and A_1/B_1 is replaced by its equivalent form from Eq. (D-5). The following expression results.

$$\left(\frac{k_1^2}{u_1}\right)\left[\frac{Y_1(u_1 r_1) - \frac{Y_0(u_1 a)}{J_0(u_1 a)} J_1(u_1 r_1)}{Y_0(u_1 r_1) - \frac{Y_0(u_1 a)}{J_0(u_1 a)} J_0(u_1 r_1)}\right] = \left(\frac{k_2^2}{u_2}\right)\left[\frac{\left(\frac{A_2}{B_2}\right) J_1(u_2 r_1) + Y_1(u_2 r_1)}{\left(\frac{A_2}{B_2}\right) J_0(u_2 r_1) + Y_0(u_2 r_1)}\right] . \tag{D-10}$$

Solving for A_2/B_2 gives

$$\frac{A_2}{B_2} = \frac{Y_1(u_2 r_1) - \left(\frac{k_1}{k_2}\right)^2 \frac{u_2}{u_1} \chi_1 Y_0(u_2 r_1)}{\left(\frac{k_1}{k_2}\right)^2 \frac{u_2}{u_1} \chi_1 J_0(u_2 r_1) - J_1(u_2 r_1)} , \qquad \text{(D-11)}$$

where χ_1 is the bracketed factor on the left side of Eq. (D-10) and is given by

$$\chi_1 = \frac{Y_1(u_1 r_1) - \frac{Y_0(u_1 a)}{J_0(u_1 a)} J_1(u_1 r_1)}{Y_0(u_1 r_1) - \frac{Y_0(u_1 a)}{J_0(u_1 a)} J_0(u_1 r_1)} . \qquad \text{(D-12)}$$

At the second dielectric interface, $\rho = r_2$, a similar expression for A_2/B_2 is derived. It is given by

$$\frac{A_2}{B_2} = \frac{Y_1(u_2 r_2) - \left(\frac{k_1}{k_2}\right)^2 \frac{u_2}{u_1} \chi_2 Y_0(u_2 r_2)}{\left(\frac{k_1}{k_2}\right)^2 \frac{u_2}{u_1} \chi_2 J_0(u_2 r_2) - J_1(u_2 r_2)} , \qquad \text{(D-13)}$$

where

$$\chi_2 = \frac{Y_1(u_1 r_2) - \frac{Y_0(u_1 b)}{J_0(u_1 b)} J_1(u_1 r_2)}{Y_0(u_1 r_2) - \frac{Y_0(u_1 b)}{J_0(u_1 b)} J_0(u_1 r_2)} . \qquad \text{(D-14)}$$

Combining Eqs. (D-11) and (D-13) gives a final transcendental eigenvalue equation for the TM_{0n} modes,

$$\frac{\left(\frac{k_1}{k_2}\right)^2 \frac{u_2}{u_1} \chi_2 J_0(u_2 r_2) - J_1(u_2 r_2)}{\left(\frac{k_1}{k_2}\right)^2 \frac{u_2}{u_1} \chi_1 J_0(u_2 r_1) - J_1(u_2 r_1)} = \frac{\left(\frac{k_1}{k_2}\right)^2 \frac{u_2}{u_1} \chi_2 Y_0(u_2 r_2) - Y_1(u_2 r_2)}{\left(\frac{k_1}{k_2}\right)^2 \frac{u_2}{u_1} \chi_1 Y_0(u_2 r_1) - Y_1(u_2 r_1)}, \tag{D-15}$$

with χ_1 and χ_2 given by Eqs. (D-12) and (D-14).

TE$_{0n}$ Modes

In a fashion similar to the TM$_{0n}$ mode derivations, the TE$_{0n}$ modes of the waveguide are found from Eqs. (A-2) with m = 0. In the dielectric region defined by ε_1, the field components are given by

$$H_{z1,3} = u_1^2 \left[C_{1,3} J_0(u_1\rho) + D_{1,3} Y_0(u_1\rho)\right], \tag{D-16a}$$

$$E_{\phi 1,3} = j\mu\omega \left[C_{1,3} \frac{\partial}{\partial\rho} J_0(u_1\rho) + D_{1,3} \frac{\partial}{\partial\rho} Y_0(u_1\rho)\right], \tag{D-16b}$$

and

$$H_{\rho 1,3} = -\beta \left[C_{1,3} \frac{\partial}{\partial\rho} J_0(u_1\rho) + D_{1,3} \frac{\partial}{\partial\rho} Y_0(u_1\rho)\right], \tag{D-16c}$$

where the subscript 1 applies for $a < \rho < r_1$ and the subscript 3 applies for $r_2 < \rho < b$. The TE field components for $r_1 < \rho < r_2$, where the relative permittivity is ε_2, are given by

$$H_{z2} = u_2^2 \left[C_2 J_0(u_2\rho) + D_2 Y_0(u_2\rho)\right], \tag{D-17a}$$

$$E_{\phi 2} = j\mu\omega \left[C_2 \frac{\partial}{\partial\rho} J_0(u_2\rho) + D_2 \frac{\partial}{\partial\rho} Y_0(u_2\rho)\right], \tag{D-17b}$$

and

$$H_{\rho 2} = -\beta \left[C_2 \frac{\partial}{\partial\rho} J_0(u_2\rho) + D_2 \frac{\partial}{\partial\rho} Y_0(u_2\rho)\right]. \tag{D-17c}$$

Again the Bessel function property, Eq. (D-9), can be applied to Eqs. (D-16b), (D-16c), (D-17b), and (D-17c).

At the infinitely conducting metal walls, the tangential E component must vanish. For these TE modes, $E_\phi = 0$ at both $\rho = a$ and $\rho = b$. Then

$$\frac{C_1}{D_1} = -\frac{Y_1(u_1 a)}{J_1(u_1 a)} \quad , \tag{D-18}$$

and

$$\frac{C_3}{D_3} = -\frac{Y_1(u_1 b)}{J_1(u_1 b)} \quad . \tag{D-19}$$

At $\rho = r_1$, the tangential components E_ϕ and H_z are continuous across the dielectric interface. Thus, for H_z,

$$u_1^2 D_1 \left[\left(\frac{C_1}{D_1}\right) J_0(u_1 r_1) + Y_0(u_1 r_1)\right] = u_2^2 D_2 \left[\left(\frac{C_2}{D_2}\right) J_0(u_2 r_1) + Y_0(u_2 r_1)\right], \tag{D-20}$$

and for E_ϕ,

$$u_1 D_1 \left[\left(\frac{C_1}{D_1}\right) J_1(u_1 r_1) + Y_1(u_1 r_1)\right] = u_2 D_2 \left[\left(\frac{C_2}{D_2}\right) J_1(u_2 r_1) + Y_1(u_2 r_1)\right]. \tag{D-21}$$

Using Eq. (D-18) to eliminate C_1/D_1, and dividing Eq. (D-21) by Eq. (D-20) yields

$$\frac{1}{u_1}\left[\frac{Y_1(u_1 r_1) - \frac{Y_1(u_1 a)}{J_1(u_1 a)} J_1(u_1 r_1)}{Y_0(u_1 r_1) - \frac{Y_1(u_1 a)}{J_1(u_1 a)} J_0(u_1 r_1)}\right] = \frac{1}{u_2}\left[\frac{\left(\frac{C_2}{D_2}\right) J_1(u_2 r_1) + Y_1(u_2 r_1)}{\left(\frac{C_2}{D_2}\right) J_0(u_2 r_1) + Y_0(u_2 r_1)}\right]. \tag{D-22}$$

Then solving for C_2/D_2 gives

$$\frac{C_2}{D_2} = \frac{Y_1(u_2 r_1) - \frac{u_2}{u_1} Z_1 Y_0(u_2 r_1)}{\frac{u_2}{u_1} Z_1 J_0(u_2 r_1) - J_1(u_2 r_1)} , \qquad \text{(D-23)}$$

where Z_1 is the factor in the brackets on the left side of Eq. (D-22) and is given by

$$Z_1 = \frac{Y_1(u_1 r_1) - \frac{Y_1(u_1 a)}{J_1(u_1 a)} J_1(u_1 r_1)}{Y_0(u_1 r_1) - \frac{Y_1(u_1 a)}{J_1(u_1 a)} J_0(u_1 r_1)} . \qquad \text{(D-24)}$$

At the second dielectric interface, $\rho = r_2$, the tangential field components are also continuous, which leads to a similar expression for C_2/D_2 given by

$$\frac{C_2}{D_2} = \frac{Y_1(u_2 r_2) - \frac{u_2}{u_1} Z_2 Y_0(u_2 r_2)}{\frac{u_2}{u_1} Z_2 J_0(u_2 r_2) - J_1(u_2 r_2)} , \qquad \text{(D-25)}$$

where

$$Z_2 = \frac{Y_1(u_1 r_2) - \frac{Y_1(u_1 b)}{J_1(u_1 b)} J_1(u_1 r_2)}{Y_0(u_1 r_2) - \frac{Y_1(u_1 b)}{J_1(u_1 b)} J_0(u_1 r_2)} . \qquad \text{(D-26)}$$

Equations (D-23) and (D-24) are combined to give the transcendental eigenvalue equation for the TE_{0n} modes,

$$\frac{\frac{u_2}{u_1} Z_2 J_0(u_2 r_2) - J_1(u_2 r_2)}{\frac{u_2}{u_1} Z_1 J_0(u_2 r_1) - J_1(u_2 r_1)} = \frac{\frac{u_2}{u_1} Z_2 Y_0(u_2 r_2) - Y_1(u_2 r_2)}{\frac{u_2}{u_1} Z_1 Y_0(u_2 r_1) - Y_1(u_2 r_1)} , \qquad \text{(D-27)}$$

where Z_1 and Z_2 are presented in Eqs. (D-24) and (D-26).

Modal Solutions

Solutions to Eqs. (D-15) and (D-27) that lead to guided propagating modes require that β be imaginary and thus $\beta^2 < 0$. In the frequency regions where $\beta^2 > 0$, modes experience attenuation only and thus die out rapidly. The cutoff frequency, ω_c, is defined as that frequency above which free wave propagation occurs and below which only modal attenuation occurs. In this multilayer dielectric waveguide where relative permittivities can be complex, modal solutions for β are also complex, having both real and imaginary components, when $\omega > \omega_c$. Field waves are then freely propagating yet attenuated.

As discussed in Appendix A, a TEM mode can exist in a waveguide structure only if E_z and H_z both equal zero for all values of ρ. Then Eqs. (D-1a) and (D-3a) must be simultaneously zero at $\rho = r_1$, as will Eqs. (D-16a) and (D-17a). Similar sets of equations can be identified for the $\rho = r_2$ interface. Using the TM_{0n} mode equations, Eqs. (D-1a) and (D-3a) at $\rho = r_1$, as a baseline to illustrate the situation, the following expressions result:

$$0 = u_1^2 \left[A_1 J_0(u_1 r_1) + B_1 Y_0(u_1 r_1) \right] , \tag{D-28}$$

and

$$0 = u_2^2 \left[A_2 J_0(u_2 r_1) + B_2 Y_0(u_2 r_1) \right] . \tag{D-29}$$

Solutions to these equations require that $u_1 = 0$ and $u_2 = 0$. But since $k_1 \neq k_2$, except when the two dielectrics are identical, a contradiction exists for the multilayer media. Thus, no TEM mode is possible. If the static values of the material relative permittivities are such that $\varepsilon_1 > \varepsilon_2$, then the TM_{01} mode is of lowest order for this coaxial transmission line structure. This mode exists at all frequencies and is cutoff only at $\omega = 0$.

REFERENCES

1. (a) H. Bassen and R. Peterson, "Complete measurement of electromagnetic fields with electro-optic crystals," in *Biological Effects of Electromagnetic Waves, Selected Papers from USNC/URSI Annual Meeting*, Vol. II, C.C. Johnson, ed., HEW Publication (FDA)77-8011, pp. 310-323 (1976).

   (b) A. J. Rogers, "Optical methods for measurement of voltage and current in power systems," *Optics and Laser Tech.*, **9**, pp. 273-283 (1977).

   (c) K. Kyuma, S. Tai, M. Nunoshita, N. Mikami and Y. Ida, "Fiber optic current and voltage sensor using a $Bi_{12}GeO_{20}$ single crystal," *IEEE J. Lightwave Tech.*, **LT-1**, pp. 93-97 (1983).

   (d) J. C. Wyss, "Photonic sensors for electromagnetic field measurements," *IEEE Ant. and Prop. Newsletter,* **26**, pp. 5-9 (1984).

2. G. A. Massey, D. C. Erickson and R. A. Kadlec, "Electromagnetic field components: their measurement using electro-optic and magneto-optic effects," *Appl. Opt.*, **14**, pp. 2712-2719 (1975).

3. F. Buckholtz, K. P. Koo, A. D. Kersey and A. Dandridge, "Fiber optic magnetic sensor development," *Proc. SPIE,* **718**, pp. 56-65 (1986).

4. Atlantic Research Corp., "High sensitivity RF current probe," specification 452 (1969).

5. J. G. Hewitt, Jr., "Instrumentation for making broadband measurements on electro-explosive devices," *Sixth Symposium on Electroexplosive Devices*, Denver Research Institute Rpt. (1969).

6. (a) S. Gibes, E. Jensen, M. Sun and K. Wickersheim, "An improved fiberoptic current sensing system for high frequency susceptibility testing," *EMC Technology*, **6**, No. 7, pp. 45-50 (1987).

   (b) R. W. Cernosek, "High frequency fluoroptic thermometry current sensing for

weapon susceptibility testing," *EMC EXPO '88 Symposium Record*, Washington, D.C. (1988).

(c) T. H. Grady, "New instrument reduces hazards in EED tests," *EMC Technology*, **9**, No. 3, pp. 17-20 (1990).

(d) K. A. Wickersheim and M. H. Sun, "Small minimally perturbing fiberoptic sensor for measurement of microwave fields and power," *Fifth Conf. on High Power Microwave Tech.*, West Point, N.Y. (1990).

7. (a) A. Yariv and H. Winsor, "Proposal for detection of magnetic fields through magnetostrictive perturbations of optical fiber," *Opt. Lett.*, **5**, pp. 87-89 (1980).

(b) A. D. Kersey, M. Corke, D. A. Jackson and J. D. C. James, "Detection of dc and low frequency ac magnetic fields using all single-mode fibre magnetometer," *Electron. Lett.*, **19**, pp. 469-471 (1983).

8. F. Bucholtz, D. M. Dagenais and K. P. Koo, "High frequency fibre-optic magnetometer with 70 $fT/\sqrt{Hz}$ resolution," *Electron. Lett.*, **25**, pp. 1719-1721 (1989).

9. F. Bucholtz, D. M. Dagenais and K. P. Koo, "Mixing and detection of RF signals in fibre-optic magnetostrictive sensor," *Electron. Lett.*, **25** (1989).

10. S. J. Martin and M. A. Butler, "Wideband optical fiber magnetic field sensor," *Proc. SPIE*, **566**, pp. 197-200 (1985).

11. B. T. Neyer, J. Chang and L. E. Ruggles, "Calibrated Faraday current and magnetic field sensor," *Proc. SPIE*, **566**, pp. 201-205 (1985).

12. M. N. Deeter, A. H. Rose and G. W. Day, "Faraday-effect magnetic field sensors based on substituted iron garnets," *Proc. SPIE*, **1367**, pp. 243-248 (1990).

13. M. N. Deeter, A. H. Rose and G. W. Day, "Fast, sensitive magnetic field sensors based on the Faraday effect in YIG," *J. Lightwave Technol.*, **8**, pp. 1838-1842 (1990).

14. R. W. Cernosek, "High frequency response of fiber current sensors with

noncircular and noncentered coils," *Proc. 8th Optical Fiber Sensors Conf.*, pp. 398-401 (1992).

15. (a) G. W. Day, J. D. O. McFadden, L. R. Veeser, G. I. Chandler and R. W. Cernosek, "Optical fiber sensors for the measurement of pulsed electric currents," *AGARD Proc No. 383, Guided Optical Structures in the Military Environment*, pp. 8-3 thru 8-9 (1985).

    (b) G. W. Day, L. R. Veeser, G. I. Chandler and R. W. Cernosek, "Progress in the design of fiber sensors for the measurement of pulsed electric currents," *Proc. Workshop on Measurements of Electric Quantities in Pulsed Power Systems*, Gaithersburg, Md. (1986).

16. (a) A. J. Rogers, "Optical measurement of current and voltage on power systems," *IEE J. Elect. Power Applics.*, **2** , p. 120 (1979).

    (b) A. J. Rogers, "Optical-fibre current measurement," *Int. J. Optoelectronics*, **3**, pp. 391-407 (1988).

    (c) A. N. Tobin, A. P. Steer, S. J. Turner, P. R. B. Farrie, D. King, R. P. Tatum, J. D. C. Jones and D. A. Jackson, "Application of an optical fibre current sensor to electricity supply protection," *Proc. SPIE*, **1169**, pp. 201-209 (1989).

17. (a) A. Papp and H. Harms, "Magnetooptical current transformer. 1: Principles," *Appl. Opt.*, **19**, pp. 3729-3734 (1980).

    (b) H. Aulich, W. Beck, N. Doukalias, H. Harms, A. Papp and H. Schneider, "Magnetooptical current transformer. 2: Components," *Appl. Opt.*, **19**, pp. 3735-3740 (1980).

    (c) H. Harms and A. Papp, "Magnetooptical current transformer. 3: Measurements," *Appl. Opt.*, **19**, pp. 3741-3745 (1980).

18. L. Veeser, D. Kania, B. Freemman, P. Kruse and E. Zimmermann, "Measurement of megampere currents with optical fibers," *Proc. SPIE*, **280**, pp. 300-304 (1983).

19. G. I. Chandler, P. R. Forman, F. C. Jahoda and K. A. Klare, "Fiber-optic

heterodyne phase-shift measurement of plasma current," *Appl. Opt.*, **25**, pp. 1770-1774 (1986).

20. (a) H. S. Lassing, A. A. M. Oomens, R. Woltjer, P. C. T. van der Laan and G. G. Wolzak, "Development of a magneto-optic current sensor for high pulsed currents," *Rev. Sci. Instrum.*, **57**, pp. 851-854 (1986).

    (b) H. S. Lassing, W. J. Mastop, A. F. G. van der Meer and A. A. M. Oomens, "Plasma current measurement by Faraday rotation in a single-mode fiber," *Appl. Opt.*, **26**, pp. 2456-2460 (1987).

21. G. W. Day and S. M. Etzel, "Annealing of bend-induced birefringence in fiber current sensors," *Tech. Dig., Conf. on Integrated Opt. and Opt. Fiber Comm.*, Venice, pp. 871-874 (1985).

22. Dingding Tang, A. H. Rose, G. W. Day and Shelley M. Etzel, "Annealing of linear birefringence in single-mode fiber coils: application to optical fiber current sensors," *J. Lightwave Technol.*, **9**, pp. 1031-1037 (1991).

23. M. P. Varnham, R. D. Birch and D. N. Payne, "Helical core circularly birefringent fibres," *Tech. Dig., IOOC/ECOC '85*, Venice, pp. 135-138 (1985).

24. R. I. Laming and D. N. Payne, "Electric current sensors employing spun highly birefringent optical fibers," *J. Lightwave Technol.*, **7**, pp. 2084-2094 (1989).

25. (a) K. Shiraishi, S. Sugaya and S. Kawakami, "Fiber Faraday rotator," *Appl. Opt.*, **23**, pp. 1103-1106 (1984).

    (b) K. Shiraishi, K. Nishino and S. Kawakimi, "Temperature insensitive fiber Faraday rotator," *Appl. Opt.*, **24**, pp. 1896-1897 (1985).

26. P. E. Sanders, D. A. Krone and M. S. Maklad, "Faraday rotator single mode fiber," *Proc. SPIE*, **566**, pp. 317-320 (1985).

27. (a) S. B. Poole, D. N. Payne and M. E. Fermann, "Fabrication of low-loss optical fibres containing rare earth ions," *Electron. Lett.*, **21**, pp. 737-738 (1985).

    (b) J. E. Townsend, S. B. Poole and D. N. Payne, "Solution doping techniques for

fabrication of rare earth doped optical fibres," *Electron. Lett.*, **23**, pp. 329-331 (1987).

28. S. B. Poole and D. N. Payne, "Special optical fibres," *Proc. SPIE*, **734**, pp. 92-103 (1987).

29. M. S. Maklad, P. E. Sanders, E. Dowd and A. Kuczma, "Single mode fibers for sensing applications," *Proc. SPIE*, **718**, pp. 97-109 (1986).

30. (a) A. H. Rose, M. N. Deeter and G. W. Day, "Submicroampere per root Hz, high bandwidth current sensor based on the Faraday effect in Ga:YIG," *Proc. 8th Optical Fiber Sensor Conf.*, pp. 394-397 (Monterey, 1992).

(b) A. H. Rose, M. N. Deeter and G. W. Day, "Submicroampere per root Hz, high bandwidth current sensor based on the Faraday effect in Ga:YIG," *Opt. Lett.*, **18**, pp. 1471-1473 (1993).

31. R. Wolfe, E. M. Gyorgy, R. A. Lieberman, V. J. Fratello, S. J. Licht, M. N. Deeter and G. W. Day, "High frequency magnetic field sensors based on the Faraday effect in garnet thick films," *Proc. 8th Optical Fiber Sensors Conf.*, pp. 390-393 (1992).

32. J. A. Gaj, R. R. Galazka and M. Nawrocki, "Giant exciton Faraday rotation in $Cd_{1-x}Mn_xTe$ mixed crystals", *Solid State Commun.*, **25**, pp. 193-195 (1978).

33. A. D. Kersey, F. Bucholtz and A. Dandridge, "Sensitivity-bandwidth limitation in optical-fiber Faraday-rotation current sensors," *Intl. J. Optoelectronics*, **3**, pp. 323-332 (1988).

34. R. W. Cernosek, "Expanded coaxial transmission cells for electromagnetic testing," *Sandia National Laboratories Technical Rpt.*, SAND91-0768 (1991).

35. H. Piller, "Faraday Rotation," Ch. 3 in *Semiconductors and Semimetals*, Vol. 8, R. K. Willardson and A. C. Beer, eds. (Academic Press, 1972).

36. P. A. Williams, A. H. Rose, G. W. Day, T. E. Milner and M. N. Deeter, "Temperature dependence of the Verdet constant in several diamagnetic glasses,"

Appl. Opt., **30**, pp. 1176-1178 (1991).

37. M. A. Butler and E. L. Venturini, "High frequency Faraday rotation in FR-5 glass," *Appl. Opt.*, **26**, pp. 1581-1582 (1987).

38. M. A. Butler, S. J. Martin and R. J. Baughman, "Frequency-dependent Faraday rotation in CdMnTe," *Appl. Phys. Lett.*, **49**, pp. 1053-1055 (1986).

39. M. J. Weber, "Faraday rotator materials for laser systems," *Proc. SPIE*, **681**, pp. 75-90 (1986).

40. (a) M. J. Weber, "Faraday rotator materials," *Lawrence Livermore Laboratory Rpt.*, M-103 (1982).

(b) M. J. Weber, "Magnetooptical materials," Sect. 2-2 in *Handbook of Laser Science and Technology, Vol. II, Optical Materials, Part 2*, M. J. Weber, ed. (CRC Press, 1986).

41. S. C. Rashleigh and R. Ulrich, "Magneto-optic current sensing with birefringent fibers," *Appl. Phys. Lett*, **34**, pp. 768-770 (1979).

42. W. F. Hemsing, "VISAR: 2.5 minutes for data reduction," *Proc. SPIE*, **427**, pp. 199-202 (1983).

43. H. J. Arditty, Y. Bourbin, M. Mapuchon and C. Puech, "Current sensor using state-of-the-art fiber optic interferometric techniques," *Tech. Dig. Third Intl. Conf. on Integrated Opt. and Opt. Fiber Comm.*, San Francisco (1981).

44. (a) L. R. Veeser and G. W. Day, "Faraday effect current sensing using a Sagnac interferometer with a 3 x 3 coupler," *Proc. 7th Optical Fibre Sensors Conf.*, pp. 325-328 (1990).

(b) K. B. Rochford, G. W. Day and P. R. Forman, "Polarization dependence of response functions in 3 x 3 Sagnac optical fiber current sensors," *Proc. 9th Optical Fiber Sensors Conf.*, Post-deadline 6, Florence, Italy (1993).

45. G. W. Day and A. H. Rose, "Faraday effect sensors: state of the art," *Proc. SPIE*, **985**, pp. 138-150 (1988).

46. G. W. Day, K. S. Lee, A. H. Rose, L. R. Veeser, B. J. Papatheofanis and H. K. Whitesel, "Optical fiber sensors for electromagnetic quantities," *Proc. 34th Intl. Instrumentation Symp., ISA*, Albuquerque, N.M., pp. 205-207 (1988).

47. A. M. Smith, "Polarization and magnetooptical properties of single mode optical fiber," *Appl. Opt.*, **17**, pp. 52-56 (1978).

48. S. C. Rashleigh, "Origins and control of polarization effects in single mode fibers," *IEEE J. Lightwave Tech.*, **LT-1**, pp. 312-331 (1983).

49. D. N. Payne, A. J. Barlow and J. J. Ramskov Hansen, "Development of low- and high-birefringence optical fibres," *IEEE J. Quantum Electron.*, **QE-18**, pp. 477-488 (1982).

50. R. Ulrich, S. C. Rashleigh and W. Eickhoff, "Bending induced birefringence in single mode fibers," *Opt. Lett.*, **5**, pp. 273-275 (1980).

51. (a) R. C. Jones, "A new calculus for the treatment of optical systems," *J. Opt. Soc. Am.*, **31**, p. 488 (1941).

(b) W. J. Tabor and F. S. Chen, "Electromagnetic propagation through materials possessing both Faraday rotation and birefringence: experiments with ytterbium orthoferrite," *J. Appl. Phys.*, **40**, p. 2760 (1969).

52. R. Ulrich and A. Simon, "Polarization optics of twisted single mode fibers," *Appl. Opt.*, **18**, pp. 2241-2251 (1979).

53. L. Li, J. R. Qian and D. N. Payne, "Current sensing using highly birefringent bow-tie fibers," *Electron. Lett.*, **22**, pp. 1142-1144 (1986).

54. Dingding Tang and G. W. Day, "Progress in the development of miniature optical fiber current sensors," *Tech. Dig., IEEE Lasers and Electro-Optic Soc. Annual Conf.*, Santa Clara, Ca. (1988).

55. P. A. Williams, G. W. Day and A. H. Rose, "Compensation for the temperature dependence of the Faraday effect in diamagnetic materials: applications to optical fibre sensors," *Electron. Lett.*, **27**, pp. 1131-1132 (1991).

56. M. A. Butler, "Wavelength and temperature dependence of the Faraday effect in $Cd_{1-x}Mn_xTe$," *Solid State Commun.*, **62**, pp. 45-47 (1987).

57. N. Kullendorff and B. Hok, "Temperature independent Faraday rotation near the band gap in $Cd_{1-x}Mn_xTe$," *Appl. Phys. Lett.*, **46**, pp. 1016-1018 (1985).

58. O. Kamada, H. Minemoto and S. Ishizuka, "Mixed rare earth garnet (TbY)IG for magnetic field sensors," *J. Appl Phys.*, **61**, pp. 3268-3270 (1987).

59. G. W. Day, "Compact sensors for the measurement of low level electric currents," *Tech. Dig., 4th Intl. Conf. on Opt. Fiber Sensors*, Tokyo (1986).

60. R. W. Cernosek, "Travelling wave Faraday effect fiber current sensors," *Proc. 7th Optical Fibre Sensors Conf.*, pp 72-76 (1990).

61. A. Sommerfeld, *Electrodynamics*, pp. 177-193 (Academic Press, 1952).

62. A. Yariv, *Optical Electronics*, 3rd. ed., Ch. 9 (Holt, Rinehart and Winston, 1985).

63. G. W. Day, "Recent advances in Faraday effect sensors," *Optical Fiber Sensors, Proceedings of the 6th International Conference, OFS '89*, H. J. Arditty, J. P. Dakin and R. T. Kersten, eds., pp. 250-254 (Springer-Verlag, Berlin, 1989).

64. C. T. Chang, J. A. and H. F. Taylor, "Fibre-optic delay-line devices for RF signal processing," *Electron. Lett.*, **13**, p. 678-680 (1977).

65. K. P. Jackson, S. A. Newton, B. Moslehi, M. Tur, C. C. Cutler, J. W. Goodman and H. J. Shaw, "Optical fiber delay-line signal processing," *IEEE Trans. Microwave Theory Tech.*, **MTT-33**, pp. 193-209 (1985).

66. C. M. Gee, G. D. Thurmond and H. W. Yen, "17 GHz bandwidth electro-optic modulator," *Appl. Phys. Lett.*, **43**, pp. 998-1000 (1983).

67. R. C. Weast, ed., *Handbook of Physics and Chemistry*, 54th ed., sect. E (CRC Press, 1973).

68. K. A. Wickersheim and R. V. Alves, "Recent advances in optical temperature measurement," *Industrial Res. and Dev.*, **21**, p. 82 (1979).

69. C. G. Malmberg and A. A. Maryott, "Dielectric constant of water from 0° to

100°C," *J. Res. Nat'l Bur. Stand.*, **56**, pp. 1-8 (1956).

70. B. B. Owen, R. C. Miller, C. E. Milner and H. L. Cogan, "The dielectric constant of water as a function of temperature and pressure," *J. Phys. Chem*, **65**, pp. 2065-2070 (1961).

71. C. Kittel, *Introduction to Solid State Physics*, 2nd. ed., pp. 175-179 (Wiley, 1956).

72. J. B. Hasted, "The experimental data for liquid water," Ch. 2 in *Aqueous Dielectrics*, (Chapman and Hall, London, 1973).

73. J. R. Wait, *Electromagnetic Wave Theory* (Harper and Row, New York, 1985).

74. D. E. Amos, "A subroutine package for Bessel functions of a complex argument and nonnegative order," *Sandia National Laboratories Technical Rpt.*, SAND85-1018 (1985).

75. R. W. Cernosek, "High frequency models for travelling wave optical fiber current sensors," *Tech. Dig., 1992 Optical Society of America Annual Meeting*, Albuquerque, N.M., p. 20 (1992).

76. R. E. Bolz and G. L. Tuve, eds., *Handbook of Tables for Applied Engineering Science*, 2nd ed., Sect. 2 (CRC Press, 1979).

77. W. W. Macalpine and R. O. Schildknecht, "Coaxial resonator with helical inner conductor," *Proc. IRE*, pp. 2099-2105 (1959).

78. M. L. Crawford, "Generation of standard EM fields using TEM transmission cells," *IEEE Trans. Electromagn. Compat.*, **EMC-16**, pp. 189-195 (1974).

79. M. L. Crawford and J. L. Workman, "Using a TEM cell for EMR measurements of electronic equipment," *NBS Technical Note 1013* (1981).

80. T. Moreno, *Microwave Transmission Design Data* (Artech House, 1989).

81. C. E. Baum, "The conical transmission line as a wave launcher and terminator for a cylindrical transmission line, " *Air Force Weapons Laboratory Sensor and Simulation Notes,* Vol. 2, EMP 1-2, Note SSN 31 (1967).

GLOSSARY OF SPECIAL SYMBOLS AND TERMS

a	radius of coaxial transmission line inner (center) conductor
a_0	radial distance from coaxial line axis to nearest point on fiber segment
b	radius of coaxial line outer conductor
c	speed of light in vacuum
d	diameter of fiber coil
d/x_0	ratio of diameter to pitch of helical fiber coil
dW/dV_0	energy density for coaxial line dielectric
dW/dz	total energy per unit length along axis in a coaxial line dielectric
e	magnitude of the electric charge
f	modulation frequency
f_c	cutoff frequency of higher order modes in coaxial transmission lines
f_{co}	cutoff frequency (first null) in optical fiber sensor response
f_R	resonance center frequency
g′	fiber twist material parameter
h	half-height of rectangular coil
i	static or steady state current amplitude in a conductor
i_{det}	average optical detector output current
j	$\sqrt{-1}$
k	electromagnetic wave vector
k	wave propagation parameter (general)
$k_{1,2}$	wave parameter for dielectric regions 1, 2
k_B	Boltzmann's constant
l	fiber length variable (general)
l	length vector
ℓ	short fiber or optical material length (usually less than one turn)
ℓ_1	length of fiber lead
m	integer counter for series, azimuthal mode number in coaxial transmission line
m′	integer counter for response resonances
n	fiber refractive index
n	surface normal vector
r	radial distance from conductor axis to fiber axis
$r_{1,2}$	inner, outer radius of fiber mandrel, radii at dielectric transitions
r_f	fiber radius
t	time variable (general)
$t_{a,b}$	time at points a, b on a short circular fiber loop
$t_{0,1,2,...}$	time or time delay at designated points: starting or reference, 1, 2,... in a fiber coil or lead
u	Bessel function wave number, $u^2 = k^2 + \beta^2$
$u_{1,2}$	Bessel function wave number for dielectric regions 1, 2
u_{mn}	Bessel function wave number for the mnth coaxial waveguide mode
v	velocity variable (general)
v_f	velocity of light in fiber

v_{light}	velocity of light in a planar waveguide
v_{ph}	phase velocity of EM wave in transmission line
w	half width of rectangular coil
x_0	pitch of helical fiber coil
z	axial length dimension in cylindrical coordinates, length along coaxial transmission line
$\hat{\mathbf{z}}$	axial unit vector in cylindrical coordinate
A,B,C,D	integration constants used with electric and magnetic field components
A(z)	amplitude of propagating EM wave in a coaxial line
A_0	initial amplitude of EM wave
$A_{1,2,3}$	constant in dielectric regions 1, 2, and 3
$B_{1,2,3}$	constant in dielectric regions 1, 2, and 3
$C_{1,2,3}$	constant in dielectric regions 1, 2, and 3
$D_{1,2,3}$	constant in dielectric regions 1, 2, and 3
$\mathbf{B}$	magnetic flux density vector
B_0	static or low frequency magnetic flux density
C_{eff}	integration constant used in determining effective parameters for multilayer dielectrics
$\mathbf{D}$	displacement vector (general)
$\mathbf{D}_{1,2}$	displacement vector for dielectric regions 1 and 2
$\mathbf{D}_{eff}$	effective displacement vector for the multilayer dielectric material
$\mathbf{E}$	electric field vector (general)
$E_{1,2}$	electric field components for dielectric regions 1 and 2; they may have arbitrary direction
$E_{x,y}$	complex electric field amplitude components for light in fiber
$E_{\rho,\phi,z}$	electric field components in a coaxial line (cylindrical coordinates)
$E_{\rho 1,\rho 2,\rho 3}$	radial electric field components for different dielectric regions in a coaxial line
$E_{\phi 1,\phi 2,\phi 3}$	azimuthal electric field components for different dielectric regions in a coaxial line
$E_{z1,z2,z3}$	axial electric field components for different dielectric regions in a coaxial line
E_{eff}, $\mathbf{E}_{eff}$	effective electric field in a multilayer dielectric, effective electric field vector
E_m	dielectric or breakdown electric field strength
F	Faraday rotation per unit length
$\mathbf{H}$	magnetic field vector (general)
$H_{\rho,\phi,z}$	magnetic field components in a coaxial line (cylindrical coordinates)
$H_{\rho 1,\rho 2,\rho 3}$	radial magnetic field components for different dielectric regions in a coaxial line
$H_{\phi 1,\phi 2,\phi 3}$	azimuthal magnetic field components for different dielectric regions in a coaxial line
$H_{z1,z2,z3}$	axial magnetic field components for different dielectric regions in a coaxial line
H_{sat}	saturation magnetic field for ferromagnetic crystals
I	optical intensity
I_0	initial state (maximum) optical intensity
J_0	Bessel function of the first kind of order 0

J_1	Bessel function of the first kind of order 1
J_m	Bessel function of the first kind of order m
J'_m	first derivative of Bessel function of the first kind of order m
K_λ	fiber stress-optic parameter
L	total length of fiber or optical material
L_l	length of fiber in one coil turn
N	number of turns of optical fiber
N_d	molecular density
N_c	total number of turns in an optical fiber coil
N_δ	total number of delta function interactions or number of close passes of the fiber by the conductor
P	power (general)
P_{max}	maximum power handling capacity of a coaxial line
R	optical fiber coil radius
R_l	radius of curvature of fiber lead
R_f	amplifier feedback resistance
R_ℓ	radius of short circular fiber loop
S	planar surface area
S_{11}	electromagnetic reflection scattering parameter
S_{21}	electromagnetic transmission scattering parameter
T	absolute temperature
T_R	molecular reorientation time
V	Verdet constant
V_{ab}	voltage between conductors in coaxial line
X	radial length of an optical fiber lead
X_l	radial distance from center of fiber coil to electrical conductor
Y_0	Bessel function of the second kind of order 0
Y_1	Bessel function of the second kind of order 1
Y_m	Bessel function of the second kind of order m
Y'_m	first derivative of Bessel function of the second kind of order m
Z	impedance
Z_0	transmission line characteristic impedance
α_s	molecular static polarizability
α_c	attenuation due to conductor losses in a coaxial line
α_D	attenuation due to dielectric losses (absorption) in a coaxial line
α_m	attenuation of higher order modes in a coaxial line
β	waveguide (transmission line) propagation constant
β_{mn}	propagation constant for the mnth transmission line mode
δ	Dirac delta function, dielectric loss angle
δ'	electrical skin depth
λ	free space wavelength
ε	permittivity
$\varepsilon_{1,2}$	relative permittivities for dielectric regions 1 and 2

ε', ε''	real and imaginary components of relative permittivity
ε_0	free-space permittivity
ε_r	material relative permittivity (complex quantity)
ε_s	static (low frequency) relative permittivity
ε_{eff}	effective relative permittivity
μ	permeability
μ_0	free-space permeability
μ_r	material relative permeability
μ_f	fiber material permeability
η	electromagnetic wave impedance
κ	permittivity constant, ε_s - 1
ϕ	azimuthal angle in cylindrical coordinates
$\hat{\phi}$	azimuthal unit vector
ϕ'	total birefringence in optical medium
ς'	phase matching parameter in planar waveguide sensor
ρ	radial dimension in cylindrical coordinates
$\hat{\rho}$	radial dimension unit vector
σ	conductivity
$\theta_{1,2}$	taper angles for the center and outer conductors in a conical transmission line launcher
ξ	ratio of time delay to light transit time in a single fiber turn (fraction indicating light entry point in the fiber coil)
ξ_f	number of twists per unit length in optical fiber
ω	angular modulation frequency (general)
ω_c	cutoff angular frequency of higher order modes in coaxial transmission lines
ω_{co}	cutoff angular frequency (first null) in optical fiber sensor response
ω_R	angular resonant frequency
ω_u	angular frequency at which rotation relative magnitude is reduced 3 dB
$\omega\tau/2$	normalized frequency for optical fiber coil sensor
$\omega\tau_1/2$	normalized frequency for a single-turn fiber sensor
τ	transit time of light through fiber
τ_1	transit time of light through one turn of fiber
τ_d	light propagation delay time between fiber coils
τ_ℓ	transit time of light through length of fiber ℓ
τ_R	material magnetic ion relaxation time
ζ	normalized frequency parameter for traveling wave sensor
∞	infinity
α	rotary angle between dl and an arbitrary reference point on a fiber loop
α', β'	angles in the fiber coil plane used to locate a light segment in a fiber lead
α_0	initial value of α at time t = 0
β'_{max}	maximum value of the angle β'
γ	angle between the magnetic flux density vector **B** and the fiber length vector dl in the plane of the fiber coil

ψ	angle between the wave vector **k** and the fiber length vector **dl** out of the plane of the fiber coil
ΔB	3 dB bandwidth
ΔL	change in total fiber length in helical coil
$\Delta\beta$	linear birefringence or retardance per unit length
Ω'	twisting rotation per unit length
Θ	rotation in the plane of polarization (general); usually refers to Faraday rotation
$\Theta(\omega)$	frequency-dependent rotation
$\Theta_\delta(\omega)$	frequency dependent rotations due to delta function interactions
Θ_0	static or low frequency rotation
$\Theta_{1,2,3,\ldots}(\omega)$	rotations in different segments of fiber
$\Theta_m(\omega)$	frequency and material dependent Faraday rotation in paramagnetic crystals and glasses
$\Theta_\ell(\omega)$	frequency dependent rotation in short fiber length ℓ
Θ_F^{sat}	saturation rotation in ferromagnetic material
ANA	automatic network analyzer
APD	avalanche photodiode
BEF	bandwidth enhancement factor
DC (or dc)	direct current
EM	electromagnetic
EMI	electromagnetic interference
HOM	higher order modes
MM	multimode (fiber)
NEI	noise equivalent current
PIN	positive-intrinsic-negative
RF	radio frequency
SBP	sensitivity-bandwidth product
SM	singlemode (fiber)
S/N	signal-to-noise ratio
SWR	standing wave ratio
TE	transverse electric
TE_{mn}	mnth transverse electric mode
TEM	transverse electromagnetic
TM	transverse magnetic
TM_{mn}	mnth transverse magnetic mode
UV	ultraviolet
YIG	yttrium iron garnet
Ga:YIG	gallium substituted YIG

DISTRIBUTION:

1 Gordon W. Day
National Institute of Standards and Technology
Mail Code 815.00
325 Broadway
Boulder, CO 80303

1 Allen H. Rose
National Institute of Standards and Technology
Mail Code 815.03
325 Broadway
Boulder, CO 80303

5	MS 0351	R.W. Cernosek, Org. 1315
1	MS 0351	J.J. Wiczer, Org. 1315
1	MS 0175	W.W. Plummer, Org. 13214
1	MS 0899	Central Technical Files, Org. 8523-2
5	MS 0899	Technical Library, Org. 13414
1	MS 0619	Technical Publications, Org. 13416
10	MS 0100	Document Processing for DOE/OSTI, Org. 7613-2